Development and application of fluorescence lifetime imaging and super-resolution microscopy

Frederik Görlitz

Photonics Group

Department of Physics

Imperial College London

Thesis submitted in partial fulfilment of the requirements

for the degree of Doctor of Philosophy (Ph.D.)

Imperial College of Science, Technology and Medicine

To my father

Abstract

This PhD thesis reports the development and application of fluorescence imaging technologies for studying biological processes on spatial scales below the diffraction limit. Two strategies were addressed: firstly fluorescence lifetime imaging (FLIM) to study molecular processes, e.g. using Förster resonance energy transfer (FRET) to read out protein interactions, and secondly direct imaging of nanostructure using super-resolution microscopy (SRM).

For quantitative FRET readouts, the development and characterisation of an automated multiwell plate FLIM microscope for high content analysis (HCA) is described. Open source software was developed for the data acquisition and analysis, and approaches to improve the performance of time-gated imaging for FLIM were evaluated including different methods to despeckle the laser illumination and testing of an enhanced detector. This instrument was evaluated using standard fluorescent dye samples and cells expressing fluorescent protein-based FRET constructs. It was applied to an assay of live cells expressing a FRET biosensor and to FRET readouts of aggregation of a membrane receptor (DDR1) in fixed cells.

A novel instrument, combining structured illumination microscopy (SIM) with FLIM, was developed to explore the combination of SRM and FLIM-FRET readouts. This enabled the simultaneous mapping of molecular readouts with FLIM and super-resolved imaging. The "SIM+FLIM" system was applied to image collagen-stimulated DDR1 aggregation in cells, to image DNA structures during the cell cycle and to explore interactions between cell organelles.

A novel SRM approach based on a stimulated emission of depletion (STED) microscope incorporating a spatial light modulator (SLM) was developed to provide straightforward robust alignment with collinear excitation/depletion beams, aberration correction, an extended field of view and multiple beam scanning for faster STED image acquisition. The performance of "easySLM-STED" was evaluated by imaging bead samples, labelled vimentin in Vero cells and the synaptonemal complex in homologs of *C. elegans* germlines.

Kurzfassung[1]

Diese Doktorarbeit befasst sich mit der Anwendung und Entwicklung von fluoreszenzbildgebenden Technologien um biologische Prozesse unterhalb der Beugungsgrenze zu untersuchen. Zwei Strategien wurde nachgegangen: erstens Fluorescence Lifetime Imaging (FLIM) um molekulare Prozesse zu untersuchen, z.B. Förster Resonanz Energie Transfer (FRET) um Proteinwechselwirkungen zu messsen, und zweitens direkte Bildgebung von Nanostrukturen mit Hilfe von hochauflösender Mikroskopie (super-resolution microscopy, SRM).

Für quantitative FRET Messungen wurde ein automatisiertes Mikrotiterplatten FLIM Mikroskop für Hochdurchsatz-Screening (high content analysis, HCA) entwickelt und charakterisiert. Eine Open Source Software für Datenaufnahme und Datenverarbeitung wurde entworfen. Möglichkeiten, um die zeitgesteuerte Bildaufnahme für FLIM zu verbessern, werden vorgestellt wie verschiedene Lösungsansätze um die Granulation des Anregungslasers zu vermindern und der Test eines verbesserten Detektors. Dieses Instrument wurde mit genormten fluoreszierenden Farbstoffeproben und Zellen, welche fluoreszente proteinbasierende FRET Konstrukte exprimieren, vermessen. Es wurde verwendet in einem Assay mit lebende Zellen, welche FRET Biosensoren exprimieren, und um Aggregate von Zellmembranrezeptoren (DDR1) über FRET Messungen in fixierten Zellen darzustellen

Ein innovatives System, welches Stuctured Illumination Microscopy (SIM) mit FLIM verbindet, wurde entwickelt um die Kombination von SRM and FLIM-FRET Messungen zu erforschen. Somit wurde die gleichzeitige Vermessung von molekularen FLIM Signalen und hochauflösender Bildaufnahme ermöglicht. Das „SIM + FLIM“ Mikroskope wurde verwendet zur Bilderaufnahme von kollagenstimulierten DDR1 Aggregaten in Zellen, zur Abbildung von DNA Strukturen während des Zellzyklus und zur Erforschung von Wechselwirkung zwischen Zellorganellen.

Ferner wurde eine neuartige SRM Methode, basierend auf einem Stimulated Emission of Depletion (STED) Mikroskops mit Spatial Light Modulator (SLM), entwickelt um eine unkomplizierte und

---

[1] Translation of Abstract for German readers

robuste Justage mit kollinearen Anregungs- und Löschungslaserstrahl, Abbildungsfehlerkorrekturen, ein erweitertes Bildfeld und Laserstrahlscannen mit mehreren Laserstrahlen für schnellere STED Bildaufnahmen zu gewährleisten. Die Leistungsfähigkeit des „easySLM-STED“ Instruments wurde durch die Vermessung von Beadproben, markiertes Vimentin in Vero Zellen und dem synaptonemale Komplex in Homologs von *C. elegans* Keimlinien demonstriert.

Declaration of Originality

Declaration of originality I declare that all work presented in this thesis is my own, and that any ideas, information, data, results and figures from another source have been appropriately referenced or acknowledged. No part of this degree has been submitted for another degree or qualification.

Copyright Declarations

The copyright of this thesis rests with the author and is made available under a Creative Commons Attribution Non-Commercial No Derivatives licence. Researchers are free to copy, distribute or transmit the thesis on the condition that they attribute it, that they do not use it for commercial purposes and that they do not alter, transform or build upon it. For any reuse or redistribution, researchers must make clear to others the licence terms of this work.

Acknowledgement

I wish to thank various people for their contribution to this PhD thesis:

First of all, I would like to thank my supervisors Paul, Chris and Mark for the opportunity for this project and their guidance, help, advice and intense proofreading.

Thanks to the photonic's group; Hugh, Doug, Sean, Sunil, Hugo, Edwin, Vincent, Yuriy, Ian, Stina, James (Clegg and McGinty), Kwasi, Rob, George, Sam, Terry and in particular to my fellow inmates Elizabeth, Wenjun and Tom for the offered help and the time spent together.

Special thanks to the admin ladies Judith, Marcia and Sanja, without you I would have been lost, and the workshop guys Simon, Martin and John for the hard work on the custom-made optomechanics.

Thanks also to my collaborators David and Birgit for the preparation of DDR1 cells, Tim for the STED laser, Angel for the germlines in *C. elegans* and Lucien for the forskolin drug response curve.

Weiterer Dank gebührt zwei Personen die mein Interesse und Engagement in Physik initialisiert, unterstützt und gefördert haben; meinem Gymnasiallehrer Herrn Otmar Siegel und ehemaligen Gruppenleiter Johann Engelhard.[2]

Ferner danke ich meiner Familie und Freunden für Beistand und Ermutigungen.[3]

I would like to acknowledge my studentship funding provided by the Engineering and Physical Sciences Research Council via the Institute of Physics.

---

[2] Additional thanks to two persons who initialised, support and encouraged my interest in physics; my school teacher Mr. Otmar Siegel and former group leader Johann Engelhard

[3] Further I would like to thank my family and friends for assistance and encouragement

Abbreviations

A.D.	Anno Domini
ADC	Analogue-to-digital converter
AFM	Atomic force microscopy
AMPK	adenosine monophosphate activated protein kinase
ATP	Adenosine triphosphate
BrdU	Bromodeoxyuridine
C. elegans	Caenorhabditis elegans
cAMP	Cyclic adenosine monophosphate
CCD	Charged-coupled device
CGH	Computer-generated hologram
CFD	Constant fraction discriminator
CFP	Cyan fluorescent protein
CMOS	Complementary metal–oxide–semiconductor
CNGC	Cyclic nucleotide–gated channels
COM	Communication port
CROCC	Ciliary rootlet coiled-coil protein
DAQ	Data acquisition
DAPI	4',6-diamidino-2-phenylindole
DC	Direct current
DDR	Discoidin domain receptor
DM	Deformable mirror
DNA	Deoxyribonucleic acid
DONALD	Direct optical nanoscopy with axially localized detection
dSTORM	Direct STORM
ECTM	Extracellular and transmembrane

EdU 5-Ethynyl-2'-deoxyuridine

EGFP Enhanced green fluorescent protein

EGFP Enhanced GFP

Epac Exchange protein directly activated by cAMP

FCS Fluorescence correlation spectroscopy

FLIM Fluorescence lifetime imaging

FOV Field of view

FP Fluorescent protein

FRET Förster resonance energy transfer

FWHM Full width half maximum

GFP Green fluorescent protein

GOI Gated optical imager

Gorasp2 Golgi reassembly-stacking protein

GSDIM Ground state depletion microscopy followed by individual molecule return

H2B Histone 2B

HRI High rate imager

HXT Hoechst 33342

IP3 Inositol trisphosphate

IRF Instrument response function

LSFM Light sheet fluorescence microscopy

MCP Micro-channel plate

mTqFP mTurquoise fluorescent protein

NA numerical aperture

ND Neutral density

NIR Near-infrared

OTF Optical transfer function

PALM Photo activated localization microscopy

PBS Phosphate-buffered saline

PFA Paraformaldehyde

pH Potential of hydrogen

PIP2 Phosphatidylinositol 4,5-bisphosphate

PKA Protein kinase A

PMT Photon multiplier tube

PSF Point spread function

QWP	Quarter wave plate
R6G	Rhodamine 6G
RB	Rhodamine B
RESOLFT	Reversible saturable optical linear fluorescence transitions
RFP	Red fluorescent protein
ROI	Region of interest
RTK	Receptor tyrosine kinases
SAF	Super critical angle fluorescence
SC	synaptonemal complex
SCIM	Scanning ion-conductance microscope
sCMOS	Scientific CMOS
SIM	Structured illumination microscopy
SLM	Spatial light modulator
SMLM	Single molecule localization microscopy
SNOM	Scanning near-field optical microscopy
SSIM	Saturated SIM
stdev	Standard deviation
STED	Stimulated emission of depletion
STORM	Stochastic optical reconstruction microscopy
TAC	Time-to-analogue converter
TCSPC	Time correlated single photon counting
TDE	2,2'-thiodiethanol
TE	Trypsin-EDTA solution
TEM	Transverse electromagnetic mode
TIFF	Tagged image file format
Ti:Sapphire	Titanium-Sapphire
TM1	Transmembrane
TSA	Trichostatin A
TVB	Time varying background
VFP	Venus fluorescent protein
YFP	Yellow fluorescent protein

Contents

Abstract **i**

Declaration of Originality **iv**

Copyright Declarations **iv**

Acknowledgement **v**

Abbreviations **vi**

1 Thesis Overview **1**

2 Introduction **5**

2.1 Fluorescence 5

2.1.1 Overview 6

2.1.2 Absorption/Emission Spectra 6

2.1.3 Fluorescence lifetime 8

2.2 Microscopy 9

2.2.1 A brief history of microscopy 9

2.2.2 Diffraction limited resolution of a microscope 10

2.2.3 Diffraction limited microscopy 11

2.2.4 Super-resolution microscopy 19

2.3 Fluorescence lifetime microscopy (FLIM) 31

2.3.1 Frequency domain FLIM 31

2.3.2 Wide-field time-gated FLIM 32

2.3.3 Time-correlated single-photon counting 35

2.4 FLIM analysis 37

2.4.1 Instrument response function 37

2.4.2 Background signals in FLIM 39

2.4.3 Global decay analysis 40
2.5 Förster resonance energy transfer (FRET) 41
2.5.1 Photophysics of FRET 41
2.5.2 Methods to read out FRET 43
2.5.3 FRET biosensors 44
2.6 Adaptive optics in microscopy 46
2.6.1 Aberration correction in optical microscopy 46
2.6.2 Devices for adaptive optics 47
2.6.3 Application of adaptive optics in microscopy 48
2.6.4 Zernike polynomials 50
2.7 Summary 51

3 Open FLIM HCA with FRET readout 53
3.1 Open source FLIM HCA system 53
3.1.1 Instrument design 54
3.1.2 Operating software 55
3.1.3 Work-flow 56
3.2 Standardized high content FLIM assays 58
3.2.1 Assay of mono-exponential dyes with distinct lifetimes 58
3.2.2 Assay using plasmids expressing FRET constructs 60
3.2.3 Assay of FRET plasmids simulating a biosensor 62
3.2.4 Performance comparison of FRET plasmids in assay 64
3.3 Biological application: cAMP Epac biosensor 65
3.3.1 Biological background 65
3.3.2 Epac biosensor response upon forskolin stimulation 65
3.4 Summary 67

4 Advances in wide-field time-gated fluorescence lifetime imaging 69
4.1 New generation of high rate intensifiers 70
4.1.1 Resolution enhancement via a magnetic field 70
4.1.2 Enhancing fluorescence lifetime precision using longer time-gates 74
4.2 Evaluation of time-gated FLIM for cell biology 77
4.2.1 Effect of varying excitation power on lifetime determination 78
4.2.2 Effect of varying integration time on lifetime determination 80
4.3 Optimising the homogeneity of the laser illumination 82
4.3.1 Scanning "top-hat"engineered diffuser 83
4.3.2 Deformable mirror 84

4.3.3 Vibrating multimode optical fiber 85
4.4 Summary 87

5 **Mapping super-resolved structures to functional readout** **89**
5.1 SIM+FLIM instrument design 91
5.2 Performance evaluation 92
5.2.1 Lifetime precision assessment 92
5.2.2 Image registration between SIM and FLIM port 93
5.2.3 Imaging biological test sample 97
5.3 SIM+FLIM of genomic structures during cell cycle 98
5.3.1 Biological background 98
5.3.2 Imaging changes in DNA density 100
5.3.3 Imaging open and closed chromatin by labelling histones 105
5.4 SIM+FLIM of interactions between organelles (Golgi apparatus and ciliary rootlets) 107
5.4.1 Biological background 107
5.4.2 Control FLIM-FRET measurements of interacting organelles 108
5.4.3 SIM+FLIM of molecular interactions between Golgi apparatus and ciliary rootlets 109
5.5 Summary 111

6 **Application of FLIM and SIM to study activation of the discoidin domain receptor (DDR1)** **112**
6.1 Biological background 113
6.2 Introduction to the SNAP-tag labelling technique 114
6.3 Comparison of FLIM HCA using fluorescence protein and SNAP-tag labelling approaches 115
6.3.1 Comparison of FRET signals 116
6.3.2 FLIM HCA of DDR1 mutants to study DDR1 activation mechanism 117
6.3.3 Specificity of labelling approaches 118
6.3.4 Alternative labelling approaches to enhance FRET contrast for DDR1 aggregation 120
6.4 Evaluation of labelling approaches for SIM of DDR1 activation 122
6.4.1 SIM reveals labelling artefacts of antibodies 123
6.4.2 From aggregation to phosphorylation 124
6.5 SIM+FLIM applied to DDR1 aggregation 126
6.6 Summary 128

7 Stimulated emission depletion microscopy (STED) with a single spatial light modulator (SLM) for collinear alignment, aberration correction and multiplexed imaging 130

7.1 easySLM-STED 131
    7.1.1 easySLM-STED instrument design 132
    7.1.2 easySLM-STED performance evaluation 134
    7.1.3 easySLM-STED of biological sample: vimentin in Vero cells 136
    7.1.4 easySLM-STED of biological sample: *C. elegans* germline 138
7.2 Mosaic easySLM-STED with aberration correction 140
    7.2.1 Chromatic aberration for large FOVs 141
    7.2.2 Sequential aberration correction for mosaic easySLM-STED 143
    7.2.3 Mosaic easySLM-STED of biological samples: vimentin in Vero cells 147
7.3 Multibeam easySLM-STED 148
    7.3.1 Generation of multiple beams 149
    7.3.2 Performance of multibeam easySLM-STED scanning separate sub-regions . 154
7.4 Summary 158

8 Conclusion and outlook 159

9 Supplementary 166

9.1 Cell culturing and transfection 166
9.2 Switch on procedure SIM+FLIM setup 167
9.3 Procedure for SIM+FLIM image registration 169
9.4 DDR1 staining techniques 169
9.5 STED setup manual 171
    9.5.1 Switch on procedure for easySLM-STED 173
    9.5.2 General alignment 174
    9.5.3 Fine alignment 177
    9.5.4 Specific alignment procedures for mosaic easySLM-STED 178
    9.5.5 Specific alignment procedures for multibeam easySLM-STED 179
    9.5.6 Doughnut first aid 181
    9.5.7 Software manual: easySLM-STED control program 185
    9.5.8 Software manual: hologram control program 191
    9.5.9 Bead sample preparation 195

Publications 196

Copyright Clearances 198

A Depletion laser manual **241**

List of Figures

2.1 Absorption and emission spectrum of anthracene and Jablonski diagram 6

2.2 Molecular probability function of electron transition 8

2.3 Drawing of cork from Robert Hooke 9

2.4 Schematics of wide-field microscope and confocal microscope 13

2.5 Spinning disk scheme 14

2.6 Schematic of single, two and three photon excitation 16

2.7 x-z excitation intensity distribution for a confocal microscope and a 4π microscope 17

2.8 Original configuration of light sheet microscope 1902 18

2.9 STORM concept 21

2.10 Moiré effect 22

2.11 SIM concept 24

2.12 Nonlinear SIM concept 25

2.13 Jablonski diagram for the stimulated emission effect in fluorescence and effective PSF shape for STED principle 27

2.14 STED principle 28

2.15 Two colour STED microscopy images of amphibian nuclear protein complexes and STED microscopy image and intensity line profile of fluorescent nitrogen vacancy centre 28

2.16 Depletion beam shaping devices 29

2.17 3D STED PSF 30

2.18 Wide-field time-gated FLIM outline 33

2.19 GOI concept 34

2.20 Schematic of TCSPC circuitry 36

2.21 CFD concept 36

2.22 Simulation of a measured fluorescence decay profile impacted by an IRF 38

2.23 Time-gated, GOI based image of a reflected light shows the radial distribution of the t_0 shift. 38

2.24 Necessary conditions for FRET 42
2.25 Inter- vs Intramolecular FRET biosensors 45
2.26 Wavefront distortion in high NA objective microscopy by specimen induced aberrations 46

3.1 Schematic of the automated wide-field time-gated multiwell plate FLIM microscope with optical sectioning. 54
3.2 Schematic structure of *µManager* control software 55
3.3 High content dye mixing ratio template 58
3.4 Fluorescence lifetimes and mixing ratios obtained from FLIM measurements of exemplar multiwell dye sample plate with different ratios of Rhodamine 6G and Rhodamine B 60
3.5 FRETing construct assay in COS-7 cells 61
3.6 FRETing construct assay lifetime graph 61
3.7 Simulated FRET biosensor assay with FRET constructs. 63
3.8 FRET parameters obtained from simulated biosensor assay with FRET constructs. 64
3.9 Performance comparison of different FRET plasmids 64
3.10 cAMP activation curve of Epac FRET biosensor upon forskolin stimulation 66
3.11 cAMP activation visualisation of Epac FRET biosensor upon forskolin stimulation at a single FOV 67

4.1 Outline of a wide-field time-gated FLIM microscope 69
4.2 Schematic of gated optical image intensifier 71
4.3 Spatial resolution measurements with radial test chart 72
4.4 Intensity merged fluorescence lifetime and time-integrated fluorescence intensity images of stained (convallaria) sample 73
4.5 Time-gated optically-sectioned fluorescence intensity images of HEK293T cell . . . 74
4.6 IRFs measured using back-scattered excitation light 74
4.7 Histogram of lifetimes measured for solutions of Rhodamine 6G and Rhodamine B 75
4.8 Wide-field time-gated FLIM data of R6G and RB simulating FRET efficiencies . . 76
4.9 Plate map and variation of number of cells found by the *FLIMfit* segmentation tool for different excitation intensities (ND filter 0, 0.1, 0.2 and 1) and HRI gate widths (1 ns and 4 ns). 78
4.10 Variation of the mean lifetimes and standard deviations measured for cells expressing mTq5A and mTq17V as a function of excitation intensity (ND filters 0, 0.1, 0.2 and 1) and gate width (1 ns and 4 ns) 79

4.11 *FLIMfit* segmentation tool recognized cells for different integration times ranging from 25 ms to 800 ms 80
4.12 Variation of the mean lifetimes (a,b) and standard deviations (c,d) measured for cells expressing mTq5A (a,c)) and mTq17V (b,d) as a function of different camera integration times 81
4.13 Top-hat diffuser configuration in wide-field time-gated FLIM setup. 83
4.14 Intensity distributions of laser light transmitted by an engineered diffuser 84
4.15 Intensity distributions of laser light reflected from a deformable mirror 85
4.16 Intensity distributions of laser light passing a MOF with a core diameter of 50 μm 86
4.17 Intensity distributions of laser light passing a MOF with a core diameter of 100 μm 87

5.1 SIM+FLIM design 91
5.2 FLIM data obtained from 75 μM Coumarin 6 in ethanol 92
5.3 Fluorescence bead image acquired by FLIM port 93
5.4 Three color fluorescence bead images acquired using the SIM port (presenting wide-field, deconvolved and SIM images) 94
5.5 Visualisation process of a SIM+FLIM image of 200 nm diameter fluorescent beads 95
5.6 SIM+FLIM images of a stained Convallaria sample 97
5.7 Spatial levels of nucleus structure 99
5.8 S-phase NIH3T3 cells with less-dense (open) and denser DNA (closed chromatin) imaged with SIM+FLIM. 102
5.9 SIM+FLIM of mitotic and S-phase cells. 103
5.10 Intensity-weighted Alexa 594 (FRET donor) lifetime histogram for cells in different stages during cell division 105
5.11 Histone acetylation with and without TSA treatment 106
5.12 SIM image of Golgi apparatus and rootletin 107
5.13 SIM+FLIM images of Golgi apparatus protein interaction 108
5.14 SIM+FLIM image of Golgi apparatus and rootletin 110

6.1 Schematic of DDR1 protein structure 113
6.2 DDR1 labelling approaches with fluorescence proteins and SNAP-tags 115
6.3 Donor fluorescence lifetime change over time after stimulation with collagen for COS-7 cells expressing DDR1 labelled with either fluorescent protein or SNAP-tag FRET constructs 117
6.4 Collagen response of DDR1 mutants 118
6.5 Fluorescence lifetime images of COS-7 cells transfected with FRET constructs encoding DDR1 with fluorescent proteins or SNAP-tag conjugated dyes 119

6.6 Heterodimer and homodimer configurations of labelled DDR1 120
6.7 Comparison of donor lifetimes with stdev observed for DDR1 labelled with SNAP-tags labelling donor only, stochastically labelling mixtures of heterodimers and homodimers or labelling only homodimers 121
6.8 Different labelling approaches of aggregated DDR1 122
6.9 Two color wide-field and SIM images of collagen-stimulated DDR1 labelled with antibody and SNAP-tag 123
6.10 Three color SIM images of collagen-stimulated DDR1 in fixed COS-7 cells with SNAP-tag labelled DDR1, antibody labelled DDR1 and antibody against phosphorylated DDR1 125
6.11 SIM+FLIM images of collagen-stimulated COS-7 cells expressing DDR1 using the SNAP-tag approach to provide a FRET readout of aggregation 126
6.12 SIM and FLIM control images 127

7.1 easySLM-STED design 132
7.2 Time resolved depletion and excitation laser pulse shapes 133
7.3 easySLM-STED PSF 135
7.4 easySLM-STED image of fluorescence beads 135
7.5 easySLM-STED resolution in dependency of depletion laser intensity 136
7.6 easySLM-STED image of vimentin in Vero cells 137
7.7 Line scans through features in Figure 7.6 137
7.8 Germline in *C. elegans* and synaptonemal complex 138
7.9 Confocal image and easySLM-STED images of synaptonemal complex gap of separate germlines in *C. elegans* from the end of the transition phase 139
7.10 Normal and mosaic confocal imaging of USAF target 140
7.11 Two laser scanned bead samples without and with aberration correction in mosaic mode 141
7.12 Gold bead sample without and with aberration correction in easySLM-STED mode 142
7.13 easySLM-STED fluorescent bead sample without and with aberration correction in mosaic mode 143
7.14 Normalised intensity localization images in confocal and easySLM-STED mode (corrected and uncorrected) 144
7.15 FWHM localization images in confocal and easySLM-STED mode (corrected and uncorrected) 145
7.16 Radial dependence of localized intensities and FWHM of fluorescent beads in mosaic and normal imaging modes 146

7.17 Performance comparison of normal and mosaic approach in confocal mode 146
7.18 Mosaic easySLM-STED image of vimentin in Vero cells 147
7.19 Multibeam easySLM-STED line and lattice pattern generation 150
7.20 Generation of differently spaced easySLM-STED beams 151
7.21 Generation of different numbers of easySLM-STED beams 152
7.22 Four beam easySLM-STED beams compared to single beam easySLM-STED . . . 153
7.23 Multibeam easySLM-STED of fluorescent bead sample 154
7.24 Line profiles over fluorescent beads acquired via multibeam easySLM-STED 156
7.25 Multibeam STED image of synaptonemal complex in *C. elegans* 157

9.1 easySLM-STED design with abbreviations 172
9.2 Simulation of ideal depletion PSF. 181
9.3 Simulation of depletion PSF with beam-hologram misalignment 182
9.4 Simulation of the depletion PSF with beam-objective misalignment 183
9.5 Simulation of the depletion PSF with astigmatism and spherical aberrations. . . . 184
9.6 Simulation of the depletion PSF with polarisation and blaze grating mismatch. . . 185
9.7 Control software overview 186
9.8 Control software for setting scan patterns 187
9.9 Control software mosaic with aberration correction 189
9.10 Hologram control software main frame 192
9.11 Hologram software aberration frame 193
9.12 Hologram control software multibeam frame 194

List of Tables

2.1 Zernike polynomials in polar coordinates 50

3.1 FRETing construct assay mean lifetime 62

4.1 Mean lifetime and standard deviation in ps of measurements of solutions of R6G and RB for different time-gate widths. 75

5.1 DNA packaging during cell division. 104

5.2 Intensity-weighted cell-averaged lifetimes measured for H2B labelled with FRET donor-only or FRET donor and acceptor in presence of TSA. 106

5.3 Donor fluorescence lifetime data corresponding to Figure 5.13 for study of intermolecular FRET between Gorasp2 and GM130 109

7.1 Multibeam easySLM-STED of fluorescent bead sample data 155

Chapter 1

Thesis Overview

This PhD thesis reports the development and application of fluorescence imaging technologies for studying biological processes on scales below the diffraction limit. Molecular processes can be probed using spectroscopic readouts, e.g. using Förster resonance energy transfer (FRET) to read out changes in fluorophore separations on a scale below 10 nm and thereby study fluorescently labelled protein interactions. Structure and function can also be directly imaged using super-resolved microscopy (SRM) techniques to provide information on spatial scales below 200 nm. This thesis address both strategies, firstly through the use of fluorescence lifetime imaging (FLIM) to provide quantitative readouts of FRET, and secondly through the use of structured illumination microscopy (SIM) and stimulated emission depletion microscopy (STED) to realise SRM.

Chapter 2 introduces the science behind the experiments and analysis presented in this thesis, including the basic photophysics of fluorescence imaging and spectroscopy, including the main fluorescence microscopy techniques, fluorescence lifetime imaging (FLIM) and super-resolved fluorescence microscopy techniques. An overview of adaptive optics and the compensation of optical aberrations is also presented.

Fluorescence lifetime and FRET measurements provide spectroscopic readouts that can be used to probe molecular processes. Usually they are implemented in manual wide-field epifluorescence or laser scanning confocal or multiphoton microscopes. Because quantitative fluorescence lifetime-based FRET measurements of complex decay profiles require more photons than fluorescence intensity imaging, it can be challenging to acquire sufficient photons without causing photobleaching (and phototoxicity in live samples). Such image-based measurements are well suited to global analysis techniques where data with lower photon counts can be fitted over multiple pixels and multiple fields of view under the assumption that fluorescence lifetime components are spatially invariant. Implementing FLIM over 100's of fields of view of similarly prepared samples can be realised using multiwell plate sample arrays to provide statistical robustness, even with relatively small changes in fluorescence lifetime. Automated imaging of multiwell plate arrayed samples for image-based analysis is commonly described as high content analysis (HCA) and is widely used in drug discovery and molecular biology, e.g. to identify and quantify cell signalling processes. FLIM of FRET can be used to quantify protein-protein interactions or to map the concentration of analyses using appropriate FRET biosensors. However, commercially available automated microscopes for HCA do not currently offer FLIM, although instruments for spectral ratiometric intensity-based FRET are available. FLIM of FRET requires only measurement of the donor fluorescence and so avoids the need for spectral calibration with reference samples that need to be done for each experimental set-up. **Chapter 3** presents "openFLIM-HCA", an FLIM HCA platform that has been developed using open source software and published component lists to make it easy to replicate by other researchers. The performance of the FLIM HCA instrument with standard dye-based assays and with live cells expressing an Epac FRET biosensor for cAMP upon forskolin stimulation is discussed.

The advantages of wide-field time-gated FLIM are rapid image acquisition and low photobleaching compared to laser scanning FLIM microscopy. The key component in most time-gated FLIM systems is a gated optical image intensity (GOI). This component typically limits the performance in terms of spatial resolution and precision of lifetime determination. However, the results obtained ultimately depend on the whole system. In **Chapter 4**, work to improve the time-gated imaging system is reported, including the testing of different strategies to realise uniform excitation intensity across the field of view and the evaluation of a new GOI developed by Kentech Instruments Ltd to provide enhanced spatial resolution and longer time-gate widths. The dependence of the precision of lifetime determination was studied as a function of excitation light doses and image acquisition time for the new GOI and the established commercially available technology. This study was undertaken with dye-based reference samples and with cells expressing fluorescent protein-based FRET constructs.

The resolution of the wide-field fluorescence lifetime imaging system described in this thesis is limited by diffraction and by the GOI. To enable the functional readouts afforded by FLIM and FRET to be correlated with variation of the nanostructure in a sample, a novel instrument combining wide-field time-gated FLIM with structured illumination microscopy (SIM) was developed. SIM is a wide-field fluorescence imaging technique that effectively increases the spatial frequency bandpass of the microscope by a factor of 2. It entails acquiring a number of spatially modulated fluorescence images and combining them to calculate a higher spatial resolution image, with practical resolutions of ∼100 nm being achievable. **Chapter 5** describes the imaging instrumentation, data acquisition and analysis work-flows that were developed together with its evaluation and the application of “SIM+FLIM” to image genomic structures, such as DNA and histones, where FLIM-FRET was used to image chromatin compaction in s-phase and mitotic cells. SIM+FLIM was also explored as a tool to image interactions between cell organelles, including Golgi apparatus and ciliary rootlets, where the sensitivity of FRET to proximity within 10 nm can be combined with SIM images of organelle interactions.

Both the openFLIM-HCA and the SIM+FLIM instruments were applied to studies of discoidin domain receptor (DDR) aggregation upon stimulation with collagen, as discussed in **Chapter 6**. DDR oligomerisation is an essential process in the cell cycle, cell differentiation, cell survival and cell migration but the underlying mechanisms are not yet clear. FLIM FRET provides a means to read out aggregation of proteins if they are stochastically labelled with donor and acceptor fluorophores. Studies were undertaken comparing the performance of FLIM HCA with DDR1 labeled with fluorescence proteins or with SNAP-tags conjugated to organic dyes. DDR1 aggregation was also investigated using SIM, comparing the performance of labelling DDR1 with fluorescent proteins, antibodies and SNAP-tags. Finally, the SIM+FLIM approach was applied to correlate FLIM-FRET readouts of DDR1 aggregation with SIM images of the DDR1 distribution after collagen stimulation.

In **Chapter 7**, a different SRM technique was explored that can also be combined with FLIM and which provides resolution below 100 nm. Stimulated emission of depletion (STED) microscopy is a laser scanning SRM technique that has the potential for arbitrary resolution improvement, subject to the sample being able to tolerate high incident laser intensities, and is compatible with live cell imaging. However, most implementations of STED microscopy are relatively complex, challenging to maintain in alignment and are relatively slow and sensitive to aberrations. To address these challenges, a new technique called easySLM-STED is presented that uses a single spatial light modulator (SLM) to shape the depletion beam profile while also compensating aberrations in both beams as necessary and extending the achievable super-resolved field of view (to 100 μm) using a chromatic shift corrected mosaic technique. This builds on the earlier easySTED technique but provides more flexibility in terms of wavelengths and compensation of aberrations. It also works with initially collinear excitation and depletion beams that remain collinear through the entire optical path to the microscope objective lens. The SLM is employed in a way that it acts sequentially and differently on the excitation and depletion beams in a double pass configuration that enables the correction of chromatic walkoff between the beams, including that arising in the scanner (thereby increasing the achievable super-resolved field of view), as well as the electronically controlled compensation of chromatic and spherical aberrations in the microscope and sample. An extended STED field of view was realised using a mosaic approach combined with the SLM-based chromatic aberration correction. The SLM can also be used for fine tuning of the alignment and focusing of each beam. The performance of this easySLM-STED system was evaluated using fluorescent nanoparticle reference samples, a biological reference sample of fixed Vero cells with dye-stained vimentin and was applied to image the synaptonemal complex in homologs of *C. elegans* germlines. A further feature of the easySLM-STED approach is the ability to program the SLM to diffract multiple pairs of excitation and depletion beams that can be scanned in parallel to decrease the STED image acquisition time. This was demonstrated using four parallel scanned excitation/depletion beam pairs, realising the same resolution as with a single scanned beam pair when imaging fluorescent nanoparticles and the synaptonemal complex in *C. elegans* but with only a quarter of the acquisition time of a single scanning beam. A manual with instructions to configure and operate the easySLM-STED microscope is provided in the supplementary of this thesis.

Chapter 8 concludes the thesis, summarizing the work undertaken, the lessons learned and the opportunities for future development of the technologies discussed in this thesis.

Chapter 2

Introduction

This chapter provides the scientific background of the various instruments and techniques discussed in this PhD thesis. It aims to explain the phenomenon of fluorescence and its properties. A description of the main microscopy techniques currently in use, along with more detailed discussion of super-resolution microscopy, is given. Förster Resonance Energy Transfer is described with particular focus on its detection and quantification using Fluorescence Lifetime IMaging (FLIM). Different FLIM methods are described and the analysis of time domain FLIM data is discussed. Finally, a summary of adaptive optics in microscopy is given. Unless stated otherwise, further information concerning the material in this chapter can be found in the classic textbook by Lakowicz [Lak06].

2.1 Fluorescence

Fluorescence was first mentioned 1852 by G.G. Stokes: *"... I am almost inclined to coin a word, and call the appearance fluorescence, from fluor-spar, as the analogous term opalescence is derived from the name of a mineral. ..."* [Sto52](:479). Fluorescence imaging and metrology are key techniques in biology, chemistry, medicine and physics. Fluorescence spectroscopic and imaging methods can be applied utilising a range of fluorescence properties, including the absorption and emission spectra and the temporal characteristic, the fluorescence lifetime. Fluorescence-based readouts are used in a variety of applications such as microscopy of cell biology, flow cytometry, preclinical and clinical imaging, DNA sequencing and drug discovery.

2.1.1 Overview

Luminescence is a term for any emission of light from a material. It can occur if a substance has at least one electronically excited state, from which an excited orbital electron can relax back to its ground state and the energy released may be converted into a photon. Two different types of luminescence are reported fluorescence and phosphorescence. For fluorescence, the excited electron has the opposite spin to the electron in the ground state. Thus, transitions between electronic energy levels are permitted according to Pauli's Principle [Pau25], and relaxation typically occurs in the nanosecond range. Phosphorescence, on the other hand, occurs on a time scale of milliseconds to seconds, because the excited electron is in a triplet state with the same spin orientation as the ground state electron and the transition between electronic energy levels is per se prohibited. However, perturbation theory of spin-allowed electronic transitions using intensity borrowing can explain a relaxation into the forbidden state [Bar17].

2.1.2 Absorption/Emission Spectra

Every substance has its own characteristic absorption and emission spectra, which are a function of the underlying electronic energy level structure. As an example, the absorption and emission spectra for anthracene are presented in Figure 2.1 (a). When illuminating a sample with white light, only light at specific characteristic wavelengths will be transmitted, and this information can be used to determine the absorption spectrum of the substance. In addition, excited fluorophores emit light at specific characteristic wavelengths. To understand the origins of the shape of the

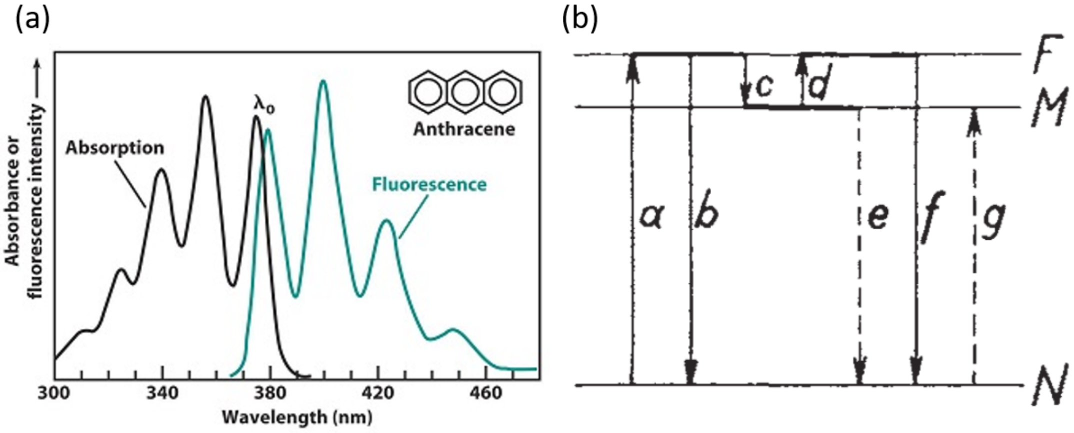

Figure 2.1: *(a) Absorption and emission spectrum of anthracene [Byr91] and (b) generalised form of a Jablonski diagram [Jab33].*

absorption and emission spectra, it is useful to consider a few key aspects of fluorescence, which can be discussed with the aid of the Jablonski diagram, the Stokes shift and the Franck-Condon principle.

The Jablonski diagram shown in Figure 2.1 (b) indicates different energy levels of a molecule with the possible transitions for an electron. An electron can be excited (a) almost instantaneously from its ground electronic state (N) into any of the vibrational and rotational energy levels (F) of the first excited electronic energy level. By internal vibrational relaxation (c), it converts into the lowest vibrational energy level of the first excited electronic energy level (M) in picoseconds, from where it relaxes down to its ground state (e) in nanoseconds by emitting a photon. The difference between the excitation energy and the emission photon energy accounts for the energy of the internal vibrational relaxation and is called the "Stokes shift" [Sto52], which is the reason why fluorophores emit light at longer wavelengths compared to the wavelength of the light used to excite them. Photon energy and wavelength are related via the relationship $E = \frac{hc}{\lambda}$, where E is the energy of photon, h is Planck's constant, c is the velocity of light and λ is the wavelength.

The Franck Condon principle[1] [Con26] explains the shape of the absorption and emission spectra with its individual peaks, as well as the mirror symmetry between them. Every electronic state has vibrational energy levels with associated probability functions. The vibrational probability functions for different electronic excited states are typically identical. The probability of an electron to be excited into an excited state depends on the overlap of the two probability functions. Thus, there are preferred transitions positions with higher probabilities and specific energies, depending on the overlap integral. These high probability transitions describe the characteristic peaks of absorption and emission spectra, such as those depicted in Figure 2.1 (a) and Figure 2.2 (b). Since the probability functions of the vibrational states are the same for the excited and ground state, the probability distribution to excite from the lowest vibrational energy level of the ground state to a specific energy level in the excited state (e.g. $0 \Rightarrow 2$) is the same as the probability distribution of relaxation from the lowest vibrational energy level of the excited state to the specific energy level of the ground state, (i.e. $2 \Rightarrow 0$). Therefore, the emission spectrum typically has a mirror symmetry with the absorption spectrum, as shown in Figure 2.2.

---

[1] Note the Franck Condon principle assumes the molecule-electron distance is constant. This assumption can be made because the excitation (10 ^{15} s) is much faster than the core vibration (10 ^{13} s).

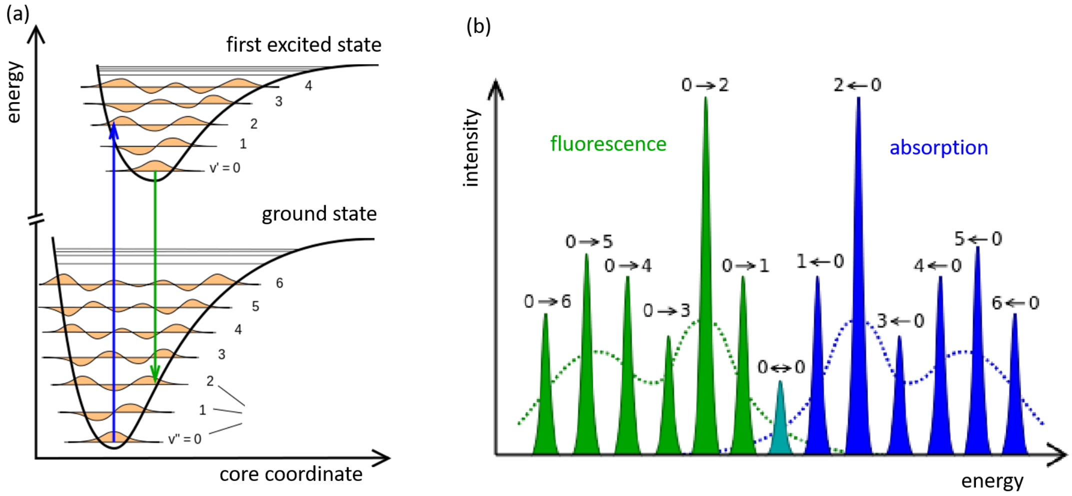
(a)
energy
first excited state
4
3
2
1
v' = 0
ground state
6
5
4
3
2
1
v" = 0
core coordinate
(b)
intensity
fluorescence
absorption
0→2
2←0
0→5
0→4
0→6
0→3
0→1
1←0
0↔0
3←0
4←0
5←0
6←0
energy

Figure 2.2: *Molecular probability functions of electron transitions: (a) probability functions of an electron in the ground and excited state and (b) mirror rule with characteristic energy transitions. Pictures adapted from [Con17].*

2.1.3 Fluorescence lifetime

The average time an electron spends in its excited state is a characteristic of a specific fluorophore, described as the fluorescence lifetime. The electron can return to its ground state by emitting a photon or via other non-radiative processes, for example quenching or Förster Resonance Energy Transfer (FRET). For first order kinetics, the fluorescence signal after excitation has ceased is:

$$S_1(t) = S_0 \ exp^{-t*\Gamma} \tag{2.1}$$

where S_1 is the number of photons remaining in the excited state and Γ is the total decay rate. The fluorescence lifetime is $\tau = 1/\Gamma$. This total decay rate is often separated into the radiative (or "natural") decay rate, (Γ_{rad}), corresponding to fluorescence, and a non-radiative rate (Γ_{nonrad}) corresponding to non-emissive decay pathways. The non-radiative term can be several times larger than the natural decay rate, so it can have a large effect on the fluorescence intensity and lifetime, and is sometimes referred to as "quenching". Quenching can be due to collisions of the fluorophore with other molecules such as molecular oxygen or non-radiative energy transfer, e.g. FRET.

2.2 Microscopy

2.2.1 A brief history of microscopy

This section is based on the ”Notes on the Early History of Microscopy” from Singer et al [Sin14] and the Carl Zeiss webpage [Zei17a]. “Who invited the microscope?” is more a philosophical than a scientific question, as first it is necessary to define what is a microscope. If only a magnification effect defines a microscope, this history begins thousands of years ago. A. D. 63 is the first written proof of a human using an item to magnify an object. Seneca noted that he could magnify letters by looking through a glass sphere filled with water. Around 10th century, Alhazen used curved mirrors to acquire magnified images. During the 13th century, Salvino D'Armate, produced lenses to gain a magnification of 6–10x. However, the invention of the microscope is often ascribed to Zacharias Jansen and Johannes Zachariassen, son and father. Around the 1590's, they used two lenses to gain a magnification of around 9x. Antonie von Leeuwenhoek and Robert Hooke (reporting in his masterpiece Micrographia) were the first people to use microscopes to study biological structures such as bacteria, yeast and the circulation of blood cells. Hooke's Micrographia includes his famous illustrations of fleas and cork (Figure 2.3). In cork, he discovered small compartments which he named “cells” and was the first person to report observing a biological cell. After a 200-year break without any significant improvements in microscopy, Carl Zeiss was working around 1850 on methods to obtain higher quality lenses for his microscopes. He founded a prominent microscope company, within the glass specialist Otto Schott made significant improvements to the lenses around 1880 while working as the company's research and development manager. The Carl Zeiss company also employed an engineer named Ernst Abbe to optimise the manufacturing process of the optical instruments. Abbe defined the diffraction limit which is still the basis of modern microscopy. In 1904, August Köhler was the first person to observe fluorescence under a microscope. In 1908, he and Henry Siedentopf developed the first

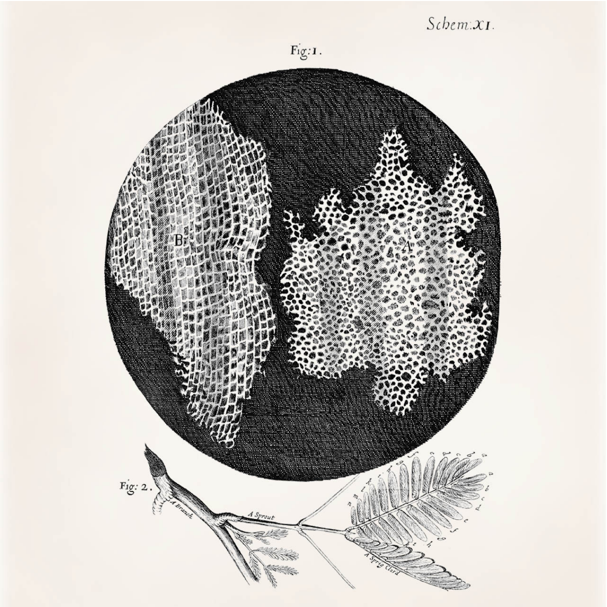

Figure 2.3: *Drawing of cork from Robert Hooke [Hoo65], British Library Board (435.e.19.XI).*

fluorescence microscope, although it was presented as a luminescence microscope. From 1911 onwards, Karl Reichert made significant improvements towards developing the modern fluorescence microscope.

2.2.2 Diffraction limited resolution of a microscope

In 1873, Ernst Abbe established the theoretical resolution limit of an optical microscope d_{Abbe}, which is only dependent on the diffraction of light. *"... die physikalische Unterscheidungsgrenze ... hängt allein vom Öffnungswinkel ab uns ist dem Sinus seines halben Betrags proportional."*[2] [Abb73](:466), with λ is the wavelength, NA is the numeric aperture ($NA = n * sin(\alpha)$), n is the refractive index and α is the acceptance ("opening") angle of the microscope (objective):

$$d_{Abbe} = \frac{\lambda}{2NA} \tag{2.2}$$

Rayleigh took a different approach and developed previous work from Airy [Air35] to define a resolution limit for telescopes, called the "Rayleigh criterion". He considered the Airy rings of two separate pinholes which he transferred to microscopy. He defined two single point objects as resolvable if the Airy disc maximum of the first object is not closer than the first minimum of the Airy disc of the second object. *"We may consider this to be about the limit of closeness at which there could be any decided appearance of resolution."* [Ray79](:266):

$$d_{Rayleigh} = 1.22\,\frac{\lambda}{2NA} \tag{2.3}$$

The Airy function is the ideal diffraction-limited image of an infinitely small point when the limiting aperture in the microscope is circular. More generally, ideal diffraction-limited image of an infinitely small point is described as the point spread function (PSF). For practical reasons, the full width half maximum (FWHM) of the PSF is often used to describe a resolution limit in an experimental context. The performance of a microscope can also be considered in terms of spatial frequencies, which can be considered as the set of sinusoidal waves that make up the image when superimposed. The optical transfer function (OTF) is the Fourier transform of the PSF. It is a function of spatial frequency that determines how spatial frequencies (and therefore image information) are transmitted through an optical instrument. The larger is the extent of the OTF, the higher the spatial frequencies that can be transmitted to the image and therefore, the narrower will be the PSF and the higher will be the resolution of the optical image. The cut-off spatial frequency (i.e. the highest spatial frequency that will be present in the image) is limited by the numerical aperture of a microscope. For conventional microscopes with circular apertures limited by the NA, the following expressions have been derived for the lateral (d_{FWHMxy}) and axial (d_{FWHMz}) resolution in terms of the FWHM of the PSF of an isolated point-like object [Wil11]:

---

[2] "... the physical discrimination limit ... depends only on the opening angle and is proportional to the half of its sinus."

$$d_{FWHMxy} = 0.51\,\frac{\lambda}{NA} \tag{2.4}$$

$$d_{FWHMz} = 0.89\,\frac{\lambda}{n-\sqrt{n^2-NA^2}} \tag{2.5}$$

If an image with the highest physical resolution should be digitized with an electronic camera, the pixel size is an important consideration (as is the pixel size in scanning microscopy). The pixels should be sufficiently closely spaced to not lose any spatial information. The Nyquist–Shannon sampling theorem [Nyq28] sets the maximum pixel size for lossless sampling to be less than half the achievable resolution at the camera imaging plane. There is usually no benefit to oversampling and the pixels should not be much smaller in order to maximise the number of resolution elements and therefore field of view (FOV) for the instrument.

To estimate the resolution achieved in an imaging experiment, a Gaussian function can be fitted to the smallest discernible object and the 1/e width (standard deviation, σ) can be determined. The FWHM of the Gaussian function is related to σ by $FWHM = 2\sqrt{2\ln 2} * \sigma$. This provides a rapid means to estimate the resolution without specific knowledge of the optical system and its theoretical resolution limit. This method can fail if the smallest discernible object is larger than the resolution limit and so resolution is commonly estimated by imaging fluorescent beads of a known diameter that are much smaller than the expected resolution limit. This method can also lead to errors when dealing with non-standard point spread functions (PSF), for which second order effects can become significant [Ric59a].

2.2.3 Diffraction limited microscopy

There are a wide variety of fluorescence microscopy techniques and this introduction will only describe a selection of the most common methods. It is useful to discriminate between diffraction limited fluorescence microscopy and super-resolution microscopy that provides resolutions below the conventional diffraction limit.

Bright-field microscopy is the most basic microscopy technique, where white light is passed through a condenser lens to illuminate a sample that absorbs and/or scatters light depending on its composition. This leads to intensity variations between different regions of the transmitted light across the sample. The objective lens collects the transmitted light and forms an image with a second lens that can be detected by the human eye (via the ocular lens) or by a camera. The disadvantages of bright-field microscopy include a high background of light that does not interact with the sample and a lack of (molecular) contrast for typical biological samples such as cells.

Wide-field fluorescence microscopy

Fluorescence microscopy provides molecular contrast that can be enhanced using appropriate labels and, because of the Stoke's shift, the background excitation light can be effectively eliminated using spectral filters, enabling emission from single molecules to be detected. The easiest way to implement fluorescence microscopy is epifluorescence microscopy, for which the essential components are an appropriate light source for fluorescence excitation; an objective lens that is used to both illuminate and collect fluorescence from the sample, a dichroic beamsplitter to separate the excitation light and fluorescence emission and an emission filter that prevents excitation light from reaching the detector.

A typical setup for an epifluorescence microscope is depicted in Figure 2.4 (a). The light source should be bright in the excitation spectrum of the fluorophores but spectrally restricted such that no source light can reach the detector. Often a mercury lamp with an emission bandpass filter or a laser is used for excitation. To achieve uniform (Köhler) illumination, a lens is used to focus an image of the light source onto the back focal plane of the objective lens, which functions as both condenser and collecting lens. Modern objectives are infinity-corrected, such that rays emanating from each point on the object are collimated. A "tube lens" focuses these rays to form a real image in its focal plane where the camera chip is located. The light collected from the sample consists of the emitted fluorescence, which conveys the desired image information, and backscattered laser light that would introduce an unwanted background if not properly rejected. A dichroic beamsplitter, which reflects the excitation radiation and transmits the fluorescence (or vice versa), in conjunction with an emission filter before the detector that transmits only the fluorescence signal, blocks the unwanted excitation light. The last component is the wide-field detector, which could be a camera or the human eye. The resolution of an epifluorescence microscope is limited by diffraction, as described by Abbe (subsection 2.2.2), and can be further degraded by optical aberrations or misalignment. For live cell imaging, the sample would typically be enclosed in a chamber (incubator) with controlled temperature, humidity, CO2 perfusion, etc.

Confocal microscopy

Compared to wide-field epifluorescence microscopy, confocal microscopy is superior in resolution and signal to background ratio for thick specimens. As first proposed by Minsky [Min61, Min88], it typically entails a single excitation beam focused onto the sample, as shown in Figure 2.4 (b), and scanned over a FOV in the focal plane of the objective lens. The use of a scanned excitation beam typically results in lower acquisition rates than for wide-field microscopy and the higher excitation intensity in the scanned spot can lead to photobleaching and phototoxicity for live samples. The excited fluorescence is collimated by the objective lens and focused by the "tube lens" onto an aperture (pinhole) that is comparable to or smaller than the lateral PSF, after which it is usually detected by a photomultiplier. The resolution is determined by the product of the excitation and emission PSF and in the ideal case of an infinitely small detection pinhole, the excitation and emission PSFs are identical, such that the PSF of the confocal microscope is the square of the conventional PSF (i.e. the Airy disk pattern), leading to a resolution enhancement of $d_{confocal} = \frac{d_{FWHMxy}}{\sqrt{2}}$. This confocal microscope PSF also benefits from reduced side lobes, which reduces lateral cross talk and improves the image contrast. The pinhole in front of the detector suppresses out of focus light, which is not focused as efficiently through the confocal pinhole, and

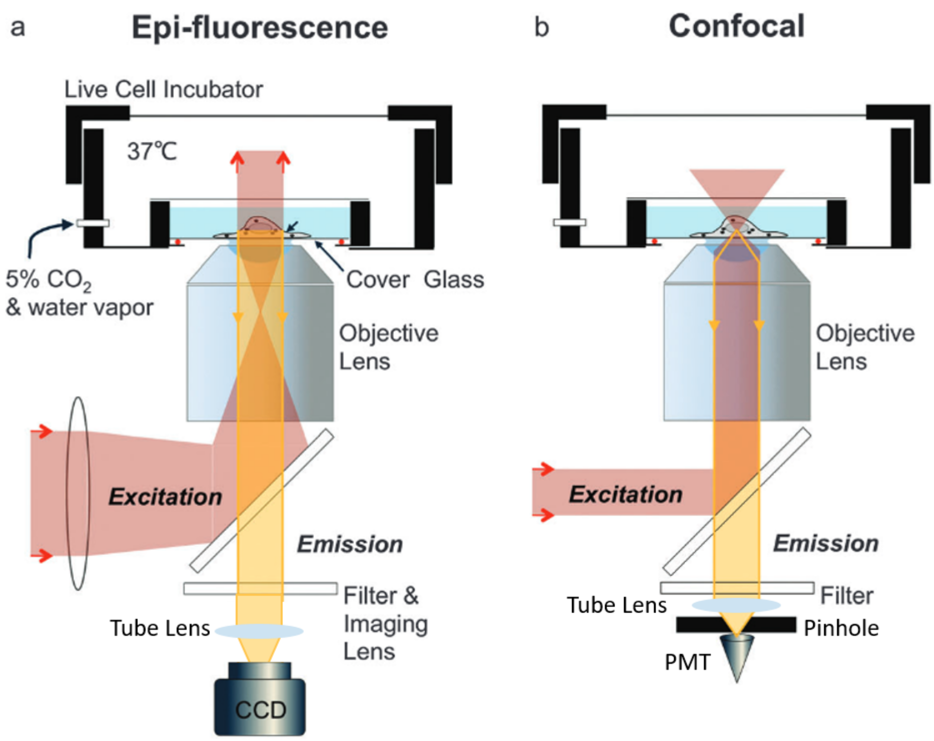
a
Epi-fluorescence
b
Confocal
Live Cell Incubator
37℃
5% CO$_2$
& water vapor
Cover Glass
Objective Lens
Excitation
Emission
Tube Lens
Filter &
Imaging
Lens
CCD
Objective Lens
Excitation
Emission
Tube Lens
Filter
Pinhole
PMT

Figure 2.4: *Schematics of (a) wide-field microscope and (b) confocal microscope. Adapted from [Par15].*

this leads to a higher signal to noise ratio when imaging thick samples, because light from other planes above or underneath the focal plane is rejected. This discrimination in favour of light from the focal plane is described as "optical sectioning". Since an infinitely small pinhole would not transmit any light to the detector, generally, the pinhole size is chosen to match the diameter of the first minimum in the Airy disk pattern and this provides optically sectioned imaging but minimal improvement in lateral resolution compared to wide-field microscopy.

Spinning disk microscopy

A method to retain the advantages of the confocal microscope, such as image contrast enhancement and optical sectioning, without the disadvantage of the lower acquisition rate, is "spinning disk" microscopy [Wil84]. It uses multiple excitation spots produced by illuminating a Nipkow disk (Figure 2.5) that contains many pinholes in a specific pattern that are scanned rapidly by rotating the Nipkow disk. When imaged onto the sample, this rotating pattern sweeps focused excitation spots across the whole FOV. A disadvantage of this approach is that the total area of the pinholes is a small fraction of the disc area and so the excitation light transmission is very inefficient. Some spinning disk units have a microlens array aligned to the pinhole pattern on the Nipkow disk to efficiently focus incident collimated light through the pinholes on the disk [Fav92]. This method can acquire images as fast as epifluorescence microscopy. However, the confocal microscopy performance is reduced because of crosstalk between neighboring pinholes that leads to a pedestal on the axial and lateral PSF [Egn02].

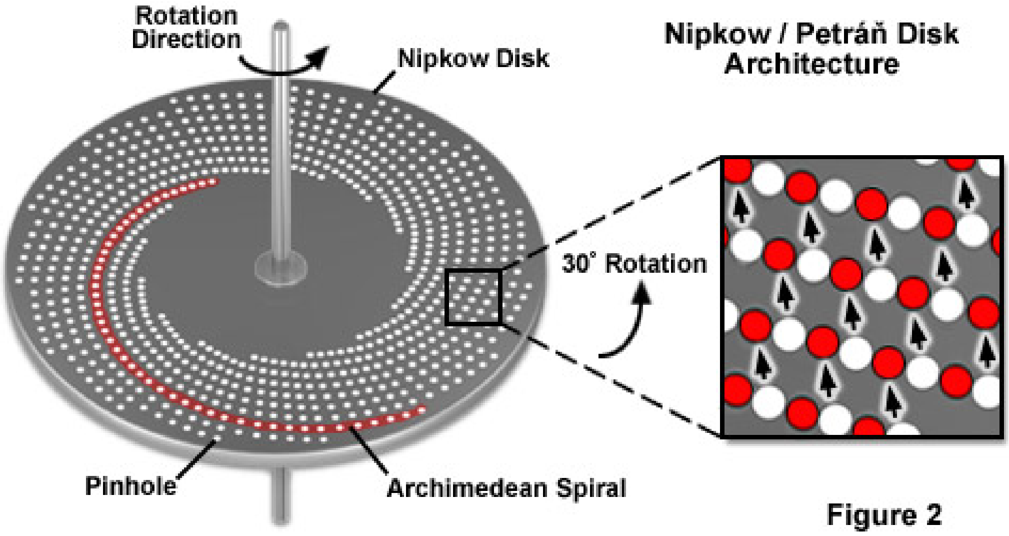

Figure 2.5: *Spinning disk scheme, [Zei17a] Carl Zeiss Microscopy.*

Total Internal Reflection Fluorescence and Supercritical Angle Fluorescence microscopy

Total internal reflection fluorescence (TIRF) microscopy is another technique to reduce out of focus light [Axe81]. It achieves optical sectioning through total internal reflection, whereby the excitation light is incident at or above the critical angle for internal reflection at the coverslip and so only an evanescent field penetrates into the sample, and decays on a scale much smaller than the excitation wavelength with an exponential function, $I(z) = exp^{-z/d}$, where the penetration depth is $d = \frac{\lambda}{4\pi} * (n_3^2 \sin^2(\theta - n_1^2))^{-0.5}$, depending on the excitation wavelength λ, the refractive index of the coverslip n_3, the refractive index of the imaging media n_1, the incident angle θ and the polarisation [Axe01]. Thus, only the fluorophores close to the coverslip can be excited and no background fluorescence from deeper into the sample is excited. This leads to a higher signal to noise ratio than conventional epifluorescence microscopy and this is often exploited for single molecule imaging studies studies [Dic98, Yil03, RP06] and for super-resolved localisation microscopy [Hen11]. Of course, the TIRF microscopy technique is limited to imaging only structures that are very close to the coverslip. It is possible to tune the angle of incidence of the exaction radiation to increase the imaging depth into the sample. This approach has been described as HILO microscopy [Tok08]. An alternative approach to acquire fluorescence images of fluorophores very close to the coverslip is to detect super critical angle fluorescence (SAF) [Ruc00], which can also be used for super-resolution microscopy, such as DONALD [Bou15].

Multiphoton microscopy

Another approach to realise optical sectioning and to reduce background signal is multiphoton microscopy. Here, the fluorophore is not excited with a single photon at a wavelength corresponding to the energy gap between ground and excited state, but is excited by the simultaneous absorption of multiple lower energy photons at correspondingly longer wavelengths [GM31], as illustrated in Figure 2.6. For example, two photon microscopy [Den90] entails the simultaneous absorption of two photons with twice the wavelength (half the energy) required for single photon excitation, and three photon microscopy [Hel96] entails the simultaneous absorption of three photons at thrice the wavelength. Like confocal microscopy, multiphoton microscopy is usually implemented as a laser scanning microscopy technique and therefore offers relatively low image acquisition rates compared to wide-field microscopy, although significant progress has been made developing high-speed laser scanning systems.

The excitation process is nonlinear and therefore a function of the incident intensity of excitation radiation, which is maximum at the focus and falls away quickly above and below the focal plane. For two photon microscopy, the fluorescence intensity is proportional to the square of the excitation intensity. Accordingly, the PSF of the multiphoton microscope is the square of the conventional PSF, which leads to optical sectioning and a resolution enhancement of $\sqrt{2}$ without the need for a confocal detector pinhole. However, the longer excitation wavelength means that the multiphoton PSF (and therefore resolution) is larger for multiphoton microscopy than for confocal microscopy of the same fluorophores with single photon excitation. For three photon excitation, the fluorescence intensity scales with the cube of the excitation intensity and the width of the PSF is reduced by $\sqrt{3}$, albeit for a PSF of three times the wavelength required for single photon excitation.

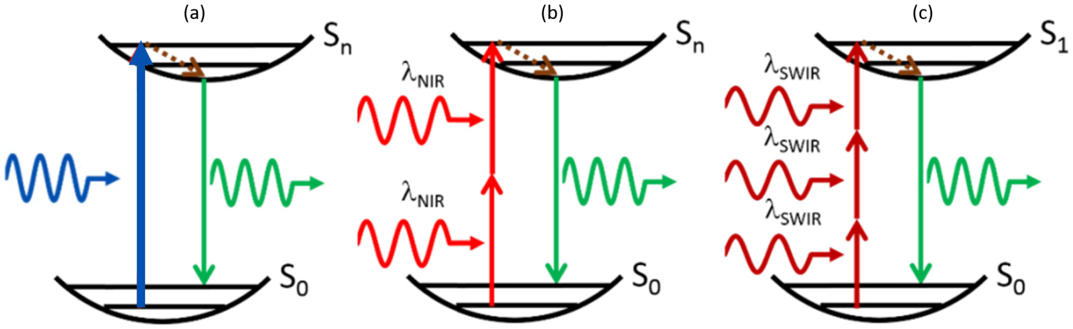

Figure 2.6: *Schematic of (a) single, (b) two and (c) three photon excitation. Adapted from [Yan16].*

Since multiphoton absorption excites only fluorophores in the focal plane, without the need to introduce a confocal pinhole at the detector, the detection efficiency is higher than for confocal microscopy, particularly when imaging in samples that scatter the emitted photons since any detected photons can be assumed to originate from the focus of the excitation beam. Additionally, since absorption and optical scattering cross-sections decrease with increasing wavelength in biological tissue from the visible to the near-infrared (NIR) spectral region, the depth to which the excitation light can be focused in tissue is higher for multiphoton microscopy compared to confocal microscopy. For these reasons, multiphoton microscopy is widely used for fluorescence imaging in biological tissue. Disadvantages of multiphoton microscopy include the low excitation efficiency (which is much lower than for single photon excitation) and the consequent requirement for a high intensity excitation source. Since high power radiation can de damaging to samples, particularly for cell biology experiments, it is important to minimise the average excitation power while maximising the intensity. This is typically realised using ultrashort pulse trains with low duty cycles, e.g. ∼100 fs duration pulses at repetition rates of >80 MHz from mode locked lasers. Commercially available Ti:Sapphire lasers provide tunable femtosecond pulses from ~650–1100 nm and are widely used for multiphoton microscopy, although there is significant interest in developing ultrashort pulse laser sources at longer wavelengths to increase the imaging depth in biological tissue. A drawback of the high excitation intensities required for multiphoton microscopy is the increased photobleaching (and phototoxicity for live samples) in the focal plane. Compared to single photon excitation, however, the photobleaching/phototoxicity is much lower outside the focal plane for samples (such as biological tissue) that do not absorb strongly at the wavelength of the incident (NIR) excitation radiation. For this reason, multiphoton microscopy is well-suited for z-stack acquisitions where the out-of-plane photobleaching for confocal microscopy could be a significant problem.

4π microscopy

The majority of fluorescence microscopy techniques only excite or detect light from one side of the sample. 4π microscopy is a laser scanning microscopy technique exciting the sample and/or collecting emission via two opposed objective lenses to enhance the axial resolution. Fluorescence is omnidirectional and so detection over any solid angle, regardless of its orientation with respect to the excitation light, can provide useful information.

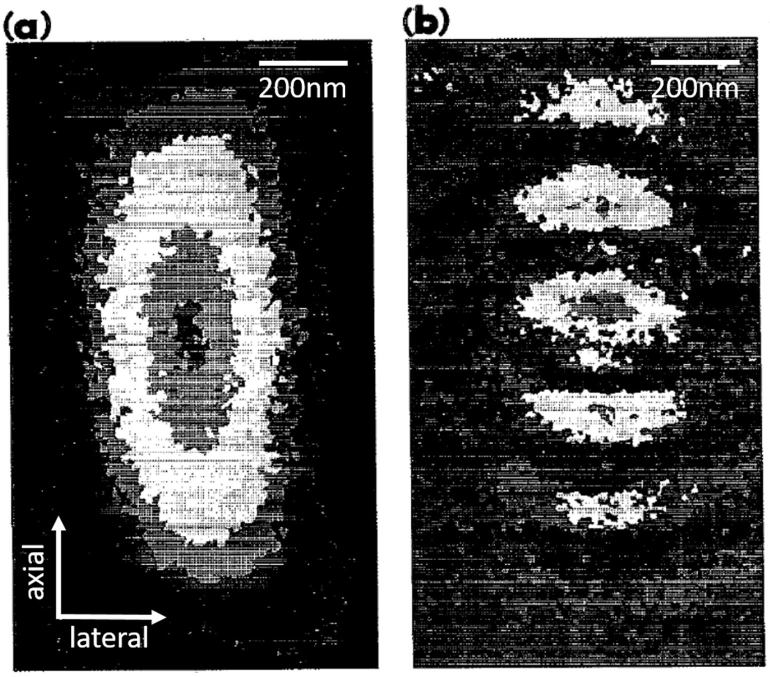

Figure 2.7: *x-z excitation intensity distribution for a confocal microscope (a) and a 4π microscope (b) [Hel94a].*

One objective lens can only cover a limited range of solid angles and even a lens with an acceptance angle of 2π would only collect half of the emitted light. An additional objective lens on the other side of the sample could double the solid angle of collection up to the ideal of spherical detection covering a solid angle of 4π radians [Hel94a]. If both of the opposing objective lenses are also used for coherent excitation, an axial standing wave will be established via interference. Image Figure 2.7 illustrates the x-z excitation intensity distribution for a confocal microscope and a 4π microscope with such a standing wave. The lateral resolution is not altered but the axial resolution can be significantly enhanced by deconvolving the side lobes, e.g. by a three-point deconvolution [Lan07], or by suppressing the side lobes via stimulated emission [Cur15] or fluorophore deactivation [Bö16]. The downside of 4π microscopy is the complex optical set-up, the severe impact of optomechanical instability and the sample preparation, because thin samples are needed to fit between the two opposed high NA objective lenses within their short working distances.

Light sheet fluorescence microscopy

Another approach to achieving optically sectioning microscopy is light sheet fluorescence microscopy (LSFM), as first introduced in 1902 as a scattered light microscope by Siedentopf and Zsigmondy, who arranged the objective lens and detection light path to be orthogonal to the condenser and the excitation light path [Sie02], as depicted in Figure 2.8. The "waist" of excitation PSF is arranged to extend across the FOV in the lateral plane of the imaging path like a thin "sheet" such that the axial PSF is defined by the width of this "sheet" rather than the PSF of the objective lens in the imaging path. In more recent developments [Hui04], this light sheet can

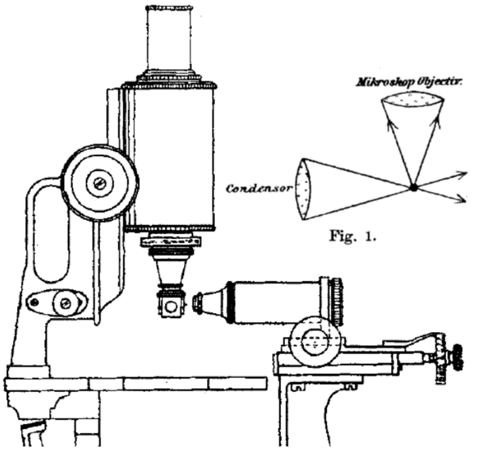

Figure 2.8: *Original configuration of light sheet microscope 1902, Siedentopf and Zsigmondy [Sie02].*

be made to cover the full FOV of the imaging objective lens with reasonably uniform thickness by using appropriate cylindrical optics. The image detection is essentially a wide-field microscope applied to image fluorescence that originates only within the light sheet that is arranged to be in the focal plane of the objective lens. This provides a fast optically sectioning microscopy technique, particularly when implemented with high frame rate sCMOS cameras. In alternative configurations, the excitation light sheet can be realised by rapidly scanning a "pencil" of excitation light (from a weakly focused laser beam) laterally across the FOV of the imaging objective lens [Kel08]. LSFM is the subject of intense development and widespread application, as reviewed in [Tom13].

2.2.4 Super-resolution microscopy

The rapidly developing field of super-resolved microscopy (SRM, i.e. microscopy with resolution beyond the optical diffraction limit typically considered to be ~200 nm) is currently dominated by far-field fluorescence techniques that are lower cost, more convenient and more applicable to biological samples than previously used approaches to SRM. These can be broadly categorized into, single molecule localisation microscopy techniques, structured illumination techniques and RESOLFT techniques including stimulated emission depletion (STED) microscopy. With the exception of linear structured illumination microscopy (SIM), these fluorescence-based SRM techniques utilise switching properties of the fluorophores to beat the diffraction limit. Following an introduction to the context of super-resolved fluorescence microscopy, these techniques are discussed in the following sections with particular emphasis on SIM and STED microscopy which are subsequently used in this thesis.

Optical microscopy, and the ability to study the fundamental structures underlying cell biology and other branches of science, were recognised to be practically limited by the Abbe resolution limit since 1873. Since the resolution depends on the wavelength, the use of shorter wavelength radiation is of interest, but optical radiation below ~400 nm is significantly phototoxic to biological samples and excites unwanted background fluorescence in optical glass elements such as lenses and microscope slides. It is also difficult to obtain optical components that are corrected for radiation shorter than 400 nm and much shorter radiation, e.g. X-rays, is difficult to collimate and focus. However, electron beams can be focused for imaging applications and electron microscopy remains the gold standard for imaging structures on the nm scale. De Broglie postulated in 1923 that matter has wave properties with the energy of the matter being inversely proportional to its wavelength [DB23]. With the invention of electron lenses in 1926 [Bus26], Ernst Ruska built the first electron microscope in 1936 [Kno32] and the technology has developed to the point that modern electron microscopes can achieve resolutions under 50 pm in fixed [Ern09] samples and around 8 nm in live cells [Liv16]. However, electron microscopes are much more expensive to purchase and maintain that optical microscopes and require significant, complex sample preparation techniques that are usually not compatible with live samples. Additionally, the contrast is typically lower than for fluorescence microscopy, because the limited labelling approaches do not have high molecular specificity and the image signal is often compromised by background signals.

An early strategy to beat the diffraction limit was to image in the near field, where the diffraction limit does not apply. Scanning near-field optical microscopy (SNOM) [Dü86] is a development of atomic force microscopy (AFM) [Bin86] where a small cantilever is used to mechanically scan the sample and an interaction between the sample and the cantilever, described by the Lennard-Jones potential [LJ31], forces the cantilever to bend. The degree of bending can be measured with a laser beam reflected from the back surface of the cantilever and this can provide a map of the surface profile with 3 nm precision [Bin86]. In SNOM, the scanning cantilever has a small hole in the middle guiding light to and from the sample that can be used to record fluorescence. This is usually implemented using an optical fibre with a coating at the end to restrict the light to a small aperture of ∼10's nm diameter. Since the light is detected very close to the sample, there is no diffraction and the resolution is defined by the size of the detection aperture. Replacing the cantilever with a capillary electrode and monitoring the conductance of the solution in the capillary instead the bending of the cantilever enables the concentration of ions to be mapped: this surface scanning microscopy technique is called scanning ion-conductance microscope (SCIM) [Han89]. A major disadvantage of such surface (near field) scanning techniques is that only the surface can be imaged, so features within a structure such as a cell are not accessible, and the imaging speed is relatively slow.

A recent and radically different approach to resolving structure below the optical diffraction limit is expansion microscopy [Che15a], which uses a sample preparation method that results in a physical expansion of the sample by integrating a polymer network inside the mounting medium of a biological specimen that swells to increase the volume by up to a factor of 4.5. The expanded sample can be imaged with any microscope and conventional microscopy can provide images of the physically magnified structures that would normally be below the resolution limit. The achieved resolution is around 70 nm. A further development uses iterative expansion processes and can increase the volume by a factor of 20 with a resolution of 25 nm [Cha17].

Single molecule localisation microscopy Single molecule localisation microscopy (SMLM) technique are the most straightforward SRM techniques to utilise since they can be implemented on conventional wide-field microscopes, although they are often combined with TIRF microscopy. The most widespread approaches are stochastic optical reconstruction microscopy (STORM) [Rus06] and photoactivated localisation microscopy (PALM) [Bet06], which both entail sequentially imaging sparse subpopulations of fluorophores that typically present no more than one active fluorophore within the PSF of the microscope. In this situation, the images of each isolated fluoroprobe can be analysed (e.g. by fitting them to a Gaussian profile) to locate its centre of mass to high precision (equal to the FWHM of the PSF divided by the square root of the number of photons collected) and this co-ordinate can be recorded as the position of the fluorophore. By sequentially switching on and off different subpopulations of the fluorophores, the co-ordinates of all the fluorophores can be recorded to provide the super-resolved image. The mechanism for switching the fluorophore emission on and off varies according to the specific method employed.

In PALM, the sample is labelled with photoswitchable fluorescent proteins. A laser at one wavelength is used to first deactivate all the fluorophores and then a second laser at a different wavelength excites a subpoparion of them to emit fluorescence that is imaged using a camera. This activated subpopulation is continuously excited and imaged until it is photobleached and then the activation laser is used to activate a further subpopulation of fluorophores. This three-step process of activation, excitation and photobleaching is repeated until all the fluorophores are photobleached.

In STORM, the sample is labeled with photoswitchable dyes than can be activated, deactivated and excited using lasers at specific wavelengths, as shown in Figure 2.9. Subsequent developments of this approach include methods to realise SMLM using a single laser wavelength, such as ground state depletion (GSDIM) [Fol08] and direct STORM (dSTORM) [vdL08] that use metastable dark-states or triplet states to provide self-sustained activation/deactivation ("blinking") of fluorophores that is enhanced using special chemical buffers.

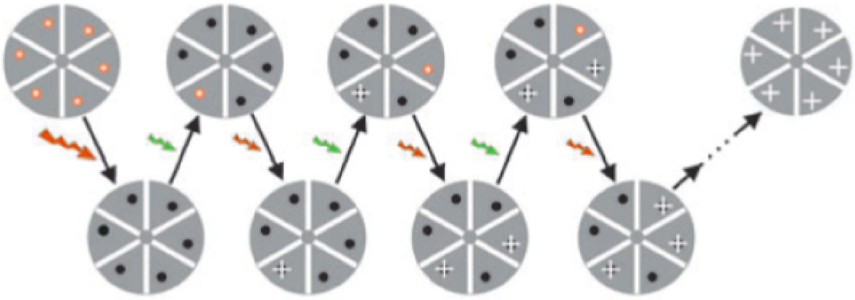

Figure 2.9: *STORM concept: sequential use of two lasers switch the fluorophores separately on and off. These blink events carry super-resolution information [Rus06].*

SMLM can be used with a wide range of fluorophores and multiple color SMLM is routinely used. When implemented in a TIRF microscope, the evanescent wave excitation provides optical sectioning and strong rejection of out of focus fluorescence [Hen11]. SMLM can also be extended to 3D SRM using techniques to localize the PSF of each fluorophore axially as well as laterally [Hua08, Jue08]. While PALM can be implemented in live cells, the chemical buffers used for dSTORM are not compatible with live cell imaging. In general, it is difficult to implement SMLM in tissue or live organisms because the background fluorescence impacts the wide-field detection and makes it challenging to image and localize individual fluorophores. If this is required, SMLM can be combined with an optically sectioning technique such as LSFM [Gus17].

Structured illumination microscopy (SIM)

With structured illumination microscopy (SIM), lateral resolutions up to twice the conventional wide-field microscopy limit are achievable [Gus00], down to 100 nm laterally and down to 300 nm in the axial dimension. Due to its wide-field illumination, linear SIM is less phototoxic to samples than laser scanning SRM techniques and time-course imaging of live samples is possible [Li15]. Although linear SIM is commonly described as a super-resolved microscopy technique, it is still limited by diffraction. However, it is a means to increase the spatial frequency content of the image (and therefore the resolution) beyond the usual limit supported by the numerical aperture of a conventional wide-field microscope. If combined with nonlinearity or photoswitchable fluorophores, SIM can provide true super-resolved imaging with resolutions having been achieved down to 50 nm resolution in biological samples [Reg12]. In the following sections, the principles underlying SIM are presented followed by a discussion of nonlinear SIM.

The Moiré Effect [Gus05] is frequently invoked to an insight into the principle of SIM. It describes how the multiplication of two finely spatially modulated patterns form a coarser (i.e. lower spatial frequency) pattern when superimposed (i.e. multiplied), as shown in Figure 2.10. If an unknown pattern (the sample), containing high spatial frequency information that is outside the detectable

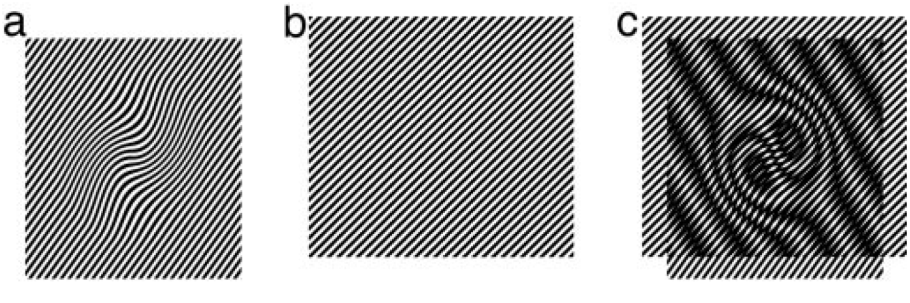

Figure 2.10: *Moiré effect, two finely structured patterns (a,b) overlaid (multiplied together) produce a pattern containing new higher and lower frequencies (c). It is the new coarse (lower) frequencies that are most apparent in (c), described as the Moiré fringes [Gus05].*

range (OTF cut-off spatial frequency) of a microscope, is multiplied by a known “reference” pattern, described with a spatial frequency inside the OTF, the resulting product will be a “coarser” pattern of lower spatial frequency. This “coarse” pattern corresponds to the difference in spatial frequencies on the unknown (sample) pattern and the known reference pattern. If it is recorded, it can be used with the known reference pattern to calculate the unknown pattern (i.e. the image of the sample) containing spatial frequencies beyond the OTF cut-off frequency.

The illumination of a sample by a known spatially modulated excitation intensity pattern (usually a sinusoidal pattern) to generate an image including information about spatial frequencies outside the OTF of the microscope is the basis of SIM. Essentially, structured illumination of the sample with the known reference pattern shifts higher spatial frequencies present in the sample from outside to inside the detectable range of the optical system (i.e. the OTF). The highest spatial frequency that can be projected onto the sample is limited by the OTF and so the highest spatial frequency that can be shifted into the OTF by SIM is given by plus and minus the OTF cut-off frequency. Therefore, the maximum improvement in resolution that SIM can provide is a factor of 2. Since the modulated (“coarse”) pattern recorded in SIM results from a multiplication of the unknown (sample) and known reference patterns in real space, this corresponds to a convolution of their Fourier transforms in spatial frequency space. Therefore, the post processing algorithm to calculate the unknown sample image containing the higher spatial frequencies can be obtained by deconvolving the known reference pattern from the recorded modulated image in Fourier space.

In practice, it is necessary to acquire more than one modulated image to reconstruct a satisfactory SIM image with higher spatial frequencies and a full explanation requires more details of the underlying mathematics. The modulated image in real space, ($E(r)$), is a convolution ($\circledast$) of the PSF ($PSF(r)$) with the multiplication of the fluorophore density distribution ($D(r)$)) and the illumination profile ($I(r)$):

$$E(r) = [D(r)I(r)] \circledast PSF(r) \tag{2.6}$$

In deconvolution microscopy, a theoretical or experimental PSF is used to deconvolve Equation 2.6. Changing to Fourier space ($\sim$) with spatial frequency k, the modulated image transforms to:

$$\widetilde{E}(k) = [\widetilde{D}(k) \circledast \widetilde{I}(k)]OTF(k) \tag{2.7}$$

A sinusoidal illumination pattern can be described as $I_a(r,k) = 0.5[1 + sin(2\pi kr + \Phi_a)]$, where Φ is the phase and k the spatial frequency of the projected sinusoidal pattern. For SIM, k has to be smaller than or equal the maximum transmittable (cut-off) frequency $k_0 = \frac{2NA}{\lambda}$ with NA is the numerical aperture and λ the emission wavelength. Inserting $I_a(r,k_0)$ into Equation 2.7 forms an equation with three harmonics (Equation 2.8).

$$\widetilde{E}_a(k) = 0.5[\widetilde{D}(k) + 0.5e^{i\phi_a}\widetilde{D}(k+k_0) + 0.5e^{i\phi_a}\widetilde{D}(k-k_0)]OTF(k) \tag{2.8}$$

The recorded modulated image corresponds to the original fluorophore density distribution, $\widetilde{D}(k)$, and this distribution shifted to be centred on $+k_0$ and $-k_0$. To be able to unmix this recorded spatial frequency information and reconstruct the resolution-enhanced SIM image, three modulated images with three different phases have to be acquired. This will provide resolution enhancement only in one direction (perpendicular to the projected sinusoidal fringes). To obtain a homogenous 2D resolution enhancement the procedure must be repeated, projecting fringe patterns in different directions. While gratings projected at an infinite number of orientations are required to realise perfectly homogeneous resolution enhancement, this is not practical and a reasonable compromise that addresses the need to minimise photobleaching and image acquisition time is to acquire three phase-shifted sets of images with fringes projected at three equally spaced orientations. Therefore, to obtain an enhanced resolution 2D SIM image, a total of nine modulated images must be acquired. Figure 2.11 illustrates the formation of Moiré fringes, the OTF of a conventional wide-field microscope and how this can be extended using structured illumination to realise 2D SIM.

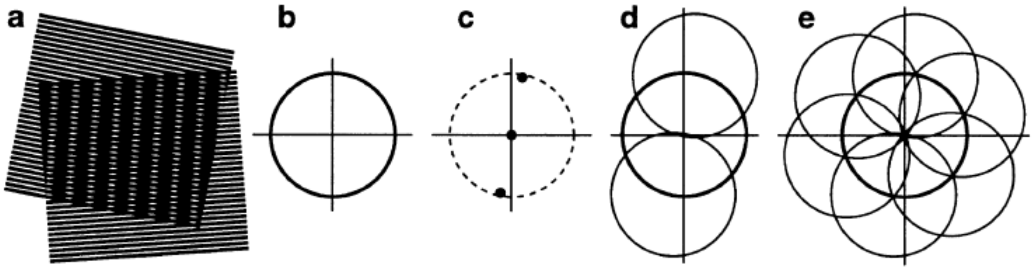

Figure 2.11: *SIM concept: (a) Moiré effect, (b) wide-field microscope OTF, (c) Fourier transform of a sinusoidal grating, (d) convolution of (c) and (d) illustrating extended OTF in one direction and (e) resulting extended OTF for 2D SIM image realised by three rotated orientations of (d) [Gus00].*

SIM enhancing the axial resolution can be achieved by extending the OTF in the third dimension [Sch08]. This requires additional phase shifted images to be acquired. For a 3D z-stack, a total of 15 modulated images per z-plane have to be acquired to obtain a 3D resolution-enhanced image.

Nonlinear SIM Nonlinear SIM, also called saturated SIM (SSIM) [Gus05], is an approach to achieve theoretically unlimited resolution by applying the SIM method with the effective sample excitation modulation containing frequencies beyond the OTF of the microscope. For normal (linear) SIM, the projected sinusoidal modulation of excitation light must have a spatial frequency within the OTF, typically it is close to the OTF cut-off frequency and so that the resolution enhancement is twice the wide-field limit. To further increase the spatial frequency content of the SIM image, the required higher spatial frequency excitation patterns are realised by using sufficiently high excitation intensities to saturate the fluorophore absorption and therefore the modulated fluorescence pattern. The carrier frequency of the projected sinusoidal grating is still inside the OTF but higher (harmonic) frequencies are generated inside the sample via the nonlinear response. Thus, information about high spatial frequencies can be brought within the microscope OTF and encoded in the recorded modulated image, as shown in Figure 2.12.

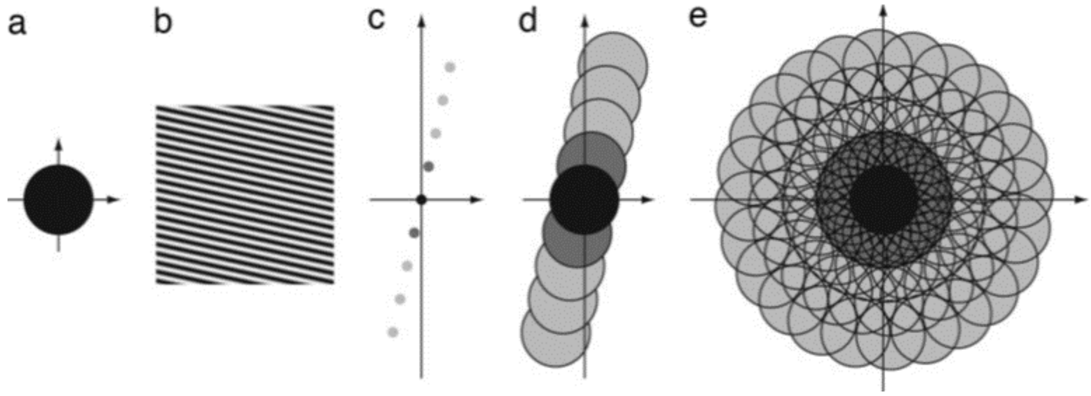

Figure 2.12: *Nonlinear SIM concept: (a) confocal OTF, (b) saturated sinusoidal grating, (c) Fourier transform of (b), (d) extended OTF in 1D and (e) extended OTF of nonlinear SIM with a resolution enhancement with a factor of 5 [Gus00].*

With SSIM, the resolution enhancement can be continuously increased provided that the strength of saturation of the emitted fluorescence can be increased. Two major issues prohibit such improvement in resolution: for every higher order (harmonic) spatial frequency component introduced into the modulated fluorescence pattern, additional phase shifted images have to be acquired and this leads to increasing total image acquisition time and increasing photobleaching (and phototoxicity). Thus, the combination of increased light exposure and increasing total image acquisition time effectively limit the resolution achievable with SSIM of biological samples to 50 nm [Reg12].

Stimulated emission of depletion microscopy (STED)

Stimulated emission of depletion microscopy (STED) was the first true SRM technique, demonstrated in 1994 by Hell [Hel94b]. STED uses stimulated emission to reduce the effective PSF size in a laser scanning (confocal) scanning microscope to achieve higher resolution than confocal microscopy. This concept of engineering a narrow PSF by switching off fluorescence with a shaped switching beam was later generalized to a class of techniques called "RESOLFT" (reversible saturable optical fluorescence transitions), which has been implemented with photoswitchable fluorescence probes in laser scanning microscopes [Hof05], for which the switching powers are much less than those required for deletion by stimulated emission.

Stimulated emission depletion In 1917 Einstein published "On the Quantum Theory of Radiation" which included a paragraph about the interaction between excited molecules and light. He described the phenomena of absorption and emission with quantum theory and proposed that an excited molecule ("Planck resonator") interacting with a photon could experience an impulse to stimulate the molecule to emit another photon with the same wavelength and the same direction as the incoming photon *"Es seien Z_n und Z_m zwei im Sinne der Quantentheorie mögliche Zustände des Gasmoleküls, deren Energie ϵ_n bezw. ϵ_m die Ungleichheit $\epsilon_m > \epsilon_n$ erfüllen, ... Ebenso sei ein Übergang $Z_m \Rightarrow Z_n$ unter Einwirkung der Strahlung möglich, ... Bei dem Einstrahlungsvorgang $Z_m \Rightarrow Z_n$ hat der übertragene Impuls dieselbe Größe, aber die entgegengesetzte Richtung."*[3] [Ein17](:385-387).

In a laser amplifier, stimulated emission is used to amplify an optical signal at the expense of the excited state population of the active species in medium. In STED microscopy, it is used to deplete an excited state population of fluorophores in order to switch of the fluorescence emission. The basis of a STED microscope is a confocal scanning microscope in which a second laser beam, at a wavelength that is longer than the excitation spectrum but within the emission spectrum of the fluorophores, is introduced to deplete the fluorescence signal. This "depletion" beam has a specific spatial profile when focused at the sample with an intensity minimum at the centre in order to deplete only the outer regions of the excitation PSF and thus reduce the effective excitation spot size. This principle is illustrated schematically in Figure 2.13.

---

[3] Let Z_n and Z_m be two possible quantum theoretical states of a gas molecule whose energies ϵ_n and. ϵ_m respectively, satisfy the inequality $\epsilon_m > \epsilon_n$, ... In the same way, let the transition $Z_m \Rightarrow Z_n$ under the action of the radiation also be possible, ... If we have the process $Z_m \Rightarrow Z_n$ for the case of incident radiation, the magnitude of the transferred momentum is the same, but it is in the opposite direction.

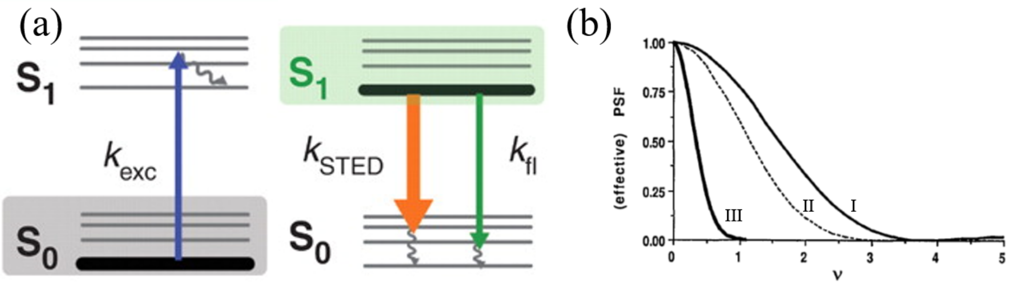

Figure 2.13: *(a) Jablonski diagram for the stimulated emission effect in fluorescence. Blue: excitation, green: fluorescence, red: STED wavelength [Hel07]. (b) effective PSF shape for STED principle. (I) shows the confocal PSF with no STED influence, (II) is with low STED intensity and (III) with high STED intensity. Adapted from [Hel94b].*

The excitation radiation transfers the fluorophores from their ground state (S_0) into their first excited state (S_1) with a rate k_{exc}. From here, the electrons can relax back to the ground state via spontaneous emission (fluorescence) or non-radiative decay with total rate k_{fl}, or they can be driven back to the ground state by stimulated emission via incident photons at the same wavelength within the emission spectrum at a rate k_{STED}. The proof of principle was demonstrated in 1994, using two depletion beams with Gaussian intensity profiles to deplete the outer regions of an excitation PSF in between them to achieve a resolution enhancement in one direction [Hel94b]. With increasing laser intensity for the depletion (STED) laser beam, the effective excitation PSF narrows in 1D, as depicted in Figure 2.13 (b).

Later this approach was modified to use a depletion beam that focuses to a “doughnut-shaped” intensity profile that is incident collinear with the excitation beam at the objective lens. This superposition of excitation PSF and STED PSF provides a lateral isotropic resolution enhancement [Kla01], as presented in Figure 2.14, that scales with the STED intensity as [Har08a]:

$$d_{STED} = \frac{d_{Abbe}}{\sqrt{1+\frac{I}{I_s}}} \tag{2.9}$$

where d_{Abbe} is the diffraction resolution limit, I is the intensity of the STED beam and I_S is the saturation intensity of the fluorophores, a characteristic property that is the inverse product of the fluorescence lifetime τ, and the absorption cross section σ, of the fluorophores at the wavelength of the STED beam, $I_S = (\sigma\tau)^{-1}$ [Hel07].

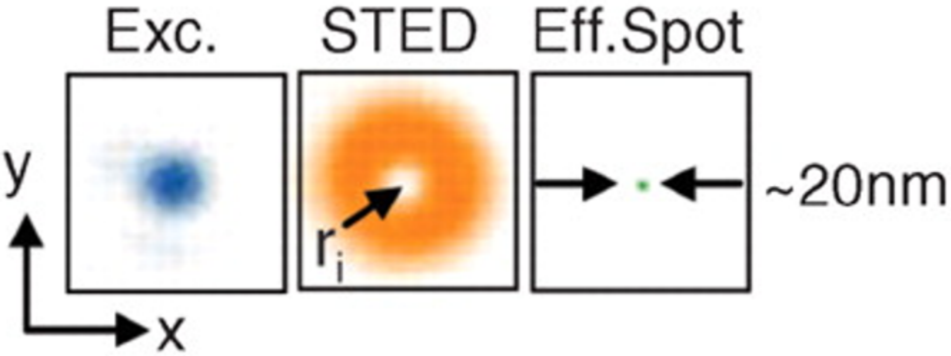

Figure 2.14: *STED principle: intensity profiles of excitation PSF (blue), STED PSF (red), effective fluorescence PSF (green) [Hel07].*

With this approach, resolutions below 20 nm have been achieved for STED microscopy of biological samples labelled with dyes [Gö13] and, in diamond samples, resolutions down to 8 nm have been obtained when imaging NV-centres [Rit09], see Figure 2.15. A new method (MINFLUX), which combines STED and localisation microscopy techniques, has achieved lateral resolutions in engineered DNA samples down to 1 nm [Bal16].

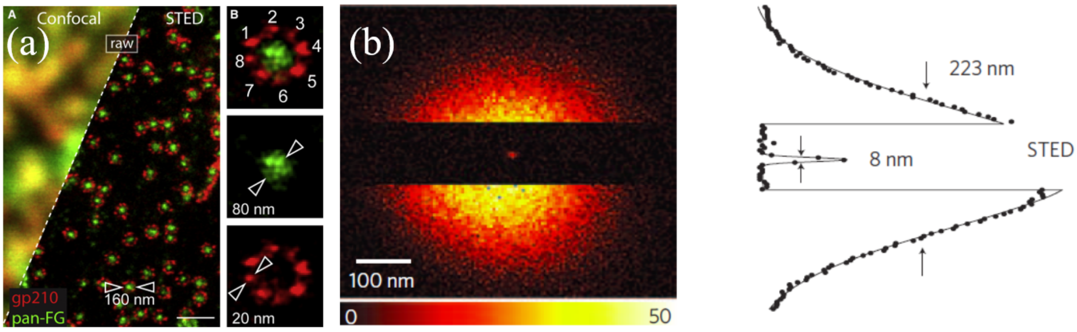

Figure 2.15: *(a) Two colour STED microscopy images of amphibian nuclear protein complexes with octametric gp210 subunits (red) and a pan-FG unit in the middle (green); Scale bar is 500 nm [Gö13]; (b) STED microscopy image and intensity line profile of fluorescent nitrogen vacancy centre [Rit09].*

Manipulating the spatial profile of the STED PSF There are two main approaches to produce a doughnut-shaped PSF. The first is to introduces a 2π phase shift in the laser beam, e.g. using a vortex phase plate [Lea04] or an SLM [Auk08], as shown in Figure 2.16. This produced a π phase difference between the wavefronts from opposite sides of the beam, with destructive interference and zero intensity on axis. When focusing the vortex beam, the laser intensity is zero at the centre of the focus, realising the doughnut intensity PSF required for STED microscopy. A vortex phase plate is typically a plate with a radial 2π ramp. Alternatively, computer-generated holograms (CGH) can be programmed onto a spatial light modulator (SLM) such that the diffracted beam forms the desired optical vortex (see Figure 2.16 (b) for an example). The CGH can additionally be programmed to provide phase profiles across the beam to precompensate for optical aberrations in the instrument [Auk08] or the sample [Len14]. The second approach utilises birefringence and is also known as the easySTED technique [Reu10]. Here, collimated excitation and STED beams propagate through a spatial arrangement of 4 $\frac{\lambda}{2}$-plates, with optical axes orientated as depicted in Figure 2.16 (c), such that each quadrant introduces a different phase change between the ordinary and extraordinary waves. The excitation beam propagates as the ordinary wave and undergoes no spatial phase modulation while the orthogonally polarized STED beam undergoes different phase delays in each quadrant such that opposite quadrants impart a phase difference of π. On axis in the focused beam, the STED waves destructively interfere to produce a point of zero intensity in the centre of the beam.

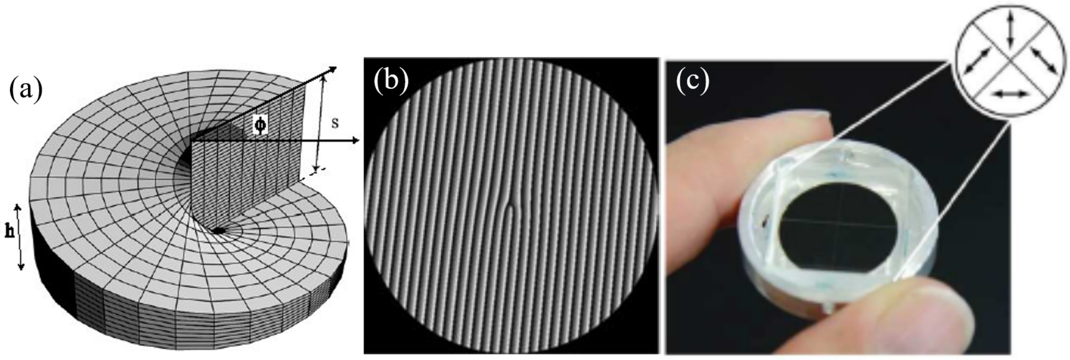

Figure 2.16: *: STED beam shaping approaches. (a) vortex phase profile [Lea04], (b) CGH on an SLM to produce a diffracted vortex beam [Len14] and (c) easySTED composite phase plate [Gö14].*

3D STED The STED beam shaping approaches discussed in section 2.2.4, can only be applied to 2D STED in their presented configuration and the axial resolution is still limited to the confocal diffraction limit. To enhance the axial resolution, STED microscopy can be implemented in a 4π microscope configuration, although this further increases the significant experimental complexity, requiring the excitation beam (and sometimes the STED beam) to be split and interfered in the sample plane via two opposing objectives to produce a structured illumination pattern in z. The centre of the resulting excitation intensity distribution has a smaller axial FHWM than a confocal PSF, albeit with unwanted side lobes. In one implementation of 4π STED [Cur15] two depletion beams produced, via an easySTED plate and opposing objective lenses, an intensity pattern which depletes these side lobes and improves the resolution in all three dimensions down to 20 nm, as shown in Figure 2.17 (a). Alternatively, the excitation PSF can be depleted in three dimensions using a π-phase ring to produce a "bottle-beam" shaped PSF that provides strong axial resolution enhancement and weaker enhancement of the lateral resolution [Kla00]. More recently the doughnut and bottle-beam depletion PSF were implemented in separate STED beams that were combined to realise 3D STED [Har08b]. This entails significant experimental complexity since both STED beams and the excitation beam have to be aligned to overlap their respective PSF at the sample. A more robust and flexible approach was demonstrated utilising one SLM that is multi-passed to diffract the collimated STED laser beam subsequently off two CGHs (on the same SLM) with the laser beams' polarisation being rotated in between passes so that one CGH at each pass can be imposed [Len14]. Examples of the doughnut and bottle beam PSFs produced this way are shown in Figure 2.17 (b).

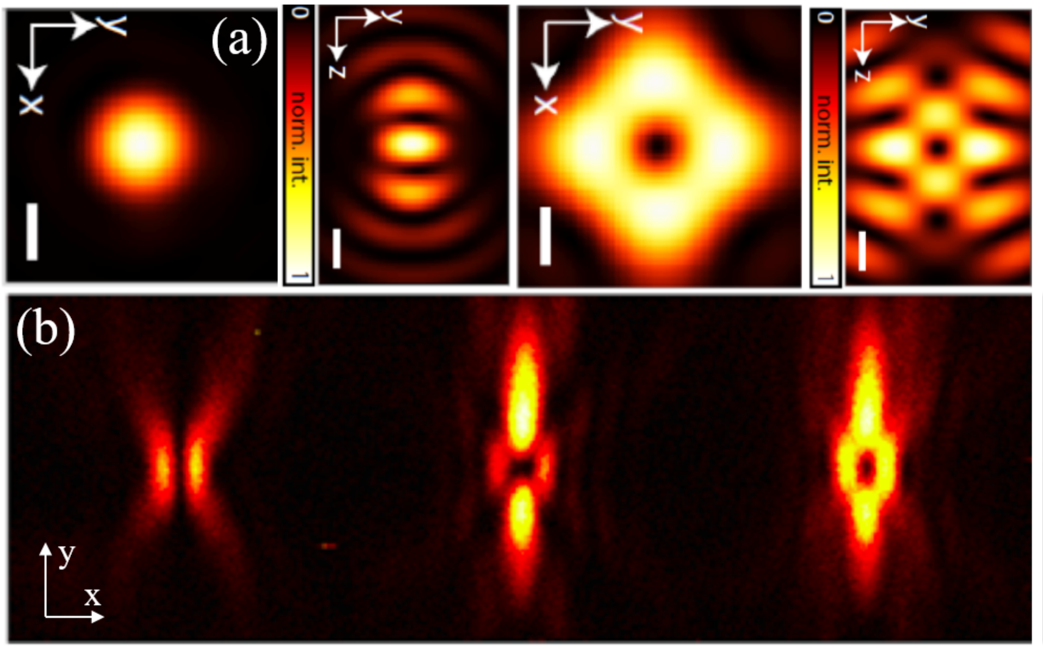

Figure 2.17: *3D STED PSF: (a) 4π excitation PSF in x-y and x-z planes (left) with corresponding STED PSF produced with easySTED phase plate (right) [Cur15], scale bars: 200 nm; (b) x-z images of doughnut (left), bottle beam (middle) and combined (right) STED PSF generated with CGHs [Len14].*

Many variations of STED microscopy have been implemented including multi-color and fluorescence-lifetime imaging [Bü11], two-photon STED [Mon09], STED lithography [Kla14], STED-enhanced light sheet microscopy [Fri11] and STED FCS [Mue13]. Temporal discrimination of the confocal and STED signals can achieve higher spatial resolution, e.g. via time-gating [Auk08, Vic11]. The imaging speed can be increased with parallel detection using separated depletion beams [Bin11] or a lattice of depletion beams with several thousand zero points [Yan14, Ber15]. STED microscopy has been applied to live cell imaging, including studies of the endoplasmic reticulum in yeast cells [Ran11], actin in intact brain tissue [Urb11] and hippocampal synapses in mice [Att15], and in vivo STED microscopy has been demonstrated imaging GFP in *C. elegans* [Ran11]. RESOLFT microscopy with photoswitchable fluorescent proteins has also been implemented, including with a lattice of photoswitching beams [Chm13] and to enhance axial resolution in light sheet microscopy [Hoy16].

2.3 Fluorescence lifetime microscopy (FLIM)

Fluorescence lifetime imaging (FLIM) entails measuring the fluorescence lifetime in every pixel of an image. FLIM can be implemented in a wide range of optical instruments including endoscopes and tomographic imaging systems but is most commonly implemented in microscopes. There are essentially three approaches to measuring fluorescence lifetime. Frequency domain measurements typical entail exciting the sample with a sinusoidally modulated excitation light source and measuring the phase shift and demodulation of the resulting fluorescence signal with respect to the excitation. Time domain measurements can be undertaken by digitization of the fluorescence decay profiles, by temporal gating of repetitive fluorescence decay profiles excited by high repetition rate pulsed laser or by time correlated single photon counting (TCSPC) [Mar14]. Frequency domain FLIM and time-gated FLIM can be implemented in laser scanning microscopes but are most commonly applied in wide-field microscopes. TCPSC is mainly applied in laser scanning microscopes. Typical implementations are shot-noise limited and so TCSPC is the most accurate technique to characterise a fluorescence decay profile for a given number of detected photons. However, laser scanning TCSPC FLIM is significantly slower than wide-field FLIM techniques that acquire information (photons) from all pixels in parallel and can achieve a given precision of lifetime determination in a shorter measurement time.

2.3.1 Frequency domain FLIM

In frequency domain FLIM, a (usually sinusoidally) modulated excitation light source is used in conjunction with sinusoidally modulated detection of the fluorescence signal. For a single excitation frequency (ω), fluorescence lifetime information can be obtained from measurements of the relative phase shift (ϕ) or change in modulation depth (m) of the fluorescence with respect to the excitation according to: $\tau_\phi = \frac{1}{\omega}\, tan(\phi)$ and $\tau_m = \frac{1}{\omega}\left(\frac{1}{m^2} - 1\right)^{\frac{1}{2}}$ [Lak06]. If the fluorescence decay is mono-exponential, then $\tau_\phi = \tau_m$ and if this equality is not met, then the fluorescence decay profile is complex. By making multiple measurements at different excitation harmonic frequencies, it is possible to characterise multi-exponential decay profiles. Although this calculation can be done analytically for a pure double-exponential decay profile, it is usually necessary to utilise non-linear fitting techniques to analyse complex fluorescence decay profiles, particularly if background terms and instrument response function are to be taken into account [Gra83, Lak85]. Alternatively, frequency domain data is increasingly analysed using phasor analysis [Cla04, Dig08], a graphical approach that can present complex fluorescnce lifetime data and provide insights with no fitting of the exponential decay profiles. However, some kind of quantitative analysis (fitting) of the graphical data is required to provide parameter values such as population fractions. Freqency domain FLIM can also be implemented with non-sinusoidal exaction modulation, e.g. using pulse trains from mode locked lasers [So95]. One or more of the harmonic components of the modulated fluorescence signal can be analysed: the first order component can be used to determine an average fluorescence lifetime and higher order components can be utilised to characterise more complex fluorescence decay profiles, e.g. for FRET experiments [Squ00].

Frequency domain (FD) FLIM was initially implemented using sinusoidally modulated image intensifiers [Gad93] in front of CCD readout cameras, requiring a minimum of three images to be acquired at different phase shifts relative to the excitation signal for the measurement of a mono-exponential decay profile excited by a sinusoid. For complex decay profiles or fluorescence signals excited by pulse trains, it is necessary to acquire images at significantly more phase-steps to avoid aliasing. This sampling of the fluorescence signal at different phase steps impacts the imaging speed and the number of incident fluorescence photons required for FD FLIM [Eld08, Eld09]. More recently, sinusoidally modulated CMOS cameras have been developed that provide much higher quantum efficiency and can simultaneously acquire photons at two phase steps without the loss of photons due to sampling [Esp06]. When combined with modulated excitation LED or laser diode sources [Fra15], this approach provides a relatively cost-effective implementation of wide-field FLIM, which may be particularly suitable for applications requiring only an estimation of mean fluorescence lifetime.

2.3.2 Wide-field time-gated FLIM

Wide-field time-gated FLIM implemented with mode-locked excitation lasers [Scu96, Dow98] is similar to FD FLIM in terms of the data acquisition, with time-gated images being recorded at different delays relative to the excitation pulses (as opposed to sinusoidally modulated images acquired at different phase shifts). However, with pulsed excitation and detection, a single time-gated FLIM acquisition can determine complex lifetime parameters, capturing information that would require multiple acquisitions at different harmonic frequencies using FD FLIM, and the data analysis is undertaken in the time domain. A typical set-up for wide-field FLIM is illustrated in Figure 2.18: an ultrashort pulsed laser source is used to excite fluorescence in the sample and the resulting fluorescence image is relayed to the photocathode of a gated optical imager (GOI) which functions like an ultrafast shutter, either blocking or amplifying the signal according to the applied gating voltage. A lens relay then images the intensified image at the phosphor screen of the GOI onto a readout camera.

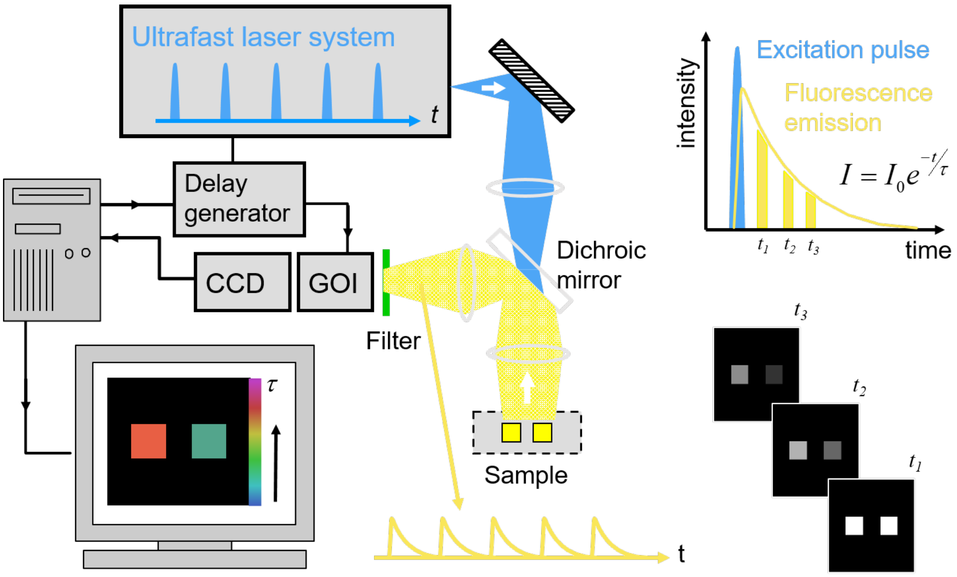

Figure 2.18: *Wide-field time-gated FLIM outline [Els04].*

The GOI is the key component for wide-field time-gated FLIM and its basic function of amplification is similar to a photomultiplier tube (PMT) [Pho07b]. Photons incident at the photocathode are converted to photoelectrons via the photoelectric effect. These electrons are accelerated by a pulsed gating voltage to a micro channel plate (MCP), which is an array of glass capillaries across which a high voltage (V_{MCP} ~750 V) is applied. This acts like an array of photomultiplier dynodes, with electrons colliding with the capillary walls to producing cascades of secondary electrons that are accelerated to generate further secondary electrons and hence amplify the original photoelectron image. The MCP capillaries limit the lateral spread of the photoelectrons and determine the maximum spatial resolution of the time-gated images. The pixelated electron streams from the MCP are accelerated towards a phosphor screen by a voltage, V_s, where they generate photons to produce the amplified gated optical image.

Gate ON at point (a)

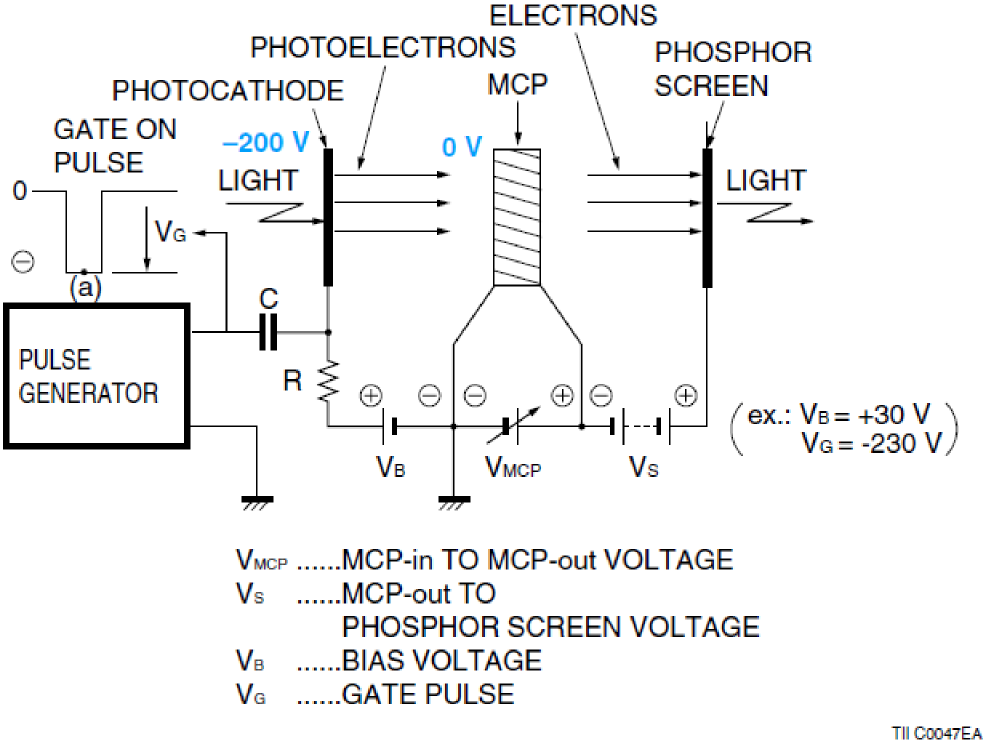
ELECTRONS
PHOTOELECTRONS
PHOSPHOR SCREEN
PHOTOCATHODE
MCP
GATE ON PULSE
−200 V
0 V
0
LIGHT
LIGHT
V_G
⊖
(a)
C
PULSE GENERATOR
R
⊕
⊖
⊖
⊕
⊖
⊕
(ex.: V_B = +30 V
V_G = -230 V)
V_B
V_{MCP}
V_S
V_{MCP} ......MCP-in TO MCP-out VOLTAGE
V_S ......MCP-out TO PHOSPHOR SCREEN VOLTAGE
V_B ......BIAS VOLTAGE
V_G ......GATE PULSE
TII C0047EA

Gate OFF at point (b)

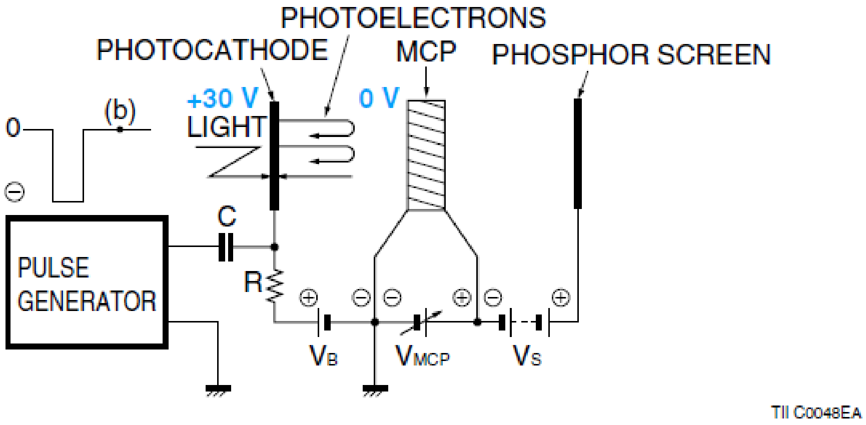
PHOTOELECTRONS
PHOTOCATHODE
MCP
PHOSPHOR SCREEN
0
(b)
+30 V
0 V
LIGHT
⊖
C
PULSE GENERATOR
R
⊕
⊖
⊖
⊕
⊖
⊕
V_B
V_{MCP}
V_S
TII C0048EA

Figure 2.19: *GOI concept. Gate ON state is shown in (a) and the OFF state in (b) [Pho16] Hamamatsu Photonics K.K.*

As illustrated in Figure 2.19, in the off state there is a positive bias voltage (V_B ~30 V) acting against the propagation of electrons from the photocathode to the MCP. During the off state of the GOI the pulse voltage is decrease to 0 V and the positive bias voltage forces the electrons back to the photocathode, so no photoelectrons are enhanced by the MCP. When the negative gating voltage ($|V_G| > |V_B|$) is applied, the bias voltage is overcome and gain of the GOI is switched on. For the GOI manufactured by Kentech Instruments Ltd, this occurs in 50 – 100 ps, allowing time-gates as short as ~200 ps to be realised and longer time-gates to be precisely set with steep (<100 ps) edges that determine the temporal resolution of the time-gating. The time-gating voltage signal is applied periodically in synchronism with the incident periodic excitation pulses, such that the readout camera integrates a time-gated image at a fixed time-gate delay with respect to the excitation pulses. Typical readout camera integration times of 100 μs to 1 s, accumulate time-gated fluorescence from 8000 to 8x10^7 pulses for an 80 MHz excitation pulse rate. For each FLIM acquisition, the time-gate delay is adjusted such that the fluorescence decay profile can be appropriately sampled, according to the complexity of the decay model to be fitted. The outcome is a three-dimensional data set with two spatial dimensions and a time dimension. For every pixel in the FOV, the series of time-gated fluorescence intensity values can be used to calculate a fluorescence lifetime analytically or the data can be fitted to a suitable model of the fluorescence decay to obtain its characteristic parameters. For many applications, it is useful to combine the information from multiple pixels to improve the precision of the lifetime determination (at the cost of spatial resolution) or global analysis techniques can be used, as discussed in subsection 2.4.3.

2.3.3 Time-correlated single-photon counting

Time-correlated single-photon counting (TCSPC) is the most accurate imaging method to determine lifetime information, with a shot-noise-limited signal/noise ratio proportional to the square root of the number of detected photons [Kö92]. It works by using fast electronic circuitry to measure the arrival time of individual fluorescence photons with respect to the laser excitation pulses in order to build up a histogram that contains the fluorescence decay information, which can be fitted to an appropriate fluorescence decay model [Bug89]. TSCPC is used in single channel instruments, such as time-resolved fluorometers, and it is often implemented in laser scanning fluorescence microscopes to realise FLIM. In multiphoton microscopes, the pulsed excitation source is already available, and it is relatively cost effective to convert it to FLIM by adding a single photon detecting PMT and a TCSPC card. To convert a laser scanning confocal microscope to FLIM, a pulsed excitation laser must also be supplied. The principles underlying modern TCSPC instrumentation are explained in detail in the Becker & Hickl (BH) handbook [Bec14] and outlined in Figure 2.20.

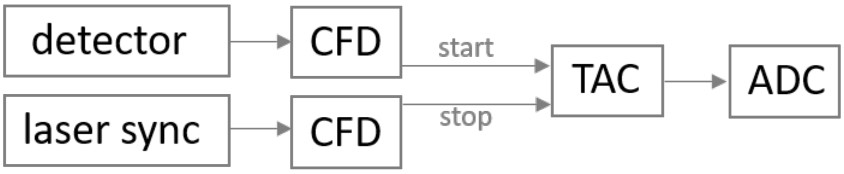

Figure 2.20: *Schematic of TCSPC circuitry.*

Briefly, a pulsed laser is used to excite the sample with the excitation power set to a level at which less than one photon is detected per excitation pulses. In practice, on average at the detector, the photon detection rate is set to 0.1 – 1 % of the pulse rate [Vic07]. Each detected photon generates an electrical signal that is compared with an electrical signal from the excitation laser and the relative timing of the laser sync and detector pulses is precisely determined using a constant fraction discriminator (CFD) to eliminate artefacts from fluctuations in signal amplitudes that could lead to errors for timing circuits that trigger when the signal reaching a pre-determined voltage value. As depicted in Figure 2.21, an electrical pulse incident at the CFD is split into two pulses and one pulse is inverted and shifted in time. At the output of the CFD, the two pulses are summed, and the resulting pulse shape has a zero-crossing point between the minimum and maximum voltages that is, to first order, independent of the amplitude of the incident pulse. Thus, a voltage trigger set to zero-crossing point will not be influenced by the amplitude of the incoming pulses and so provides reliable timing information. The precisely timed signals from the detector CFD starts a time-to-amplitude converted (TAC) that generates a linear voltage ramp that grows until the signal from the laser synch CFD is used as the stop signal. Thus, the TAC voltage is proportional to the time difference between the two CFD signals. An analogue-to-digital converter (ADC) then converts the TAC voltage to a computer readable format. After a certain time, the system resets so that a new photon event can be detected.

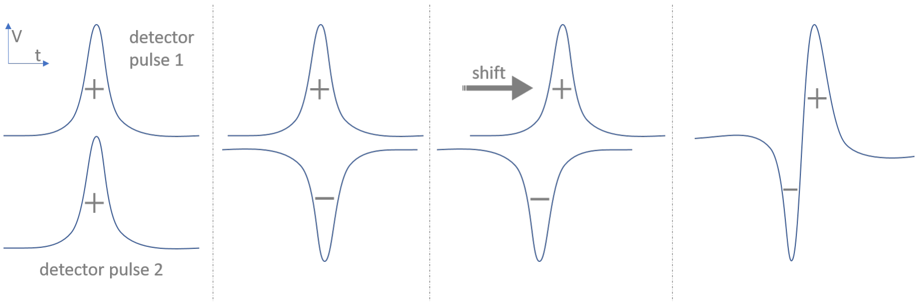

Figure 2.21: *CFD concept. The incoming pulse is split into two signals, one of which is inverted and shifted in time. These pulses are summed to obtain a zero-crossing point that is independent of the pulse amplitude.*

Historically, the ADC was the rate-limiting step for TCSPC since most commercially available ADCs were either too slow or not sufficiently accurate. However, the introduction of a modified dither process enabled a fast and accurate ADC [Bec02] and the maximum count rate of current TCSPC systems are limited by the system dead time, i.e. the time required for the TAC to reset (typically >100 ns). If the photon detection rate is too high, such that a further photon arrives at the TAC before it has been reset, then this later photon will not be detected. This phenomenon, described as "pulse pile-up", leads to the recorded photon histograms being biased towards earlier arriving photons and therefore to errors. The limitation in photon detection rate set by the TCSPC circuitry can limit the FLIM acquisition rate for a TCSPC microscope. Thus, although TCSPC is the most accurate method for FLIM, it is relatively slow due to the sequential pixel acquisition inherent in laser scanning microscopes and/or to the limitation in photon detection rate imposed by the TCSPC circuitry, typically <10 MHz [Tur14].

2.4 FLIM analysis

This section gives an overview of the issues to be considered when fitting experimental FLIM data to fluorescence decay models, following reference [War13] and Dr Sean Warren's PhD thesis [War14]. Fluorescence decay profiles, along with a variety of physical phenomena such as radioactive decay, vibrational damping, chemical reactions and more, can be modelled using a first order differential equation, $\frac{dN}{dt} = -\Gamma N$, where N is the population of a specific physical state and Γ is the exponential decay constant. The solution to this rate equation is an exponential function where I_o is the maximum intensity and the lifetime τ is the inverse of Γ:

$$I(t) = I_o \; exp\left(-\frac{t}{\tau}\right) \tag{2.10}$$

2.4.1 Instrument response function

A temporal input profile will always differ from the temporal output signal when passing through an experimental set-up. Thus, the recorded signal is impacted by the detection system itself [Gad11]. The instrument response function (IRF) is the temporal response of a system to a delta function input signal. For a detector used to record a fluorescence decay, the output time dependent profile, $h(t)$, is a convolution ($\circledast$) of the IRF, $g(t)$, and the actual fluorescence signal, $i(t)$:

$$h(t) = g(t) \circledast i(t) \tag{2.11}$$

The main factors contributing to the IRF in a time domain fluorescence lifetime measurement are the excitation laser pulse width and the response time of the detector, which is the inverse of its bandwidth, and any temporal noise or jitter between the excitation pulses and the detection electronics. Since laser excitation pulses are typically <100 ps, they are much shorter than the fluorescence lifetime of most fluorophores encountered in microscopy and are usually shorter than the detector response time, indeed femtosecond pulses are a good approximation to a delta function for FLIM. For TCSPC, the PMT response times are typically <200 ps, although specialised PMT are available with response times <50 ps [Beb86]. For wide-field time-gated FLIM, the IRF is dominated by GOI time-gate shape, which can be set between 200 ps and >6 ns. The convolution of a typical fluorescence decay profile (τ = 3 ns) and IRFs of 200 ps (such as a laser pulse) and 4 ns (such as a GOI time-gate width) are simulated in Figure 2.22.

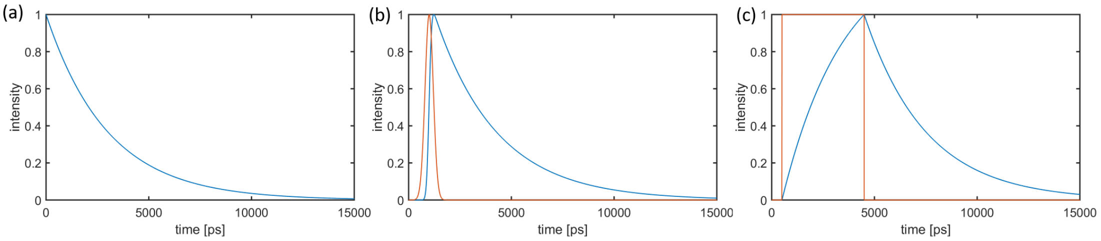

Figure 2.22: *Simulation of a measured fluorescence decay profile impacted by an IRF: (a) an ideal mono-exponential fluorescence decay profile with* τ = *3 ns together with its convolution with (b) a 200 ps Gaussian shaped IRF; and (c) a rectangular IRF of 4 ns. The fluorescence signal is shown blue and the IRF in red.*

Since the laser excitation pulse approximates well to an impulse (delta function), the IRF can be determined by measuring the excitation signal, e.g. from a scattering sample or a mirror in the sample plane. In the wide-field time-gated FLIM spinning Nipkow disc microscope used in chapter 3, the IRF can be measured via a FLIM acquisition of the excitation light scattered from the Nipkow disk [Kel14]. In Figure 2.23 the measured IRF vary across the FOV, this is particularly pronounced for time-gated FLIM where there can be an appreciable (up to ~100ps) time for the gating voltage to reach the whole of the FOV in some

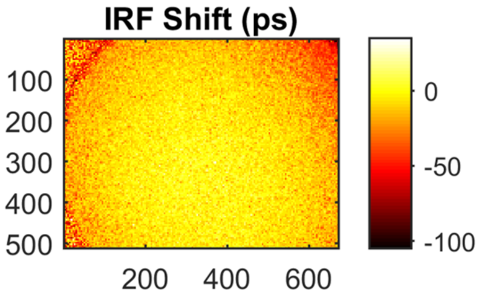

Figure 2.23: *Time-gated, GOI based image of reflected light shows the radial distribution of the* t_0 *shift. X and Y coordinate in pixel,* t_0 *shift in picoseconds.*

GOIs, resulting in a spatially varying IRF with a radial dependence. This is described as the "IRF shift map".

Since the excitation radiation is at a different wavelength from the fluorescence, it can take a different light path from the sample (and the back-scattered light from the spinning disc takes a significantly different path). It is therefore necessary to determine the difference in the arrival time at the detector between the excitation pulses and the emitted fluorescence. This time difference is called the "t_0 shift" in this thesis. To find the value of t_0, i.e. the time by which the scattered excitation IRF must be shifted to match the fluorescence data, a fluorescence lifetime image of a reference fluorophore with a known lifetime should be acquired and the t_0 shift can be obtained by fitting this data to a mono-exponential decay model. This value for the t_0 shift is used with the IRF shift map to provide the appropriate delay between the measured scattered excitation light IRF and the fluorescence signal for each pixel in the FOV to be used when fitting the experimental fluorescence data.

2.4.2 Background signals in FLIM

Various sources of background light can significantly impact FLIM analysis, particularly for weak fluorescence signals. Sources of background light include any stray room light reaching the photocathode, any unwanted fluorescence generated from the optical components or the container holding the sample as well as fluorescence from the cell medium or contributions from cellular autofluorescence. In addition, there can be an offset on the CCD digital number as well as thermal noise and dark noise in the CCD. A routinely used method in our lab is to subtract the background before fitting, thus the fluorescence lifetime will appear longer than it should for an underestimation of the background, while an overestimation leads to a shorter lifetime when fitting to a mono-exponential decay model. Two categories of background contributions can be considered: a constant DC background and a time varying background.

Constant backgrounds A DC background here is one that is constant over the fluorescence decay profile. This could be a camera offset in wide-field FLIM, but also background light, e.g. room light, leaking into the detection path. Such DC background contributions can be subtracted from each time-gated image or the fitting model can be adjusted to fit a background or to incorporate a fixed background.

Time varying backgrounds Time varying background contributions are more challenging to take into account and their impact should be minimized as much as possible, most straightforwardly by optimizing the system to maximise the fluorescence signal to noise ratio. Any contributions originating from the excitation laser pulse will not be constant over the duration of the decay. These could include fluorescence excited in optical materials in the light path (e.g. glue, optical fibers or plastic bottomed wells) or fluorescence excited in the biological sample (auto fluorescence of cells or imaging media). Any leakage of excitation light into the detector, such as scattered excitation light, could also contribute to the time-varying background. The main approach used to correct for a time-varying background is to measure it, e.g. by undertaking FLIM of unlabeled cells, and subtracting the corresponding value from each time-gated image according to the delay. However, in some cases, time-varying background contributions such as autofluorescence, can also vary in space and may also need to be measured or estimated locally for each cell or FOV.

2.4.3 Global decay analysis

In many studies, a complex fitting model may be required, e.g. to provide quantitative parameters from mixtures of fluorophores, such as FRETing and non-FRETing donor molecules or free and bound fluorophores. While only a few hundred photons are required to determine the lifetime of a fluorophore with a mono-exponential decay profile, thousands of fluorophores are required to fit a complex decay function [Kö92]. In many FLIM experiments, however, the photon count is practically limited to a few hundred photons per pixel or less by the photostability of the fluorophores or by considerations of phototoxicity for live samples. This can be addressed by global analysis of FLIM data, whereby the information from all pixels, across one or many FOVs, contributes to the estimation of lifetime components under the assumption that these components are the same in all pixels. This invariant assumption is valid for a two-lifetime system, which is in particular the case for FRET biosensor experiments. However, it should be noted that environmental inconsistencies, such as temperature or pH-value, in a cell or across a cell population can locally change the lifetime. If these effects are dominant, global decay analysis cannot be used because the fitting algorithm of *FLIMfit* cannot account for them. Thereby enabling the application of sophisticated fitting models, even for FLIM experiments with low ($\sim$100's/pixel) photon counts. There are two approaches to global analysis of FLIM data: global binning and global fitting [Bee92, Pel04], both of which are implemented in *FLIMfit*, a FLIM data analysis software tool developed in the our laboratory [War13].

Global binning Also known as lifetime invariant fitting, the global binning approach aggregates all pixel information into a single fluorescence decay data set that contains sufficient photons to accurately fit complex decay profiles. The obtained lifetime components are then fixed for a second fit performed on a pixel-wise basis across the whole data set that provides the relative weighting of the different lifetime components for each pixel, which are the only free parameters for this second fit. This approach is relatively easy to implement and rapid in terms of computation. However, it does not make efficient use of the information available from pixels where the contribution factors may be much higher or lower than the average, i.e. pixels that are closer to a pure decay of one of the lifetime components.

Global analysis In this approach the lifetime components are again assumed to be invariant across the FOV or multiple FOV but here they are determined by fitting the data for all the pixels in parallel to the lifetime components and the pixelwise weighting factors. This is much more challenging computationally, but it does make more efficient use of data from pixels where one or another lifetime component is dominant. *FLIMfit* provides a particularly rapid implementation of the required computation and global fitting has become the method of choice for analysing complex fluorescence decay profiles in our laboratory.

2.5 Förster resonance energy transfer (FRET)

Förster resonance energy transfer (FRET) [Fö48] between fluorophores is widely used as a functional readout in biomedical research. It is an electromagnetic dipole-dipole interaction that can occur over distances between appropriate fluorophores up to ∼10 nm. This sensitivity to nm-scale distances can be used to interrogate molecular interactions, including in live cells, and so measurements of FRET are of interest for molecular cell biology [Bas99, Lak06]. In our laboratory we have used FRET to study quantify protein-protein interactions, e.g. [Mar16] and to spatially resolve the activation of FRET biosensors, e.g. [Che16].

2.5.1 Photophysics of FRET

The following outline of the principles underlying FRET is based on a review from Gadella [PB11]. If two fluorophore dipoles satisfy specific conditions, it is possible for an excited dipole to transfer its energy to an unexcited dipole in close proximity [Fö48]. For FRET to occur, three conditions must be met, as illustrated in Figure 2.24. First, the emission spectrum of the excited fluorophore, called the “donor”, needs to overlap with the absorption spectrum of the initially unexcited fluorophore, the “acceptor”. Second, the donor and acceptor need to be in sufficiently close proximity to each other to enable the electromagnetic dipole-dipole interaction, typically within 10 nm. Finally, the dipoles of the donor and acceptor must have a parallel vector component, i.e. they are not allowed to be perpendicular to each other.

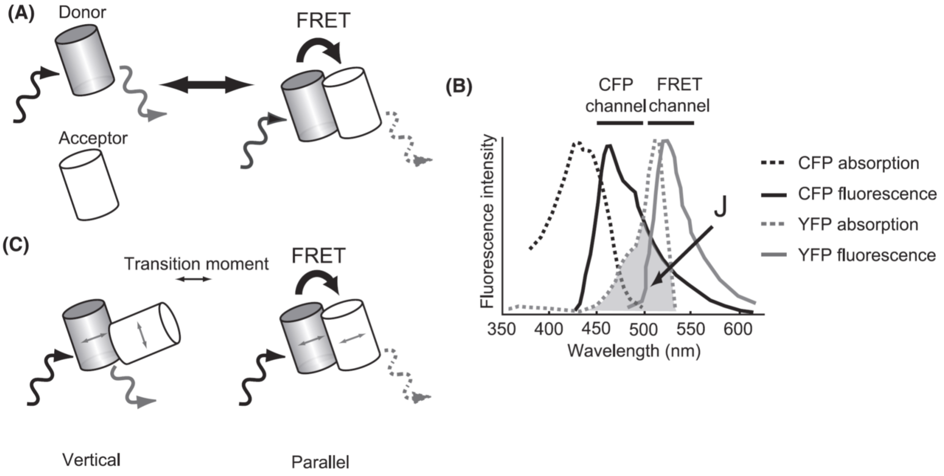
(A)
Donor
FRET
Acceptor
(B)
CFP channel
FRET channel
Fluorescence intensity
J
CFP absorption
CFP fluorescence
YFP absorption
YFP fluorescence
350
400
450
500
550
600
Wavelength (nm)
(C)
Transition moment
FRET
Vertical
Parallel

Figure 2.24: *Necessary conditions for FRET: donor and acceptor fluorophores must be in close proximity (A), have a sufficient overlap in emission and absorption spectrum (B), here demonstrated with CFP and YFP, and the dipoles must not be perpendicular to each other (C) [Aok12].*

The FRET efficiency (E) describes the strength of the resonant energy transfer from donor to acceptor and is strongly dependent on the distance between the fluorophores (r_{DA}) according to Equation 2.12. R_0 is the Förster radius, the distance at which the FRET efficiency is 50%. It depends on the refractive index (n), the quantum yield of the donor (Q_D), the angular orientation between the two dipoles (κ) and the overlap integral (J).

$$E = \frac{R_0^6}{R_0^6+r_{DA}^6} \tag{2.12}$$

$$R_0^6 = 8.8 * 10^{23} n^{-4} Q_D \kappa^2 J \tag{2.13}$$

The Förster radius is usually in the range of nanometers ($R_0 \approx 3-6$ nm) for fluorophores used to label proteins in cells and so FRET efficiencies become significant for r_{DA} <10 nm but rapidly become negligible as r_{DA} >10 nm. FRET can be used to sense the close proximity of different labelled proteins (“intermolecular FRET”) and can be used to sense changes in the conformation of single proteins or protein complexes that have been labelled with both donor and acceptor fluorophores (“intramolecular FRET”). As discussed below, the detection of FRET is usually realised through some kind of spectroscopic measurement of fluorescence. Although the spatial resolution of fluorescence microscopes may be limited by diffraction, FRET provides a functional readout of events happening on scales far below the diffraction limit and fluorescence microscopy can incorporate FRET measurements, e.g. to map protein interactions in space and time.

FRET can be reported through the changes that it produces in the fluorescence emission of the donor and/or acceptor fluorophores. If a population of donor fluorophores are undergoing FRET, their emission intensity will decrease and the intensity of the population of acceptor fluorophores will increase. Since FRET provides an additional non-radiative decay channel for excited donor fluorophores, the fluorescence lifetime of donor fluorophores will decrease. Equation 2.14 indicates the fluorescence intensity decay profile after excitation for a fluorophore population undergoing FRET:

$$I(t) = I_0 \; exp^{-(\Gamma_{fl}+\Gamma_{FRET})t} \tag{2.14}$$

where $I(t)$ is the donor fluorescence intensity, I_0 is the fluorescence intensity immediately after excitation, Γ_{fl} the inverse of the non-FRETing donor fluorescence lifetime and Γ_{FRET} the FRET decay rate.

2.5.2 Methods to read out FRET

There is a wide range of methods to read out FRET via measurements of various fluorescence parameters of the donor and/or acceptor fluorophores [JE06]. The most commonly used techniques are ratiometric measurements of the relative intensity of the donor and acceptor emission and measurements of the fluorescence lifetime of the donor emission. Other techniques include measurements of the donor intensity before and after photobleaching of the acceptor and measurements of the fluorescence polarisation anisotropy, which decreases for the acceptor excited via FRET [Lid03].

Ratiometric intensity-based measurements of FRET There are various ways to measure FRET using spectrally-resolved intensity measurements to distinguish the emission from the donor and acceptor. Probably the most popular approach entails exciting the donor fluorophores and comparing the intensity of the donor and acceptor emission, typically using spectral filters to separate their emission or detecting both channels simultaneously using an image splitter and acquiring two images for wide-field microscopy or using a dichroic beam splitter and two detectors for laser scanning microscopy. A popular implementation is "three cube" FRET where three different standard filter sets can be used: First a donor channel cube is used (to measure donor emission with donor excitation), followed by a "sensitized emission" measurement (acceptor emission resulting from donor excitation) and finally an acceptor only measurement (acceptor emission following acceptor excitation) [Che06].

A more sophisticated approach to ratiometric intensity FRET is “spectral FRET” where the whole fluorescence spectrum is measured and the donor and acceptor signals are unmixed. Although more complex, spectral FRET has several advantages over intensity based FRET, including the ability to use donor and acceptor pairs with highly overlapping spectra, the ability to exclude background fluorescence after spectral unmixing and the ability to collect he whole emission spectrum, thereby improving the signal to noise ratio [Zim02].

Measuring the relative increase in the acceptor intensity compared to the donor intensity is a rapid technique to indicate FRET and works with relatively low fluorescence intensities and so is suitable for time-lapse imaging of live cells. Quantification of the FRET parameters is possible once the instrument has been calibrated to account for spectral bleed-through between the donor and acceptor channels and to establish the donor-acceptor stoichiometry. Typically, this entails reference measurements of samples prepared with only donor, only acceptor and donor with acceptor present [Ber03, Eri01]. Such measurements are still not able to provide the absolute FRET efficiency unless a reference sample with the same fluorophores and a known FRET efficiency is available [Hop02].

FLIM-FRET Fluorescence lifetime-based approaches to FRET only require measurements of the donor emission. FRET can be detected through the decrease in donor lifetime and fitting the fluorescence decay profile to an appropriate complex decay model (e.g. a biexponential decay model) can, in principle, directly provide the absolute FRET efficiency and the population fraction of FRETing donors without the need for reference samples or spectral calibration. Therefore, it allows the straightforward comparison of experiments between different microscopes and laboratories [Gad95]. However, fluorescence lifetime measurements require more detected photons than spectral ratiometric intensity FRET measurements, which can present challenges when imaging live cells. This can be ameliorated in FLIM-FRET experiments through the use of global analysis techniques and FLIM-FRET is probably the most widespread application of FLIM microscopy.

2.5.3 FRET biosensors

Biosensors are fluorescent constructs that can be expressed in cells to provide functional readouts of cell signalling processes and they represent a major category of the biological applications of FRET. FRET biosensors are typically constructs labelled with fluorescent proteins providing the donor and acceptor fluorophores and can report on concentrations of analytes, such as calcium [Miy97, Man06], chloride [Kun00] and potassium [Uey02], as well as signalling molecules like IP3 [Nez06], PIP2 [Nis08] and calpain [Sto05] amongst others. FRET biosensors can be divided into two groups: intermolecular and intramolecular FRET, as depicted in Figure 2.25. Intermolecular FRET biosensors comprise two separate labelled entities, a ligand and a sensor, that are consistently labelled with either the donor or acceptor fluorophore. During the activation of these biosensors, the two domains bind together and bring the donor and acceptor in close proximity, resulting in FRET. Thus, the donor fluorophores exist in two populations: the unbound, non-FRETing state and the bound, FRETing state.

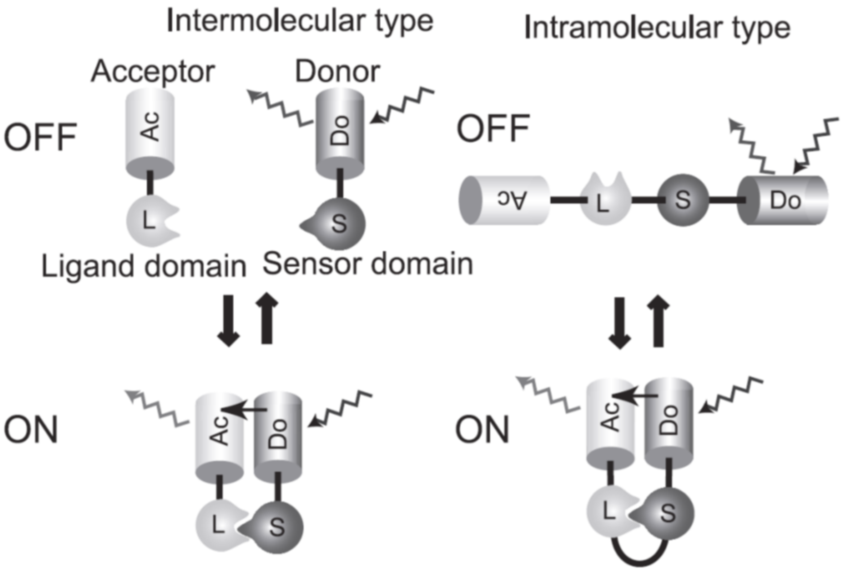

Figure 2.25: *Inter- vs Intramolecular FRET biosensors. Left: Intermolecular FRET, a ligand (L) and a sensor (S) in an unbound state do not FRET. In a bound condition FRET occurs. Right: Intramolecular FRET, FRET is not introduced in an open conformation, but will be in a closed protein conformation [Aok12].*

In intramolecular FRET, one protein construct includes both the donor and the acceptor fluorophores. This protein undergoes a conformation change upon activation. Usually, if the protein is in an open conformation there is low or no FRET, because the donor and acceptor are relatively far away from each other. In the closed conformation, FRET occurs because the donor and acceptor are brought together closer than the Förster radius. Typical fluorophore pairs used for donor and acceptor in FRET biosensors include CFP/YFP and GFP/mCherry.

2.6 Adaptive optics in microscopy

High quality images can enable multidimensional, structural and functional information to be obtained from cells, tissue and living animal studies. But image quality can be compromised by the spatially varying refractive index in biological materials, particularly when imaging deeper into tissue, e.g. through several layers of cells. Adaptive optics (AO) technology enables wavefronts to be manipulated in order to correct optical aberrations introduced by the system or the sample. This section aims to summarise the application of AO in optical microscopy and is based on review articles published by Booth [Boo07, Boo14]. It outlines aberration correction in microscopy, introducing the common mathematical treatment based on Zernike polynomials (see subsection 2.6.4), and discusses various devices used for AO with their applications in optical microscopy. AO was originally developed by astronomy [Har98] and military [Tys15] research, e.g. to enhance the quality of a telescope images of stars, satellites or targets that can be blurred by turbulence in the atmosphere. AO can also be applied to microscopy, where the instrument or sample can degrade the optical waves conveying the image information.

2.6.1 Aberration correction in optical microscopy

In microscopy an incident planar wavefront is typically transformed to a spherical wavefront by a high NA lens as shown in Figure 2.26 (a). Any distortion of these wavefront shapes introduced by the system or the specimen is called aberrations and can reduce the image quality. Such aberrations are represented by phase variations in the pupil plane of the objective lens or conjugate planes. To correct for them, the opposite phase variation can be applied in the pupil of the objective lens using a device that spatially modulates the phase of the light beam. This can be implemented

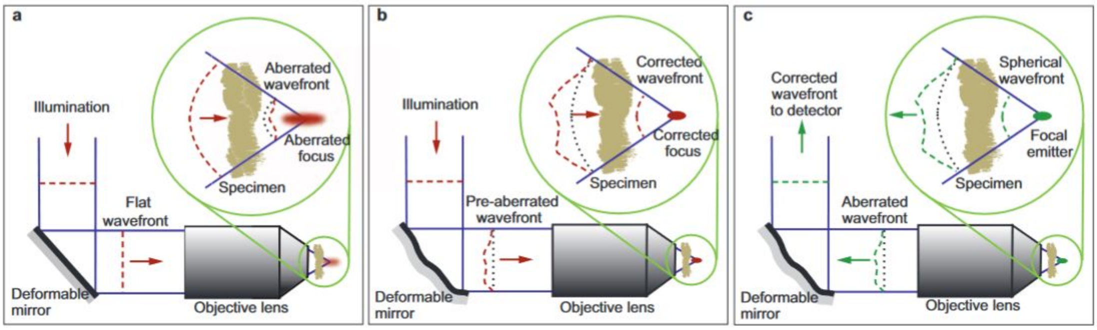
a
Illumination
Aberrated wavefront
Aberrated focus
Specimen
Flat wavefront
Deformable mirror
Objective lens
b
Illumination
Corrected wavefront
Corrected focus
Specimen
Pre-aberrated wavefront
Deformable mirror
Objective lens
c
Corrected wavefront to detector
Spherical wavefront
Focal emitter
Specimen
Aberrated wavefront
Deformable mirror
Objective lens

Figure 2.26: *Wavefront distortion in high NA objective microscopy by specimen induced aberrations. (a) aberrations induced when passing the specimen, (b) predefined aberrations cancel out distortion in the excitation path and (c) deformable mirror corrects for aberrations in the emission path [Boo14].*

in the excitation beam path to improve the focusing of the illumination light (Figure 2.26 (b)), and/or it can be implemented in the emission path (Figure 2.26 (c)) to correct the wavefronts emanating from point sources (fluorophores) in the sample. Aberrations can be represented by sums of orthogonal functions, for which the Zernike polynomials [Zer34] are widely used. Another approach, which is especially useful with a membrane based deformable mirror devices, utilises eigenmodes of the corrected elements [Pat00].

A commonly encountered aberration occurs when light is focused through a planar interface with different refractive indices, such as a coverslip with a refractive index different to that of the immersion fluid of the objective lens and the imaging media [She91]. The dominant aberrations at such an interface are spherical aberrations, which are proportional to the focusing depth and which can be described by radial symmetrically Zernike functions [Tö95]. Using water immersion objectives or objectives with a correction ring can reduce the image degradation when imaging biological samples through a coverslip, however, it is difficult to achieve full compensation of the aberrations [Sch05].

Significantly more complex aberrations are introduced by optically inhomogeneous biological samples [Bol89]. To compensate for such complex aberrations, it is necessary to measure the aberrated wavefronts, which can be accomplished using an interferometer [Sch04]. If the spatially variation of optical pathlength over the imaging region is determined, the aberrations can be calculated. This was demonstrated using differential interference microscopy [Kam01] and tomography microscopy [Cha06].

2.6.2 Devices for adaptive optics

AO devices for spatially manipulating optical wavefronts have developed from video projection technology. There are two main groups of devices: deformable mirrors (DM) and liquid crystal-based spatial light modulators (SLM). There are two categories of DMs: digital micromirror devices where sub-elements of an array of mirrors can be accessed individually or adaptive devices where an electric or magnetic field is moving membranes or actuators. SLMs are based on an array of liquid crystals that can be digitally controlled on a pixel by pixel basis. An applied electric field causes the liquid crystals to tilt and changing the tilt angle changes their refractive index, which introduces phase differences in the optical beam path that can be used, e.g. to manipulate the spatial properties of diffracted beams.

Although SLMs have a greater flexibility for modifying wavefronts due to a larger pixel count, they are mainly used in the excitation path because of their insertion loss (diffraction efficiency typically

<90% [Pho07a]) and because they are polarisation dependent and their performance can be a strong function of wavelength. Additionally, they are limited to applying phase differences of up to 2π, and so phase-unwrapping techniques may be required for some applications. In contrast, DMs operate on wavefronts in reflection rather than diffraction and are usually polarisation independent and applicable across a broad range of wavelengths, making them suitable for implementation in both excitation and fluorescence light paths. DMs, such as MEMS DMs can often provide greater than 2π phase changes and can be modulated faster than nematic liquid crystal SLMs.

To have direct access to the spatial frequency components in a microscope image, a spatially modulating device should be placed in an image plane of the object. This is typically realised using a 4-f lens relay, for which an on-axis configuration can be implemented. Alternatively, an off-axis configuration can be used, which is convenient when using SLMs because a blazed grating can be programmed onto a phase mask, which provides high diffraction efficiency into the first order and the zeroth order is blocked. In the off-axis approach, the modulation of the first order diffracted beam is more efficient than for the zeroth order beam and any unmodulated light is automatically removed. However, this arrangement is less compact than most on-axis configurations and the diffraction angle is wavelength dependent, which makes multicolor application difficult [Mau11].

2.6.3 Application of adaptive optics in microscopy

AO approaches have been used to enhance various microscopy techniques such as multiphoton microscopy, confocal microscopy, wide-field microscopy, light sheet microscopy, SIM, localisation microscopy and STED microscopy.

AO in laser scanning multiphoton microscopy: here AO is implemented only in the illumination path, because all the detected light is assumed to have originated from the excitation focus and so any distortion of the wavefronts in the emission path will not reduce the image quality [Wat10, Oli09]. SLM [Ji09, Mil11] and DM [Tao13, Bue11] approaches can increase the depth to which the excitation light can be focused to a sufficient intensity for multiphoton excitation and have been applied in multiphoton microscopy, including second and third harmonic generation microscopy [Tha11, Jes09].

AO in laser scanning confocal microscopy: confocal microscopy can benefit from AO in both the excitation and emission light paths, the latter because the fluorescence has to be focused through the confocal pinhole for detection and any distortion in the emission wavefronts will distort the confocal PSF at the pinhole and reduce the transmission to the detector. Thus, a DM may be positioned in the common beam path for excitation and emission in a confocal microscope [Tao11, Tao12]. This approach has also been applied to confocal fluorescent correlation spectroscopy [Ler13].

AO with wide-field microscopy: due to the spatially extended illumination of the entire FOV, aberrations in the illumination path have no significant effect on the image quality. Thus, AO is only used in the emission path for wide-field microscopy to correct for aberrations. Predominantly DM approaches have been implemented in transmission microscopy [Dé07] and fluorescence microscopy [Ver11, Wei15], where they are suitable for the unpolarized and spectrally broad fluorescent signal. However, a liquid crystal SLM-based transmission microscope has been demonstrated with narrow band light emitting diode illumination [War10]. Other wide-field imaging methods can also benefit from AO, such as super-resolving localisation microscopy [Bur15]. AO has also been used with modalities combining wide-field detection with shaped excitation intensity distributions including light sheet microscopy [Wil16, Roy16] and SIM [Dé08], where AO can provide benefits in both the excitation and emission light paths.

AO in STED microscopy: In STED microscopy, it is important to minimise aberrations in the excitation, depletion and emission beam paths to realise super-resolution [Den09]. AO has been applied in STED microscopy and was used to compensate system aberrations [Auk08], specimen induced aberrations [Gou12, Len14], and automated alignment [Gou13]. Further developments are presented in this thesis while using AO with a liquid crystal SLM to correct system aberrations, align laser beams and generate multiple foci for excitation and depletion beam using a single SLM.

2.6.4 Zernike polynomials

Optical aberrations are often described in terms of Zernike polynomials, which are orthogonal functions defined on a unit circle. They were first used for phase contrast microscopy by Zernike in 1934 [Zer34] and today are commonly used to describe the phase function of a wavefront in optical systems with a circular pupil. The set of Zernike polynomials can be used to form the wave aberration function ($W(\rho, \Theta)$), which describes the wavefront at the pupil with ρ being the normalised radial coordinate ($0 < \rho < 1$) and Θ the corresponding angle ($0 < \Theta < 2\pi$). A convenient presentation of the Zernike polynomials in a single index form was introduced by Mahajan [Mah94]:

$$W(\rho, \Theta) = \sum_{j=1}^{\infty} a_j \; Z_j(\rho, \Theta) \tag{2.15}$$

where Z_j is the Zernike polynomial, a_j is the aberration coefficient and the index j is a function of n and m, which are positive integers relating to the ordering of radial and azimuthal variations of the polynomials respectively. A set of Zernike polynomials in polar coordinates is presented in Table 2.1.

j	m	n	$Z_j(\rho, \Theta)$	name
1	0	0	1	piston
2	1	1	$2\rho \cos \Theta$	x tilt
3	1	-1	$2\rho \sin \Theta$	y tilt
4	2	0	$\sqrt{3}(2\rho^2 - 1)$	defocus
5	2	2	$2\sqrt{3}\rho^2 \cos 2\Theta$	x astigmatism (1st)
6	2	-2	$2\sqrt{3}\rho^2 \sin 2\Theta$	y astigmatism (1st)
7	3	1	$2\sqrt{2}(3\rho^3 - 2\rho) \cos \Theta$	x coma (1st)
8	3	-1	$2\sqrt{2}(3\rho^3 - 2\rho) \sin \Theta$	y coma (1st)
9	3	-3	$2\sqrt{2}\rho^3 \cos 3\Theta$	x trefoil (1st)
10	3	-3	$2\sqrt{2}\rho^3 \sin 3\Theta$	y trefoil (1st)
11	4	0	$\sqrt{5}(6\rho^4 - 6\rho^2 + 1)$	spherical aberration (1st)
12	4	2	$\sqrt{10}(4\rho^4 - 4\rho^2) \cos 2\Theta$	x astigmatism (2nd)
13	4	-2	$\sqrt{10}(4\rho^4 - 4\rho^2) \sin 2\Theta$	y astigmatism (2nd)
14	4	4	$\sqrt{10}\rho^4 \cos 4\Theta$	x quadrafoil (1st)
15	4	-4	$\sqrt{10}\rho^4 \sin 4\Theta$	y quadrafoil (1st)
16	5	1	$2\sqrt{3}(10\rho^5 - 12\rho^3 + 3r) \cos \Theta$	x coma (2nd)
17	5	-1	$2\sqrt{3}(10\rho^5 - 12\rho^3 + 3r) \sin \Theta$	y coma (2nd)
18	5	-3	$2\sqrt{3}(5\rho^5 - 4\rho^3) \cos 3\Theta$	x trefoil (2nd)
19	5	-3	$2\sqrt{3}(5\rho^5 - 4\rho^3) \sin 3\Theta$	y trefoil (2nd)
20	5	5	$2\sqrt{3}\rho^5 \cos 5\Theta$	x pentafoil (1st)
21	5	-5	$2\sqrt{3}\rho^5 \sin 5\Theta$	y pentafoil (1st)
22	6	0	$\sqrt{7}(20\rho^6 - 30\rho^4 + 12\rho^2 - 1)$	spherical aberration (2nd)

Table 2.1: *Zernike polynomials in polar coordinates. Adapted from [Nei00a].*

Applying phase modulation corresponding to these Zernike polynomials in the back focal plane of an objective lens enables the control of the intensity distribution in the imaging plane. For example, a confocal PSF can be moved in x or y implementing a phase ramp in an image plane of the objective according to the Zernike polynomials Z_2 and Z_3 respectively. More complex phase patterns, described by higher Zernike polynomials, can defocus the laser beam (Z_4) or compensate and introduce aberrations such as astigmatism in x (Z_5) and y (Z_6), coma in x (Z_7) and y (Z_8), trefoil in x (Z_9) and y (Z_{10}), spherical aberrations (Z_{11}) and higher order aberrations ($> Z_{11}$).

2.7 Summary

Summary This chapter has aimed to give a concise introduction to the broad field of fluorescence microscopy to underpin the work presented in this PhD thesis and a more detailed discussion of the specific techniques that are employed and/or extended in this PhD thesis. The first section discussed the photophysics of fluorescence and introduced the key fluorescence parameters. This was followed by an overview of fluorescence microscopy techniques from the early instruments to the latest advances.

After introducing the main fluorescence microscopy modalities, a more detailed summary was given of the super-resolution methods (SRM) of structured illumination (SIM) and stimulated emission of depletion (STED) microscopy. The future of fluorescence microscopy is live cell imaging where currently only wide-field methods are routinely used. Confocal approaches were, until the development of fluorescence light sheet microscopy, less common for live cell approaches due to the limited acquisition speed. The three described super-resolved techniques localisation microscopy, STED and SIM are competing for the ascendancy in SRM. Where SIM is currently the only easy to use technique for live cell imaging. But SIM is limited in resolution, therefore localisation microscopy or STED will capture its position as standard in live cell SRM over time. Neither of them is easily compatible with live cells. For localisation microscopy treatments with buffers are necessary to enable blinking, which are often toxic, and the long laser exposure times make it difficult to detect fast moving processes and leads to photobleaching over time. STED is as fast as confocal microscopy and therefore still limited in acquisition speed, however, a wide range of biological processes can be observed and the speed scales with the acquired field of view, so faster processes can be observable in a smaller field of view. The major disadvantage of STED is the high depletion laser power and the corresponding photobleaching and phototoxicity.

The next section introduced fluorescence lifetime imaging, including a short overview of FLIM instrumentation, with a particular emphasis on wide-field time-gated FLIM and TCSPC. Where TCSPC remains the gold standard for spectroscopic lifetime measurements with the most precise lifetime determination. With the limited acquisition speed TSCPC is not suitable for high throughput or live cell imaging. Wide-field time-gated FLIM contains intrinsic parallel detection and therefore fast acquisitions for high throughput and living cells, at cost of lifetime precision, are achievable.

A more extended discussion of FLIM data analysis, particularly with reference to *FLIMfit*, the software tool developed at Imperial that provides powerful FLIM analysis capabilities including global analysis, was given. This section concentrates on the practical application of fitting FLIM data and its pitfalls, which are significant such as the temporal response of the system (IRF) which is artificially broadening the acquisition data in time and the constant and temporal varying background. Not considering such effects can lead to a false interpretation of the acquired data and inconsistencies in a screen can occur.

Förster resonance energy transfer (FRET) was then introduced with a short discussion of the underlying physical principle and a brief review of different methods for FRET measurements, including FLIM. FRET probes molecular interactions on a scale below 10nm and gives an insight of protein-protein interactions. Biosensors report the active or inactive state of a protein and are often used with FRET to report the concentration of a specific ligand. FLIM-FRET biosensors constitute the majority of FLIM applications.

The final section discussed the correction of optical aberrations in microscopy and its applications. Random refractive indices mismatch, as they occur for example in cells, introduce wave front distortions leading to a reduced image quality. Adaptive elements can compensate these distortions and are specifically useful if images should be acquired in deep tissue through multiple layers of cells. They are additionally used to correct for systematic aberration in an optical system such as chromatic aberrations in mulitcolor applications.

Contribution All presented information is the result of hundreds of years of research and development. None of the presented ideas, instruments, data or images are based on my work. My contribution to this chapter is the literature search and summary.

Chapter 3

Open FLIM HCA with FRET readout

This chapter describes an open source FLIM HCA system. The first section provides an overview of the hardware, software and the work-flow. The second part discusses standardized measurements of technical and biological assays that have been used to validate the system. This is followed by the report of a biological application of FLIM HCA to read out Epac FRET biosensors expressed in HEK293T cells.

3.1 Open source FLIM HCA system

When performing biological imaging experiments, it is important to obtain statistically robust data, which is often accomplished by measuring a number of cells over multiple fields of view (FOV). For image-based studies, automated microscopy platforms have been developed to acquire 100s – 1000s of FOVs in an approach described as high content analysis (HCA). Automated HCA experiments remove the need for experimenters to manually image many individual samples with appropriate FOVs being selected manually. Automated microscopy reduces the total acquisition time, reduces the scope for human error and operator bias (particularly when selecting the FOVs) and typically enables analyses over much larger image data sets.

Currently, commercial HCA microscopes are mostly limited to intensity imaging in one or more spectral channels [Tho10, Esn18]. FLIM HCA is limited to a few research groups with the interdisciplinary know-how and significant funding required to develop their own instruments. In this chapter, an open source FLIM HCA setup is described so that it is possible for other research groups to copy and use such a system without a significant level of specialist expertise. This chapter presents a description of the hardware and software, instructions for installing the software and details about the work-flow of the open FLIM HCA system.

3.1.1 Instrument design

The hardware of the system is based on an instrument published by Kelly et al [Kel14] incorporating an automated spinning-disc wide-field FLIM microscope that comprised a microscope frame with built-in autofocus, a spinning disc scanner unit, a GOI (model HRI with control electronics), a delay box, a camera lens relay, a CCD camera and an excitation source (ultrafast laser, spectral filter wheel, neutral density filter wheel, shutter, optical fiber coupling), as shown in Figure 3.1. More details about the components of the microscope can be found in [Gö17b] or online `https://github.com/imperial-photonics/openFLIM-HCA/`. All the hardware components are commercially available, and the instrument can be assembled without specialist expertise because the majority of the components are essentially "plug and play". In the Excitation Unit the supercontinuum laser is spectrally filtered using bandpass (BP) filters in a motorised filter wheel and the intensity is controlled by a motorised neutral density (ND) filter wheel; a shutter controls the on state and the output beam is coupled into a single mode optical fiber. A single mode polarisation-preserving optical fiber guides the light to a spinning disc scanner unit connected to the microscope frame incorporating optical autofocus and a motorised x-y-stage to scan the sample. A FLIM unit is coupled to the detection port of the spinning-disk unit, comprising the HRI, HRI control electronics, a delay box, an optical relay consisting of two camera lenses and a CCD camera. The delay box is triggered by a signal from the supercontinuum laser that is passed

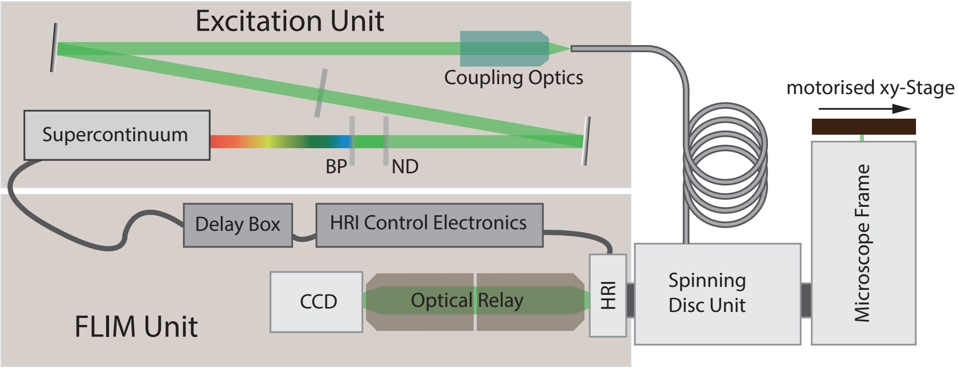

Figure 3.1: *Schematic of the automated wide-field time-gated multiwell plate FLIM microscope with optical sectioning.*

through an R.F. amplifier. The computer controls the microscope frame, the motorised x-y-stage, the delay box, the camera, the spectral and ND filter wheels and the mechanical shutter. It also controls the CCD camera and stores the acquired time-gated images for subsequent analysis.

There are only two optical alignment procedures needed to set up the instrument: the optical fiber coupling inside the excitation unit and the adjustment of the two relay lenses between the GOI and the camera. For practical reasons these lenses are two commercially available camera lenses. The GOI phosphor should be imaged onto the camera therefore it has to be aligned every time the GOI is moved relative to the CCD. To align the lenses, a small amount of diffuse light should illuminate the front of the GOI (noting that the GOI can easily be damaged if exposed to room light) such that single photon events are seen as separate spots on the camera. The foci of the lenses should be set to infinity, during this process so that the single photon events will focus to sharp dots for the optimum alignment.

3.1.2 Operating software

The software controlling the microscope is written in *µManager* [Ede14] and a *Java*-plugin was written using the integrated development environment *NetBeans* [Ora16]. *µManager* is widely compatible and many commercially available devices associated with microscopy are provided with a device adapter. For the device lacking a device adapter, which was the delay box, this was written in *C++* using *Microsoft Visual Studios Express 2010* [Mic16].

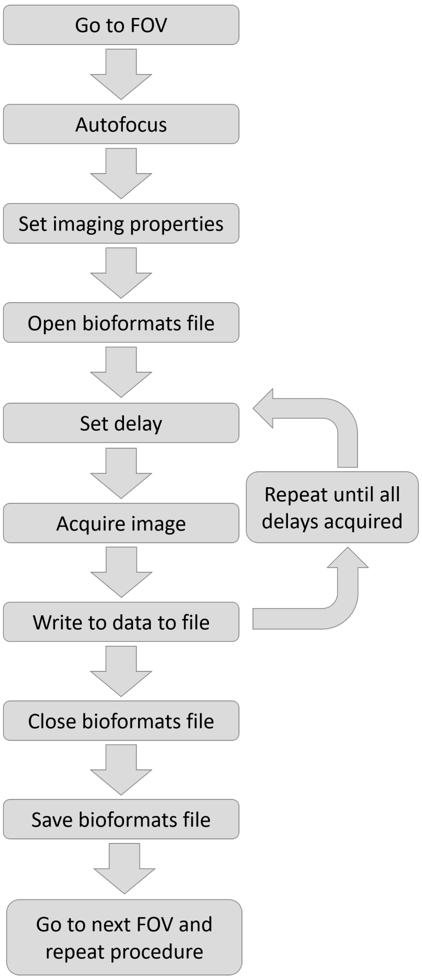
Go to FOV
Autofocus
Set imaging properties
Open bioformats file
Set delay
Acquire image
Write to data to file
Repeat until all delays acquired
Close bioformats file
Save bioformats file
Go to next FOV and repeat procedure

Figure 3.2: *Schematic structure of* µManager *control software.*

The *µManager* image acquisition program is set up in three main stages. The first is the control of the motorised stage. Here the user should set the multiwell plate parameters. There are some default plate parameter files, such as the parameters for the 48 or 96 well plates from Greiner. Additionally, the user can specify which wells to image and how many FOVs per well. Different strategies to position the FOVs in each well are available: a spiral, a ring with variable radius, manually selected positions or a set of positions automatically generated from a "prefind" scan that can be run under the control of an *ImageJ* macro prior to FLIM acquisition. In the second stage, the FLIM parameters must be set by the user, including the delays of the time-gates. This can be done manually or set automatically with logarithmically distributed time-gates [Gö17b]. The last stage is the setting of the imaging parameters, in which the user can define the excitation wavelength by selecting an excitation filter, set the excitation power by selecting a neutral density filter, set the filter cube and emission filter to match the fluorophore spectrum and adjust the integration time, binning dimension and frame accumulation to use the full dynamic range of the camera.

The software can run in different operation modes: sequential multicolor imaging with different filter sets for every FOV, or the same filter set for the whole multiwell plate acquisition. The integration time and the time-gate delays can also be adjusted in the FLIM control section. Additionally, the software can be configured to acquire time course images for live cell imaging, which can be applied over the full plate or for specific individual FOV. Combinations of time course and imaging parameters can also be implemented in the software. The fundamental operation structure of the software is shown in Figure 3.2.

3.1.3 Work-flow

This subsection gives a brief overview over the work-flow for the open source FLIM HCA system. A more detailed step by step description can be found in [Gö17b] which includes a tutorial video.

(i) Set up preliminary properties; which should not be changed during an experiment:
   (a) Plate definition file: to define the plate dimensions.
   (b) Base folder: to ensure all the necessary data is saved in an allocated folder.
   (c) Calibration file: to account for the interplay of delay box and laser. The delay settings of the delay box are frequency-dependent and every laser/delay box combination requires a specific calibration file.
   (d) GOI settings: over the duration of the experiment, the gain voltage, the triggering and the time-gate width should be constant.

(ii) Generate calibration data: each experiment requires calibration measurements to be performed to ensure reliable data (for more details please refer to section 2.4):
   (a) Scattered IRF: to obtain a spatial varying IRF across the FOV of the GOI, a time

resolved image of scattered excitation light, e.g. off the reflecting surface of the spinning disk, should be acquired. The GOI time-gate delays should be set to sample the complete interpulse range of the laser in small increments of $\leq$ 50 ps.

  (b) Dye sample: to determine the relative timing of the scattered excitation light IRF compared to the fluorescence signal, a dye sample presenting a mono-exponential decay profile should be measured (from which the "t_0" photon arrival time can be reliably obtained through fitting). Combined with (a), this gives a time-shift map that enables the IRF to be temporally aligned to the fluorescence emission across the field of view of the GOI.

(iii) Perform FLIM experiment:

  (a) Gating strategy: select the time-gate delays.

  (b) Ancillary files: two background measurements are needed. The first is a measurement of the constant background present in all acquired images, which consists of the DC camera offset and any constant background light reaching the GOI. The second is a measurement of the time-varying background (TVB) resulting from background fluorescence, e.g. from cell media and/or autofluorescence. For extended information refer to section 2.4.

  (c) Define experiment parameters: set which wells to image, how many FOVs to image and in which pattern they should be organized. Imaging parameters including excitation and neutral density filters and the filter cube should be set along with the integration time of the camera and the delay of the time-gates. For time course experiments, it is necessary to set the macro time at which FLIM data should be acquired.

  (d) Start experiment

(iv) Analysis: *FLIMfit* [War13] may be used to analyse the data. The two links `http://www.openmicroscopy.org/site/products/partner/flimfit` and `https://github.com/imperial-photonics/openFLIM-HCA` describe how to use *FLIMfit*. Here an overview is given:

  (a) Load ancillary and calibration data: the scattered IRF, the t_0-shift, the TVB and the constant background should be loaded.

  (b) Load acquired plate data: load multiwell FLIM data (the entire data set or subsets) for analysis.

  (c) Choose fitting parameters: select the fitting model (mono-exponential, double-exponential or more complex models) and the fitting strategy, e.g. pixelwise fitting, global binning or global analysis.

  (d) Save the analysed data.

3.2 Standardized high content FLIM assays

Standardized measurements or validation experiments provide a useful means to evaluate and compare different instruments and to check for systematic errors. This can be especially useful for researchers replicating open source instruments such as the open FLIM HCA instrumentation. For such comparisons and calibration experiments, it is important to use consistent samples but, to date, there are no commercially available calibration samples for FLIM. In the following section readily reproducible FLIM HCA assays are presented, which could be used for validation experiments.

3.2.1 Assay of mono-exponential dyes with distinct lifetimes

The simplest and most reproducible samples for validating fluorescence lifetime instrumentation are dyes with known mono-exponential decay profiles. However, these should be prepared with caution as the lifetime can depend on environmental conditions such as temperature, concentration and pH. To evaluate the ability to measure samples with complex fluorescence decay profiles, reproducible samples can be prepared by mixing two dyes with similar spectral properties, but distinct fluorescence lifetimes and thereby prepare a plate with wells presenting different dye ratios from 0% to 100%. FLIM data can then provide the lifetimes of the 0%/100% dye solutions and these can be used in a fit to a double-exponential decay model to determine the mixing ratio.

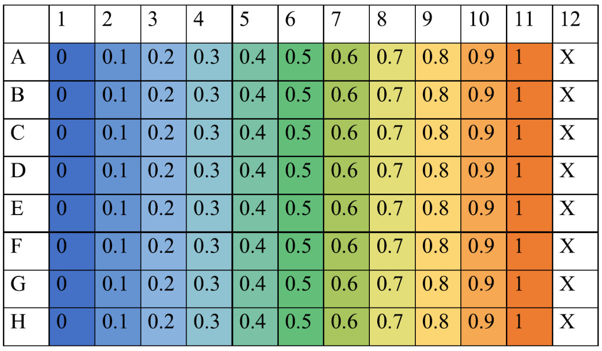

	1	2	3	4	5	6	7	8	9	10	11	12
A	0	0.1	0.2	0.3	0.4	0.5	0.6	0.7	0.8	0.9	1	X
B	0	0.1	0.2	0.3	0.4	0.5	0.6	0.7	0.8	0.9	1	X
C	0	0.1	0.2	0.3	0.4	0.5	0.6	0.7	0.8	0.9	1	X
D	0	0.1	0.2	0.3	0.4	0.5	0.6	0.7	0.8	0.9	1	X
E	0	0.1	0.2	0.3	0.4	0.5	0.6	0.7	0.8	0.9	1	X
F	0	0.1	0.2	0.3	0.4	0.5	0.6	0.7	0.8	0.9	1	X
G	0	0.1	0.2	0.3	0.4	0.5	0.6	0.7	0.8	0.9	1	X
H	0	0.1	0.2	0.3	0.4	0.5	0.6	0.7	0.8	0.9	1	X

Figure 3.3: *High content dye mixing ratio template. Dye ratio (Rhodamin 6G and Rhodamin B) of test sample. Column 1 contains no Rhodamin 6G, which is increasing in 10% steps [Spa17].*

A multiwell plate with different mixing ratios of Rhodamine 6G (R6G) and Rhodamine B (RB) was used to simulate a sample presenting different double-exponential lifetime components, as might be expected for a FRET experiment. The 96 well plate was loaded with solutions of increasing dye ratio from 0% to 100% of R6G compared to RB, as presented in Figure 3.3. The lifetime of R6G was measured to be 3989 ps (stdev 74 ps) and of RB was 1581 ps (stdev 32 ps). For this experiment, the GOI model HRI-HL-S was used with a gain voltage of 750 V and a time-gate width of 1 ns. The excitation power was 180 μW at the sample plane using a 20x objective. 3 FOVs per well were imaged with an integration time of 200 ms per time-gated acquisition resulting in a total acquisition time of 72 minutes, including moving the stage to select the required FOV, auto-focusing, acquiring the image and saving the data. The filter set used comprised an excitation filter (525/50 nm), a dichroic (602 nm) and an emission filter (660/70 nm). The set-up presented in Figure 3.1 was extended for "magic angle" detection [Lak06] by using a wire grid polarizer in the excitation path and an additional wire grid polarizer rotated of an angle of 54.7° in a 4-f configuration (two 40 mm lenses) in the detection path between the microscope frame and the GOI.

For the sample preparation, 10 μM solutions of each dye were prepared by dissolving the solid powder in 1 ml methanol, before diluting it with 49 ml purified water. The dye solutions were then mixed to the specific ratios and 200 μl were added per well into a plastic bottomed 96 well plate (plate map shown in Figure 3.3). Column 12 contained purified water for background measurements. The relative brightness of the dyes needs to be taken into account in the analysis. For dyes of equal brightness, the fractions from a double-exponential fit could be obtained directly from Equation 3.1:

$$I_{FLIMfit}(t) = I_0 \left[\beta \exp^{-\frac{t}{\tau_1}} + (1-\beta) \exp^{-\frac{t}{\tau_2}} \right] \tag{3.1}$$

However, due to the different relative brightness of the two dyes, Equation 3.2 should be applied to obtain the mixing ratios:

$$I_{FLIMfit}(t) = A_{RB} * \beta * \exp^{-\frac{t}{\tau_1}} + A_{R6G} * (1-\beta) * \exp^{-\frac{t}{\tau_2}} \tag{3.2}$$

Since *FLIMfit* determines the population fraction using Equation 3.1, these have to be adjusted using Equation 3.3 to determine the correct mixing fractions [Spa17]:

$$\beta' = \frac{A_{RB} * \beta}{A_{RB} + A_{R6Gg} * (1-\beta)} \tag{3.3}$$

Applying a column-wise global mono-exponential fit, the resulting lifetime increases linearly with the R6G concentration from the pure RB lifetime, as displayed in Figure 3.4 (a). For a global double-exponential fit to each column, the resulting fractions of R6G over RB also present a linear trend of the mixing ratios, as shown in Figure 3.4 (b).

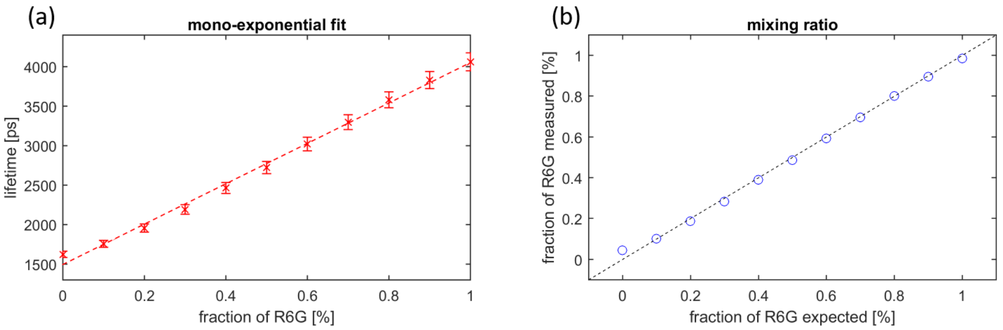

Figure 3.4: *Fluorescence lifetimes and mixing ratios obtained from FLIM measurements of exemplar multiwell dye sample plate with different ratios of Rhodamine 6G and Rhodamine B: (a) global mono-exponential fit of the lifetime per column and (b) fraction of Rhodamine 6G per column obtained from a column-wise global fit to a double-exponential model [Spa17].*

3.2.2 Assay using plasmids expressing FRET constructs

Precisely formulated chemical samples like dye solutions are a useful way to evaluate the performance of FLIM instrumentation. However, their signal to noise ratio is high compared to typical biological samples and so they do not give an accurate indication of the performance expected for cell-based assays where the fluorescence signals will be lower compared to background and photobleaching higher. Accordingly, the following biological assay was established, based on the transfection of standard fluorescent protein-based FRET constructs directly linking donor to acceptor fluorophores that were based on the Vogel laboratory's constructs [Kou06]. Vogel's constructs consist of a CeruleanFP as donor, which was replaced with mTurquoiseFP in the vectors pCxV and pC5A, linked to VenusFP as the acceptor, which was retained. This transformation simplifies the FLIM-FRET data analysis because mTurquoise presents a fluorescence decay profile that is much closer to a mono-exponential and it is a factor of 1.5x brighter [Goe10]. Using mTurquoise fluorescence protein, mTqFP, as the donor with Venus fluorescence, VFP, as the acceptor, FRET constructs were engineered with linker lengths of 5, 17 and 32 amino acids between donor and acceptor to present different FRET efficiencies. mTqFP was coupled to AmberFP, a mutation of YFP, which is non-fluorescent and therefore is not able to FRET, with a linker length of 5 amino acids to be used as a negative control. These constructs are subsequently referred to as mTq5V, mTq17V, mTq32V and mTq5A respectively.

A 96-well plate was populated with COS-7 cells expressing these FRET constructs such that each construct was expressed over three columns. The first three columns contain the negative FRET constructs, mTq5A. The cells in columns 4 – 6 are transfected with mTq5V, columns 7 – 9 with mTq17V, columns 10 – 12 with mTq32V and row H contain untransfected cells for background measurements. The transfection density was similar for all plasmids and a clear donor lifetime contrast was observed, as shown in Figure 3.5.

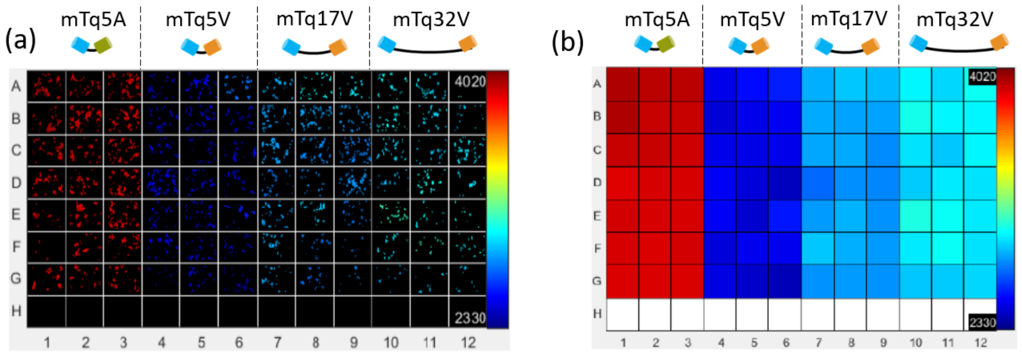

Figure 3.5: *FRETing construct assay in COS-7 cells. (a) intensity-weighted lifetime image of the first FOV per well and (b) lifetime map representing the mean lifetime per well. Colorscale in ps [Gö17b].*

Details about the transfection and cell culture can be found in section 9.1. The automated FLIM microscope described in section 3.1 was used for this experiment using the spinning disc unit with a CFP filter set (excitation 434/17 nm, dichroic 458 nm, emission 483/32 nm). Three FOVs were acquired per well with an integration time of 200 ms per time-gate, with time-gate delays at 6250 ps, 7000 ps (at the peak intensity) and 6 further time-gate delays distributed logarithmically (7525 ps, 8200 ps, 9075 ps, 10275 ps, 12375 ps, 16500 ps), which was independent of the lifetimes to cover a wide range of lifetimes. The GOI gain was set to 750 V and the time-gate width was 4 ns. The total data acquisition time was ~160 minutes and the analysis time on a computer with 10 cores, 64 GB RAM and a 2.6 GHz processor was ~92 s.

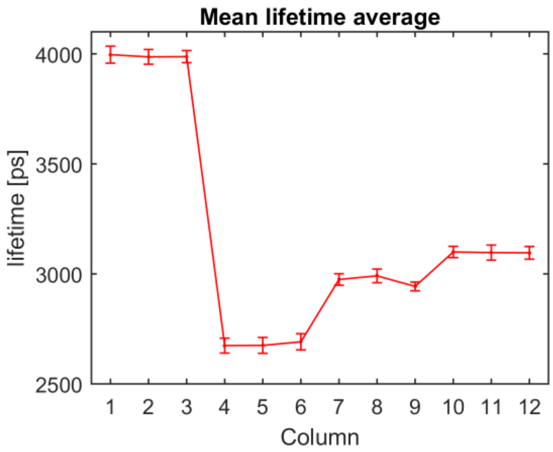

Figure 3.6: *FRETing construct assay lifetime graph. Error bars are stdev over FOVs [Gö17b].*

Figure 3.6 presents the mean donor fluorescence lifetimes measured when using *FLIMfit* to globally fit the measured data over each set of three columns of wells to a double-exponential decay model. The longest donor lifetime appears in the mTq5A columns 1 – 3 where there is no lifetime reduction due to FRET. The columns with the Venus acceptor show shorter lifetimes with the different FRET efficiencies, due to varied linker length, being apparent. The shortest lifetime in columns 4 – 6 corresponds to mTq5V, the middle lifetime of the FRETing constructs in columns 7 – 9 to mTq17V and the longest in columns 10 – 12 to mTq32V, as presented in Figure 3.6 and Table 3.1.

	per Well	stdev	error
mTq5A	4008	32	12
mTq5V	2717	35	13
mTq17V	3004	26	10
mTq32V	3133	30	11

Table 3.1: FRETing construct assay mean lifetime in ps with standard deviation (stdev) and standard error [Gö17b].

3.2.3 Assay of FRET plasmids simulating a biosensor

When using FRET biosensors in an experiment, the FRETing fraction indicates the fraction of donor fluorophores undergoing FRET, which can correspond to the population fraction of activated biosensors or interacting proteins. To obtain this value, the measured fluorescence decay profiles are fitted to the double-exponential model of Equation 3.1. In manual cell experiments, usually less than a few hundred cells are contributing to this measurement, whereas in HCA several thousand cells arrayed in a well plate can be automatically measured, enhancing the achievable sensitivity and accuracy.

To simulate a FRET biosensor assay, the constructs introduced in subsection 3.2.2, can be utilised, with the non-FRETing construct, mTq5A, representing the inactive biosensor and mTq17V the active biosensor. As discussed in subsection 3.2.4, it was found that mTq17V was better tolerated in live cells than mTq5V and mTq32V. By expressing mixtures of the two constructs (according to plasmid weight), different FRET population fractions can be simulated. A 96-well plate with an increasing fraction of mTq17V per column was prepared using HEK293T cells (see details about transfection in subsection 3.2.2). Every well in each column contains the same mixing ratio. Column 1 contains mTq5A only (negative control) and the concentration of mTq17V was increased in 10 % steps up to 100 % in Column 11 (positive control). Column 12 contains untransfected cells for background measurements. Results are presented in Figure 3.7 showing the intensity-weighted population fraction map of the first FOV in each well and the heat map presents the mean population fraction per well.

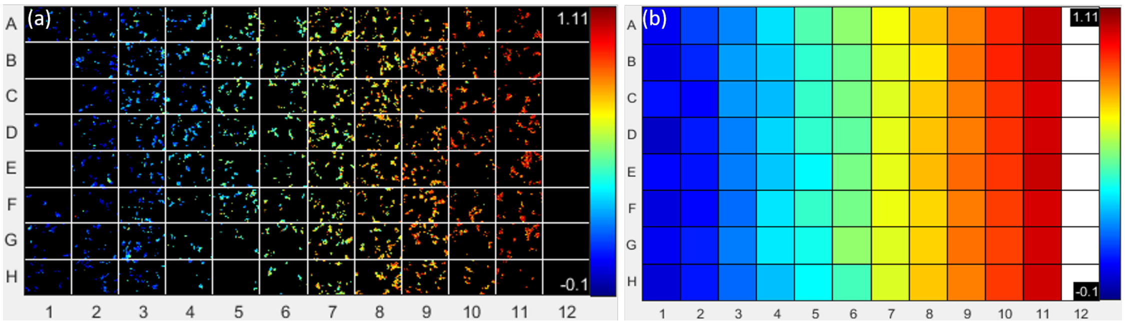

Figure 3.7: *Simulated FRET biosensor assay with FRET constructs. (a) intensity-weighted fraction image of the first FOV per well and (b) fraction map displaying the mean fraction per well. (color scale in %) [Spa17].*

For this experiment, a 434/17 nm excitation bandpass filter was used with a dichroic beamsplitter at 458 nm and a 483/32 nm emission filter. The integration time for each time-gate was 200 ms and 4 FOVs were acquired per well. The gating strategy included one gate at 6250 ps, one at the peak intensity of 7000 ps and the remaining 6 gates were distributed logarithmically (7525 ps, 8200 ps, 9075 ps, 10275 ps, 12375 ps, 16500 ps). This experiment was performed on the wide-field imaging configuration of the set-up described in section 3.1. The GOI time-gate width was set to 4 ns and the GOI gain voltage was 750 V. A 20x objective was used and the excitation laser power in the sample plane was 180 μW.

mTq5A presents a mono-exponential fluorescence decay profile, but mTq17V is better fitted to a double-exponential decay model. Thus, the fitting model was extended from a simple double-exponential decay, as shown in Equation 3.4.

$$I(t) = I_0 \left[\gamma \left(\beta \exp^{-\frac{t}{\tau_{11}}} + (1-\beta) \exp^{-\frac{t}{\tau_{12}}} \right) + (1-\gamma) \exp^{-\frac{t}{\tau_2}} \right] \tag{3.4}$$

γ is the population fraction of the two different expressed plasmids, τ_{11} and τ_{12} are the two lifetime components of the FRETing plasmid (mTq17V), whereas β describes the weight of the two components of mTq17V and τ_2 is the lifetime from the non-FRETing plasmid (mTq5A).

Global fitting with a mono-exponential fitting model was applied to Column 1 to obtain $\tau_2 = 3.8$ ns. Then a double-exponential fitting model was globally applied to Column 11 to identify the parameters $\tau_{11} = 3.1$ ns, $\tau_{12} = 0.7$ ns and $\beta = 0.64$. These parameters were fixed in the model described in Equation 3.4 and a global fit of columns $2 - 10$ provided the parameters I_0 and the mixing ratio γ of the plasmids for each pixel. As shown in Figure 3.8, the mTq17V fraction increased linearly as expected, following the experimental mixing ratio.

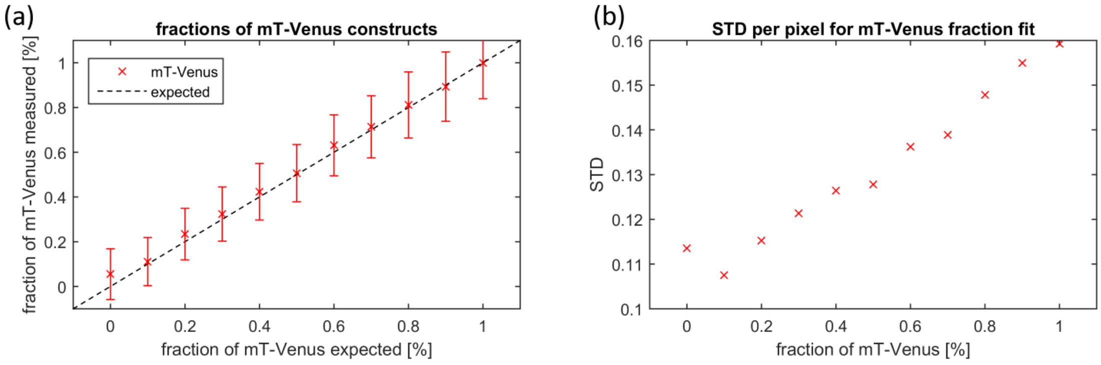

Figure 3.8: *FRET parameters obtained from simulated biosensor assay with FRET constructs. (a) ratio of the expressed plasmid mTq17V; experimental data shown in red, the error bars represent the stdev per pixel and the expected mixing ratio (blacked dotted line) and (b) stdev of (a) [Spa17].*

3.2.4 Performance comparison of FRET plasmids in assay

In Figure 3.9 the plate experiment discussed in subsection 3.2.3 was performed for three different plasmids (mTq5V, mTq17V, mTq32V). Only the construct mTq17V follows closely the expected trend. These observations are not fully understood: it may be that the expression rates of the plasmids mTq5V and mTq32V are different from that of mTq5A or that these constructs are more toxic to the cells. An additional indication for the different cell toxicities is that it was only possible to obtain useful stable cell lines from the mTq17V construct. The mTq32V stable cell line showed a low transfection efficiency and cells looked unhealthy. The mTq5V stable cell line did not survive.

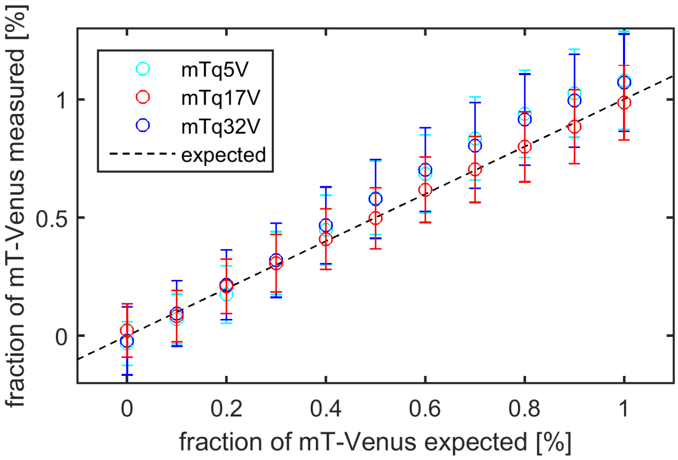

Figure 3.9: *Performance comparison of different FRET plasmids: multiwell plate FLIM experiments with FRET construct plasmids mixed with mTq5A in a ratio increasing across the plate in 10% steps for mTq5V (cyan), mTq17V (red) and mTq32V (blue).*

3.3 Biological application: cAMP Epac biosensor

3.3.1 Biological background

Cyclic adenosine monophosphate (cAMP) is a second messenger and a derivative of adenosine triphosphate (ATP). Its primary function is intracellular signal transduction, especially for protein kinases. For the discovery of cAMP as second messenger, Earl W. Sutherland was awarded the Nobel Prize in Physiology and Medicine in 1971[1] [Nob15]. The first stage in the cellular cAMP production is an activation of a G protein coupled receptor, e.g. by hormones or neurotransmitters, which stimulates adenylyl cyclase to convert ATP into cAMP. FRET biosensors are increasingly used to monitor spatial and temporal cAMP activation. Available cAMP biosensors include cyclic nucleotide-gated channels (CNGCs), cAMP dependent protein kinases (PKAs) and exchange protein directly activated cAMP (Epac) [Wil08]. Epac is the newest of these biosensors and is based on a Rap1 guaninenucleotide-exchange factor that is directly activated by cAMP [dR98]. The cAMP biosensor used in the following experiment is based on Epac (Epac-S^{H188}), where the mTurquoise2 fluorescence protein is incorporated as the donor and two Venus fluorescence proteins are utilised as acceptors [Kla15]. Forskolin is a well-known cAMP stimulator, which is used in experimental biochemistry and pharmacology. Due to its activation of cAMP, it was explored for potential therapies of heart disease, asthma, thrombosis and obesity [Kav10]. It is used in the body builder community as a fat burner, albeit without scientific evidence to support this application [Kre10]. Here the Epac FRET biosensor is used to read out cAMP stimulated by forskolin in an automated multiwell plate assay.

3.3.2 Epac biosensor response upon forskolin stimulation

The system described in section 3.1 was applied to a time course study of cAMP activation following forskolin stimulation read out using the Epac FRET biosensor. In the absence of cAMP, the Epac biosensor is in its inactive, FRETing, condition and upon cAMP activation, FRET decreases due to a conformational change of the biosensor. HEK293T cells expressing the Epac biosensor were stimulated at time point 120 s with forskolin and a time series of FLIM images of one FOV were acquired over 10 minutes in 10 s steps. Fitting to a mono-exponential decay model indicated an increase in donor lifetime, and therefore cAMP activation, after addition of forskolin as shown in Figure 3.10 (a). For a more quantitative analysis, the donor fluorescence decay data were fitted to a double-exponential decay model and the FRETing population fraction obtained is presented in Figure 3.10 (b). The time points at 120 s and 130 s were removed because the addition of forskolin introduced a z-shift due to the addition weight, which led to a defocus effect and a decrease in fluorescence intensity. A CFP filter set was utilised (excitation 434/17 nm, dichroic at 458 nm, emission 482/32 nm), the integration time per time-gated image was 250 ms and a 40x (0.60 NA) objective was used. The GOI gain voltage was 750 V and the time-gate width was 4 ns. The gating strategy included a time-gate at 1300 ps, one at the peak intensity of 4300 ps and the remaining 6 gates were logarithmically distributed (4919 ps, 5678 ps, 6656 ps, 8035 ps, 10391 ps and 16000 ps).

---

[1] "for his discoveries concerning the mechanisms of the action of hormones"

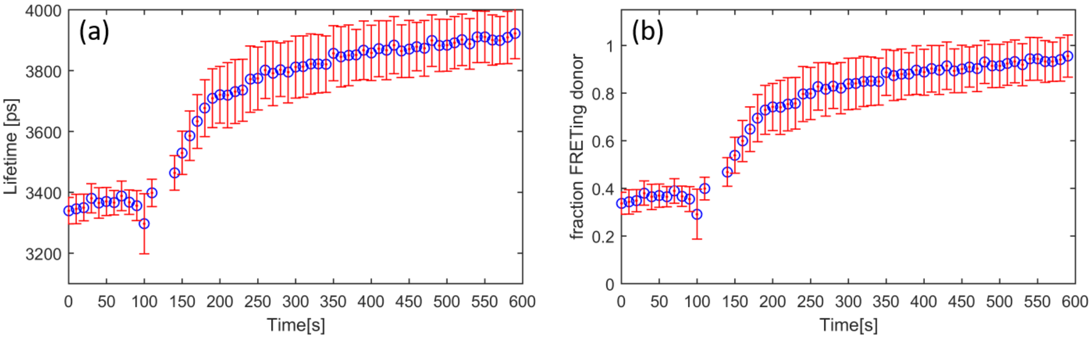

Figure 3.10: *cAMP activation curve of Epac FRET biosensor upon forskolin stimulation. (a) mean lifetime per cell, (b) FRETing population fraction. Forskolin stimulation at 120 s [Gö17b].*

If the data from individual cells are compared, the donor lifetime increase observed is not the same in all cells. This might be due to different cAMP states in different cells, to differences in cell growth or to some other biological process inside the cell. Following stimulation, the donor lifetime for all cells increased up to a saturation value, as displayed in Figure 3.11.

For the FLIM data analysis, the cells were segmented in *FLIMfit* and all ancillary parameters, such as constant background, TVB and spatial varying IRF shift, were determined according to the protocol given in section 2.4. The mono-exponential fit was applied pixelwise and the global analysis leading to the FRETing population fractions in Figure 3.10 (b) entailed fitting to a double-exponential model (Equation 3.1) with the lifetime components fixed to $\tau_1 = 3964 \pm 21$ ps and $\tau_2 = 3022 \pm 27$ ps. These lifetime components were obtained by global fitting the data for the first three timepoints to a double-exponential decay model using global binning.

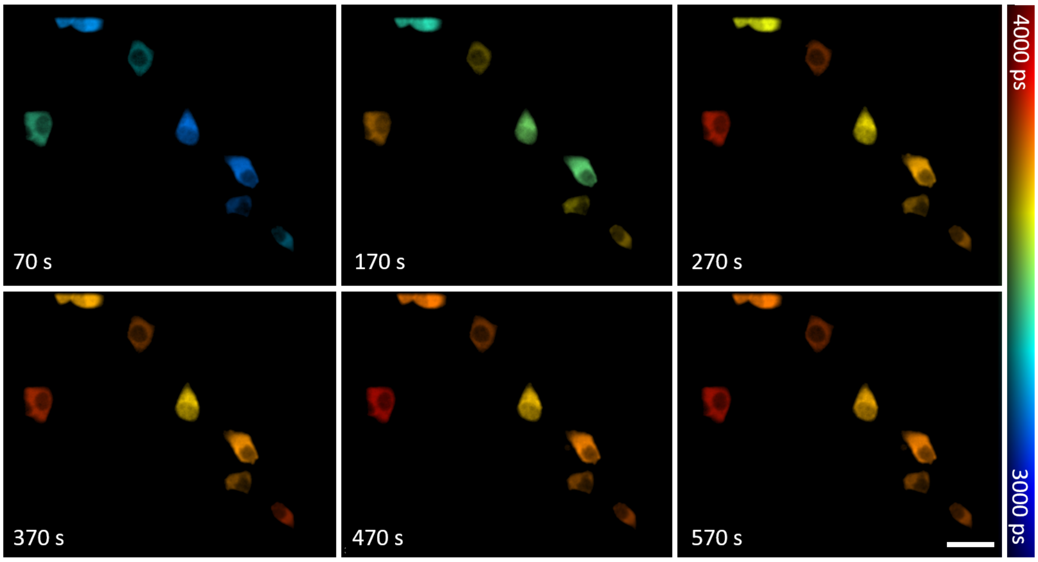

Figure 3.11: *cAMP activation visualisation of Epac FRET biosensor upon forskolin stimulation at a single FOV. Intensity-weighted lifetime images of a time laps experiment of cAMP activation. Scale bar: 10 μm*

3.4 Summary

Summary This chapter describes an open source FLIM HCA microscope with its hardware, software and the corresponding work-flow. The commercially available hardware components and the published open source code of the software offers a solution for other groups to rebuild the system and extent or adjust the functionality of automated FLIM microscopy to their specific needs. We hope that this will help other biomolecular research groups to perform automated FLIM and FLIM-FRET experiments which is currently a minority due to the complexity and limited availability of such instruments.

Further, standardized assays were introduced to enable comparisons between different instruments, including dye-based assays and more realistic cell-based assays simulating FRET biosensor assays using mixtures of FRET constructs in cells. These standardized assays will help to evaluate the performance of FLIM-FRET experiments across different instruments, laboratories and FLIM techniques. However, it is important to be aware of the sources of uncertainty for a valid comparison. Reasons for systematic errors are, among others, pipetting of mixtures, time shifts between the laser pulse and the detected signal compared to the calibration measurement and in the cell-based experiments construct expression levels, toxicity and autofluorescence. The statistic error is dominant in the dye experiments, because the systematic errors can be controlled easily. In cell-based experiments it is more difficult to control or calculate systematic errors and they become dominant.

Finally, an exemplar biological time lapse FLIM-FRET assay was presented utilising the Epac FRET biosensor to read out forskolin stimulation of cAMP. This experiment proves that the tested FRET biosensor, which was specifically designed for FLIM readouts, can be used to study cellular activation of cAMP.

Contribution I inherited an automated plate reading microscope with the hardware originally controlled using *LabVIEW* and an incomplete *μManager* code written by a former PhD student Dr. Douglas Kelly, which I finished and extended to provide additional functionality. With the help of Dr. Kelly, I established an open source environment with the online manual on GitHub. The dye multiwell plate was prepared and analysed by Dr. Hugh Sparks and myself. I undertook the transfections for the FRETing construct experiments as well as the experimental measurements and the data analysis. The preparation of the cAMP Epac cell-based assay was undertaken by Dr. Lucien West, with whom I worked to perform the experiment and analyse the data.

Chapter 4

Advances in wide-field time-gated fluorescence lifetime imaging

This chapter reports work undertaken to improve the performance of wide-field time-gated fluorescence lifetime imaging (FLIM) based on gated optical intensifiers (GOI), as presented in Figure 4.1.

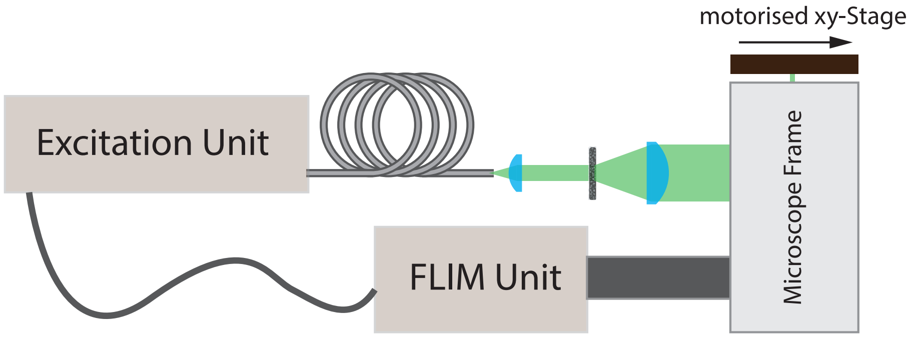

Figure 4.1: *Outline of a wide-field time-gated FLIM microscope. The excitation unit consists of an ultrafast supercontinuum laser source with spectral and neutral density filters to control the excitation wavelength and intensity. The excitation light is guided via a single-mode optical fiber to a rotating diffuser before being coupled into the microscope to illuminate the sample. The FLIM unit in the detection path contains a GOI with two relay lenses and a readout camera. Dedicated electronics synchronised to the excitation laser control the GOI, the camera and an electronic delay box to implement time-gated FLIM.*

The most important properties of a FLIM microscope are the lifetime precision, the image resolution and the signal-to-noise ratio. For wide-field time-gated FLIM, the performance is primarily determined by the GOI. The work presented here utilises GOI technology from Kentech Instruments Ltd, specifically the High Rate Imagers (HRI) models designed for use with high repetition rate (>10 MHz) excitation lasers. This chapter explores the improvement of the current state of-the-art of time-gated FLIM, initially using the "standard HRI", and then investigating the performance achievable with the next generation HRI designated "HRI-HL-S". Here, 'HL' refers to the ability of the HRI to work in modes with high or low duty cycle, which impacts the range of available time-gate widths, and the 'S' denotes a special prototype that incorporates a magnetic focusing system [Spa17].

The magnetic focusing of the HRI-HL-S improves the spatial resolution of the HRI by decreasing the lateral spread of electrons between the photocathode and the microchannel plate (MCP). The signal to noise ratio can be enhanced by increasing the time-gate widths to collect more photons and thereby improve the precision of fluorescence lifetime determination, which can permit the use of shorter acquisition times. The image quality can be further enhanced by improving the homogeneity of the illumination intensity across the field of view, for which different approaches to time-average the laser speckle have been explored.

4.1 New generation of high rate intensifiers

The precision of lifetime determination for FLIM is a function of the signal-to-noise level. For wide-field time-gated FLIM, the number of detected photons can be increased by increasing the time-gate width. The standard HRI (Kentech Instruments Ltd) can provide time-gate widths from 200 ps up to 1000 ps and is routinely used with the 1000 ps gate width for FLIM of biological samples. For the work reported in this chapter, a new prototype GOI from Kentech Instruments was evaluated, the "HRI-HL-S", which could provide time-gate widths of several nanoseconds and incorporated a magnetic field to increase the spatial resolution. Thus, the HRI-HL-S was expected to enhance the lifetime precision and the spatial resolution.

4.1.1 Resolution enhancement via a magnetic field

As depicted in Figure 4.2, a standard GOI essentially comprises a photocathode, an MCP and a phosphor screen, with the gain being provided by a high voltage accelerating photoelectrons across the MCP and the modulation being applied via the voltage between the photocathode and the MCP that enables the GOI gain to be switched with a rise time of ∼50 ps. With a standard HRI, (fluorescence) light is incident at the photocathode where photons generate photoelectrons that are accelerated to the MCP by the gating voltage (typically a negative voltage is applied as the front face of the MCP is grounded). The MCP comprises an array of glass tubes across which a high voltage is applied that accelerates the electrons entering the microchannels to energies at which they excite secondary electrons when they collide with the sides of the channels. In this way, a single incident photoelectron produces a cascade of secondary electrons (in a manner analogous to a photomultiplier) and these secondary electrons are converted to light at the phosphor screen, typically producing an output that is of higher intensity than the incident intensity distribution. A lens relay images the phosphor plane onto a readout camera (typically a cooled CCD camera) to record the intensified image. By switching the gating voltage such that the photoelectrons are not accelerated to the MCP, the overall gain of the HRI can be modulated to provide time-gated imaging.

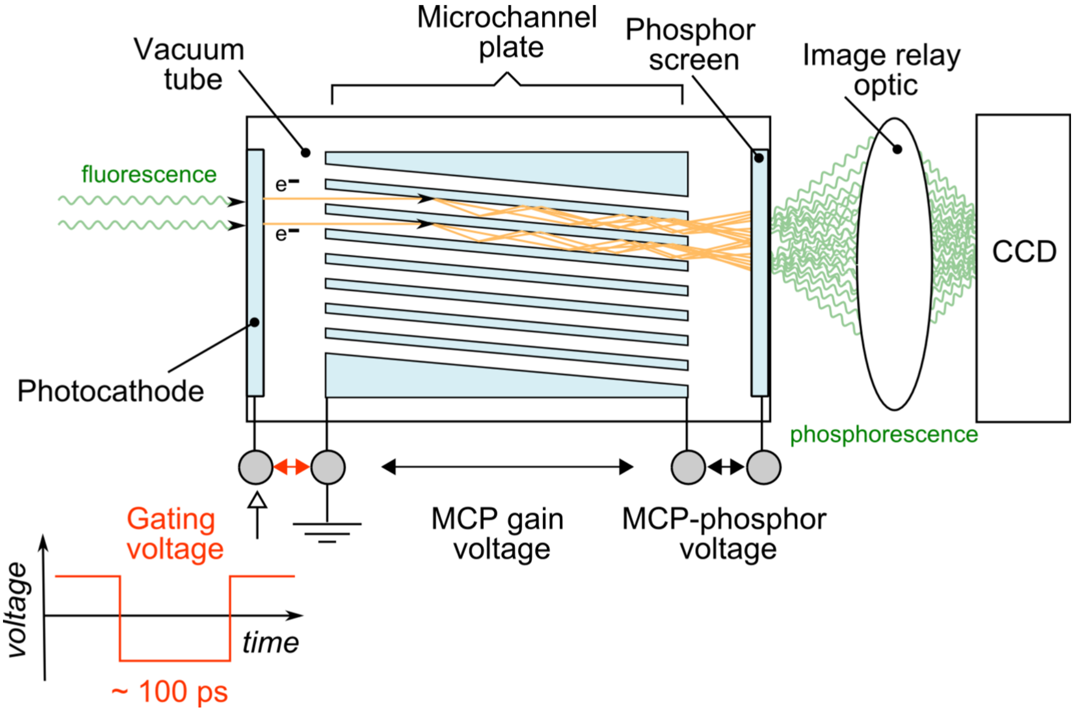
Microchannel plate
Phosphor screen
Vacuum tube
Image relay optic
fluorescence
e⁻
e⁻
CCD
Photocathode
phosphorescence
Gating voltage
MCP gain voltage
MCP-phosphor voltage
voltage
time
~ 100 ps

Figure 4.2: *Schematic of gated optical image intensifier [Spa17].*

The spatial resolution of the HRI is ultimately limited by the pitch of the MCP but can be degraded by cross talk between the microchannels. This is an issue because the photoelectrons emerging from the photocathode have transverse velocity components and they spread out from their original "pixel" as they are accelerated to the MCP. This electron image transfer is called "proximity focusing" [Ebe77]. Since the transverse drift decreases with the transit time, the spatial resolution will depend on the average accelerating voltage between the photocathode and the MCP. For frequency domain FLIM, the use of a sinusoidally modulated gating voltage means that the time-averaged voltage and therefore spatial resolution will be lower than for time-gated FLIM. Similarly, when using longer time-gates for time domain FLIM, the time taken for the applied voltage to rise and fall at the beginning and end of the gate respectively occupies a smaller fraction of the time-gate opening time and the spatial resolution will be higher as shown in Figure 4.3 (c).

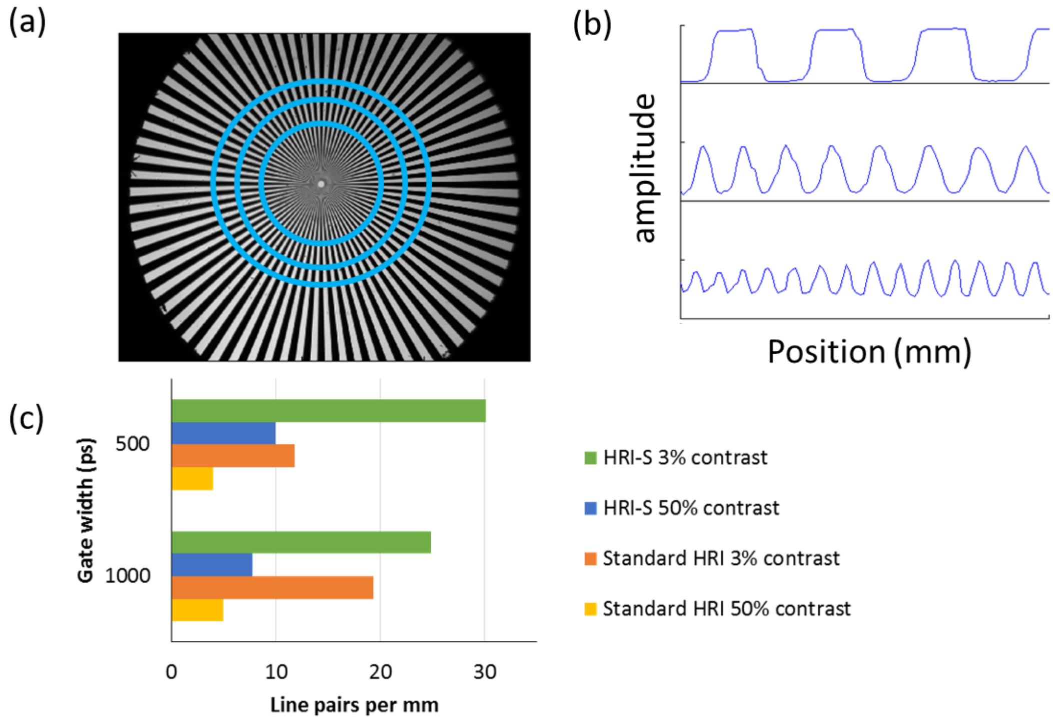

Figure 4.3: *(a) radial test chart used to measure spatial resolution; (b) modulation pattern of test chart at different distances from centre as indicated by blue circles in (a); (c) Bar chart (c) shows frequencies at which 3% and 50% contrast values were achieved for the standard HRI and the HRI-HL-S. Adapted from [Spa17].*

The loss of spatial resolution, due to the transverse drift of the photoelectrons between the photocathode and the MCP, can also be countered by adding a magnetic field aligned along the optical axis of the HRI to guide photoelectrons along helical trajectories about their principal direction [DB84, Ega05]. Ideally, the magnetic field should be chosen so that the photoelectrons on average make one complete turn of the helical trajectory between the photocathode and the MCP. This magnetic field is implemented in the HRI-HL-S, however no authorization to graphically indicate the magnetic field was given by Kentech. The improvement can quantitatively be seen in Figure 4.3, where a radial test chart was used to identify the 3% and 50% contrast limit in line pairs per mm for the standard HRI and the HRI-HL-S. For both limits the HRI-HL-S with the magnetic field shows superior performance [Spa17].

To demonstrate the benefit of the magnetic field, a commercially available dye-stained convallaria sample was imaged using the optically sectioning time-gated FLIM system described in chapter 3 with a standard HRI and an HRI-HL-S. Figure 4.4 shows the images obtained using the same instrument settings for both HRIs (1 ns gate width; 180 μW excitation power at the sample plane; MCP gain voltage of 750 V; time-gates at delays of 6250 ps, 7000 ps (peak intensity), 7525 ps, 8200 ps, 9075 ps, 10275 ps, 12375 ps, and 16500 ps). At each delay, five images were acquired for each HRI with the camera exposure times set to make the average pixel value at the peak of the fluorescence intensity more than 50% of the camera's bit depth. This resulted in total acquisition times of 20 s and 24 s for the standard and HRI-HL-S, respectively. The different acquisition times compensate differences in HRI quantum efficiency. These differences are not characteristic for the HRI model but is due to variations in the manufacturing process [Spa15].

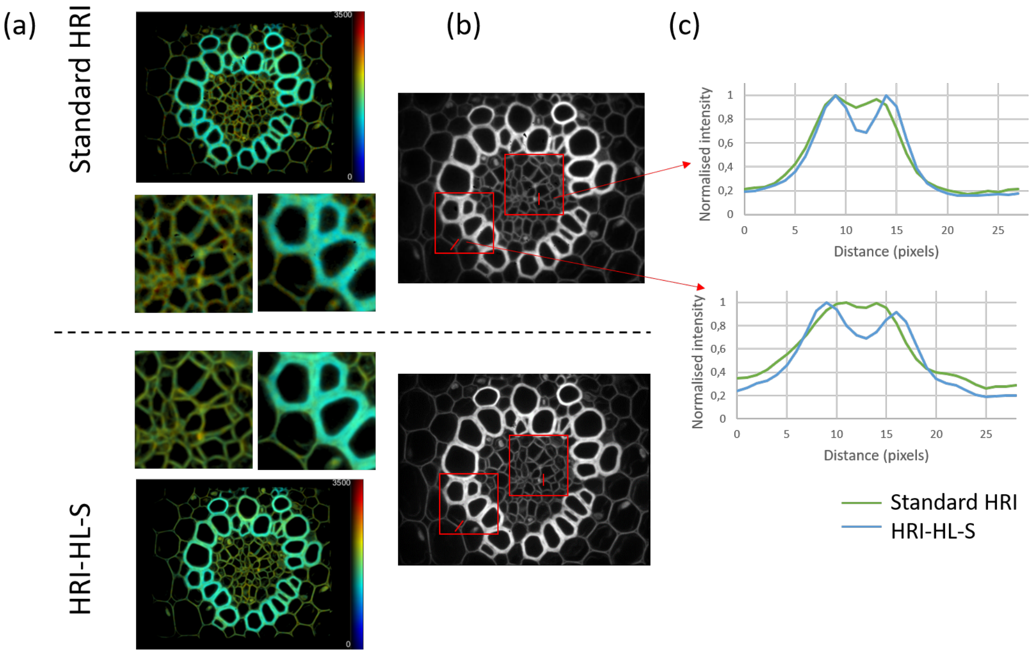

Figure 4.4: *Intensity merged fluorescence lifetime and time-integrated fluorescence intensity images of stained (convallaria) sample with higher magnification FLIM sub-images from regions indicated in intensity image for each standard HRI (upper figures) and new HRI-HL-S (lower figures) together with line profiles indicating improvement in spatial resolution. Adapted from [Spa17].*

To illustrate the resolution enhancement with a more typical biological sample, a HEK293T cell expressing mTq5A was imaged under the same experimental conditions, for which the comparison of fluorescence intensity images acquired using the standard HRI and the HRI-HL-S is shown in Figure 4.5.

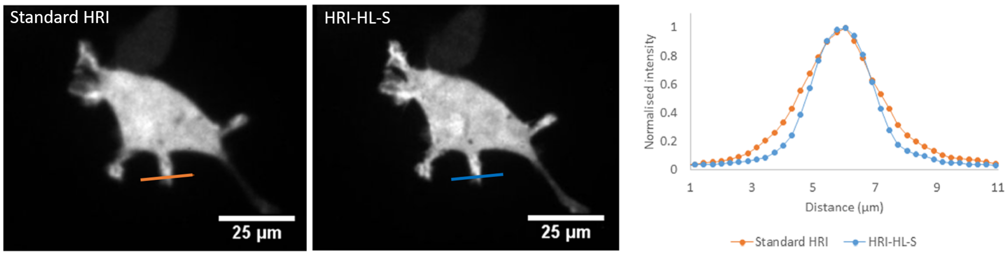

Figure 4.5: *Time-gated optically-sectioned fluorescence intensity images of HEK293T cell transfected with the mTq5A plasmid acquired with a standard HRI (left) and the HRI-HL-S prototype (middle) with corresponding line-scans through the features indicated (right) [Spa17].*

4.1.2 Enhancing fluorescence lifetime precision using longer time-gates

As outlined above, the ability of the HRI-HL-S to provide longer time-gate widths was expected to increase lifetime precision by enabling the detection of more photons per excitation pulse. While standard HRIs (Kentech Instruments Ltd) can provide time-gate widths ranging from 200 ps up to 1000 ps, the HRI-HL-S can be readily switched to provide time-gate widths up to several nanoseconds while operating in standard time-gate mode. The new HRI prototype still has the sub-100 ps optical rise time of the standard HRI, as illustrated in Figure 4.6, which shows experimental gate profiles measured on the system described in chapter 3 using excitation light back-scattered from the Nipkow disc to provide an ultrashort optical signal (IRF) and sampled with equally spaced 25 ps steps over the full range of the delay box.

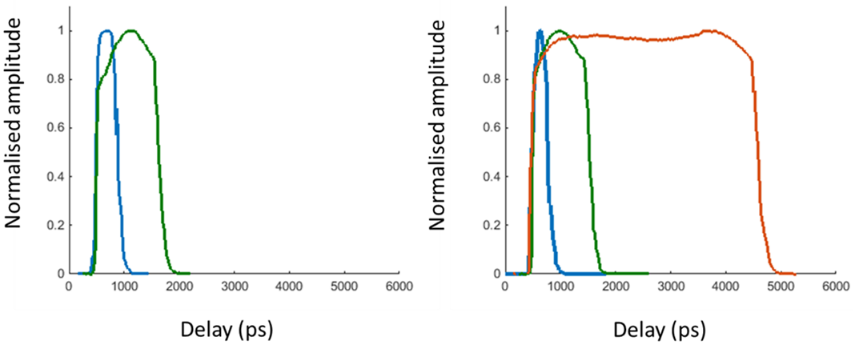

Figure 4.6: *IRFs measured using back-scattered excitation light for the standard HRI (left) set for 200 ps and 1000 ps time-gate widths and for the prototype HRI-HL-S (right) set for 200 ps, 1000 ps and 4000 ps time-gate widths [Spa17].*

For TCSPC fluorescence lifetime measurements, the signal to noise ratio for a mono-exponential fluorescence decay scales with $\sqrt{N}$, where N is the photon number [Kö92]. For time-gated FLIM, the MCP is an amplifier stage that introduces an excess noise factor (E), which reduces the precision of lifetime measurements such that the signal to noise ratio varies with $E\sqrt{N}$ [McG09]. Thus, the precision of both approaches improves as more photons are detected. For time-gated FLIM, this can be simply achieved by using longer time-gates, as illustrated in Figure 4.7, which shows the fluorescence lifetime histograms obtained when using the time-gated FLIM system described in chapter 3 to measure solutions of Rhodamine B (RB) and Rhodamine 6G (R6G) dyes, which both exhibit mono-exponential decay profiles (∼1.6 ns for RB and ∼4 ns for R6G), with different time-gate widths using the standard HRI and the HRI-HL-S. The lifetime histograms are plotted in Figure 4.7, illustrating how the width of the histogram decreases as the time-gate width increases. Table 4.1 gives the mean and standard deviation of the lifetime values measured for each time-gate width.

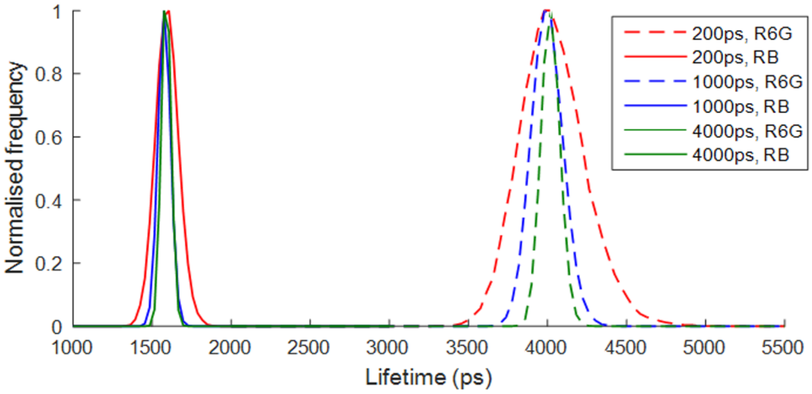

Figure 4.7: *Histogram of lifetimes measured for solutions of Rhodamine 6G and Rhodamine B fitted pixelwise to a mono-exponential decay model for acquisitions with different time-gate width settings of the HRI-HL-S [Spa17].*

For these measurements, the HRI gain voltage (across the MCP) was set to 750 V and the excitation power at the sample plane was ∼180 μW. The fluorescence decay profiles were sampled with seven logarithmically spaced time-gates and the camera integration time was set to 200 ms time, for measurements with the 200 ps time-gate width, so that the complete dynamic range of the camera was used at the peak intensity. To prevent saturation of the camera readout for longer

time-gate width	lifetime RB	stdev	lifetime R6G	stdev
200	1595	74	3998	224
1000	1579	39	3968	118
4000	1581	32	3989	74

Table 4.1: *Mean lifetime and standard deviation in ps of measurements of solutions of R6G and RB for different time-gate widths [Spa17].*

time-gate widths, multiple images were acquired with shorter integration times set to keep the overall acquisition time constant. The FLIM data were analysed using *FLIMfit* to fit a mono-exponential decay per pixel to this dye data.

Figure 4.8 shows a dye-based experiment that resembles a functional image-based assay such as a FRET assay, similar to that presented in chapter 3. Rhodamine B and Rhodamine 6G dyes were dissolved in different ratios by weight to simulate FRETing and non-FRETing fluorophores and FLIM was undertaken using both the standard HRI with a 1 ns time-gate and the HRI-HL-S prototype with a 1 ns and a 4 ns time-gate. The acquisition parameters were held constant for each measurement and 3 FOVs per well were imaged in an automated experiment. The data was globally fitted to a double-exponential decay model using *FLIMfit* and the relative dye concentration were obtained using the correction presented following Sparks et al [Spa17].

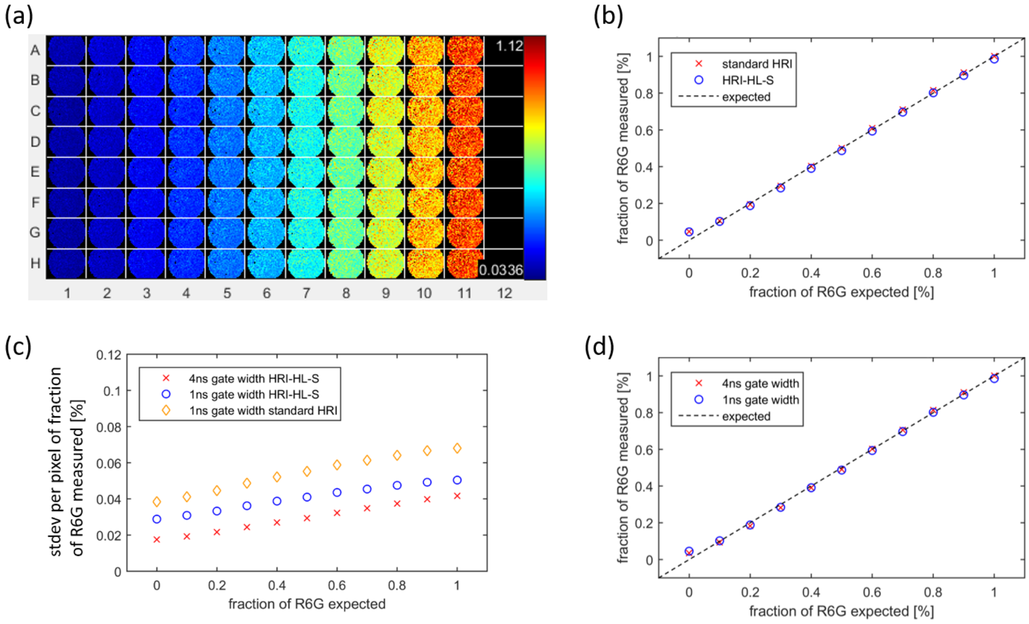

Figure 4.8: *Wide-field time-gated FLIM data: (a) montage showing the mean fluorescence lifetime image of one field of view from each well; ((b) and (d)) R6G/RB dye ratio obtained by global fitting for FLIM data (b) acquired with 1 ns gates for the standard HRI and new HRI-HL-S; (c) standard deviation in measured R6G fraction calculated per pixel (errors from graph (b) and (d)) and (d) acquired with new HRI-HL-S using 1 ns and 4 ns time gates. Adapted from [Spa17].*

There is no significant difference apparent in Figure 4.8 (b,d) between the recovered mean fractions of R6G obtained using both HRIs and time-gate widths. This is because this mixture of bright fluorophores with mono-exponential decay profiles averaged over many FOV provides a high signal to noise ratio for all the measurements. However, the standard deviations (Figure 4.8

(c)) associated with these measurements do illustrate the superior performance of the HRI-HL-S compared to the standard HRI and the 4 ns gate width measurements compared to those with 1 ns gate width.

4.2 Evaluation of time-gated FLIM for cell biology

To evaluate the potential of the prototype HRI-HL-S for time-gated FLIM, it is necessary to test it with samples that more faithfully represent those encountered in cell biology studies. While the dye-based samples enable quantitative comparisons between different instruments, it is important to also compare performance with cell-based assays where the fluorophores may be less bright, less homogeneous (e.g. due to variation in the transfection/expression of fluorescent proteins and in cell density), prone to photobleaching and present with background noise, e.g. from cellular autofluorescence or culture media. To this end, a study was undertaken using the automated optically sectioning multiwell plate FLIM instrument described in chapter 3 to measure cells expressing FRET constructs comprising fluorescent proteins linked with short amino acid chains: mTq5A is mTurquoiseFP linked to the non-fluorescent protein, Amber by a 5-amino acid chain; mTq17V is mTurquoiseFP linked to VenusFP by a 17-amino acid chain. This relatively reproducible biological sample enables systematic optimisation of experimental parameters for FLIM and FRET and objective comparisons of the performance of different FLIM instruments.

In this section, the FLIM instrumentation is applied to cells expressing these FRET constructs under conditions with relatively low numbers of detected photons with a view to demonstrating the advantages of longer time-gate widths for rapid time-gated FLIM of biological samples, or time-gated FLIM of samples of low brightness, such as cells with endogenous proteins fluorescently labelled. The prototype HRI-HL-S was used with the gain voltage set to 750 V and the cells were imaged using a 20x microscope objective and a CFP filter cube (with 434/17 nm excitation bandpass filter, 458 nm dichroic beamsplitter and 483/32 nm emission filter). A 96 well-plate was prepared with HEK293T cells expressing either mTq5A or mTq17V with each column of the plate contained cells transfected with only one of the plasmids, alternating from Column 1 and starting with cells expressing mTq5A. The alternating columns provide a check that there is no systematic variation due to a temporal variation of the instrument, such as variations in excitation intensity or a temporal excitation pulse drift. In this experiment the top and bottom rows (A and H) were used for background measurements, as shown in Figure 4.9 (a). For more details of the plasmids and cell culturing please refer to subsection 3.2.2 and section 9.1.

To study the performance of the time-gated FLIM system as a function of the number of detected photons, the control software was modified so that either the excitation power could be changed, on a well by well basis by changing the neutral density filters in front of the excitation laser, or the integration time of the readout CCD camera could be changed. For these experiments, the excitation power or CCD integration time was changed on a column by column basis and measurements were undertaken using time-gate widths of 1 ns or 4 ns.

4.2.1 Effect of varying excitation power on lifetime determination

In this experiment, the laser excitation power was reduced using neutral density filters of optical density 0, 0.1, 0.2, 1 and 2. The camera integration time was set to 200 ms, which filled 75% of the dynamic range of the camera with no ND filter present and this integration time was used for measurements at all excitation powers. For each well, six FOVs were imaged such that the global fitting could be applied over 36 FOV per condition. Where cells were transfected with such low efficiency that the fluorescence was not detectable above the background noise using the *FLIMfit* segmentation tool, those cells were not included in the analysis. Figure 4.9 (b) shows how the number of cells with detectable fluorescent signal varied as a function of the ND filters and time-gate width used. For higher excitation intensities, more cells contributed to the analysis, whereas, the number of cells decreased with lower excitation laser powers. A higher cell count was found for the 4 ns time-gate at lower excitation laser intensities compared to when using the 1 ns time-gate width. Since a visual inspection indicated a homogeneous seeded density of transfected cells, the reduction in the number of cells was not due to sparsity of cells but to insufficiently collected fluorescence signal.

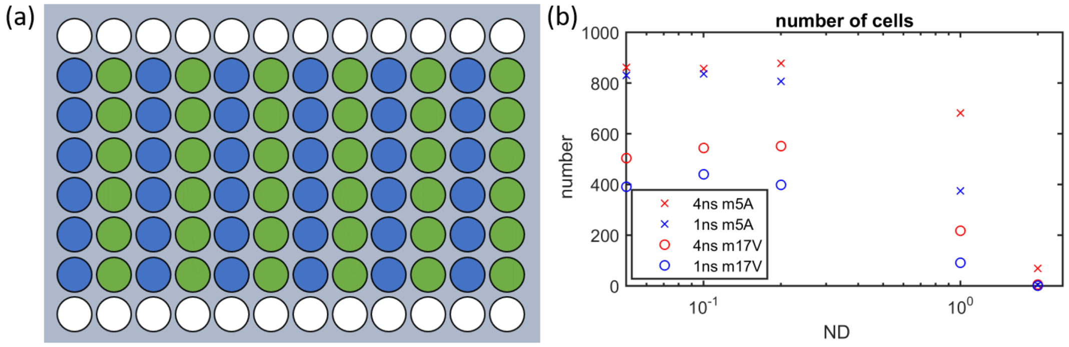

Figure 4.9: *Plate map. White indicates untransfected cells, blue indicates transfection with mTq5A and green with mTq17V. (b) Variation of number of cells found by the* FLIMfit *segmentation tool for different excitation intensities (ND filter 0, 0.1, 0.2, 1 and 2) and HRI time-gate widths (1 ns and 4 ns). ND 0 cannot be plotted on a log scale, thus a value close to 0 (10^{-6}) was chosen to represent this data point.*

Figure 4.10 illustrates how the measured mean fluorescence lifetimes and standard deviations varied as the excitation power was decreased. For this analysis, the FLIM data where loaded into *FLIMfit*, separated into two groups corresponding to the different plasmids and the segmentation tool was used to segment the cells in every FOV. A global fit was applied to a mono-exponential decay model for the cells expressing mTq5A and to a double-exponential decay model for the cells expressing the mTq17V construct. The mean lifetimes and standard deviations were calculated per segmented cell. It should be noted that there were only two cells detected for the combination of ND 2 in the excitation path measured using the 1 ns gate and therefore the results for this single data point are excluded. Figure 4.10 demonstrate the ability of the time-gated FLIM system to measure lifetimes at relatively low excitation intensities and, as expected, the standard deviation increases for lower excitation intensities and the standard deviation of the 1 ns time-gate width is inferior compared to the 4 ns time-gate width.

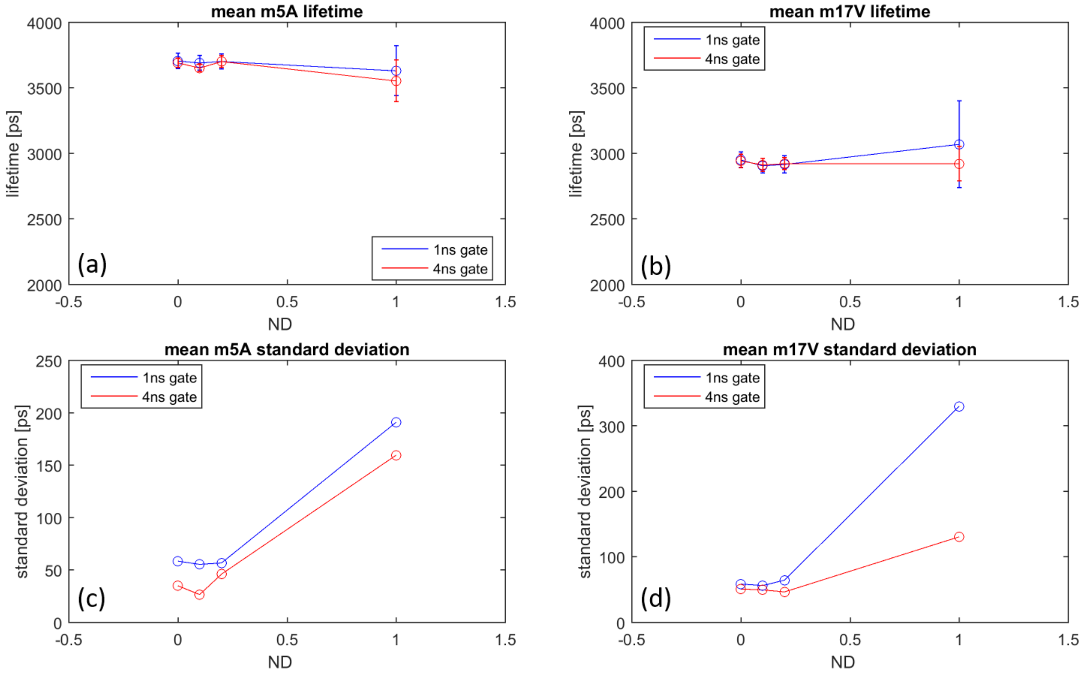

Figure 4.10: *Variation of the mean lifetimes (a,b) and standard deviations (c,d) measured for cells expressing mTq5A (a,c) and mTq17V (b,d) as a function of excitation intensity (ND filters 0, 0.1, 0.2 and 1) and time-gate width (1 ns and 4 ns). Error-bars are the standard deviation per segmented cell for mTq5A (c) and mTq17V (d) [Spa17].*

4.2.2 Effect of varying integration time on lifetime determination

In this experiment, the number of detected photons is systematically reduced by decreasing the camera readout integration time from 800 ms to 600 ms, 400 ms, 200 ms, 100 ms, 75 ms, 50 ms and 25 ms with the excitation laser intensity fixed to use the full dynamic range of the camera for the longest camera integration time of 800 ms. As described in subsection 4.2.1, the *FLIMfit* segmentation tool was applied to detect cells at the different experimental conditions and the number of cells found for each condition are plotted for measurements with different camera integration times and time-gate widths. Once again, more cells are detected for the 4 ns width time-gate compared to the 1 ns time-gate width. In general, more cells expressing mTq5A could be found than cells expressing mTq17V. This is due to the lower intensity of the FRETing mTq17V construct, because the energy that is resonantly transferred to the acceptor does not contribute to the donor fluorescence signal.

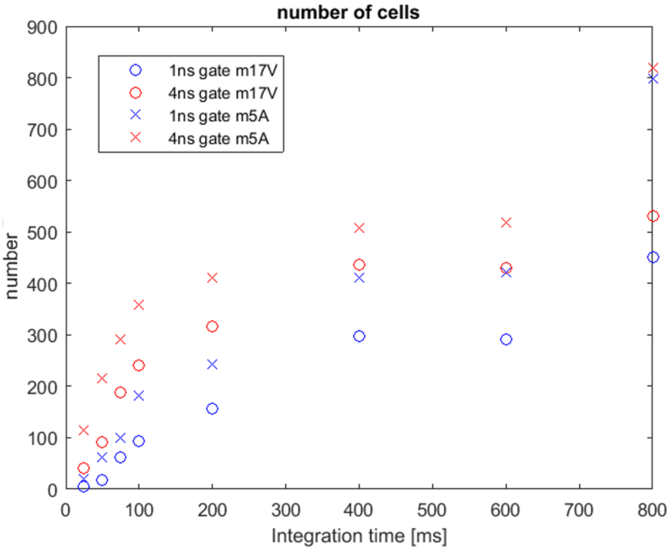

Figure 4.11: FLIMfit *segmentation tool recognized cells for different integration times ranging from 800 ms down to 25 ms (600 ms, 400 ms, 200 ms, 100 ms, 75 ms, 50 ms) and gate widths (1 ns and 4 ns).*

As shown in Figure 4.12, the mean lifetimes for cells expressing the mTq5A and mTq17V constructs are approximately constant as a function of integration time for values above 100 ms. For shorter integration times, the poor signal to noise ratio leads to fluctuations in the determined mean lifetimes, which are associated with high standard deviations. The expected improvement in standard deviation for measurements performed with the 4 ns time-gate width compared with the 1 ns width is less clear than in Figure 4.10, although the overall trend that lower integration times and shorter time-gate widths give less precise results is still apparent. This poorer performance at lower numbers of detected photons may be due to less efficient transfections and fewer bright cells for this experiment.

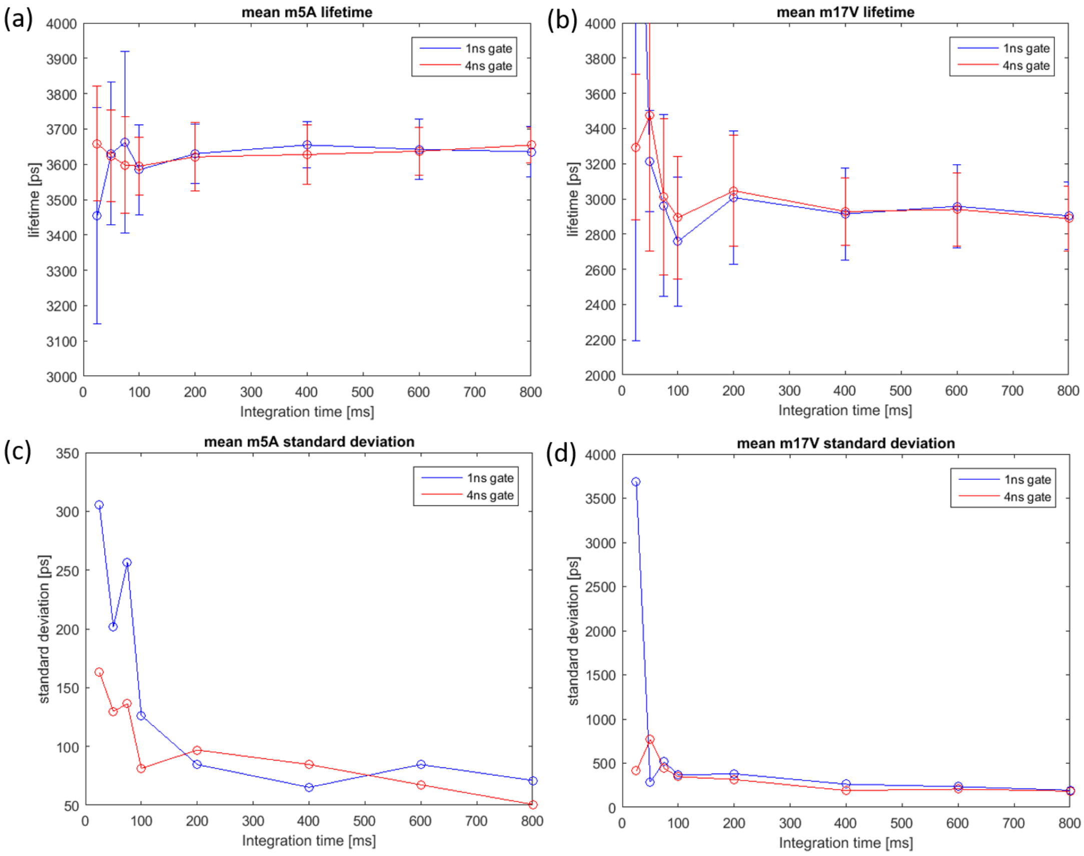

Figure 4.12: *Variation of the mean lifetimes (a,b) and standard deviations (c,d) measured for cells expressing mTq5A (a,c)) and mTq17V (b,d) as a function of different camera integration times (800 ms, 600 ms, 400 ms, 200 ms, 100 ms, 75 ms, 50 ms and 25 ms) and two different time-gate widths. Error-bars are the standard deviation per segmented cell for mTq5A (c) and mTq17V (d).*

4.3 Optimising the homogeneity of the laser illumination

An inhomogeneous illumination pattern can degrade the quality of fluorescence intensity images and reduce the signal to noise ratio for FLIM. Imperfections in the optical system, such as misalignment, impurities in the material of elements such as lenses, optical fibers or filters, or dust or scratches on their surfaces, can scatter or refract the excitation laser beam and impart phase shifts that cumulatively can produce coarse inhomogeneities in the beam profile or pseudorandom, grainy patterns of intensity modulation, called speckle patterns [Dai84]. Speckle occur due to constructive and destructive interference of light having taken a range of different light paths to the sample. The sample can also contribute to modulation of speckle patterns and speckle analysis can be used for various applications, for example medical imaging [Bas12]. For most imaging techniques, however, a uniform, illumination (excitation) intensity distribution is desired and steps are taken to minimise speckle inhomogeneities. There are three main approaches to reduce speckle patterns: (1) averaging over multiple speckle patterns (in the situation where the speckle is (pseudo)randomly changing over time), (2) reducing the spatial coherence such that the speckle size is below the resolution of the detector or in the case of significant scattering, speckle can be reduced by decreasing the temporal coherence or (3) applying digital processing techniques [Wan13] in which the object information can be separated from the speckle modulation, e.g. using digital holography with Fourier transform domain filtering [May07] or wavelet filtering [Sha08]. A further general source of inhomogeneity in the illumination intensity distribution encountered with laser beam illumination is the Gaussian intensity profile of the laser beam. For wide-field illumination, this can be addressed using specially engineered refractive elements [Hof00] or diffractive elements, such as holographic diffusers, that transform the Gaussian intensity distribution across the field of view to a rectangular or "top-hat" distribution.

This section addresses three different approaches to improve the illumination intensity homogeneity achievable using a TEM_{00} excitation laser beam that all aim to minimise speckle artifacts by averaging over rapidly varying speckle patterns during the acquisition time of the camera. The first approach utilises a commercially available holographic diffuser that is engineered to diffract the incident last beam to produce the desired "top-hat" intensity distribution. This diffuser is translated to time-average the speckle, following the conventional approach that is often implemented with a ground glass diffuser. The second approach utilises a deformable mirror that can rapidly modulate the phase profile of the illuminating light field and the third approach uses a vibrator in conjunction with a multimode optical fibre.

Prior to this work, the standard approach in this lab for wide-field FLIM utilising a spectrally filtered supercontinuum laser source (SC-400-4, Fianium Ltd) coupled into an optical fiber as the excitation source was to use a rotating holographic diffuser to time-average the speckle but this holographic diffuser resulted in an illumination that retained a Gaussian intensity profile. In order to achieve a uniform illumination over the field of view, the back focal plane of the objective lens had to be overfilled, which resulted in a significant loss of excitation power. A further drawback of this approach is that the rapid (10's Hz) rotation of the diffuser produced unwelcome noise and vibrations in the laboratory.

4.3.1 Scanning "top-hat"engineered diffuser

The "top-hat" engineered diffuser (ED1-S20-MD, Thorlabs) utilised here is superior to widely used diffusers like ground glass or holographic diffusers, because it incorporates a micro-lens array designed to convert an incoming laser beam with a Gaussian intensity profile to a uniform top-hat intensity profile [Tho17a]. The engineered diffuser was mounted such that it could be translated using an eccentric cam mechanism driven by a DC electric motor. It was deployed with an optical fibre-delivered laser beam in the configuration shown in Figure 4.13, with the diffuser being imaged to the back focal plane of the objective lens for fluorescence microscopy.

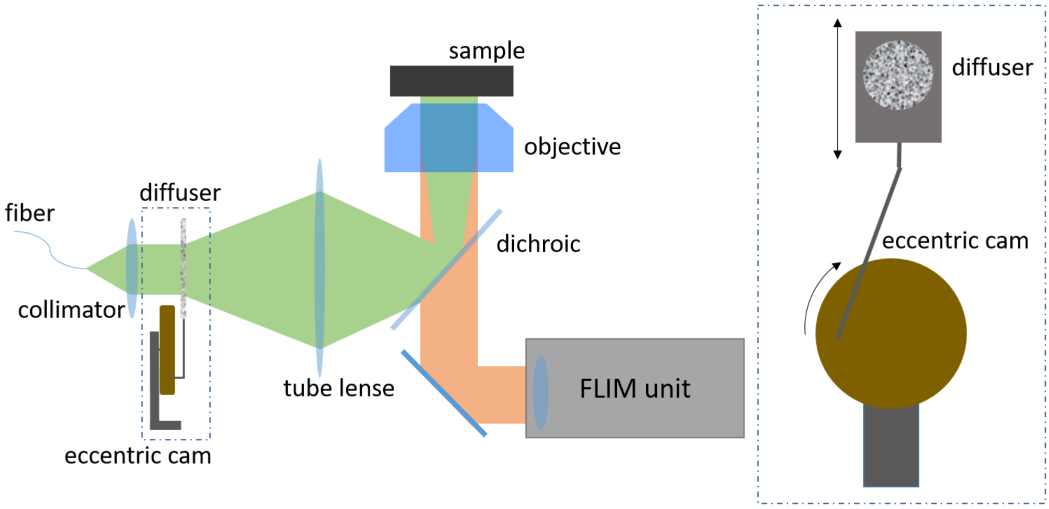

Figure 4.13: *Top-hat diffuser configuration in wide-field time-gated FLIM setup.*

To characterise the performance of this approach, a laser beam was coupled into a single mode optical fibre and collimated using a 50 mm lens before being directed to the engineered diffuser with the transmitted light propagating to a white screen where the resulting intensity distribution was imaged using a cooled CCD camera (Orca-Flash, Hamamatsu). The beam was expanded onto a screen for visualisation. For these measurements, the engineered diffuser was mounted on a device driven by an eccentric cam to enable it to be rapidly translated in order to enable averaging over enough multiple speckle patterns to obtain a homogeneous illumination profile during a CCD integration of 200 ms. As shown in Figure 4.14, when the engineered diffuser was moved around 5 mm with a frequency of ∼1 Hz the recorded intensity profiles retained some speckle structure and were seen to vary between acquisitions at different time points. Increasing the rate of translation of the engineered diffuser to 10 Hz provided sufficient averaging over multiple speckle patterns during the 200 ms acquisition time to produce a time independent uniform intensity distribution.

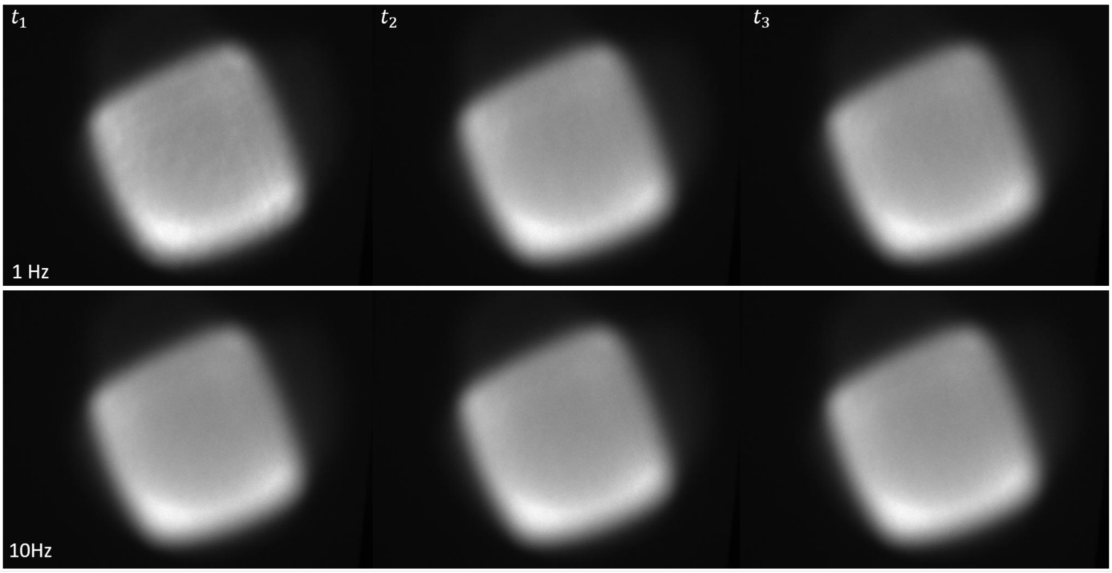

Figure 4.14: *Intensity distributions of laser light transmitted by an engineered diffuser recorded over a 200 ms acquisition time while translating the diffuser at 1 and 10 Hz acquired at different time points (t_1, t_2, t_3).*

4.3.2 Deformable mirror

In order to realise a vibration-free approach to time-average the laser speckle, a deformable mirror (DM) was explored. This custom DM (Mini-DM 1.5, Boston Micromachines Corp.) comprises 32 actuators shaping the deformable mirror surface that can be driven at up to 20 kHz in order to apply a random time varying phase shift across a laser beam reflected off the device. To evaluate its potential to provide time-averaging of speckle patterns, the laser light was again coupled into a single mode optical fibre and collimated using a 50 mm lens before being reflected off the deformable mirror and expanded onto a white screen where the intensity distribution was imaged using the cooled CCD camera (Orca-Flash, Hamamatsu) with an integration time of 200 ms. Using a home written *MATLAB* code, pseudorandom DM patterns could be applied with a maximum framerate of 3 kHz. When a frame rate of 0.5 Hz was applied to the DM a strongly modulated speckle pattern was apparent, as indicated in Figure 4.15. This observed speckle pattern is dominated by the contribution of the DM and the resulting speckles are larger than those resulting from the optical system (as would be observed if the DM was replaced with a static plane mirror). Increasing the frequency of the pseudorandom patterns sent to the DM up to 3 kHz frame rate was sufficient to average the speckles over the integration time of 200 ms. As seen in Figure 4.15, the resulting beam presents a homogeneous Gaussian intensity profile, which is therefore less efficient for microscope illumination than the flat intensity profile produced by the engineered diffuser. However, the DM approach does not introduce any vibrations and it could be combined with an engineered diffuser or a specific hologram pattern, as described in by Houzet et al [Hou16], to produce a top hat intensity profile. The main drawback would then be the relatively high cost of this approach.

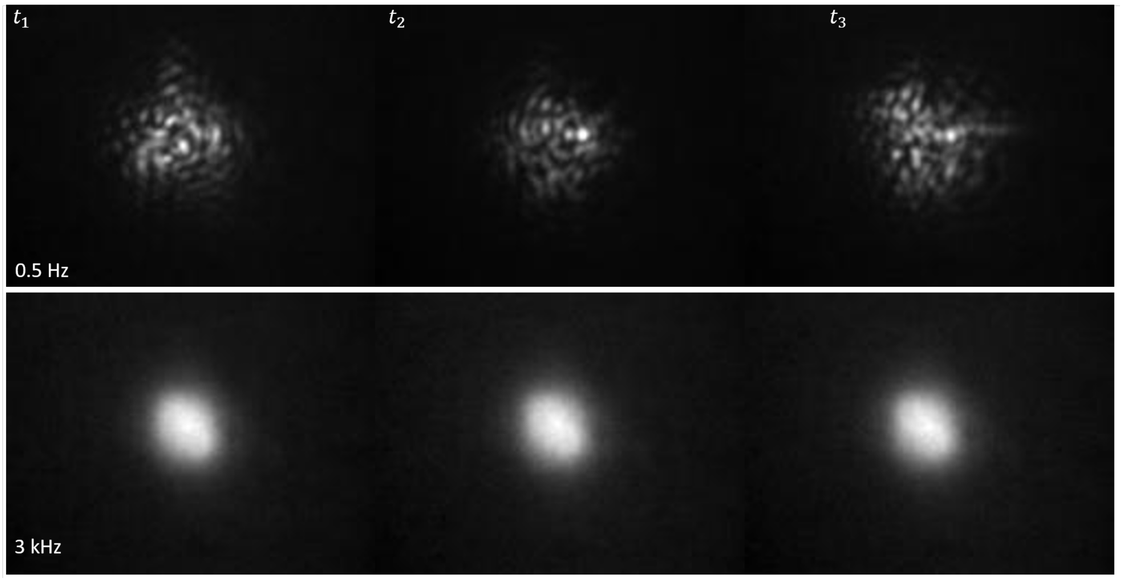

Figure 4.15: *Intensity distributions of laser light reflected from a deformable mirror recorded over a 200 ms acquisition time acquired at different time points (t_1, t_2, t_3) for two different drive frequencies (0.5 Hz and 3 kHz).*

4.3.3 Vibrating multimode optical fiber

The third approach to time-average the laser speckle for wide-field illumination is to use a multimode optical fibre (MOF). Here, this was evaluated using a step-index multimode optical fibre, which is suitable for intensity imaging but not for FLIM since dispersion in such an optical fibre would broaden the temporal instrument response function (IRF) and the IRF would also be susceptible to any drift in vibrations that impact the coupling between the modes of the MOF. However, these issues may be mitigated in a FLIM microscope system by using a graded-index

MOF, for which vibrations impact the IRF to a much smaller extent.

The vibration-induced variation in the coupling between the modes in a MOF can be exploited to time-average speckle patterns in the output of the MOF used to despeckle a laser beam since the rapid perturbations to the MOF result in pseudorandom changes in the optical path lengths of the different modes. This can be practically realised by coupling an electronic vibrator (e.g. a buzzer) to the MOF. Mode-mixing can be further enhanced by tightly bending the MOF. To evaluate this approach, the laser beam was coupled into a step-index MOF, collimated with a 40 mm focal length lens and the resulting intensity distribution on a white screen was recorded with a cooled CCD camera (Retiga R1, Photometrics) with an acquisition time of 200 ms. The beam was expanded onto a screen for visualisation. Two different step-index MOFs were tested with core diameters of 50 μm and 100 μm. A commercial vibrator and fibre bending block (Cairn Research Ltd) were used to produce time-varying speckle patterns. The intensity distributions obtained with the 100 μm core fibre have been magnified for a better visualisation of the speckle pattern.

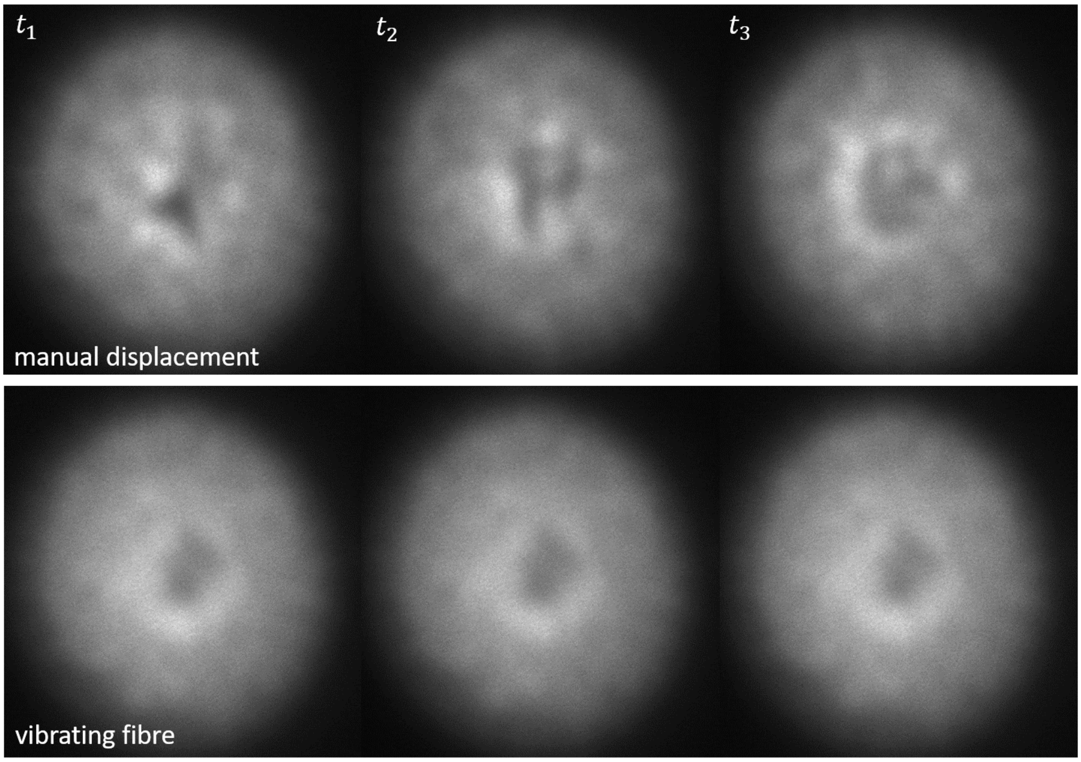

Figure 4.16: *Intensity distributions of laser light passing a MOF with a core diameter of 50 μm recorded over a 200 ms acquisition time acquired at different time points (t1, t2, t3). Upper row: no vibration active, manual displacement of fibre. Bottom row: vibration active.*

For the 50 μm core diameter MOF (Figure 4.16), the modulation of optical path lengths did not produce sufficient differences in the coupling between the modes to fully time-average the speckle, either by manually bending the fibre or applying the vibrator. It may be possible to improve this performance by increasing the vibration amplitude or using multiple vibrators. The dark hole observable in the middle may be due to higher mode effects as discussed by Ma et al [Ma17]. With the 100 μm MOF (Figure 4.17), the speckle pattern was much finer due to the higher number of propagating modes and the illumination pattern was reasonably uniform when the MOF was manually bent. Applying the vibrator effectively removed the speckle modulation. This approach has the advantages of simplicity and low-cost and, if the vibrator can be located away from the optical table or other microscope components, does not impart vibrations to the system.

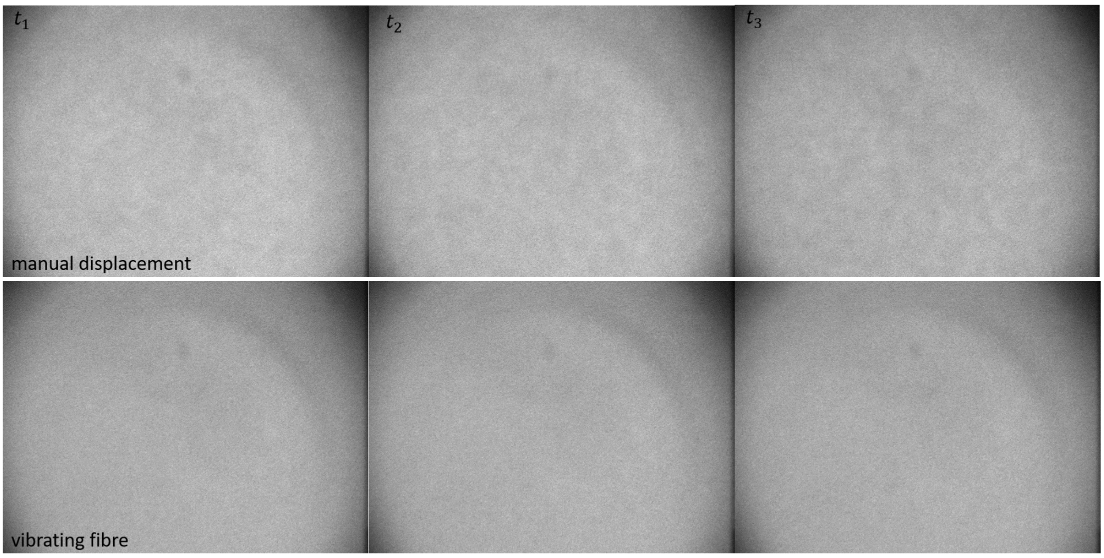

Figure 4.17: *Intensity distributions of laser light passing a MOF with a core diameter of 100 μm recorded over a 200 ms acquisition time acquired at different time points (t1, t2, t3). Upper row: no vibration active, manual displacement of fibre. Bottom row: vibration active.*

4.4 Summary

Summary This chapter investigated the enhanced performance of a novel prototype GOI (HRI-HL-S) which was found to provide better spatial resolution than the standard HRI, due to the addition of a magnetic field. A study of the benefits of longer time-gate widths demonstrated the superior performance achievable, particularly with time-gate widths of 4 ns compared to 1 ns when undertaking FLIM with relatively low numbers of detected photons. This was demonstrated using reference dye samples and representative biological samples of cells expressing fluorescent protein constructs. These new properties of the HRI, especially in combination with global analysis, allow FLIM-FRET cell imaging with low expression levels. It would be necessary to test if this improvement will also enable FLIM-FRET experiments with endogenous labelled live cells.

Three different approaches to improving the laser illumination homogeneity in a wide-field microscope by time-averaging the speckle modulation were compared. The moving engineered diffuser is the most cost-efficient and easiest to implement version of all three approaches and it generates a homogeneous illumination distribution. However, it is noisy and introduces vibrations on the optical table, which can lead to inconsistencies during sensitive measurements. The approach of the vibrating optical fibre is a very convenient way to avoid speckle patterns if the optical design of the instrument already contains a fibre to deliver the laser light. If not, the implementation is tedious and limits the flexibility of the laser sources. Additionally, the vibrating problem is still present, although, if the vibrator is not placed on the optical table, not as disruptive and the illumination profile remains Gaussian-like. The deformable mirror approach is the most elegant presented method without any vibration and corresponding noise. If enough space is available, the implementation is straight forward. The disadvantage is the high cost price and the inhomogeneous (Gaussian-like) illumination pattern. All three approaches were successful but only the moving engineered diffuser delivered a homogeneous illumination patter to reduce the loss of laser light. However, the other two approaches can be combined with a “top-hat” diffuser to provide an efficient illumination profile.

Contribution The experiments in section 4.1 were performed by Dr. Hugh Sparks and myself. The remaining experiments were performed and analysed by me.

Chapter 5

Mapping super-resolved structures to functional readout

This chapter presents the development of a microscope that combines the techniques of structured illumination microscopy (SIM) and FLIM. SIM can resolve biological structures with twice the lateral resolution of wide-field resolution diffraction-limited microscopes and provides axial resolution of half the depth of field. Fluorescence lifetime imaging can be used for molecular functional readouts including inter- and intramolecular interactions, e.g. using Förster resonance energy transfer (FRET). FLIM-FRET can provide quantitative FRET readouts, and therefore can probe interaction distances on a scale below 10 nm. The new SIM+FLIM microscope reported here provides unprecedented opportunities to obtain insights into cellular and molecular biology, e.g. by correlating changes in nanostructure with molecular function. It should be noted that the resolution limits of the combined techniques are different, SIM reveals structures down to 120 nm whereas the spatial resolution of FLIM is the conventional wide-field diffraction limit.

FLIM has previously been combined with super-resolved microscopy. In STED microscopes it was implemented with time-correlated single-photon counting (TCSPC) [Auk08]. However, STED microscopy entails high excitation and depletion intensities at the sample and is not compatible with many biological samples. SIM is a wide-field microscopy technique that uses lower illumination intensities than STED or other laser scanning techniques and can be implemented on the same microscope frame as wide-field time-gated FLIM, which also entails lower excitation intensities than laser scanning FLIM techniques and is compatible with live cell imaging, with or without optical sectioning implemented using a Nipkow disc scanner as in chapter 3.

Structured light illumination was previously utilised in combination with FLIM to provide optical sectioning [Col00] but not super-resolution microscopy. This prior work was demonstrated using dye-based labels (DASPI and Coumarin 314) and entailed acquiring a time-gated image series for each of the three grating positions separated in phase by $2\pi/3$ from which the optically sectioned FLIM image was calculated. One drawback of this approach was that the numerical calculations required for both SIM and FLIM essentially depend on the differences across series of images and so are sensitive to noise on the acquired images. Combining the methods together in this way resulted in higher noise levels in the final optically sectioned FLIM images (since the noise contributions were additive). Another disadvantage of this prior work combining FLIM with structured illumination was that the requirement to acquire a time-gated image series for each of the three grating positions resulted in a high total exposure time. This would be further exacerbated if this approach were to be applied to 2D SIM (requiring nine images) or 3D SIM (requiring 15 images). Therefore, in this work FLIM was implemented in parallel with SIM, rather than in combination, thus SIM+FLIM compromises neither technique in terms of signal to noise performance. The total image acquisition time, and therefore sample exposure time, for 3D SIM combined with FLIM using 8 time-gated images per grating position would have been 120 s for an integration time of 1 s per gate. However, the total SIM+FLIM image acquisition time with 1 s integration times for 8 time-gated images plus 15 grating position images with an integration time of 200 ms for SIM is only 11 s. It should be noted that the FLIM image resolution is diffraction-limited, according the properties of the FLIM instrumentation, whereas the SIM provides higher resolution images through the same microscope objective lens.

The SIM+FLIM system was applied to investigate the nanostructure of the nucleus of eukaryote cells and to study molecular interactions associated with organelles. In higher mammals such as humans, the nucleus carries genetic information on different spatial scales, with deoxyribonucleic acid (DNA) being the smallest structures with chromatin and chromosomes being progressively larger. During cell division, the structure of DNA is of great interest in biology, because the cell transfers its genetic information at this point. In particular, the distribution and density of DNA and chromatin, and the position and structure of the organelle which divides the DNA, the mitotic spindle, is an interesting target to study within different phases of mitosis. The SIM+FLIM microscope was applied to image the nanostructure of the DNA and the mitotic spindle and to correlate it with measurements of DNA compaction in chromatin read out via FLIM-FRET. The SIM+FLIM system was also applied to elucidate interactions between different cell organelles, with SIM localizing the organelle and sub-elements within it, and FLIM-FRET readouts providing information about interactions between different organelles on a scale ≤ 10 nm.

5.1 SIM+FLIM instrument design

The experimental set-up consisted of two separate subsystems that were coupled to a common microscope frame and objective lens. The instrument was built around a commercial (Elyra.S1, Carl Zeiss AG) SIM microscope that included a SIM excitation unit and SIM camera [Zei17b]. A custom-built wide-field time-gated optically sectioning FLIM unit (see chapter 3) was added to the left port of the Elyra.S1, as indicated in Figure 5.1. The manufacturer's specified resolution for the Elyra.S1 is 120 nm in the lateral direction and 300 nm in the axial direction. The system includes four different excitation laser lines (405 nm, 488 nm, 561 nm and 647 nm) for multi-color imaging and a CMOS camera (pco.edge 4.2, PCO GMBH) for detection. The software used for the SIM analysis was the Zen Black edition (Carl Zeiss AG), which includes a correction for chromatic shifts between images acquired at different colour channels. The FLIM unit is represented in the left part of Figure 5.1. Excitation light was provided by a spectrally filtered supercontinuum laser (WhiteLase, Fianium Ltd) where the bandpass filters were selected to match the SIM excitation lasers. A Nipkow spinning disk unit (CSU-X1, Yokogawa) provided optical sectioning for reduction of out of focus light. A GOI (HRI-HL-S, Kentech Instruments Ltd) was attached to the output of the spinning disk unit. Two relay lenses imaged the GOI phosphor onto the readout camera. Two different cameras were used to read out the GOI: initially a sCMOS (Zyla-5.5, Andor Technology) and latterly a CCD (Retiga R1, QImaging, Inc.). The acquisition software from the home-built high content analysis FLIM microscope, *openFLIM-HCA*, was adapted to be compatible with the SIM+FLIM hardware. The *FLIMfit* software package [War13] was used to analyze the FLIM data. An instruction manual for this instrument, including a detailed description of the switch-on process, is provided in section 9.2.

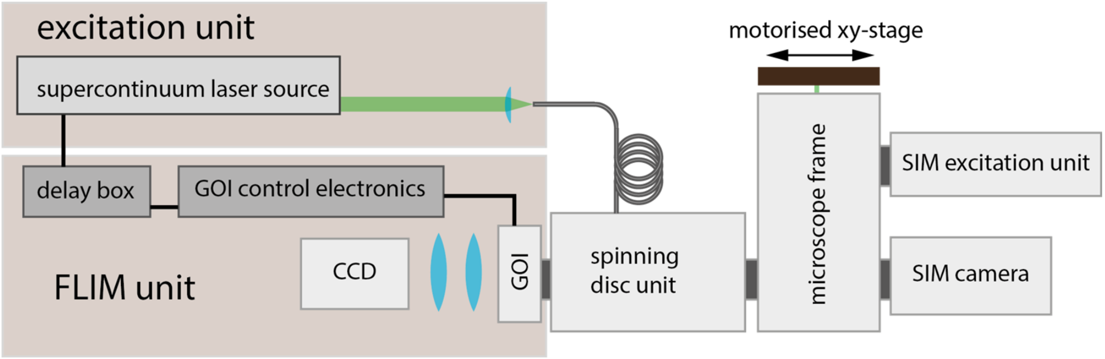

Figure 5.1: *SIM+FLIM design.*

5.2 Performance evaluation

Several reference samples were tested to validate the microscope performance. These included a fluorescence dye solution for a precise assessment of the fluorescence lifetime measurement, 200 nm diameter multispectral beads for the registration of different imaging modalities and a stained Convallaria specimen labelled with several fluorophores that was used to illustrate the performance of the system on a sample with complex structures.

5.2.1 Lifetime precision assessment

The lifetime performance was tested using a dye with a known monoexponential lifetime. Coumarin 6 (75 μM in ethanol) was imaged using the FLIM port only with a 500/25 nm excitation bandpass filter (centre wavelength/bandpass), a 488/561 nm dichroic and a 542/27 nm emission filter. The gate width of the GOI was set to 4 ns and the GOI gain voltage to 750 V was used. The gates were spaced at 25 ps intervals over 16 ns. The sCMOS readout camera integration time was set to 200 ms. Figure 5.2 (a) shows a fluorescent decay trace of the Coumarin 6 solution which presents the expected characteristic monoexponential decay. This model provides a good fit to the raw data and the structure in the normalised residuals is at a similar level to the noise. The lifetime was homogeneous over the whole FOV as shown in Figure 5.2 (b), with a pixel-averaged lifetime of 2526 ps (28 ps stdev) which is in good agreement with previous studies [Kri14].

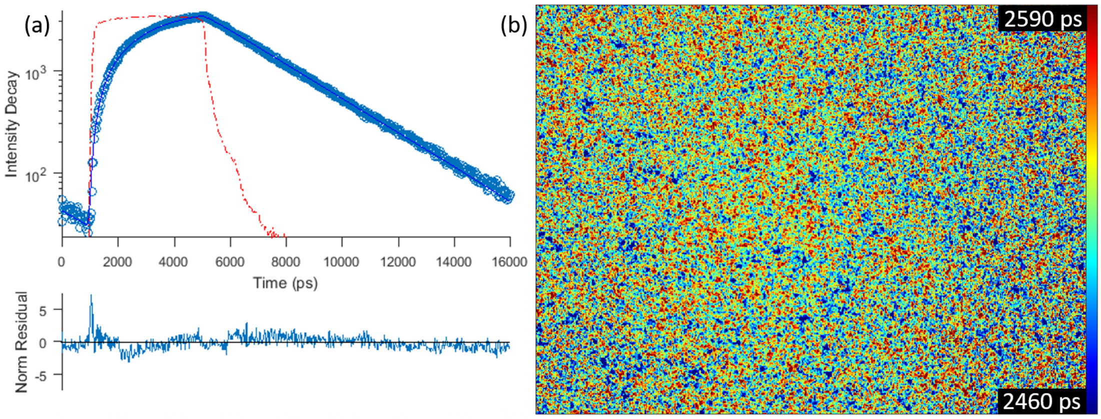

Figure 5.2: *FLIM data obtained from 75 μM Coumarin 6 in ethanol: (a) fluorescence decay profile: blue circles are data points, blue dotted line indicates fitted model, red dotted line indicates scattered light IRF, with the normalized residuals underneath; (b) corresponding lifetime map.*

5.2.2 Image registration between SIM and FLIM port

Due to the parallel implementation of SIM and FLIM, the raw digital images acquired sequentially with the two modalities do not have an intrinsic correspondence in space and size. To enable accurate correlation of these image data, a registration dataset of a fluorescence bead sample (200 nm multispectral beads, Carl Zeiss AG) was used to determine the scaling, rotation and offset factors between the SIM and FLIM images. Figure 5.3 displays a bead sample image acquired using the FLIM port. The intensity image (a) reports the bead distribution and the lifetime map with no intensity mask applied (b) for a mono-exponential fit shows the bead lifetime distribution on a pixel-by-pixel basis. The intensity-weighted lifetime image (c) and the corresponding intensity-weighted lifetime histogram shown in (d) present a mean lifetime of 2724 ps and a stdev of 354 ps for this bead sample. The resolution of the FLIM detection path is limited by the HRI [Spa17] if using a 60x (1.4 NA) objective. Fitting a 2D Gaussian to every localised bead in Figure 5.3 (a) using the ThunderSTORM μManager plugin [Ove14] results in an average FWHM of 380 nm (stdev 59 nm).

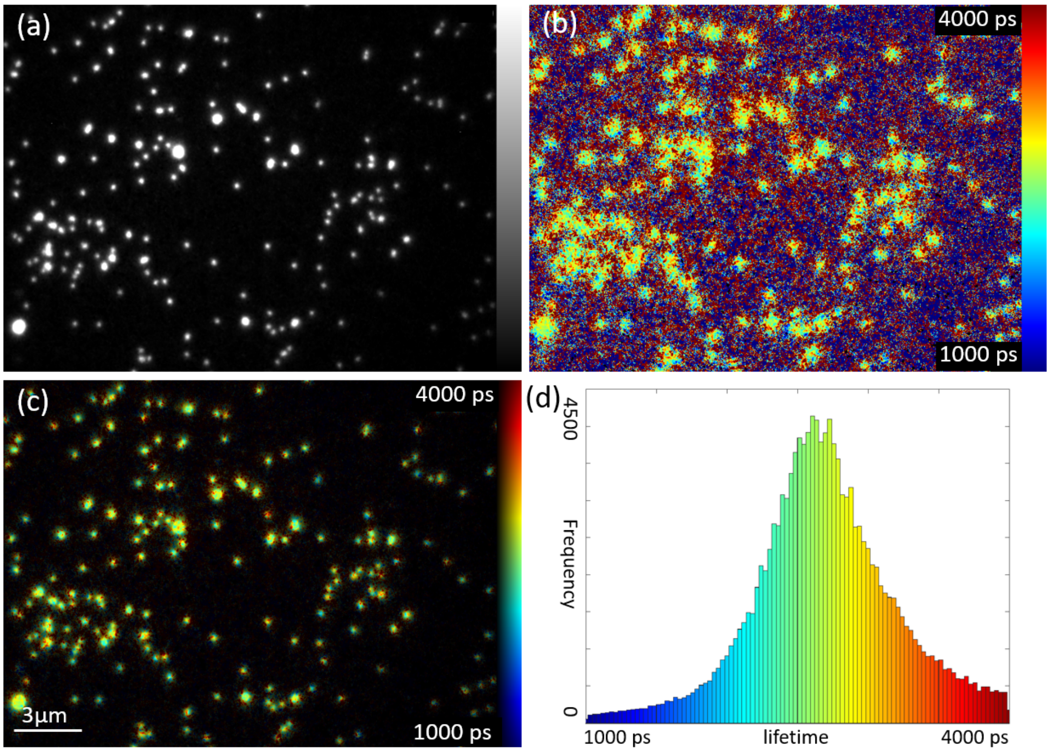

Figure 5.3: *Fluorescence bead image acquired by FLIM port. (a) Intensity image, (b) lifetime map for a mono-exponential fit with no intensity threshold, (c) intensity-weighted FLIM image and (d) intensity-weighted lifetime histogram.*

The corresponding three-color wide-field, 3D PSF deconvolved (using a theoretical PSF) and analysed SIM images from the SIM port without spatial registration are displayed in Figure 5.4 using the Zen Black software [Zei17b]. Three different color channels (488 nm, 546 nm and 647 nm) were co-registered using the Zen Black chromatic shift correction. The figure shows that the deconvolved image can resolve higher structural details than the wide-field image, whereas the SIM images present the highest resolution.

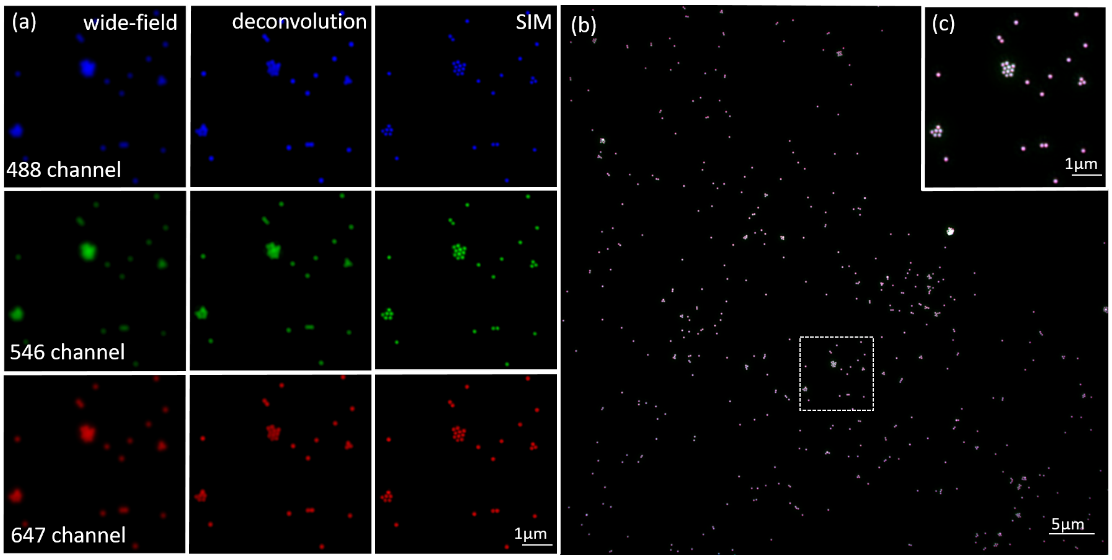

Figure 5.4: *Three color fluorescence bead images acquired using the SIM port (presenting wide-field, deconvolved and SIM images as provided by the Zen Black software): (a) separate color channel images, (b) SIM image of entire FOV with three colours superimposed and (c) expanded image with three colours superimposed of sub-region indicated in (b).*

It should be noted that the FLIM (Figure 5.3) and SIM (Figure 5.4) images have different spatial resolutions and the relative scaling, offset and rotation must be determined in order for them to be correlated. The lateral image registration is undertaken manually using *MATLAB* and needs to be repeated every time the set-up changes, e.g. due to a camera or other hardware changes. More detailed information can be found under section 9.3. Additionally, there is a z-offset, which was manually determined by sequentially imaging the beads with the SIM camera and the FLIM camera and reading the z difference when the same beads are in focus. This z-offset was measured to be 4.81 μm with 0.55 μm stdev, calculated from 5 repeats.

The visual presentation of the resulting SIM+FLIM image requires some consideration. As an example, FLIM and time-averaged intensity data are presented with the corresponding SIM data acquired with the same objective lens and shown on the same scale in Figure 5.5. It is common to weight the FLIM data by the corresponding intensity data (typically obtained by time-integrating the decay profiles), which results in an intensity-weighted FLIM image, as shown in Figure 5.5 (c). This approach gives pixels with higher intensity more significance and pixels with low photon counts, such as those in the background of the image, where there is greater uncertainty in the calculated lifetime, are de-emphasized.

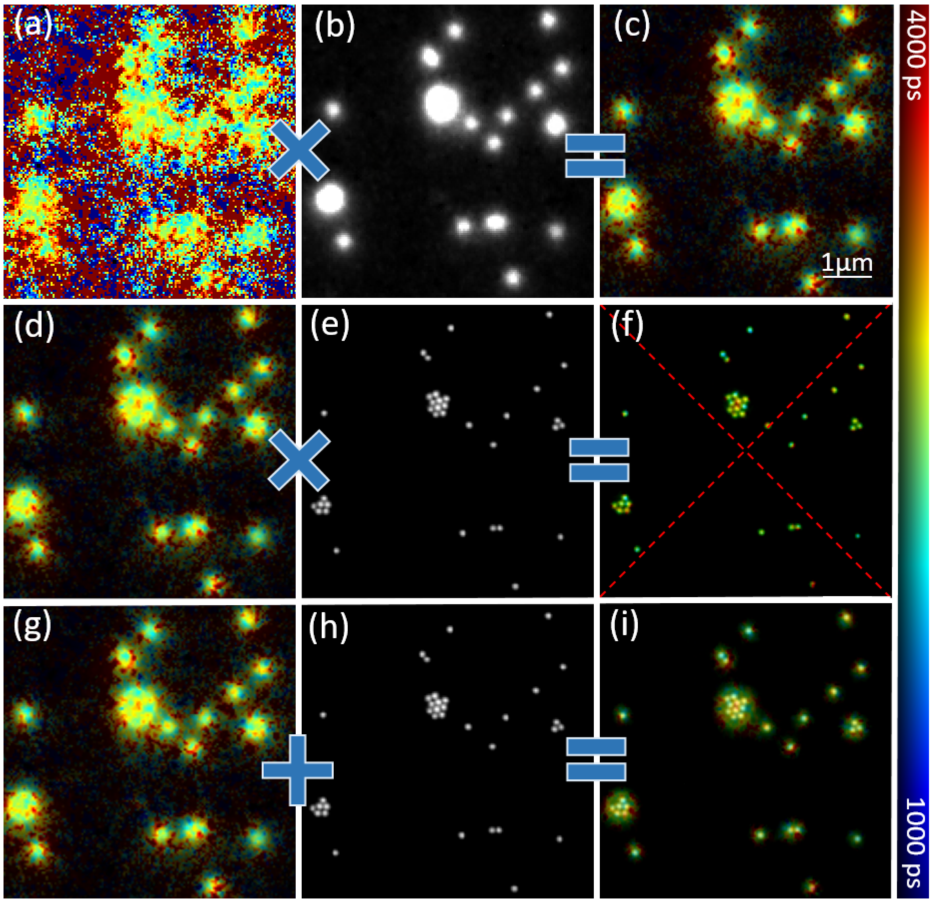

Figure 5.5: *Visualisation process of a SIM+FLIM image of 200 nm diameter fluorescent beads. First row displays the generation of an intensity-weighted FLIM image. (a) lifetime map, (b) intensity image obtained at the FLIM port and (c) intensity-weighted FLIM image. Second row shows the same analysis with the SIM image, leading to a non-physical interpretation of the data. (d) intensity-weighted FLIM image, (e) SIM intensity image and (f) fallacious multiplication of (d) and (e). The last row presents a linear method for combining the two datasets for visualization purposes. (g) intensity-weighted FLIM image, (h) SIM intensity image and (i) sum of (g) and (h).*

For the SIM+FLIM data, it was initially appealing to weight the FLIM data with the SIM intensity images but this is not valid because the resolutions of these images are different. The information in a FLIM pixel contains information from all fluorescence molecules located within the diffraction limited PSF, whereas the higher resolution SIM image contains information from an area with a diameter of only half the diffraction-limited PSF. Therefore, a multiplication of the SIM image and the lifetime map (i.e. the SIM intensity-weighted FLIM image) would appear as a super-resolved FLIM image, as shown in Figure 5.5 (f), but this could lead to errors in interpretation of this data. For example, in the cluster of beads in the centre of the FOV of the FLIM image, see Figure 5.5 (c), there is variation in the fluorescence lifetime across the cluster and a higher (red) lifetime is apparent in the centre (which is likely due to noise). In Figure 5.5 (f) where the SIM and intensity-weighted FLIM images have been multiplied, there is the potential that the viewer would interpret this image to mean that the central two beads have a longer fluorescence lifetime than the eight surrounding beads. This interpretation could be wrong because in the FLIM image the pixels corresponding to the two central beads receive contributions from all of the beads due to the size of the diffraction-limited PSF. A more valid way to present the SIM+FLIM data is to avoid the multiplication inherent in intensity weighting and instead to perform a linear addition of the SIM intensity image and the intensity-weighted FLIM image, as shown in Figure 5.5 (i). Inspecting the cluster of beads in the centre of this image, it is more apparent to the viewer that the beads are not resolved in the FLIM data. Isolated beads can be expected to present the "correct" lifetimes and the viewer can judge that they are isolated beads from the information in the higher resolution SIM image.

5.2.3 Imaging biological test sample

To illustrate the application of SIM+FLIM to complex biological structures, a Convallaria (”Lily of the valley”) sample stained with multiple fluorophores was imaged, as shown in Figure 5.6. This complex sample exhibits a range of excitation and emission bands and a range of fluorescence lifetimes and is often used to demonstrate microscope performance.

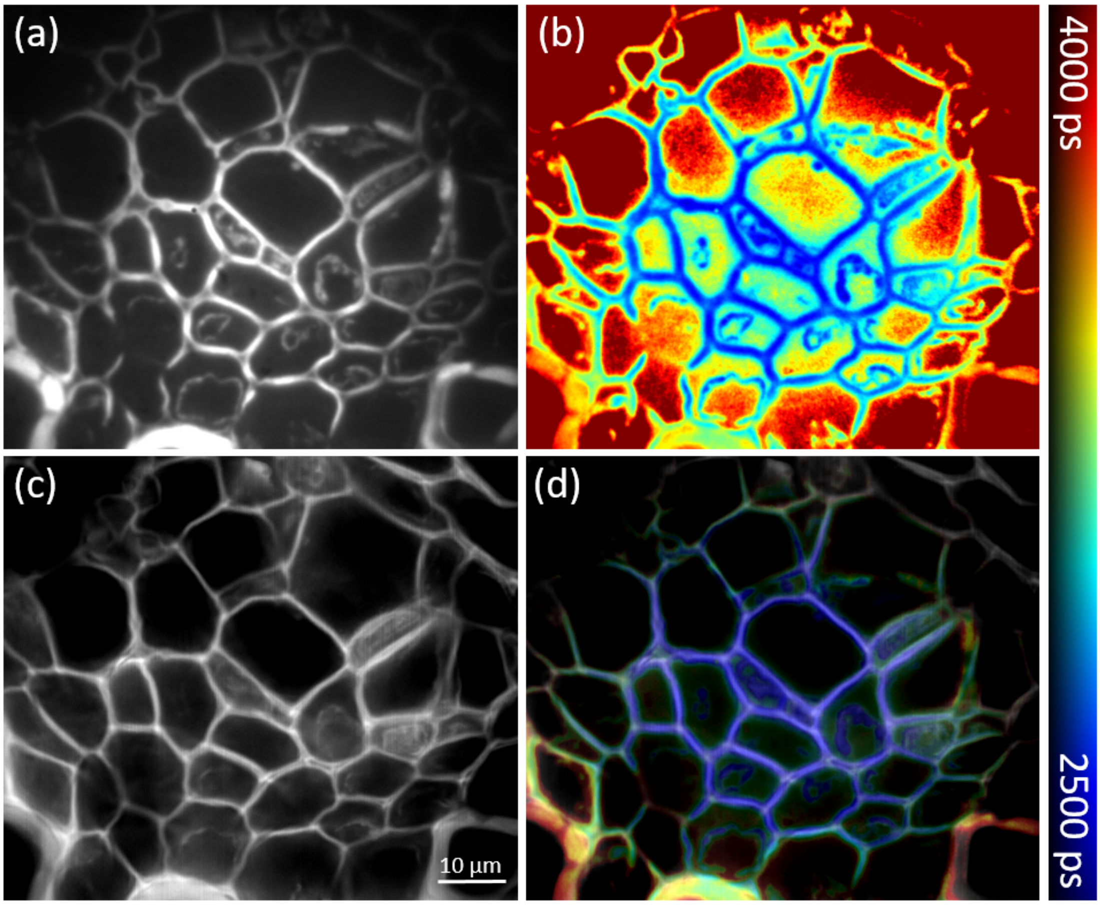

Figure 5.6: *SIM+FLIM images of a stained Convallaria sample. (a) FLIM port intensity image, (b) lifetime map, (c) SIM intensity image and (d) SIM+FLIM image.*

5.3 SIM+FLIM of genomic structures during cell cycle

Super-resolution techniques are useful tools to resolve DNA and chromosome structures that cannot be resolved with confocal microscopy. SIM has previously been used to study higher order chromosome structures, while localization-based super-resolution techniques were necessary for nanoscale imaging of chromatin [Flo11] and FRET has been used to probe chromatin structure on the nm scale [Llè09].

Here using the SIM+FLIM approach, SIM was used to monitor the DNA distribution during the cell cycle and FLIM was used to provide a FRET readout of changes in DNA density and thus to identify open and closed chromatin. DNA was stochastically labelled, either directly via EdU and click chemistry [Che09a] or using SNAP-tags incorporated into Histone 2B, with two fluorescent dyes (Alexa-594 and Alexa-647) that form a FRET pair. By imaging the donor fluorophore with SIM, the genomic architecture of the nucleus could be visualised, whereas FLIM of the donor provides information about the DNA density and chromatin status.

5.3.1 Biological background

Cell division (mitosis) is a vital step in the cell cycle that determines the inheritance of genetic information. The cell cycle consists of five phases G_0, G_1, S, G_2 and M [Coo00]. G_0 is the resting phase, where the cell has stopped division. During interphase, the cell prepares for the division during three phases: in G_1 the cell grows in size and increases the number of cell organelles; in S, a replication of the DNA occurs until a full duplication is achieved and in G_2, the cell continues growing and the reorganisation of the mitotic spindle begins. M, or mitosis, is the phase of cell division, which consists of five sub phases: during prophase, the DNA condenses and a mitotic spindle is initialized; in prometaphase, the mitotic spindle attaches to the kinetochores of the chromosomes; in metaphase, the mitotic spindle applies tension to the chromosomes, forcing them to align in one plane; in anaphase, the chromosomes are divided and, in telophase, they are moved apart to form two cells with identical genetic information.

Genetic information is encoded in the chromosomes of a cell. There are different spatial levels of the data carrier: the chromosome, chromatin and DNA [Bor12], which are depicted in Figure 5.7. Humans carry 3.3 billion bases of DNA (a), which are wrapped around histones within nucleosomes, which are themselves subunits of chromatin (b), which is packaged to form the higher level nuclear structures that are the chromosomes (d-f). During the cell cycle, the chromosomes have to unpack, and the chromatin needs to unwind for several reasons, for example to enable the DNA to be replicated or transcribed. Thus, the density of the DNA changes during the cell cycle and measurements of such changes can report on the open (less dense) or closed (more dense) status of chromatin. Open chromatin indicates areas of gene expression [MB07a]. Another interesting issue is to understand mitotic condensation of chromosomes, its compaction during mitosis was imaged via fluorescence intensity microscopy [MB07b]. This study demonstrated that the density of chromosomes is not constant or linearly increasing with time but that it varies for different states of mitosis.

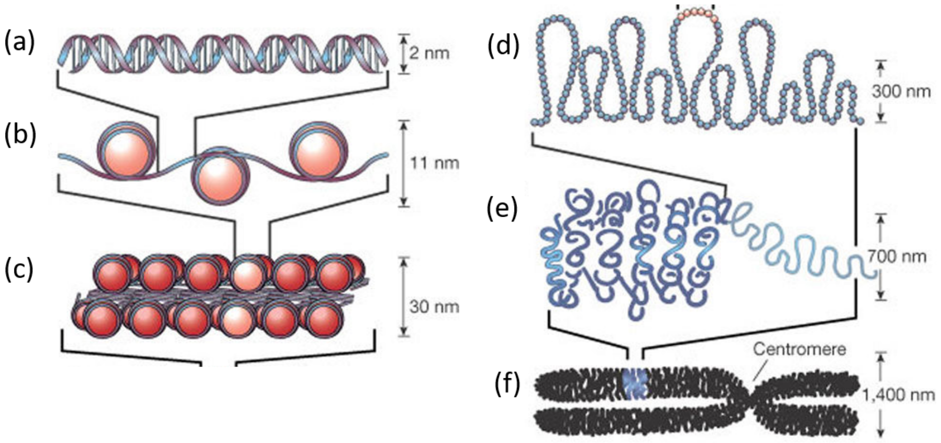

Figure 5.7: *Spatial levels of nucleus structure. (a) DNA, (b) chromatin, (c) packed nucleosomes, (d) section of extended chromosome, (e) section of condensed chromosome and (f) entire chromosome [Fel03].*

There are different ways to selectively label DNA. The classic method is by replacing thymidine with 3H-thymidine, which is radioactive and can be quantified using a scintillator [Tay57]. Alternatively, thymidine can be replaced by 5-bromo-2'-deoxyuridine (BrdU), which can be incorporated into DNA and detected using immunohistochemistry [Gra82]. However, to access the binding area of the BrdU with antibodies requires harsh treatment of the DNA, which can lead to biological artefacts due to cell damage. A method that does not require antibodies is based on the thyridine analog, 5-ethynyl-2'-deoxyuridine (EdU) [Sal08, Buc08]. The terminal alkyne group of EdU can be labelled via click chemistry [Tor02] with fluorescent azides. These are much smaller than antibodies and can easily reach their binding site without DNA denaturation. This approach was successfully applied to label proliferation cells in the nervous system [Che09b], to identify profileration cells in breast cancer via flow cytometry [DD09], to in vitro measurements of mice T-cell proliferation [Yu09], to visualize newly replicated DNA in fixed E. Coli. [Fer09] and to track stem cell in vivo [Lin10].

Different FLIM approaches have previously used to obtain information about DNA density. A cell proliferation assay based on BrdU and Hoechst 33342 (HXT), which also stochastically labels DNA with the same binding mechanism as DAPI, was demonstrated in vivo [Okk16]. BrdU quenches HXT and reduces its lifetime, thus chromosome density can be investigated. A FLIM-FRET approach to identify chromosome compaction used cells expressing H2B histones stochastically tagged with either EGFP or mCherryFP [Llè09]. If an EGFP-labelled histone is in close proximity to an mCherryFP, it will undergo FRET. Therefore, this approach can also be used to study chromosome densities.

5.3.2 Imaging changes in DNA density

The SIM+FLIM system was applied to study the nanostructure of chromosomes during the cell cycle and to monitor DNA density using FLIM-FRET. For this application, NIH3T3 cells were metabolically labelled with EdU, fixed with PFA, and the EdU was then labelled stochastically via click chemistry (Click-iT, Thermofischer Scientific) with the FRET pair: Alexa-594 and Alexa-647. S-phase cells were imaged to obtain information on two different spatial scales: with ∼120 nm resolution via SIM and with a functional, not spatial, readout below 10 nm via FLIM-FRET. In a second experiment, the same protocol was used to label DNA in NIH3T3 cells but, in addition, acetylated tubulin was labelled with Alexa-488 via antibody staining to visualise the mitotic spindle. The DNA density was obtained with the functional FRET readout, and the mitotic spindle was imaged with the SIM port using two spectral channels (one for the EdU-Alexa-594 and the other for acetylated tubulin-Alexa-488).

The acquisition parameters for the SIM microscope to image the donor Alexa-594 were: excitation wavelength 541 nm, dichroic 561/642 nm and integration time 200 ms (CCD, Retiga R1). For the experiments with the additional Alexa-488 labelling, a two color SIM image was acquired with an additional channel using 488 nm as excitation wavelength with a 488/561 nm dichroic beamsplitter. Five grating angles were used with images acquired for 5 phases at each angle. The emission filter for the FLIM unit was 560/25 nm (centre wavelength/bandwidth), the dichroic 457/514/647 nm and the emission filter 629/62 nm. The GOI gain voltage was 750 V and a 4 ns gate width was used. The camera integration time per time gate was 400 ms with one time gate acquired at the peak intensity, one 3 ns before the peak and 6 gates acquired with logarithmic distribution after the peak intensity.

S-phase cells During S-phase, cells need to replicate various cell organelles, so different genes need to be expressed or suppressed. One dynamic mechanism of the cell to prevent DNA transcription, called chromatin remodeling [Tei09], is to increase DNA density until no transcription factor can bind any more. Therefore, imaging DNA density during s-phase can enable studies of such dynamics.

In Figure 5.8, images of four cell nuclei in S-phase are presented. Two cell nuclei contain dense DNA spots (f) and the other two cell nuclei contain less-dense DNA features (a). The SIM intensity images resolve DNA densities down to 120 nm and present the spatial distribution of the DNA but cannot provide information concerning the DNA structure beyond this resolution limit.

The (intensity-weighted) FLIM image is not able to clearly resolve the separate DNA clusters but the lifetime measurements provide information concerning DNA density on a length scale of ≤ 10 nm, since the donor will have a shorter lifetime if an acceptor is closer than the Förster radius. The sum of both images enables a correlation between the information of two different spatial scales and indicates which DNA clusters present high DNA densities (closed chromatin). The pixel-averaged lifetime of the non-dense DNA (open chromatin) cell is 2215 ps (stdev of 274 ps), compared to 2013 ps (stdev of 295 ps) for the cell with denser DNA (closed chromatin). The dense spots are identified with shorter lifetimes, which substantiates that the brighter spots represent areas in the nucleus with more compact DNA.

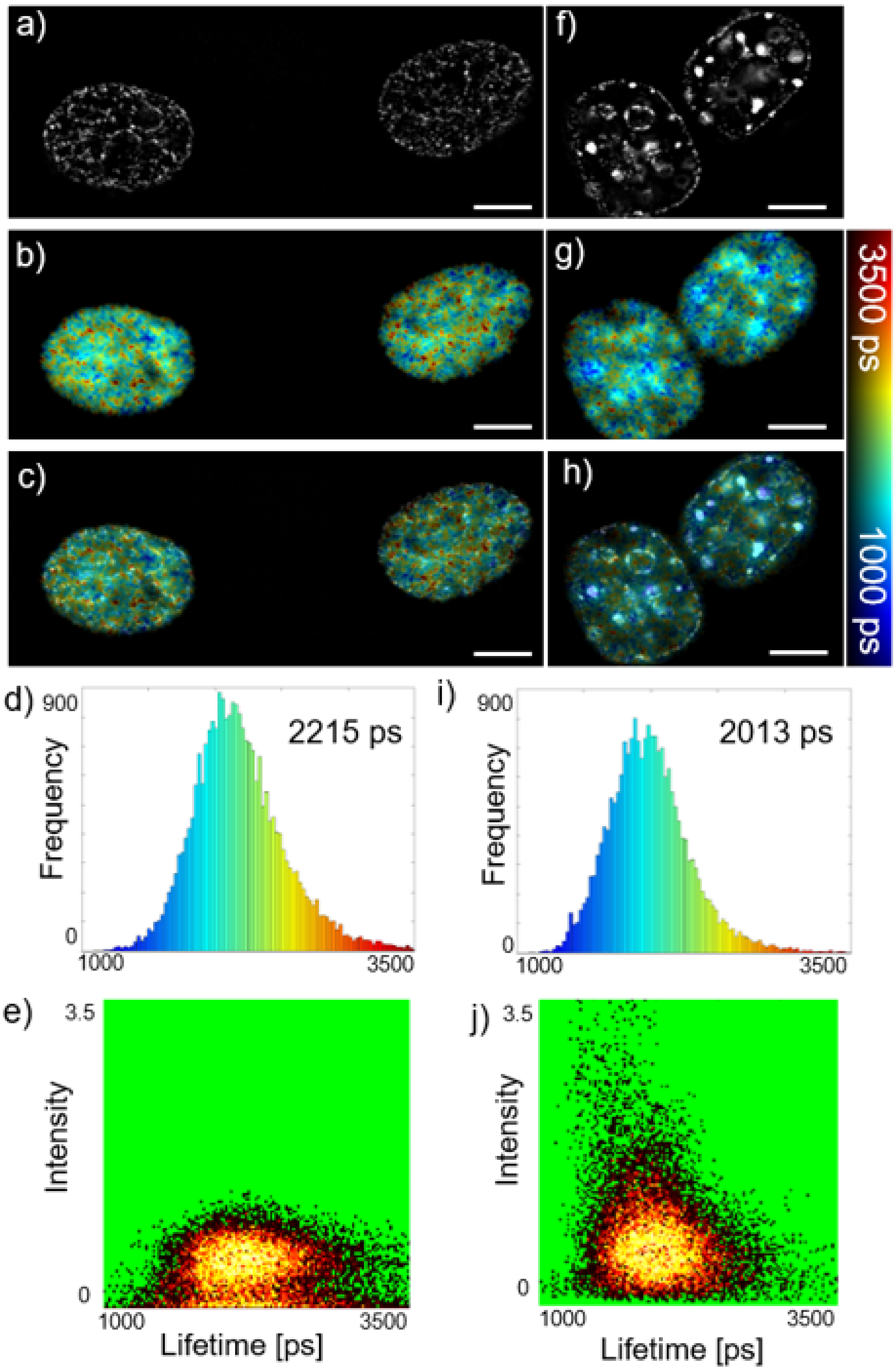
a)
f)
b)
g)
c)
h)
3500 ps
1000 ps
d)
900
Frequency
0
1000
3500
2215 ps
i)
900
Frequency
0
1000
3500
2013 ps
e)
3.5
Intensity
0
1000
3500
Lifetime [ps]
j)
3.5
Intensity
0
1000
3500
Lifetime [ps]

Figure 5.8: *S-phase NIH3T3 cells with less-dense (open) and denser DNA (closed chromatin) imaged with SIM+FLIM. (a-e) show cell with less-dense DNA, the SIM image (a), intensity-weighted FLIM image (b), SIM+FLIM image (c), intensity-weighted lifetime histogram (d) and an intensity versus lifetime scattered plot (e), respectively. (f-j) show corresponding plots for a cell with dense DNA [Gö17a]. Scale bar: 6 µm.*

Mitotic cells The FLIM-FRET signal during mitosis was further investigated and the results suggest that the DNA packing in chromosomes is neither constant nor linearly decreasing during mitosis. These results are in good agreement with previous studies using fluorescence intensity imaging [MB07b]. Figure 5.9 shows two color SIM images and FLIM data of a cell in S-phase and three cells in different stages of mitosis. The SIM images show nanostructures of the DNA labelled via EdU with the Alexa-594 FRET donor and acetylated tubulin using antibody staining with Alexa-488. Acetylated tubulin indicates the mitotic spindle during mitosis while the Alexa-594 fluorescence lifetime reports the chromosome packaging information via FLIM-FRET. Table 5.1 presents the intensity-weighted mean Alexa-594 fluorescence lifetimes for 5 cells in S-phase and 12 cells undergoing mitosis, including those depicted in Figure 5.9.

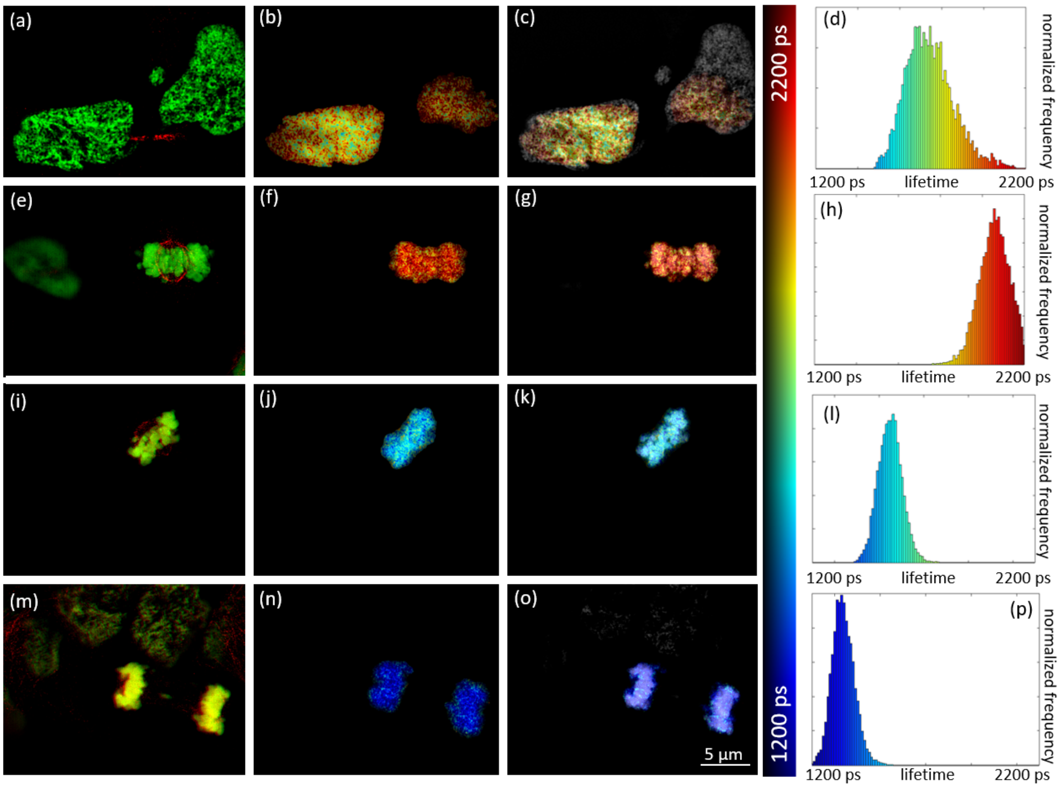

Figure 5.9: *SIM+FLIM of mitotic and S-phase cells. First row: S-phase cell with (a) two color SIM image (green - DNA/EdU-Alexa-594 and red - acetylated tubulin/Alexa-488), (b) FLIM image, (c) SIM+FLIM image and (d) corresponding lifetime histogram. Following three rows: similar plots for three different mitotic cells.*

In S-phase, Figure 5.9 (a) suggests the DNA is homogeneously distributed in the nucleus and the acetylated tubulin channel shows a cilium. During mitosis, the DNA is located in the middle of the mitotic spindle, as presented in Figure 5.9 (e) and (i). In (m) the chromosomes have already moved apart (telophase). The chromosome density, as reported by intensity-weighted lifetime histograms, displays a broader lifetime distribution for the S-phase cell with a stdev of 91 ps (average of 5 cells) than the mitotic cells with a stdev of 59 ps (average of 12 cells), as seen in Table 5.1. This is because during S-phase the nucleus contains regions of high and low gene expression, which leads to both closed and open chromatin. During mitosis, cells do not widely express genes and the majority of chromatin is either open or closed.

	lifetime [ps]	stdev [ps]
s-phase 1 (d)	1740	87
s-phase 2	1717	95
s-phase 3	1695	95
s-phase 4	1729	83
s-phase 5	1625	97
s-phase average	1701	92
mitotic 1 (h)	1886	69
mitotic 2 (l)	1501	55
mitotic 3 (p)	1258	42
mitotic 4	1695	64
mitotic 5	1455	47
mitotic 6	1738	66
mitotic 7	1244	45
mitotic 8	1835	63
mitotic 9	1792	62
mitotic 10	1765	60
mitotic 11	1789	67
mitotic 12	1843	67
mitotic average	1650	59

Table 5.1: *DNA packaging during cell division. Pixel-averaged intensity-weighted lifetime of FRET of s-phase and mitotic cells with standard deviation. Corresponding table to the lifetime histograms of Figure 5.9*

The pixel-averaged lifetime values of the intensity-weighted lifetime histograms for the mitotic cells show a wide fluctuation, with higher and lower lifetimes than for the S-phase cells. These characteristic lifetimes might identify different phases during mitosis, for example (h) → prometaphase or metaphase, (l) → anaphase and (p) → telophase. Summing up 5 S-phase cells and 12 mitotic cells produced the lifetime histograms shown in Figure 5.10. The lifetime histogram to the left is the S-phase histogram, again showing a broad distribution of lifetimes, and the histogram to the right represent the sum of 12 mitotic cells where the histogram could be divided into three characteristic lifetime contributions, which might identify mitotic cell states.

The observation that the DNA density changes during mitosis and that it is changing not monotonically is new and supported by Mora-Bermúdez et al [MB07b] which show similar results measuring the arm lengths of chromosomes with confocal microscopy. However, the number of cells analysed is too small to make a statistically significant conclusion and the allocation of specific lifetimes to mitotic phases is only a hypothesis that requires more experiments to be confirmed.

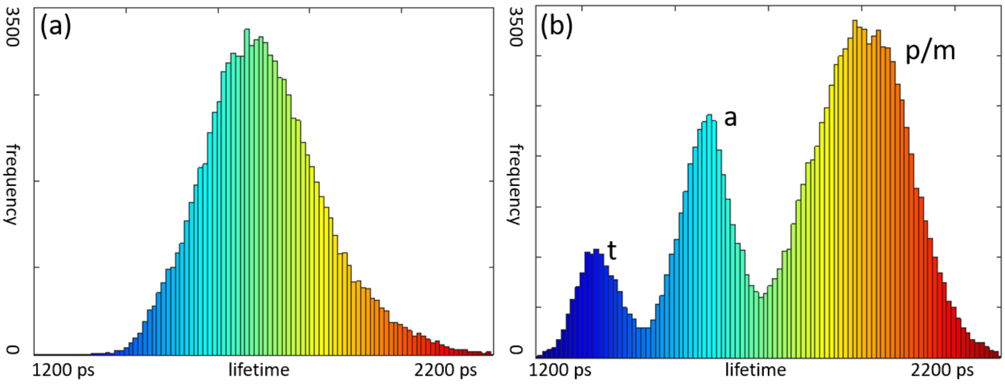

Figure 5.10: *Intensity-weighted Alexa 594 (FRET donor) lifetime histogram for cells in different stages during cell division, showing data for 5 S-phase cells (a) and for 10 mitotic cells (b) with the suggested allocation of mitotic states (p/m → prometa/metaphase, a → anaphase and t → telophase).*

5.3.3 Imaging open and closed chromatin by labelling histones

Another way to obtain information of gene packaging in the nucleus is by labelling histones. Each nucleosome consists of two duplicates of four histones (H2A, H2B, H3 and H4) around which DNA is wrapped. The nucleosomes are subunits of chromatin. In an open configuration, chromatin contain acetyl groups that prevent neighbouring histones from converging in order to allow enough space for transcription factors to bind and express genes. Closed chromatin is denser, due to the lack of acetyl groups, and gene expression is inhibited. The drug Trichostatin A (TSA) blocks histone deacetylase, which removes acetyl groups from histones and so samples treated with TSA contain predominantly acetylated H2B, i.e. open chromatin, as illustrated in Figure 5.11.

FRET can reveal closed and open chromatin, enabled by stochastic labelling of a specific histone with a donor and an acceptor fluorophore. This approach was implemented in previous FLIM-FRET studies by expressing Histone 2B (H2B) with GFP or mCherry [Llè09]. Open chromatin is indicated by a higher donor lifetime than closed chromatin, due to the greater average distance between donor and acceptor. The experiment presented here follows a similar approach, expressing a

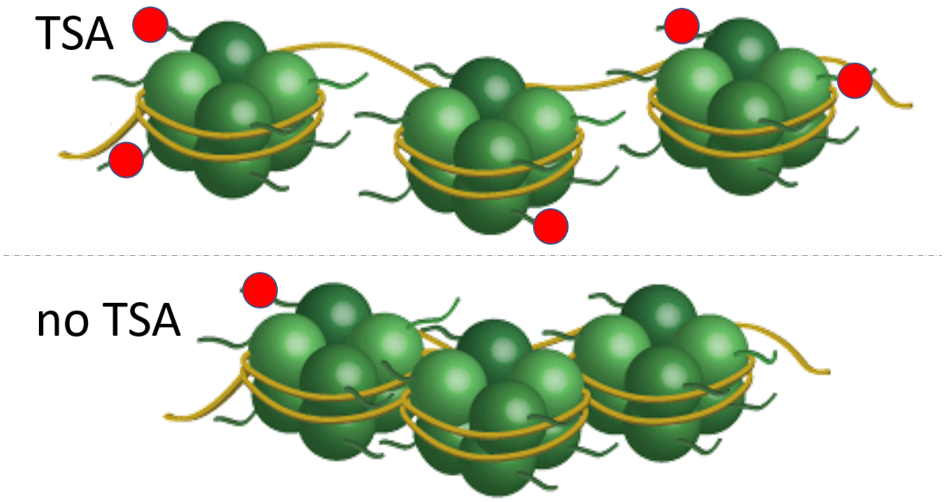

Figure 5.11: *Histone acetylation with and without TSA treatment. Upper scheme: open chromatin introduced by TSA, lower scheme: closed chromatin without TSA treatment. Green nucleosomes, yellow DNA, red circles acetyl group. Adapted from [Inc17].*

H2B-SNAP-tag vector labelled stochastically with Alexa-594 or Alexa-647. A four-hour treatment with TSA was applied in two different concentrations (1 μMol and 100 nMol) and compared to two negative controls: donor-only (Alexa-594) labelling and an untreated sample. The lifetimes measured under the different conditions are presented in Table 5.2. The donor-only negative control reports the longest lifetime, because no FRET is possible. The sample labelled with both FRET donor and acceptor, without TSA treatment, presents the lowest intensity-weighted cell-averaged lifetime because it contained open and closed chromatin at the same time. The TSA treated cells show a drug response with increasing lifetimes for higher drug concentration. In TSA treated cells open chromatin is the dominate state in the nucleus, which leads to an increase in lifetime.

	lifetime [ps]	stdev [ps]
donor only with no treatment	3774	52
FRET with no treatment	2779	138
FRET, treatment 100 $nMol$	2941	117
FRET, treatment 1 μMol	3090	126

Table 5.2: *Intensity-weighted cell-averaged lifetimes (with standard deviation for 6 repeats) measured for H2B labelled with FRET donor-only or FRET donor and acceptor in presence of TSA.*

5.4 SIM+FLIM of interactions between organelles (Golgi apparatus and ciliary rootlets)

The ability of the SIM+FLIM microscope to image nanostructure and read out FRET may be useful to study the relationships between different cell organelles. In biological studies, interactions between cell organelles are often inferred from colocalisation of proteins, as determined using confocal fluorescence microscopy [Zin01]. This established method, however, cannot provide information about molecular interactions below the ~240 nm resolution limit of confocal microscopy, noting that molecular interactions can occur with ranges under 10 nm. The SIM+FLIM approach can provide colocalisation data down to 120 nm resolution using the SIM port and elucidate molecular interactions via FLIM-FRET. In this section, a brief biological introduction to the centrosome and the ciliary rootlet is followed by a description of SIM+FLIM FRET experiments, including a control experiment to validate the application of SIM+FLIM to colocalise proteins in cell organelles and an experiment to investigate proximity of the Golgi apparatus and ciliary rootlets.

5.4.1 Biological background

Mammalian cells contain a microtubule organizing centre called the centrosome, which consists of two centrioles with barrel-like structures. The centrosome influences microtubule processes such as organelle transport, adhesion, cell shape and division [Dox05]. During S-phase, the cell duplicates the centrioles. The doublets function as a single, independent centriole pair until the beginning of

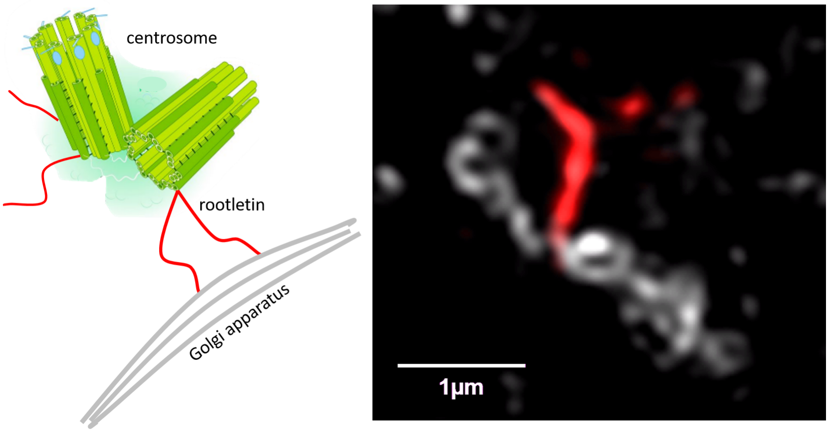

Figure 5.12: *Left: Scheme of the hypothetical constellation of centrosome (green), rootletin (red) and Golgi apparatus (grey), adapted from [Sch15]. Right: Two color SIM image of the rootletin (CROCC, red) and the Golgi apparatus (Gorasp2, grey).*

cell division [Slu05]. During mitosis, the centrosomes form two poles of the mitotic spindle.

Rootletin, or CROCC (ciliary rootlet coiled-coil), is the major structural component of the ciliary rootlet [Yan02]. It is also part of the intercentriolar linker structure and important for the centrosome cohesion. Bahe et al [Bah05] suggested that rootletin might be involved in the anchoring of the centrosome to an underlying matrix, which might be the Golgi apparatus, see Figure 5.12.

5.4.2 Control FLIM-FRET measurements of interacting organelles

A known interacting protein pair in the Golgi apparatus was chosen to test the SIM+FLIM FRET system applied to cell organelles. The Golgi reassembly stacking protein, Gorasp2, and the cis-Golgi membrane protein, GM130, have been proposed to colocalise with evidenced by fluorescence microscopy [Vin11].

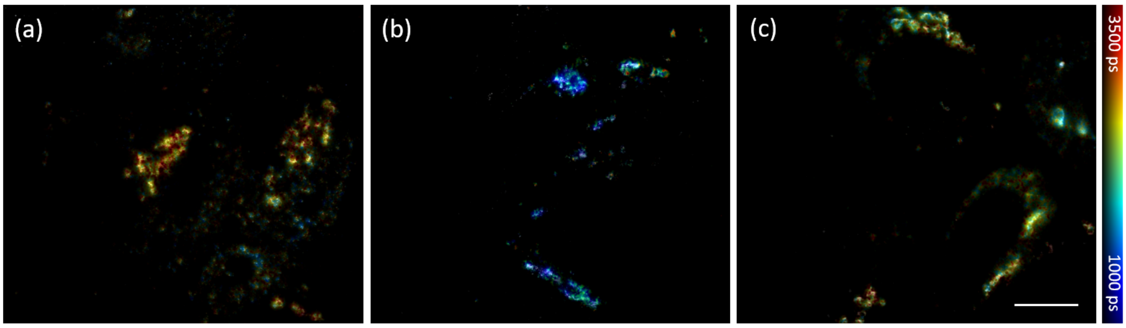

Figure 5.13: *SIM+FLIM images of Golgi apparatus protein interaction. SIM+FLIM experiment where Gorasp2 is labelled with a FRET donor and GM130 with the corresponding acceptor. (a) positive control: Gorasp2 stained with the donor only, (b) negative control: Gorasp2 stained with donor and acceptor simultaneously and (c) Gorasp2 labelled with the donor and GM130 with the acceptor. Scale bar: 5 μm.*

Here, three different samples were prepared with the FRET pair Alexa-594 and Alexa-647: a negative control (antibody Gorasp2 Alexa-594); a positive control (antibody Gorasp2 stochastic labelled with Alexa-594 and Alexa-647 using polyclonal antibodies); and a third condition prepared with an antibody against Gorasp2 (Alexa-594) and an antibody against GM130 (Alexa-647). The image acquisition parameters were the same as those used in section 5.3. The FLIM data was fitted pixelwise to a mono-exponential decay model using *FLIMfit*. The results are summarised in Figure 5.13 and Table 5.3. The negative control presents an intensity-weighted pixel-averaged lifetime of 2682 ps corresponding to the donor lifetime. A strong FRET signal is obtained in the positive control, with a reduced pixel-averaged lifetime of 1535 ps. The pixel-averaged lifetime of the interaction experiment, 2362 ps, shows a significant difference to the negative control, confirming the interaction of Gorasp2 and the cis-Golgi membrane protein, GM130.

	lifetime [ps]	stdec [ps]
Negative (donor only) control	2682	125
positive FRET control	1535	58
Gorasp2-Alexa 594 FRET with GM130-Alexa 647	2362	48

Table 5.3: *Donor fluorescence lifetime data corresponding to Figure 5.13 for study of intermolecular FRET between Gorasp2 and GM130: Pixel-averaged lifetime in ps for the negative and positive controls and the FRET experiment with Gorasp2 and GM130 with standard deviations calculated over 5 FOV.*

5.4.3 SIM+FLIM of molecular interactions between Golgi apparatus and ciliary rootlets

The SIM+FLIM was applied to explore interactions between the Golgi apparatus and rootletin. The former was labelled with a Gorasp2 antibody (Alexa-647) and the ciliary rootlet with a CROCC antibody (Alexa-594). Figure 5.12 shows the resulting SIM image but this does not report molecular interactions, specifically the limited resolution does not confirm that the rootletin is in direct contact with the Golgi apparatus. This was investigated using the FLIM port to read out FRET between the Golgi protein Gorasp2 and the ciliary rootlet protein CROCC, using the CROCC SIM image as a mask to identify potentially FRETing and non-FRETing regions.

As presented in Figure 5.14, the pixel-averaged lifetime of the non-masked region was 2758 ps (stdev 242 ps), which is not significantly different from the pixel-averaged lifetime of the CROCC masked area (2900 ps, stdev 221 ps). There are several possibilities to explain this outcome. First, there may be no interaction between these two organelles. Another possibility is that the contact proteins are not Gorasp2 and GM130 but other proteins in the Golgi apparatus and the ciliary rootlet. Other techniques such as fluorescence cross-correlation spectroscopy or immunoprecipitation could be used to explore whether there is an interaction between these proteins. It is also possible that the interaction area was too small to be isolated and the FRET signal was not significant against the background. A further possibility is that the spacing of donor and acceptor fluorophores was outside the FRET range ($\leq$ 10 nm). Finally, there are possible biological explanations as to why no interaction was observed. For example, it is possible that only a small fraction of the proteins interacts, or that the interaction was only established during specific times, such as at a certain point in the cell cycle, or during cell movement.

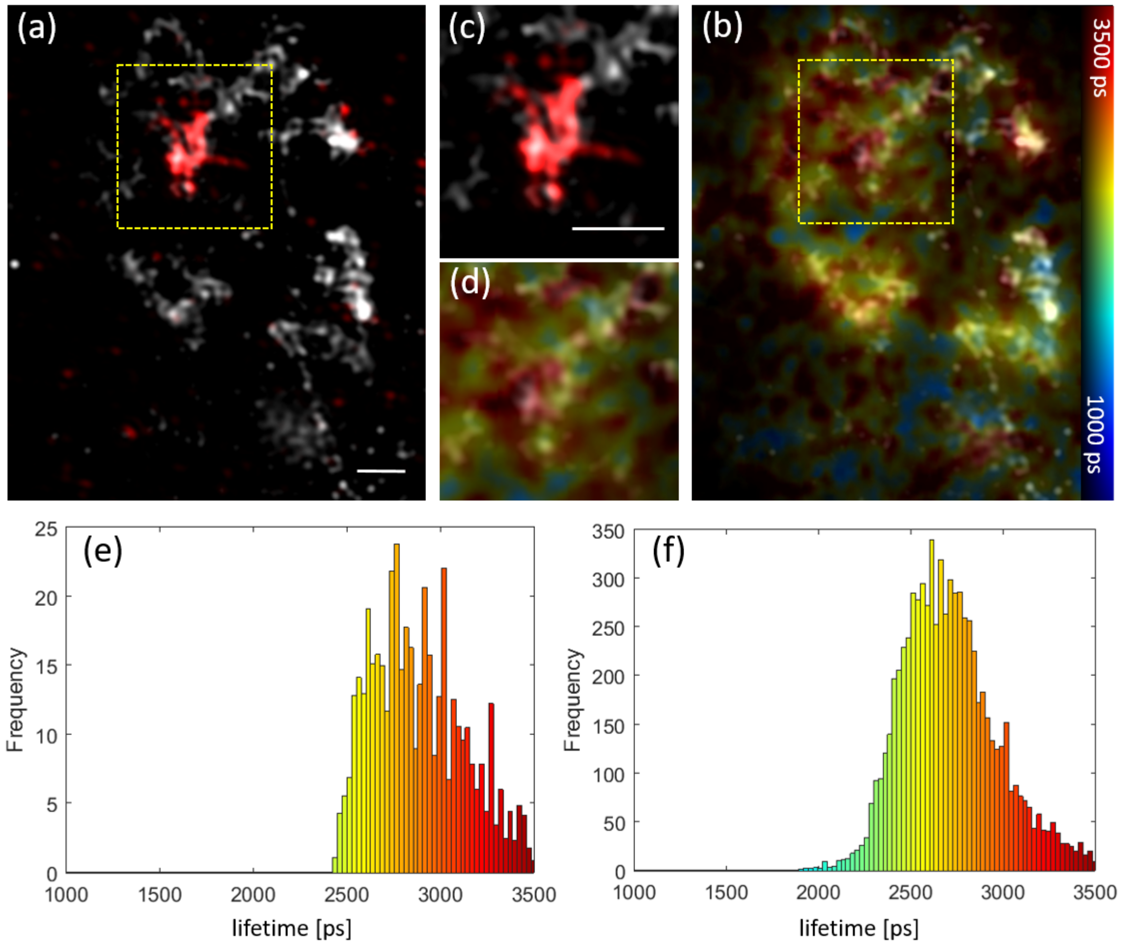
(a)
(c)
(b)
(d)
3500 ps
1000 ps
(e)
Frequency
lifetime [ps]
0
5
10
15
20
25
1000
1500
2000
2500
3000
3500
(f)
0
50
100
150
200
250
300
350

Figure 5.14: *SIM+FLIM images of Golgi apparatus and rootletin. (a) two color SIM image of the Golgi apparatus (grey) and CROCC (red), (b) corresponding SIM+FLIM image, (c) region of interest (ROI) of potential interaction in two color SIM, and (d) SIM+FLIM image of this ROI, (f,g) intensity-weighted lifetime histograms corresponding to (d,b) respectively. Scale bar: 1* μm.

5.5 Summary

Summary The parallel implementation of SIM and FLIM on a common microscope to provide super-resolved images using SIM and functional readouts, e.g. using FLIM-FRET, is described in this chapter. The set-up consists of a commercial SIM microscope (Elyra.S1, Carl Zeiss) and an in-house developed FLIM unit.

To evaluate the performance of the system, technical reference samples and biological samples were imaged: a fluorescence dye to validate the FLIM capability, multispectral beads to register the images from the two different modalities (ports) and a convallaria sample to demonstrated the application to complex biological structures.

The application of the SIM+FLIM instrument to document genomic structures was then demonstrated by imaging open and closed chromatin using several experimental strategies utilising the stochastic labelling of DNA or Histone 2B with a FRET pair. The application to study a pharmacological drug response was demonstrated using the histone deacetylase inhibitor, TSA.

Finally, the application of SIM+FLIM to molecular interactions between the Golgi apparatus and centrosomal rootletin was explored. Despite satisfactory results with control samples, no interaction between the Golgi apparatus and CROCC in the ciliary rootlet was observed using FRET. Further studies applying SIM+FLIM to more proteins in the Golgi apparatus and the ciliary rootlet would be useful to explore this potential interaction.

Contribution The FLIM unit was built by me and I adapted the open FLIM HCA software discussed in chapter 3 to be compatible with the new equipment. I imaged and analysed the data from the technical samples and contributed to the design of the experiments to image the DNA density in chromatin. Dr. Edwin Garcia prepared the samples for the DNA and chromatin experiments and helped me image the cells. The sample preparation for the Golgi/CROCC experiments was done by Dr. Robert Mahen and we imaged the cells together. I undertook the analysis of the cell images.

Chapter 6

Application of FLIM and SIM to study activation of the discoidin domain receptor (DDR1)

This chapter reports a series of experiments where FLIM or SIM+FLIM was applied to study the activation of the discoidin domain receptor (DDR1) in COS-7 cells by collagen through the oligomerisation of the DDR1 receptor, which can be read out using FRET. Labelling the DDR1 receptors is an essential component to such studies, for which a variety of techniques is available, including fluorescent proteins, antibody labelling and SNAP-tags. In general, super-resolution microscopy (SRM) requires specific fluorophore properties, e.g. photoswitching (or "blinking") for single molecule localisation microscopy techniques such as PALM, STORM or RESOLFT. Because SRM techniques require a higher number of detected photons than conventional microscopy, they require bright, stable fluorophores with low photobleaching. In general, SIM is the least demanding of the SRM techniques and might be expected to work with the same labelling strategies that work for FLIM.

Here, the performance of labelling with fluorescent proteins (FP), with antibody conjugated dyes and with SNAP-tags conjugated dyes is explored to image DDR1 aggregation with SIM and FLIM-FRET. SNAP-tags conjugated dyes were found to be superior to fluorescent proteins and antibody labelling, in terms of a more significant change in donor lifetime for FRET readouts, higher labelling specificity, better target accessibility and applicability to more sophisticated labelling strategies.

6.1 Biological background

DDR1 is a member of the receptor tyrosine kinase (RTK) family, which is a group of important regulators of the cell cycle, cell differentiation, cell survival and cell migration. All RTKs contain a tyrosine kinase domain that, upon activation, catalyses the phosphorylation of tyrosine residues contained within the receptor and on signalling molecules [Lem10]. There are 58 different human RTKs. DDR1 and DDR2 are two members of the DDR family that differ from other RTKs in three main aspects: they are stimulated by collagen [Xu14, Vog97, Shr97], which is a fundamental protein in the extracellular matrix; their activation mechanism is slow compared to other RTKs, noting that DDR1 can stay activated for days [Vog97, Shr97], and in the absence of a ligand, DDR1 occurs in non-covalent dimers, whereas most RTKs only dimerise upon ligand binding [Mih09]. A variety of diseases are associated with dysregulation of DDR1 including atherosclerosis, arthritis, organ fibrosis and many types of cancer [Lei11, Lei14, Val12]. A DDR1 monomer contains two extracellular domains, a discoidin (DS) domain and a DS-like domain [Lei03]. The binding site for collagen is located on the DS domain. The transmembrane region is followed by a long juxtamembrane domain, which is linked to the kinase domain, as shown in Figure 6.1. The activation mechanism is not completely understood but DDR1 activation by collagen triggers further processes in the cell via DDR1 autophosphorylation. It is thought that oligomerisation, stimulated by collagen, is involved in the activation of DDR1. Aggregation processes are particularly amenable to FRET studies [Raj01, Mih09], because the distances between monomers, which can be stochastically labelled with donor and acceptor fluorophores, become comparable to the Förster distance for many fluorophores upon aggregation. Thus, information about the aggregation state can be obtained through readouts of the FRET efficiency or donor fluorescence lifetime. In the case of DDR1, which occurs in dimers both before activation and after subsequent aggregation, the stochastic labelling of the DDR1 monomers in each dimer reduces the contrast for FRET readouts because FRET can already occur in the dimers before activation [Mih09]. However, the FRET signal will increase upon further aggregation because the donors will have more acceptors to which energy can be transferred. Thus, FRET can be utilised to read out the aggregation state following activation.

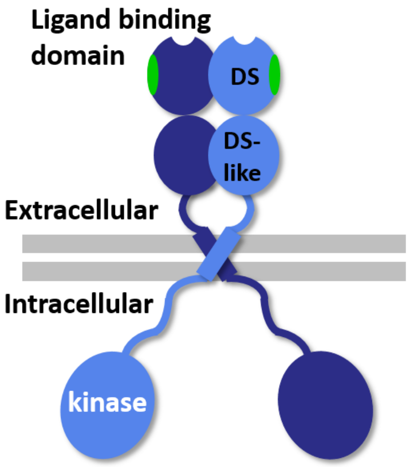

Figure 6.1: *Schematic of DDR1 protein structure. Adapted from [Gö17a].*

6.2 Introduction to the SNAP-tag labelling technique

In cell biology, techniques were developed to visualize proteins in living cells. A common method to tag proteins are fluorescent proteins, for example GFP or YFP. Although this technique is well established the photo-physics of fluorescent proteins are generally not applicable for light sensitive experiments such as single-molecule measurements, due to the low quantum efficiency and low photo-stability. For such applications fluorescent dyes are necessary with superior photo-physical properties. To utilize them, fluorescent dyes are commonly conjugated to antibodies which bind to the protein of interest. However, antibody labelling is limited to fixed, immobilized cells [Spe17].

The SNAP-protein is a derivate of a mammalian cell enzyme, which was engineered to be inactive [Jui03]. Such as GFP, the SNAP-protein can be incorporated into proteins without interfering with their functionality. To visualise the SNAP-protein, and with it the target protein, an amino group (BG-NH_2) is linked to a fluorescent dye, called SNAP-tag. The SNAP-tag covalently binds to the SNAP-protein and forms a fluorescent marker, as shown in Figure 6.2, which contains the superior photo-physical properties of fluorescent dyes and which is suitable for live cell imaging such as fluorescent proteins [Tho17b].

The SNAP-tag approach belongs to the self-labelling methods together with HaloTag and Cliptag. Due to their versatility these techniques are of increasing interest. They are usable for a wide range of specialised imaging approaches such as confocal fluorescence microscopy, super-resolution microscopy and transmission electron microscopy. SNAP-tag labeling was demonstrated with FRET measurements of oligomerization [Mau08] and it is also suitable for correlative light and electron microscopy, where only a few labelling techniques are applicable [Lis15].

6.3 Comparison of FLIM HCA using fluorescence protein and SNAP-tag labelling approaches

This section reports a comparison of the readout of DDR1 aggregation via FLIM-FRET labelled with a fluorescent protein FRET pair, EGFP and mCherry, and with a dye FRET pair, Alexa-488 and Alexa-546 introduced via SNAP-tags. Vectors encoding DDR1 with EGFP or mCherry fused to the kinase domain were obtained and expressed in COS-7 cells with a plasmid weight ratio of 1:1. DDR1 forms dimers inside the cell and they then travel to the cell membrane. Therefore, for cells expressing DDR1 labelled with EGFP or mCherry, there is a high background signal coming from inside the cell of nonfunctional labelled DDR1 proteins that are not exposed to the ligand (collagen). To reduce the nonspecific background David Corcoran incorporated a SNAP protein into DDR1, as shown in Figure 6.2. Using non-membrane permeable SNAP-tag dye substrates enable labelling of only the DDR1 that has inserted into the cell membrane and therefore has the SNAP domain located outside the cell membrane. For detailed information about the labelling procedures, please refer to section 9.4. The change in donor lifetime was compared for the fluorescence protein and SNAP-tag approaches, and the dynamic range of the fluorescence lifetime readout was investigated. Further studies were undertaken to compare the relative aggregation of different DDR1 mutants and a more sophisticated labelling approach to

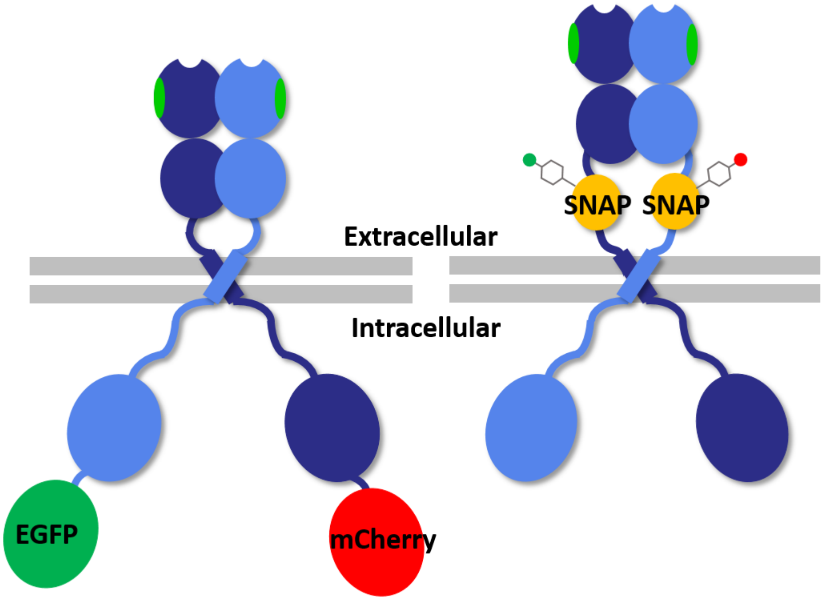

Figure 6.2: *DDR1 labelling approaches with fluorescence proteins (left) and SNAP-tags (right). Two separate DDR1 molecules are shown in pale and dark blue. The extracellular domain contains binding sections to other DDR1s (green) and to collagen (white "bites"). Adapted from [Gö17a].*

label each DDR1 dimer with either only donors or only acceptors was tested. These experiments were undertaken with fixed COS-7 cells using the open FLIM-HCA system presented in chapter 3. The filter sets used for imaging the donor of EGFP/mCherry and Alexa-488/Alexa-546 FRET pairs were identical (excitation bandpass (centre/bandwidth) 465/30 nm, dichroic double bandpass with centres at 488 nm and 561 nm, emission bandpass 520/35 nm). The camera integration times ranged between 200 ms and 400 ms and the GOI time-gate width was set to 4 ns with a GOI gain voltage of 750 V. The donor fluorescence decay profiles were sampled with 8 time-gates, one at the intensity peak, one 3 ns before the intensity peak and the remaining 6 logarithmically spaced until 16.5 ns after the intensity peak. The multiwell plate FLIM data were analysed using *FLIMfit* with a spatially varying IRF, an IRF shift value obtained via a reference dye measurement (Coumarin 6), a constant camera background subtracted from the acquired images and a time varying background, acquired from an empty well containing the same buffer media as the cells, subtracted from the acquired decay profiles. The cells were segmented in *FLIMfit* before pixel-wise fitting to a mono-exponential decay model.

6.3.1 Comparison of FRET signals

The FRET donor lifetime change upon DDR1 activation after collagen stimulation was compared for COS-7 cells either expressing DDR1 stochastically tagged with EGFP and mCherry or DDR1 with SNAP-tags inserted within DDR1 that were stochastically conjugated with Alexa-488 and Alexa-546. Separate 96-well plates were prepared for each experiment. The FP plate contained a column without collagen stimulation and 8 columns fixed at different time points after collagen stimulation (5 min, 10 min, 15 min, 20 min, 25 min, 30 min, 45 min and 60 min). In total, 32 FOVs were imaged (4 FOVs per well in 8 rows). The SNAP-tag plate consisted of a column without collagen stimulation and 5 columns fixed 5 min, 10 min, 15 min, 30 min and 60 min after collagen stimulation. For each condition, 3 replicate wells were imaged and 4 FOVs were acquired per well (12 FOVs in total). The results, shown in Figure 6.3, present a decrease in donor lifetime of ∼40 ps for the FP approach and ∼150 ps for the SNAP-tag-dye approach. This difference may be due to a higher FRETing efficiency for the dye-based labels or to a higher labelling specificity of the dyes (see subsection 6.3.3). This difference is significant, since the lifetime variation due to biological factors (e.g. variation in FP expression/maturation, variation in background from autofluorescence) is typically at least 20 ps and instrumentation and plating uncertainties can be comparable. A 150 ps change in donor lifetime is therefore a much more robust readout and is more accessible to detect.

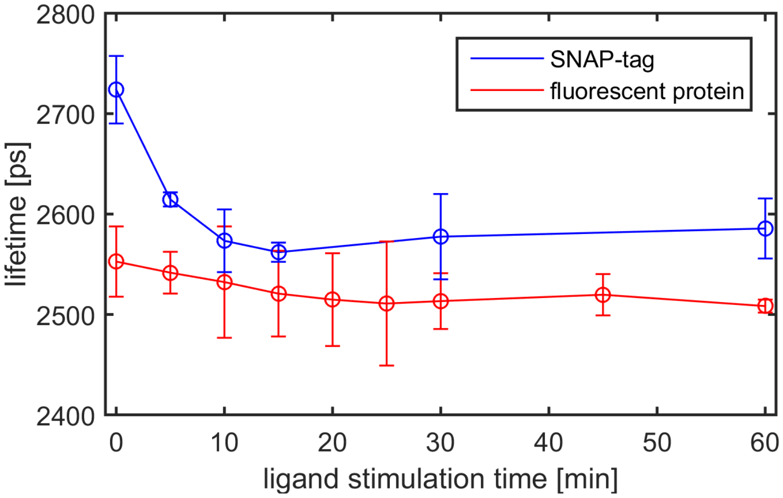

Figure 6.3: *Donor fluorescence lifetime change over time after stimulation with collagen for COS-7 cells expressing DDR1 labelled with either fluorescent protein or SNAP-tag FRET constructs. The decrease in donor lifetime reports increased aggregation state of DDR1. Error bars indicate standard error per cell.*

6.3.2 FLIM HCA of DDR1 mutants to study DDR1 activation mechanism

This section reports preliminary results from an unpublished study[1] undertaken with the laboratory of Prof. Birgit Leitinger that aimed to explore the mechanism of DDR1 activation through the analysis of two mutant DDR1 constructs. A 96-well plate was prepared with three rows of COS-7 cells expressing TM1 mutants and three rows expressing ECTM mutants, each fixed 10 min, 20 min and 30 min after collagen stimulation. A further column contained cells expressing both mutants that were not stimulated with collagen.

The TM1 construct encodes DDR1 with mutations in the transmembrane domain that results in a weakened interaction between the transmembrane domains. Two TM1 constructs were used with either EGFP or mCherry fused to the kinase domains. From wide-field microscopy studies, no DDR1 aggregation or phosphorylation is expected with collagen stimulation for this mutation. The ECTM (Extracellular and TransMembrane) mutant lacks the entire intracellular region except for six amino acids. Two variations of this ECTM mutation were constructed with either EGFP or mCherry fused on the intracellular side of the receptor. Former studies indicate that this ECTM mutant expressed in cells binds to collagen and undergoes some kind of aggregation (Leitinger unpublished), although there cannot be any DDR1 phosphorylation because the kinase domain is missing.

---

[1] Effective first of November 2017

The TM1 mutation presents a much smaller decrease in EGFP donor lifetime (∼20 ps), as shown in Figure 6.4 (a), supporting the hypothesis that there is little aggregation following collagen stimulation or at least that it is heavily disrupted. This suggests the aggregation process is dependent on the transmembrane interaction between DDR1 monomers. Figure 6.4 (a) presents a more significant decrease (∼30 ps) in the donor lifetime of the ECTM expressing cells with collagen stimulation. These results suggest DDR1 aggregation is mediated by the extracellular and transmembrane regions and not by the intracellular regions.

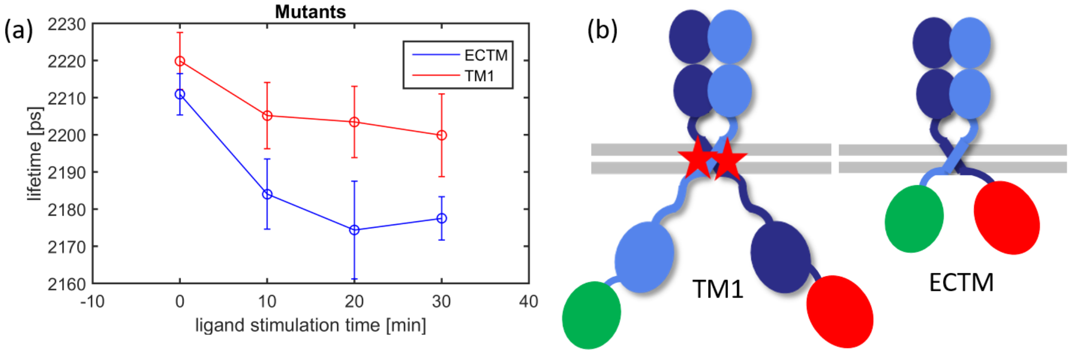

Figure 6.4: *Collagen response of DDR1 mutants. (a) graph with lifetime for different time points after collagen stimulation for TM1 and ECTM and (b) TM1 and ECTM mutant sketches. In the TM1 mutant, the star denotes a mutation to the transmembrane domain that reduces the interaction between the protein pair. In the ECTM mutant lacks the intracellular domain except for 6 amino acids. Adapted from [Gö17a].*

6.3.3 Specificity of labelling approaches

A significant difference between the FP and the SNAP-tag approaches to label DDR1 is the specificity of labelling. For the FP method, DDR1 fused to a FP is produced within the cell, and a proportion of these DDR1 molecules are trafficked to the cell membrane. At the cell membrane, the collagen binding domain is extracellular, as shown in Figure 6.2, and accessible to collagen. The intracellular pools of DDR1 are not accessible to collagen, and as such produce a "background" FRET level which is measured together with the FRET signal from DDR1 aggregating at the cell membrane due to collagen stimulation. Even when optically sectioning using the spinning Nipkow disk, this background presents a significant background that makes it difficult to read out the signal from the aggregating DDR1 on the cell surface. Conversely, the SNAP-tag approach utilises cell-membrane impermeable SNAP-tag reagents containing the fluorescence markers (Alexa-488 and Alexa-546) and therefore only the DDR1 proteins on the cell surface are labelled and contribute to the FRET readout.

Figure 6.5 shows a further comparison of COS- 7 cells labelled with EGFP/mCherry and SNAP-tag-Alexa-488/Alexa-546 with and without stimulation imaged under equal conditions described in section 6.3. For each condition 10 FOVs were acquired, analysed and the combined data is shown in the histograms of Figure 6.5, and the first FOV is displayed as an intensity-weighted lifetime image. The intensity-weighted lifetime histograms show a smaller shift between unstimulated DDR1 and stimulated DDR1 for the FP-labelling method (b,d) compared to the SNAP-tag labelling technique (f,h).

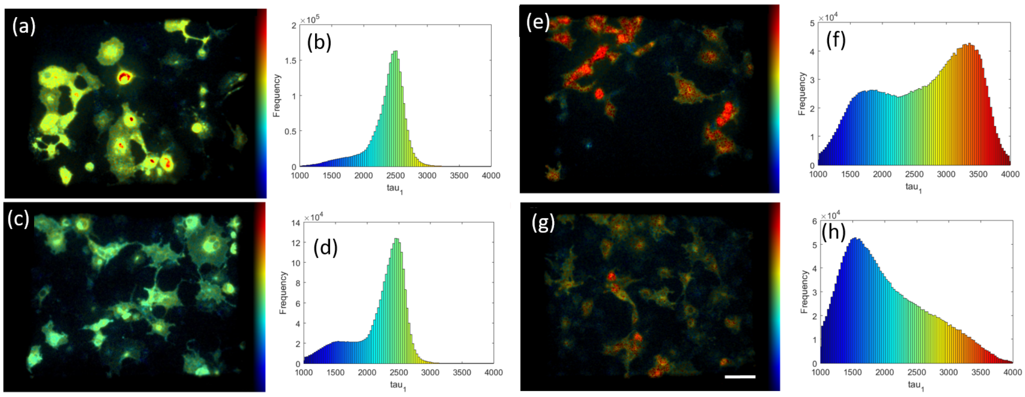

Figure 6.5: *Fluorescence lifetime images of COS-7 cells transfected with FRET constructs encoding DDR1 with fluorescent proteins or SNAP-tag conjugated dyes. (a)-(d) show the FP-labelled cells (EGFP, mCherry). (a) intensity-weighted lifetime image of unstimulated cells and (c) cells 60 min after collagen stimulation with the respective intensity-weighted lifetime histograms in (b) and in (d); (e)-(h) present the SNAP-tag-labelling approach (Alexa-488, Alexa-546) with (e) showing unstimulated cells and (g) showing cells 60 min after stimulated cells. (f) and (h) show the corresponding intensity-weighted lifetime histograms. Scale bar: 6* μ*m.*

The intensity-weighted lifetime histogram for the SNAP-tag approach clearly indicates two lifetime populations for unstimulated cells (f). These two lifetime populations are due to the presence of hetero- and homodimers resulting from the stochastic labelling technique (see also hetero-labelling in subsection 6.3.4). The longer lifetime population corresponds to the donor only dimers, whereas the shorter lifetime population corresponds to dimers labelled with both donor and acceptor. In stimulated cells (h), the longer lifetime population is extremely reduced because all labelled donor-only dimers are at the cell membrane and almost all of them undergo FRET due to their activation by extracellular collagen. This pronounced reduction of the longer lifetime population is not apparent with the FP approach, because of the background signal from the intracellular fluorescence of the DDR1 which is not exposed to collagen and therefore not activated.

6.3.4 Alternative labelling approaches to enhance FRET contrast for DDR1 aggregation

Although the SNAP-tag labelling approach provides a greater lifetime shift upon aggregation of the DDR1 dimers compared to FP labelling, the change in measured FRET efficiency and lifetime is still compromised for both the FP and SNAP-tag labelling approaches by the intradimer FRET that arises as a consequence of the stochastic labelling producing heterodimers, as illustrated in Figure 6.6 (a), which shows the three possible dimer configurations: 50% of the stochastically labelled dimers will occur as donor-acceptor heterodimers and present a reduced donor lifetime before stimulation, while 25% will occur as donor-donor homodimers and 25% as acceptor-acceptor homodimers.

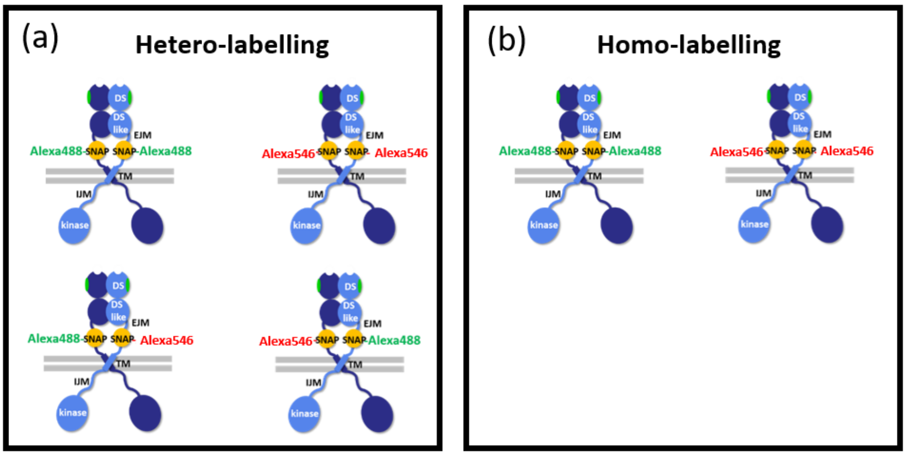

Figure 6.6: *(a) heterodimer and (b) homodimer configurations of labelled DDR1. Adapted from [Gö17a].*

The FRET contrast upon DDR1 dimer aggregation could be enhanced if the DDR1 could be labelled such that only homo-dimers are present. This can be realised with the SNAP-tag labelling by first labelling the dimers with, e.g. the acceptor only, to produces only acceptor-acceptor homodimers on the cell surface. To ensure that all DDR1 monomers are labelled with an acceptor at this point, the cells should then be saturated with the acceptor dye (Alexa-546) or non-fluorescent tags should be used to block further labelling of free SNAP-tag proteins on the cell surface. The next step is to wait until sufficient new DDR1 dimers are trafficked to the cell surface and then apply a second labelling step with only the donor dye (Alexa-488) that would label only the DDR1 newly available at the cell surface, leading to donor-donor homodimers. The existing acceptor-acceptor homodimers would not be affected by the second labelling step as they are all already bound to Alexa-546. At this point, only acceptor-acceptor and donor-donor homodimers should be present at the cell surface, as shown in Figure 6.6 (b). More details about the labelling strategies for homo- and hetero-labelling can be found under section 9.4.

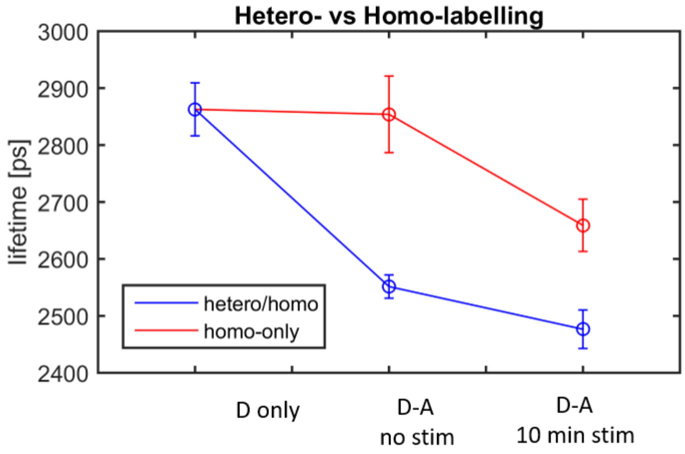

Figure 6.7: *Comparison of donor lifetimes with stdev observed for DDR1 labelled with SNAP-tags conjugated to Alexa-488 (donor) or Alexa-546 (acceptor) with either donor labelling donor only (D only), stochastically labelling mixtures of heterodimers and homodimers or labelling only homodimers. Data is plotted for lifetime measurements of cells expressing donor only (D-only), unstimulated cells expressing both donor and acceptor (D-A no stim) cells and cells expressing both donor and acceptor measured 10 min after collagen stimulation (D-A 10 min stim). Error bars show the standard deviation over cells.*

A 96-well plate of fixed cells was prepared, which contained one well with a donor-only labelling (Alexa-488), two wells with DDR1 dimers labelled as heterodimers and homodimers (unstimulated and 10 min stimulated with collagen) and two wells with DDR1 homodimer only labelling approach (unstimulated and fixed 10 min after stimulation with collagen). As shown in Figure 6.7, there is a lifetime difference in the stochastically labelled approach between donor only (D only) and unstimulated cells expressing donor-acceptor (D-A), which is not due to DDR1 aggregation and which reduces the lifetime shift of the DDR1 aggregation assay. For these cells fixed 10 min after collagen stimulation, the FRETing donor lifetime is shorter than before stimulation, as a consequence of the aggregation of the DDR1 dimers, but the change in lifetime is smaller compared to the change between D-only and D-A unstimulated. In contrast, for the cells with only labelled homodimers, there is no donor lifetime difference between D-only and D-A unstimulated cells, indicating the effectiveness of this labelling strategy, and the lifetime decrease upon collagen stimulation is larger than for the stochastic labelling case. These observations improve the performance of this assay for DDR1 aggregation and support the hypothesis of collagen-induced aggregation of DDR1 dimers, noting that the interactions between DDR1 monomers at the cell membrane would be expected to produce a lifetime change in the homodimer labelling experiment between the D-only and D-A unstimulated cells.

6.4 Evaluation of labelling approaches for SIM of DDR1 activation

SIM has also been applied to study the activation of DDR1 by collagen simulation and this section presents results obtained using antibodies and SNAP-tags as labelling approaches. The activation of DDR1 is not fully understood and the final oligomeric state of aggregated and activated DDR1 is not known but it has been suggested that aggregation of DDR1 dimers is necessary before phosphorylation can occur on the intracellular side of the membrane. Antibodies against the extracellular domain can be used to label DDR1 and image its aggregation. To observe the binding of collagen to DDR1, antibodies against collagen are deployed. Phosphorylated DDR1 can be labelled with antibodies to resolve intracellular activation, for which a possible activation state is sketched in Figure 6.8. This section presents initial results obtained from experiments undertaken to explore the potential of SIM+FLIM to study the activation of DDR1 by collagen and therefore to explore different labelling strategies.

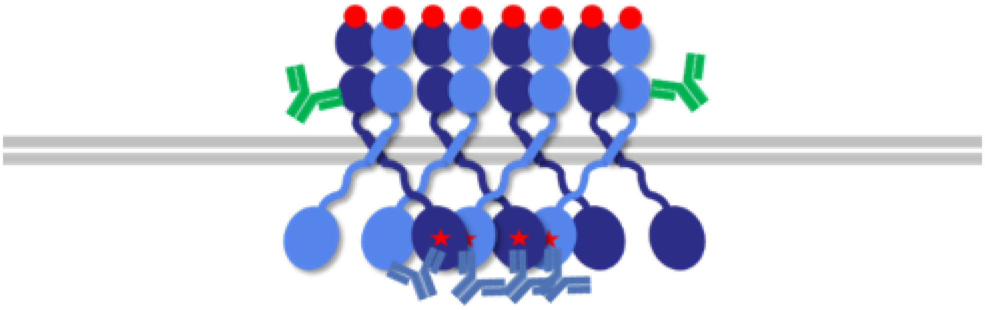

Figure 6.8: *Different labelling approaches of aggregated DDR1. Red circles indicate bound collagen, the green markers are antibody staining against DDR1, the red stars symbolise activated DDR1 and the blue markers are antibodies against phosphorylated DDR1 kinases. Adapted from [Gö17a].*

The SIM data presented in this section were obtained using a Carl Zeiss Elyra.S1 with a Plan-Apochromat 63x 1.4 Oil DIC M27 objective lens using a camera integration time of 200 ms applied in three spectral channels: Alexa-488 was excited at 488 nm with a dichroic beamsplitter BP-420-

480 + BP 495-550 + LP 650; Alexa-546 was excited at 561 nm via a dichroic beamsplitter 561/643 nm and Alexa-647 was excited at 642 nm via a dichroic 561/643 nm. More detailed information about the cell culture and labelling procedures can be found under section 9.4.

6.4.1 SIM reveals labelling artefacts of antibodies

SIM and wide-field images of aggregated DDR1 were acquired of cells labelled with primary antibodies against the extracellular DDR1 domain (with secondary antibodies conjugated to Alexa-546, after collagen stimulation and DDR1 aggregation) and with SNAP-tag proteins conjugated with Alexa-488 before collagen stimulation and DDR1 aggregation. The wide-field images of structures labelled with the SNAP-tag and antibody approaches are broadly similar, although there are regions where the antibody-labelled images are brighter, as shown in Figure 6.9.

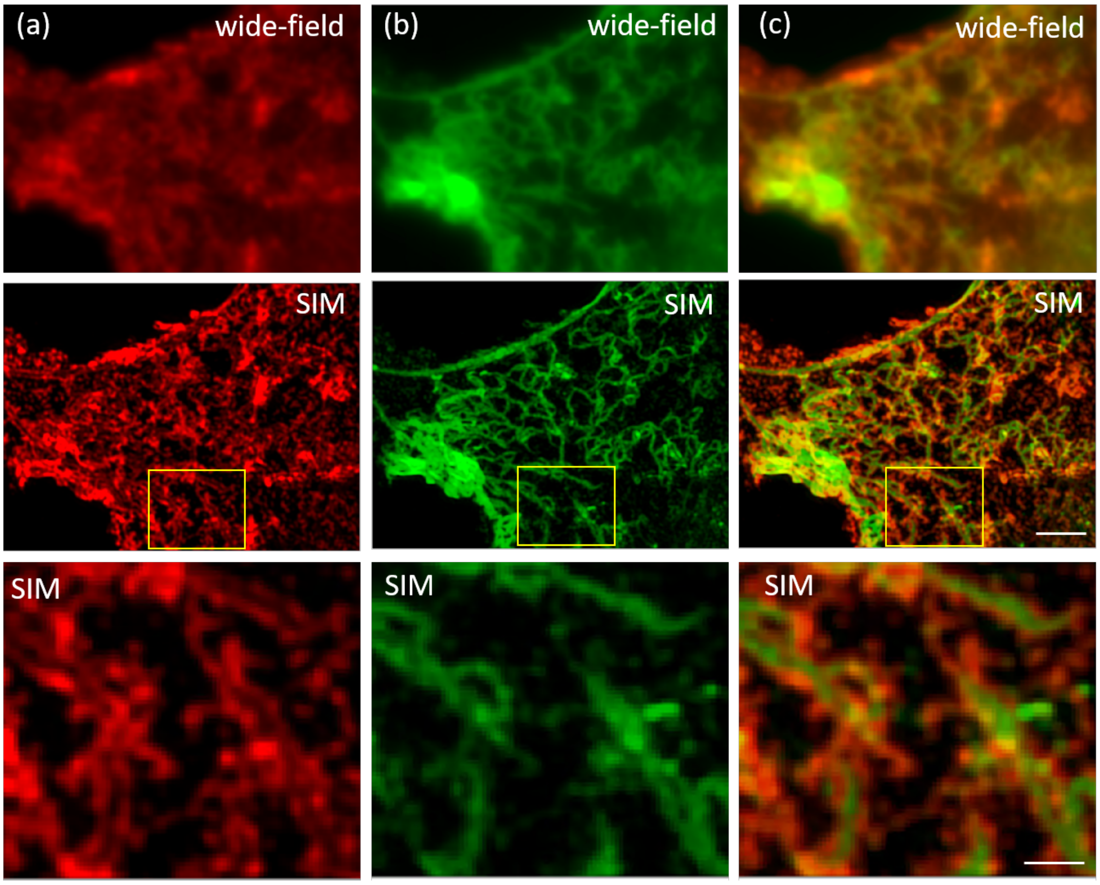

Figure 6.9: *Two color wide-field and SIM images of collagen-stimulated DDR1 labelled with (a) antibody (red, Alexa-546), (b) SNAP-tag (green, Alexa-488) and (c) overlays of (a) and (b). First row presents wide-field images, second row presents SIM images and bottom row shows magnified regions of interest. Scale bar: 3 µm for full field and 1 µm for magnified images.*

The higher resolution SIM images show greater differences between the two labelling approaches, notably a double strand structure in the antibody-labelled samples that is not apparent with the SNAP-tag labelling approach, although the SIM overlay images show that the SNAP-tag signal is localised in the gaps between the double strands of the antibody-labelled structures. This may be explained by the epitope for the anti-DDR1 antibodies not being accessible for the most aggregated DDR1 states, whereas the SNAP-tag DDR1 can label the aggregated DDR1 in the cell.

6.4.2 From aggregation to phosphorylation

The activation of DDR1 is thought to be separated into two steps, aggregation and phosphorylation [Lem12]. To explore the potential to study both of these steps, a three color SIM experiment was undertaken with collagen-stimulated DDR1 in COS-7 cells labelled with second antibody (Alexa-546) and SNAP-tag (Alexa-488) approaches and a second antibody (Alexa-647) labelling phosphorylated DDR1 kinases.

The three color SIM images, shown in Figure 6.10, illustrate again the apparently more complex structures present in the antibody-labelled DDR1 image (b) but not in the SNAP-tag labelled DDR1 image (a) or the phosphorylated DDR1 labeled image (c). In the overlay image of (d), the phosphorylation signal (blue) appears in the middle of the complex structures (red) of the antibody-labelled DDR1 image seen in (e). Thus, it seems that the epitope for the phosphorylated DDR1 antibodies may be more accessible in the aggregated DDR1, although the phosphorylation labelling does not occur everywhere reported by the SNAP-tag channel (green) labelling of the DDR1, as can be seen in Figure 6.10 (e).

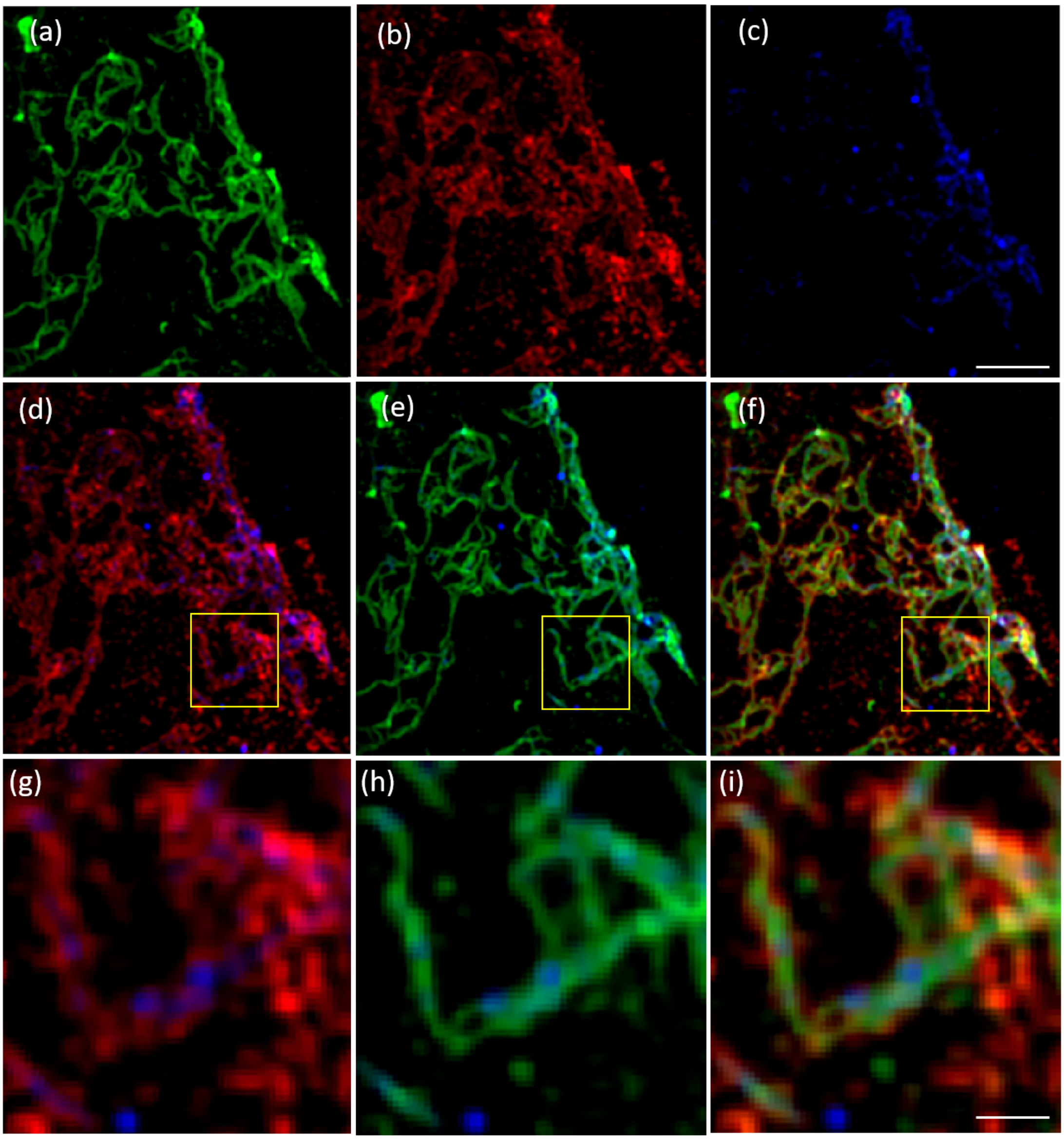

Figure 6.10: *Three color SIM images of collagen-stimulated DDR1 in fixed COS-7 cells with (a) SNAP-tag (Alexa-488, green)-labelled DDR1, (b) antibody (Alexa-546, red)-labelled DDR1, (c) antibody (Alexa 647, blue) against phosphorylated DDR1, (d) overlay of the two antibody-labelled channels, (e) overlay of SNAP-tag DDR1 and antibody phosphorylated DDR1, (f) overlay of all three channels and (g-h) magnified regions of interest. Scale bar: 3 µm for full field and 0.75 µm for magnified images.*

6.5 SIM+FLIM applied to DDR1 aggregation

The aggregation of DDR1 dimers following stimulation by collagen can be imaged using FLIM and SIM together, as described in chapter 5. If the DDR1 dimers are labelled with donor and acceptor dyes using the SNAP-tag approach, the donor fluorescence lifetime channel can provide a (diffraction-limited) map of the molecular aggregation state via FLIM-FRET, while SIM can provide a map of the DDR1 distribution of across the cell at a resolution of ∼120 nm. Figure 6.11 presents SIM+FLIM data acquired imaging COS-7 cells where the DDR1 dimers were stochastically labelled with Alexa-488 and Alexa-546 using the SNAP-tag approach and fixed 60

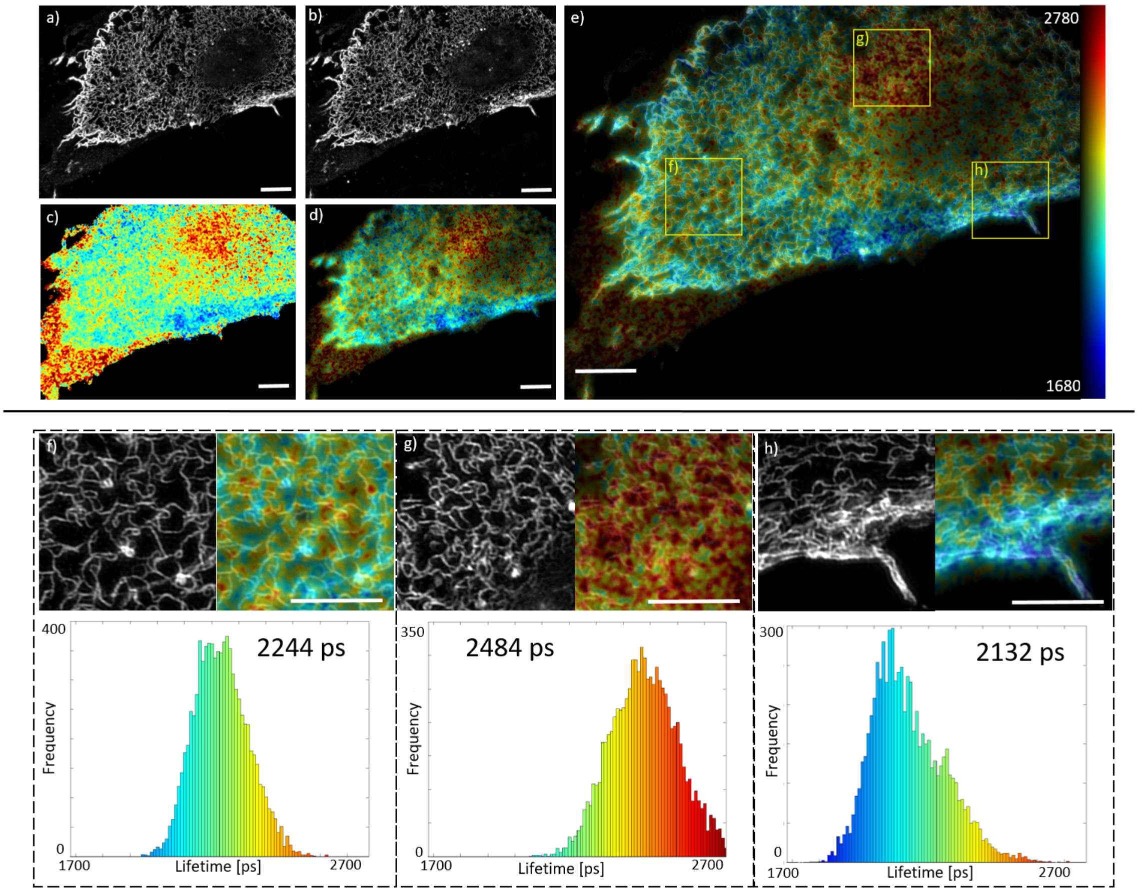
a)
b)
c)
d)
e)
2780
1680
g)
f)
h)
f)
g)
h)
400
0
2244 ps
Frequency
1700
Lifetime [ps]
2700
350
0
2484 ps
Frequency
1700
Lifetime [ps]
2700
300
0
2132 ps
Frequency
1700
Lifetime [ps]
2700

Figure 6.11: *SIM+FLIM images of collagen-stimulated COS-7 cells expressing DDR1 stochastically labeled with Alexa-488 (donor) and Alexa-546 (acceptor) using the SNAP-tag approach to provide a FRET readout of aggregation: (a) SIM image of Alexa-488, (b) SIM image of Alexa-546, (c) Alexa-488 lifetime map, (d) the intensity-weighted Alexa-488 fluorescence lifetime image and (e) SIM+FLIM image. The sub-regions indicated in (e) are expanded in (f,g,h) presenting SIM intensity and SIM+FLIM images with corresponding intensity-weighted lifetime histograms and pixel-averaged lifetime values [Gö17a]. Scale bar: 6 µm.*

.

minutes after stimulation with collagen. Regions of higher DDR1 aggregation are indicated by shorter donor fluorescence lifetimes, as indicated in Figure 6.11 (e) and the expanded images show that regions of different donor lifetime correspond to different underlying DDR1 nanostructure, as revealed by the SIM intensity images. One possible explanation for apparent variations in aggregation state could arise from inhomogeneous labelling density, e.g. weaker FRET occurring where the DDR1 is less effectively labelled with acceptor. As shown in Figure 6.12, however, the donor and acceptor SIM intensity images are reasonably well overlapped and variations in the ratio of the SIM donor and acceptor intensity do not correlate with the observed lifetime variations and so are likely to correspond to variations in DDR1 aggregation rather than to a labelling artefact.

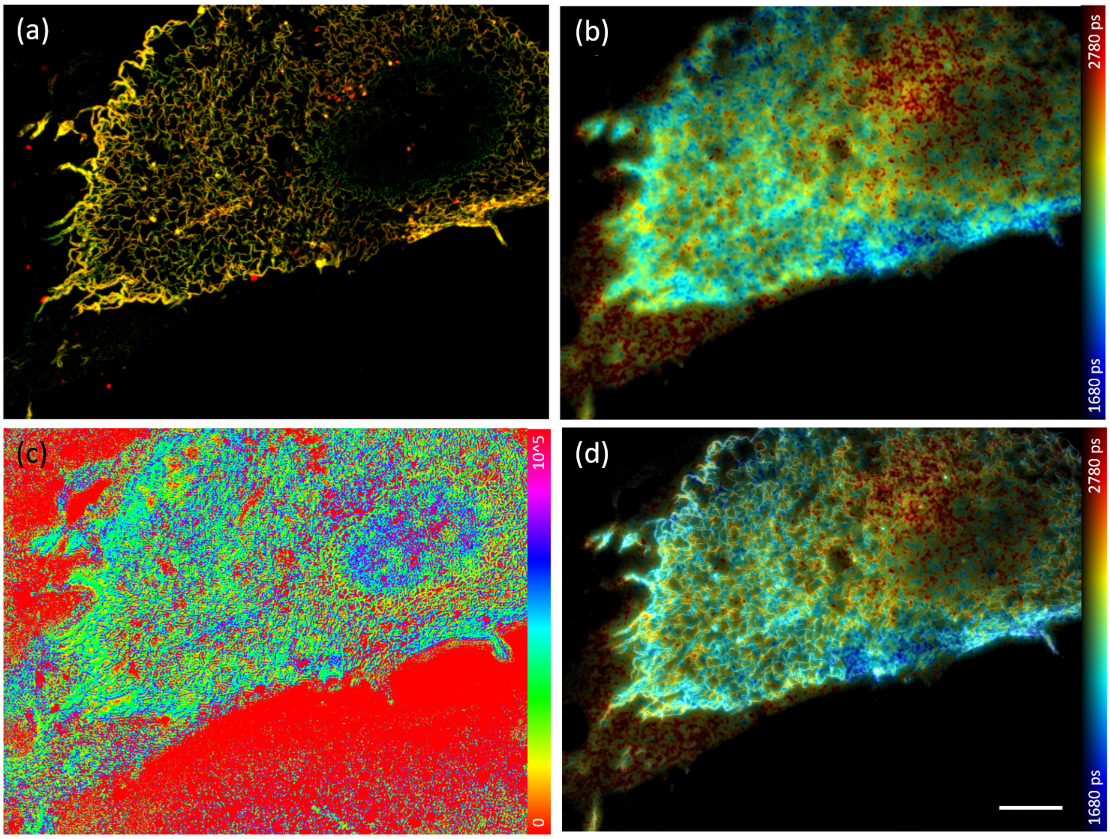

Figure 6.12: *SIM and FLIM control images: (a) SIM donor (green) and SIM acceptor (red) intensity images overlaid, (b) intensity-weighted lifetime image, (c) is the donor SIM intensity divided by that of the acceptor and (d) is the SIM+FLIM image. Adapted from [Gö17a]. Scale bar: 6 µm.*

6.6 Summary

Summary This chapter discussed the different labelling approaches explored during a preliminary FLIM and SIM study of the collagen-stimulated aggregation of DDR1 dimers at the membrane of COS-7 cells. The labelling approaches explored were fusion with fluorescence proteins, antibody labelling and labelling using SNAP-tags conjugated to cell impermeable dyes. The first section provided a brief overview of the biology underlying DDR1 aggregation.

The next section presented results from FLIM HCA experiments exploring different strategies to label DDR1 dimers. SNAP-tag labelling with dyes was shown to provide superior FLIM-FRET contrast between stimulated and unstimulated cells compared to FP labelling, partly due to the superior photophysical properties of the dyes and partly to the unwanted background from FRETing heterodimers in the cytoplasm that occurred with FP-labelling. A further demonstrated advantage of labelling using SNAP-tags was the potential to use the new labelling strategy to produce DDR1 homodimers (i.e. dimers labelled with only donor or acceptor fluorophore) to further increase the FRET lifetime contrast, albeit at the cost of greater experimental complexity. FLIM measurements of two different mutants of DDR1 supported previous suggestions that the activation of DDR1 can be divided into distinct steps of aggregation and phosphorylation.

The impact of different labelling strategies was also explored for SIM of DDR1 following collagen stimulation. Two and three colour SIM revealed that antibody-labelling of DDR1 could produce complex "double stranded" features that were not present in corresponding images of DDR1 labelled with SNAP-tags and their thought to be artefacts of the antibody labelling. It was suggested that this was because the antibodies were not able to access their epitopes for some DDR1 aggregation states while the smaller SNAP-tags were still able to effectively label DDR1. A three color SIM image presented DDR1 SNAP-tag labelling, DDR1 antibody and phosphorylation antibody labelling. The latter did not present the same complex double-strand artefact but seem to correspond better to the SNAP-tag labelled images, although the phosphorylation was not indicated everywhere that DDR1 was apparent.

Finally, the SIM+FLIM microscope described in chapter 5 was applied to image the collagen-stimulated DDR1 in fixed COS-7 cells and indicated that variations in aggregation state (as indicted by the FRET donor fluorescence lifetime) may correlate with different types of nanostructure of the labelled DDR1 as indicated by the SIM intensity images.

Contribution The DDR1 samples presented in this chapter were prepared by David Corcoran. The images were acquired by David Corcoran and myself. I did the data analysis and image processing. The DDR1 diagrams presented are adapted from figures designed by David Corcoran.

Chapter 7

Stimulated emission depletion microscopy (STED) with a single spatial light modulator (SLM) for collinear alignment, aberration correction and multiplexed imaging

STED microscopy is one of the few super-resolution techniques that can resolve biological structures under 50 nm in living samples [Hei08, Hei10]. New approaches in STED microscopy have pushed the resolution limit of live cell STED to 30 nm [Hei17], with resolutions below 25 nm being achieved for MINFIELD STED, where the region scanned is smaller than the size of the depletion doughnut[Gö17c]. However, the potential of STED microscopy in many fields ranging across biology, medicine and pharmacology is not fully realised, partly due to the relative experimental complexity (and consequent scope for instability) of the set-up, partly due to the limited acquisition speed and partly due to the impact of optical aberrations in biological media, to which STED microscopy may be more sensitive than other super-resolution techniques. In particular, the ability to correct for optical aberrations is of great importance when imaging biological samples, in which spatial variations in refractive index can drastically degrade image quality, especially as the imaging depth in tissue increases [Hel93]. Aberration correction in STED microscopy was first demonstrated with an SLM to correct aberrations in the instrument [Auk08] and later applied to also correct sample-induced aberrations [Gou12, Len14, Pat16]. Here a STED microscopy set-up is presented that reduces the complexity of the instrument and its alignment while retaining the ability to electronically correct for aberrations in the excitation and depletion beams, thereby extending the achievable field of view (FOV) for STED (and RESOLFT) microscopy. The same set-up, using a single SLM, can be readily extended to increase the STED image acquisition speed by scanning multiple beams in parallel.

This chapter first describes a novel configuration that incorporates a single SLM to shape the depletion beam profile and correct for aberrations and acts on collinear excitation and depletion beams in a manner analogous to the “easy STED” principle [Reu10]. This is convenient because excitation and depletion beams can be delivered by the same single-mode optical fibre and thus be inherently coaligned. This simplifies the alignment of the system and reduces the impact of walk-off between the excitation and depletion beams, thereby conferring greater stability of performance over time. This new approach, termed “easySLM-STED”, is demonstrated through imaging fluorescent beads, vimentin in Vero cells and *Caenorhabditis elegans (C. elegans)* germlines.

Because the single SLM can shape the excitation and depletion beams independently, it is possible to correct for aberrations in both laser beams with a single SLM such that walk-off due to chromatic aberration can be countered and STED microscopy can therefore be realised over larger FOV, which can be realised by sequential acquisition and stitching of contiguous images (i.e. implementing a mosaic approach [Pri06]). The implementation and performance of this approach, evaluated on fluorescent beads and labelled vimentin in Vero cells, is discussed.

The last section of this chapter describes the adaptation of the easySLM-STED to implement parallelized pixel acquisition by generating multiple focal spots, thereby decreasing the image acquisition time. This concept is demonstrated using 4 multiplexed excitation/depletion beams realising multiplexed STED microscopy of fluorescent beads and germlines in *C. elegans.*

7.1 easySLM-STED

The starting point of the easySLM-STED concept is to retain the advantages of SLM shaping of the depletion beam and electronic correction of aberrations while simplifying the alignment and improving stability by designing a module for use with collinear exaction and depletion beams.

The system alignment begins with the excitation and depletion laser beams (at 485 nm and 560 nm respectively) being coupled into a birefringent single mode optical fiber with orthogonal polarisations. These beams then interact twice with a SLM with a 90° polarisation rotation applied between the "bounces". This design allows the phase of the excitation and depletion beams to be modulated independently, since the nematic liquid crystal SLM only modulates the phase of light polarized in one (horizontal) plane. The beam with the correct polarisation diffracts off a computer-generated hologram on the SLM that can be programmed to modify the intensity and phase properties of the diffracted light, including the direction of propagation. This concept was previously used to independently shape the PSF of two orthogonally polarized depletion beams for 3D STED microscopy [Len14].

7.1.1 easySLM-STED instrument design

A schematic of the easySLM-STED configuration is shown in Figure 7.1 (a). A gain-switched diode laser (LDH-D-C-485, PicoQuant) provides picosecond excitation pulses at a wavelength of 485 nm and an in-house developed ultrafast fibre laser provides nanosecond depletion at 560 nm [Run15b, Run17]. The output beams from both lasers are combined with a beam splitter, using a $\frac{\lambda}{2}$-wave plate (HWP) to ensure that the beams are orthogonally polarized, and coupled into a polarization maintaining single mode fiber. The repetition rate and pulse duration of the STED

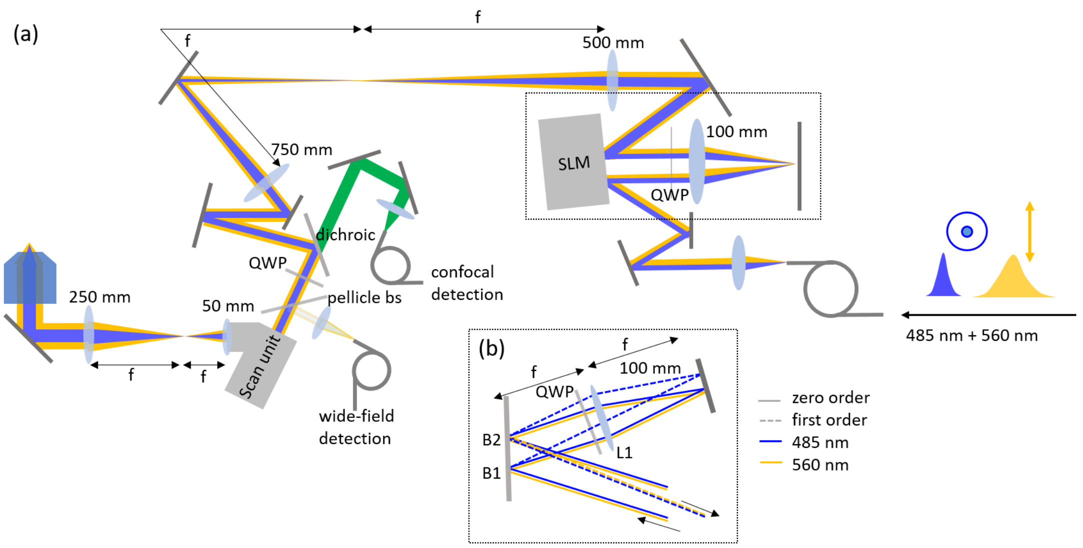
(a)
f
f
500 mm
750 mm
100 mm
SLM
QWP
dichroic
QWP
confocal
detection
pellicle bs
250 mm
50 mm
Scan unit
f
f
wide-field
detection
485 nm + 560 nm
(b)
f
f
100 mm
QWP
B2
B1
L1
zero order
first order
485 nm
560 nm

Figure 7.1: *easySLM-STED design [Gö18].*

laser can be adjusted and were set to 5 MHz and 1.3 ns respectively for the experiments reported in this chapter. Figure 7.2 shows the measured temporal pulse profiles of the excitation and depletion laser pulses measured using TCSPC detection. A signal derived from the depletion laser was used to synchronize the system, triggering the excitation laser, and a delay box (Precision Programmable Delay Line, Kentech Instruments) was used for adjusting the delay between the excitation and depletion pulses.

The SLM (LCOS-SLM, Hamamatsu) modulates both laser beams independently as the two laser beams each bounce two times off the SLM at different positions, $B1$ and $B2$ and double pass an achromatic $\frac{\lambda}{4}$-wave plate (QWP) to rotate the polarisation of both laser beams by 90° between bounces. Due to the orthogonal polarizations of the laser beams, the hologram at $B1$ only modulates the excitation beam, while only the depletion beam is modulated at $B2$. A vortex phase ramp applied to the hologram at $B2$ therefore shapes the depletion laser to produce the desired doughnut intensity profile. The beams are controlled using off-axis holograms to ensure that unmodulated (i.e. directly reflected) light is spatially separated from the modulated light. Due to their different wavelengths, the excitation and depletion beams experience different diffraction angles for a given diffraction grating frequency. The first order of the excitation beam diffracts at $B1$ from its zero-order beam, and the unmodulated depletion laser beam continues to propagate in the same direction at the zero-order, as indicated in Figure 7.1 (b). When the depletion beam is diffracted at $B2$, an offset is added to its direction to ensure that it is collinear with the excitation beam diffracted at $B1$ that is simply reflected at $B2$. Thus, the first order diffracted excitation and depletion laser beams emerge collinear and collimated from $B2$.

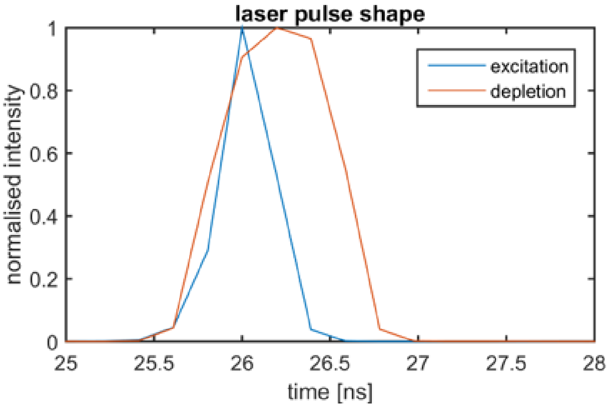

Figure 7.2: *Time resolved depletion and excitation laser pulse shapes.*

The point where the optical axis intersects the SLM at $B2$ is imaged with a 4f configuration onto the first galvo-mirror of the scan unit (Yanus IV digital scan head, FEI) using 500 mm and 750 mm focal length achromatic lenses. The first galvo-mirror is imaged onto the second galvo mirror within the scanner, and this mirror is then imaged via a 4f configuration onto the back focal plane of the objective (HCX PLA APO 100x 1.4, Leica) via a 50 mm focal length scan lens and a 250 mm achromatic "tube" lens. Before the scanner, a QWP is used to provide circular polarisation of both laser beams. During the alignment process, a removable pellicle beam splitter (pellicle bs) is used to reflect the light scattered from a test sample of gold nanoparticles onto a 1 mm core fiber, which can be considered as a wide-field detector. This enables the excitation and depletion PSF to be visualised. During fluorescence imaging and STED microscopy, the pellicle beam splitter is removed. A dichroic (zt488/561rpc, Chroma) separates the fluorescence signal from the incident laser beams and the fluorescence is focused into a 62.5 μm core diameter graded index fiber (M31L03, Thorlabs), which corresponds to a confocal pinhole of 0.74 Airy diameter. An emission filter (FF02-520/28, Semrock) is used to block excitation or depletion laser light.

The fluorescence signal is detected with single photon counting using a hybrid PMT (HPM-100-40, Hamamatsu) that converts the incident photons to electrical pulses. This electrical signal is split with one half being directed to a TCSPC card (SPC-830, Becker & Hickl) and the other half directed to a DAQ box (NI USB-6259, National Instruments), via a constant fraction discriminator (CFD). The DAQ box is used only for intensity imaging, whereas the TCSPC card can be used for time-resolved detection. The system is controlled by a *LabVIEW* program written in-house. The DAQ box also controls the scan unit, the z position (using an XYZ stage), the scan pattern (which is also sent to the TCSPC card) and a shutter in front of the depletion laser. The TCSPC card is controlled via *SPCM* software (Becker & Hickl) and the data analysis for time-gated images is performed using *SPCimage* (Becker & Hickl). A detailed manual with alignment tips and description of the software can be found under section 9.5.

7.1.2 easySLM-STED performance evaluation

Test samples were used to evaluate the performance of the STED system. For detailed information about the sample preparation see subsection 9.5.9. 80 nm gold beads imaged via the wide-field detection path were used to evaluate the shape of the depletion beam and confirm the overlay between excitation and depletion lasers. Fluorescent beads (yellow green beads, 0.046 μm, Invitrogen) were used to find the best time delay between the two laser pulses, to adjust the pinhole and to measure the resolution performance of the microscope.

Spatial beam profile: To measure the depletion beam profile, a gold nanoparticle scattering sample was used. A gold nanoparticle close to the optical axis was located and the scattered light signal recorded, as shown in Figure 7.3 (pixelsize 5 nm). It will be seen that the intensity in the zero point of the doughnut is comparable to the noise level and the intensity distribution is similar to the ideal theoretical PSF, as simulated in Figure 9.2.

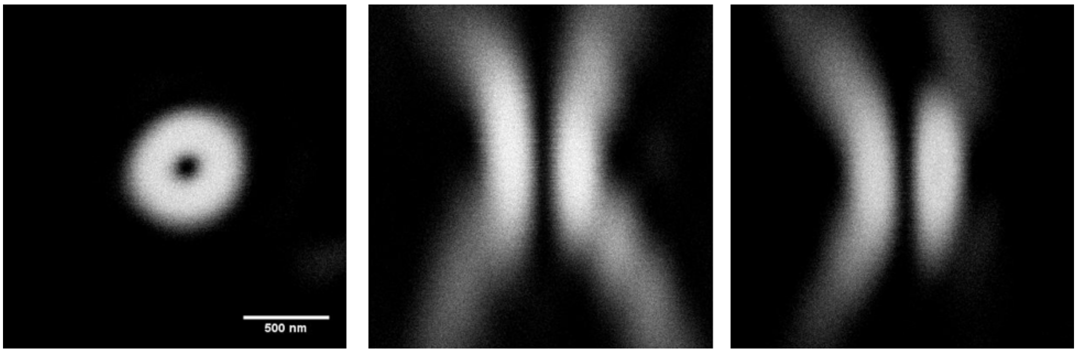

Figure 7.3: *easySLM-STED PSF for xy (left), xz (middle) and yz (right)*

Lateral resolution measurement: 46 nm diameter fluorescent beads were imaged in confocal and easySLM-STED modes to confirm super-resolved imaging. As shown in Figure 7.4, for which

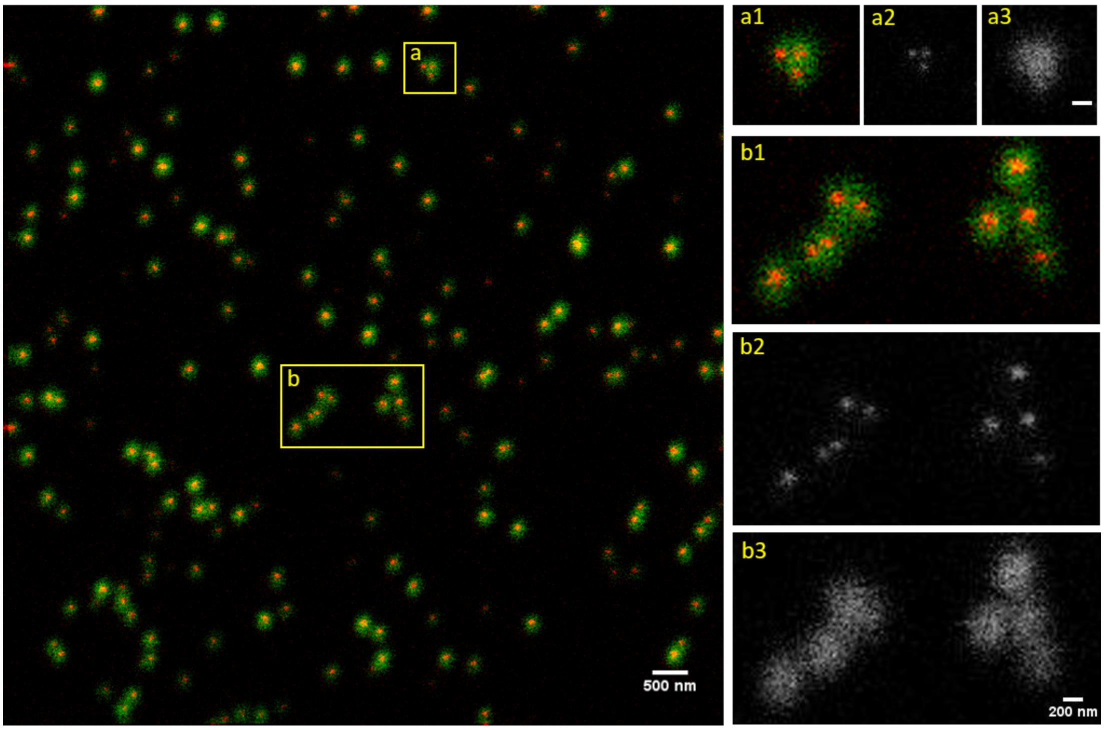

Figure 7.4: *easySLM-STED image of fluorescence beads. Green channel: confocal image, red channel: easySLM-STED image with inserts [Gö18].*

the image pixel size was 15 nm, the pixel dwell time was 300 μs, the depletion power was 22 mW and the excitation power was 12 μW, resolutions below 50 nm could be achieved. For this data, the *ImageJ* plugin *ThunderSTORM* [Ove14] was used to localize single beads and fit a 2D

Gaussian function to calculate the FWHM for each bead. The 100 smallest FWHM, equal to 50% of the detected beads, indicated a mean FWHM of 49 nm with a standard deviation (stdev) of 7.5 nm.

To prove that the STED resolution d_{STED} follows the equation [Har08a]:

$$d_{STED} = d_{Abbe}/\sqrt{1 + \frac{I}{I_s}} \tag{7.1}$$

with d_{Abbe} being the confocal image resolution, I being the depletion beam intensity and I_s the effective saturation intensity, several images of fluorescent beads were acquired with increasing intensity of the depletion beam. Figure 7.5 displays the resulting plot (blue), which follows the expected function (orange).

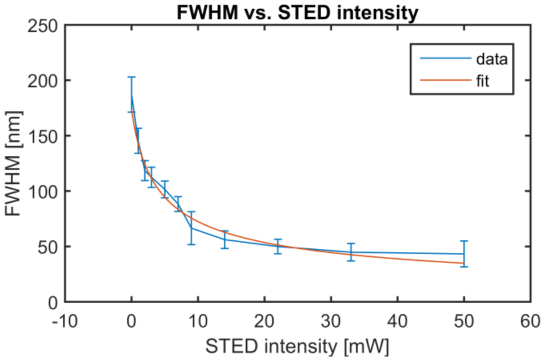

Figure 7.5: *easySLM-STED resolution in dependency of depletion laser intensity.*

7.1.3 easySLM-STED of biological sample: vimentin in Vero cells

To demonstrate easySLM-STED applied to biological samples, a sample of fixed Vero cells with vimentin stained with AbberiorSTAR488 (Abberior GmbH) was imaged. The STED image indicates smaller structures being resolved than for the confocal image as presented in Figure 7.6. The corresponding line scans shown in Figure 7.7 present features with FWHM down to 51 nm, as calculated by fitting a Gaussian function to the line profiles using *MATLAB*. The FOV is 20 μm x 20 μm with a pixel size of 25 nm. The dwell time was 100 μs and 5 frames were accumulated for each final image. The excitation and depletion beam powers were 8 μW and 3 mW respectively.

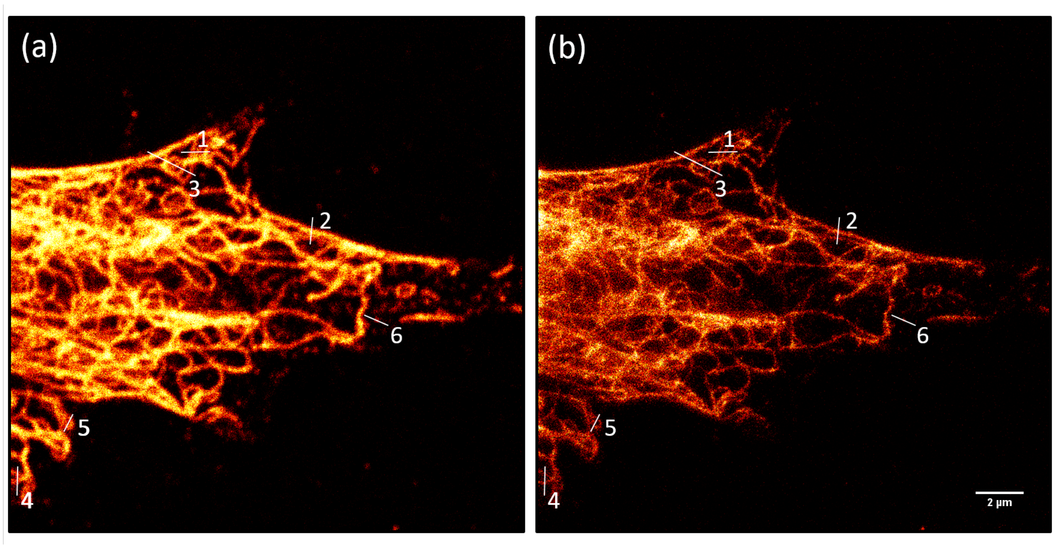

Figure 7.6: *easySLM-STED image of vimentin in Vero cells. Left confocal and right easySLM-STED image [Gö18].*

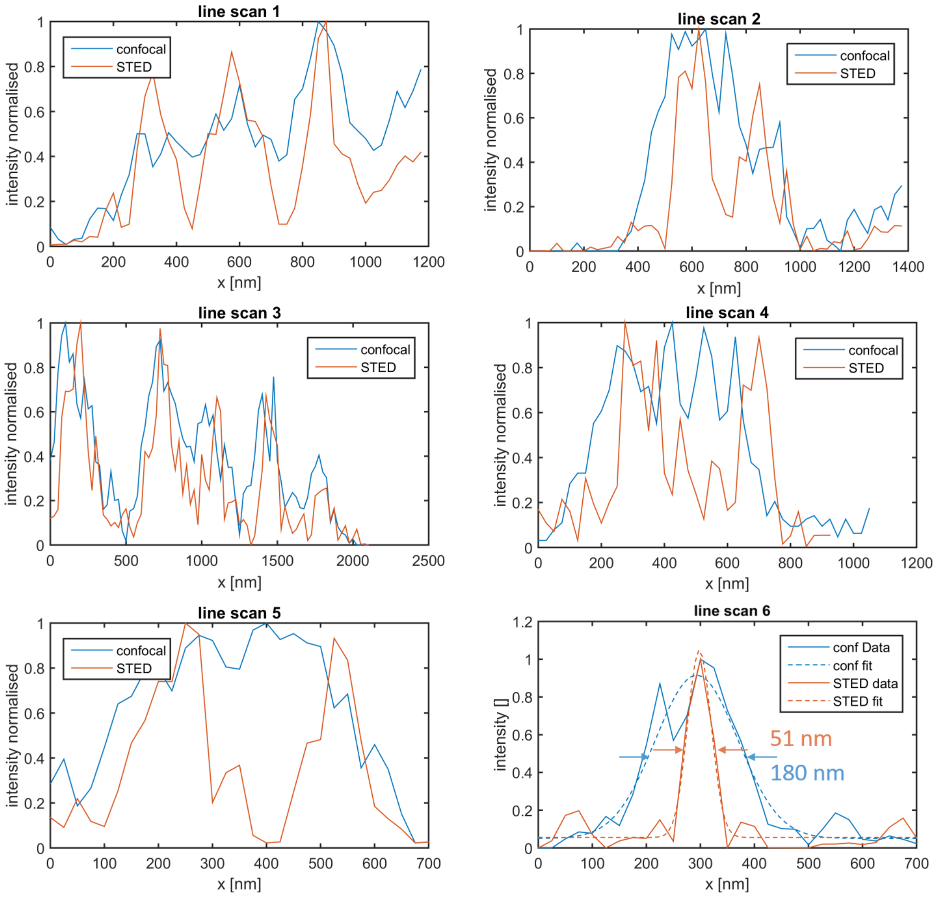

Figure 7.7: *Line scans through features in Figure 7.6 with FWHM calculated from Gaussian fits [Gö18].*

7.1.4 easySLM-STED of biological sample: *C. elegans* germline

Biological background: Meiotic processes can be conveniently followed in the germline of *C. elegans* because nuclei are ordered in a spatial–temporal gradient in which specific meiotic stages can be easily identified. The germline of *C. elegans* can be divided into different zones [MP08], as shown in Figure 7.8 (a,b): the proliferative zone, where mitotic cells replicate; the transition zone (Leptotene and Pachytene), where the DNA replication ends and homologue chromosomes (or homologs) condense and start to form the synaptonemal complex (SC) between homologs, and the Meiotic Prophase (Pachytene). The SC is a proteinaceous structure that stabilizes the interaction between homologs. At this stage, the number of chromosomes is doubled, with each chromosome being formed from two sister chromatids. At the end of the germline we can observe the meiotic divisions (Meiosis I and II). During meiosis I, homologs segregate, so every new cell contains one set of chromosomes. During meiosis II, the cell divides again and splits the chromosome into two chromatids, one per cell. The generated cells are haploid oocytes. *C. elegans* is a hermaphrodite and fertilizes itself at the end of the germline, where sperm and oocytes pair.

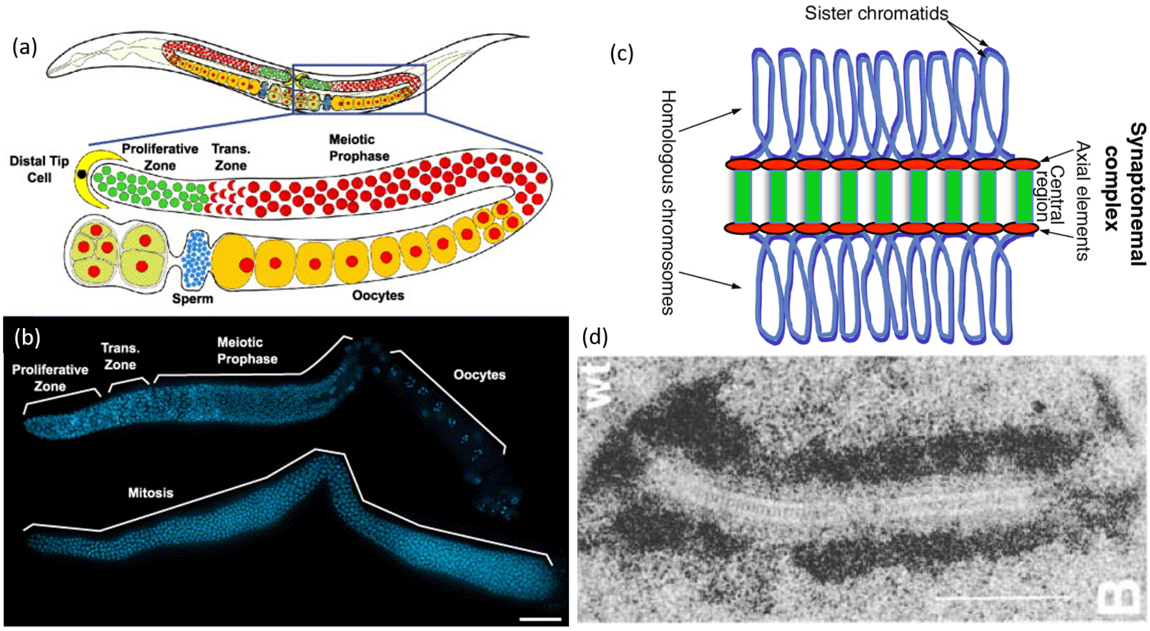
(a)
Distal Tip Cell
Proliferative Zone
Trans. Zone
Meiotic Prophase
Sperm
Oocytes
(b)
Proliferative Zone
Trans. Zone
Meiotic Prophase
Oocytes
Mitosis
(c)
Sister chromatids
Homologous chromosomes
Synaptonemal complex
Axial elements
Central region
(d)

Figure 7.8: *Germline in C. elegans and synaptonemal complex. (a) schematic of C. elegans with germline [Han04] and (b) fluorescence image of germline with a DNA DAPI staining [Han04] (scale bar: 20 µm); (c) diagram of homologous chromosomes and synaptonemal complex (SC) [Hil17] and (d) electron microscopy image of SC [Hil17] (scale bar: 500 nm).*

Synaptonemal complex in homologs of the *C. elegans* germline: At the end of the transition zone in *C. elegans* germlines, the homologs form pairs linked by the synaptonemal complex (SC). This generates a gap between the two homologue chromosomes, as illustrated in Figure 7.8 (c). This gap is around 100 nm, as established with electron microscopy (Figure 7.8 d), which is too small to be resolved with confocal microscopy, but which can be observed with STED microscopy, as shown in Figure 7.9. To visualise the SC gap with the easySLM-STED microscope, the backbone protein HTP1 of the chromosomes was marked with Alexa-488 by expressing HTP-1::GFP and using a GFP tag with Alexa-488 (GFP Tag Polyclonal Antibody Alexa Fluor 488, Thermo Fischer). Worms were dissected to extract the germlines so the Alexa-488 could reach the chromosomes, before the sample was fixed. easySLM-STED was applied with a pixel dwell time of 100 μs and a pixel size of 30 nm with 3-frame accumulation. The excitation and depletion powers were 7 μW and 3 mW respectively and the fluorescence signal was time-gated.

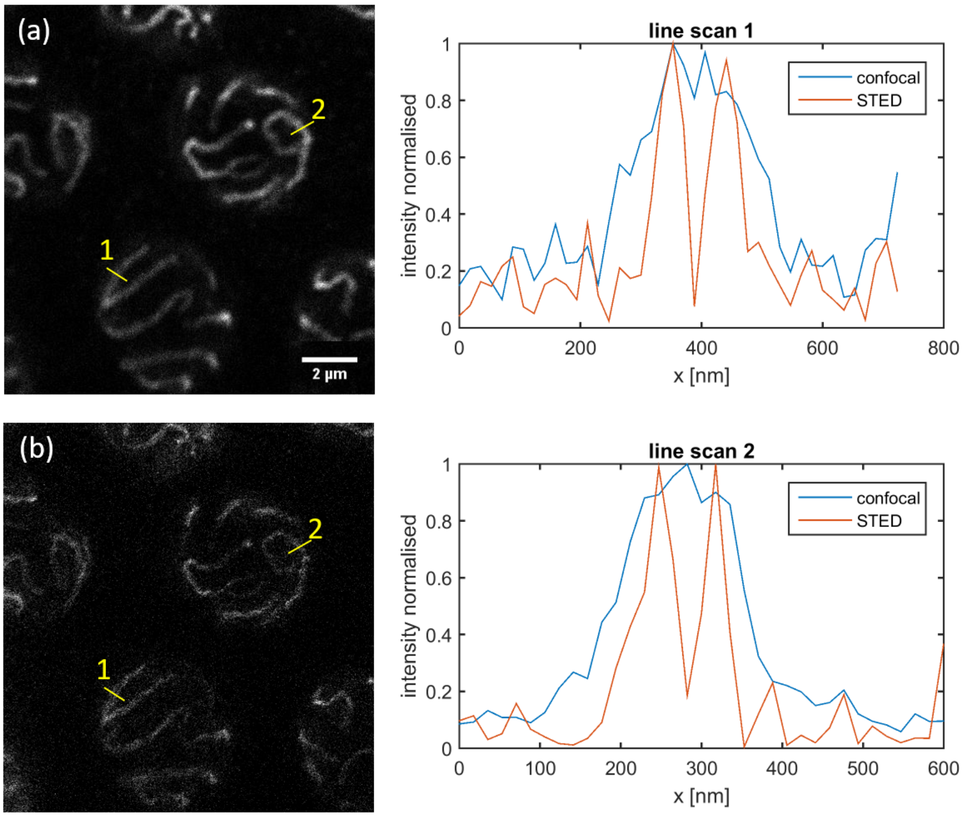

Figure 7.9: *(a) confocal image and (b) easySLM-STED images of synaptonemal complex gap of separate germlines in C. elegans from the end of the transition phase with the corresponding line scans averaged over three contiguous line profiles. Adapted from [Gö18].*

7.2 Mosaic easySLM-STED with aberration correction

Mosaic microscopy is an approach to increase the FOV of an imaging system while maintaining a high numerical aperture (and therefore light collection efficiency and spatial resolution). It simply entails acquiring multiple contiguous FOV and stitching them together. It is used in microscopy to image structures of interest that are much larger than the maximum FOV of the microscope [Pri06]. In laser scanning microscopy, the maximum practical FOV is often smaller than the maximum scan range because aberrations can occur for large scan angles that unacceptably degrade the imaging. It is sometimes possible to correct for differences between different color channels in post processing when undertaking mosaic imaging. This section, however, presents the extension of easySLM-STED to compensate for aberrations during a mosaic acquisition carried out using beam scanning rather than stage scanning. If the aberration can be compensated with an SLM, a large FOV can be divided into smaller tiles and aberration correction can be applied to the excitation and depletion laser beams for every tile individually.

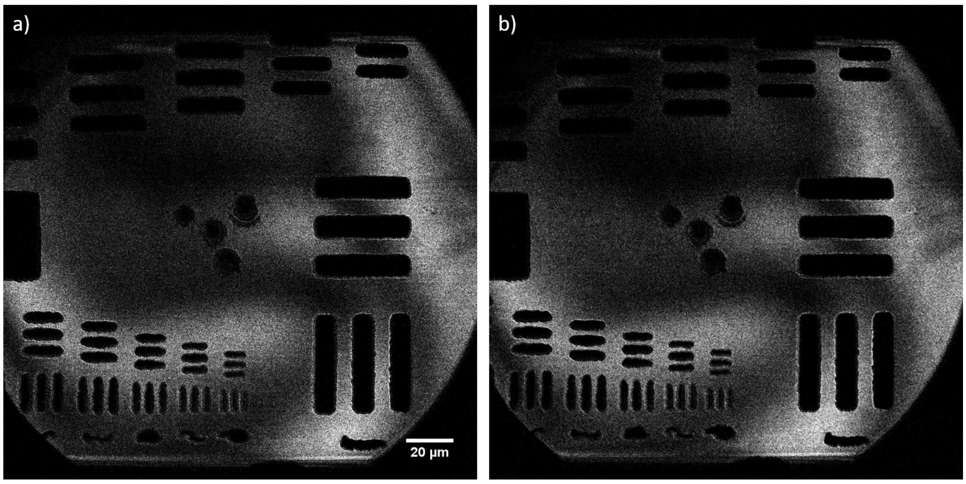

Figure 7.10: *(a) normal and (b) mosaic confocal imaging of USAF target.*

After the FOV is divided into tiles, the tiles are acquired sequentially and stitched together in post processing using *MATLAB*. A USAF target was imaged using reflected light to test the tile stitching and establish a work-flow. Confocal images over the full range of the scanner were acquired in single continuous, normal mode and also in mosaic mode, which are shown in Figure 7.10. The FOV in normal mode was 200 μm x 200 μm, for the mosaic approach, the FOV was divided into 11 x 11 tiles, each with a side of 20 μm and then was cropped to be comparable with the normal mode. In both measurements, the pixel size was 2 μm with an integration time of 200 μs. The reflected signal was detected on the wide-field detection path. The two images are almost identical, demonstrating the efficacy of the tile stitching in post-processing.

7.2.1 Chromatic aberration for large FOVs

Chromatic aberration leads to a separation of laser beams in the focal plane, depending on their wavelength, which is also referred to as chromatic shift. It is introduced because the laser beams pass optical elements with wavelength-dependent refractive indices, which results in the beams focusing to different positions in the sample plane. If the chromatic aberration is introduced by a lens, the chromatic shift is angularly independent (radially symmetric) but depends on the distance from the optic axis. In a STED microscope, the excitation and depletion laser beams are at different wavelengths and the chromatic shift can result in systematic artefacts when scanning a large FOV. For easySLM-STED in mosaic mode, an appropriate correction for the chromatic shift can be applied for each tile position in the FOV.

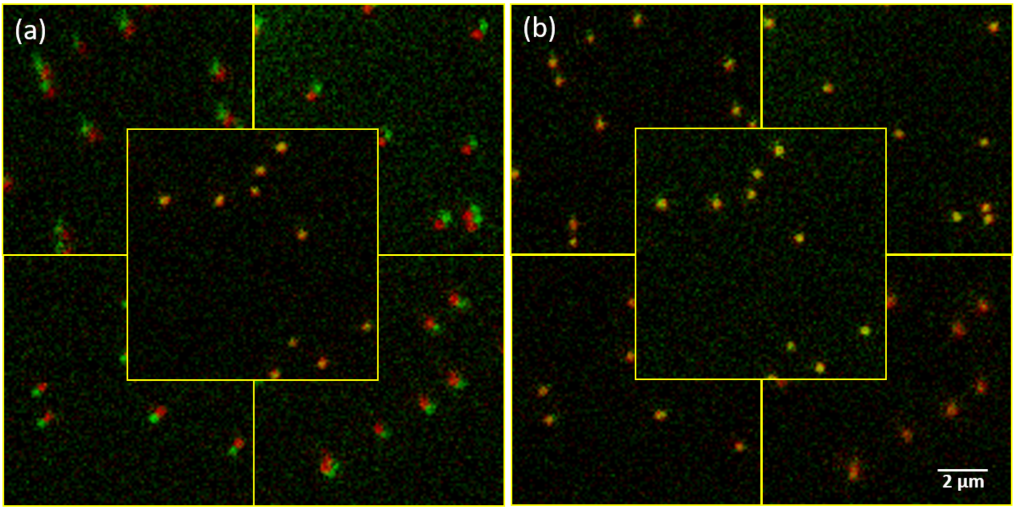

Figure 7.11: *Two laser scanned bead samples (a) without and (b) with aberration correction in mosaic mode. The field in the middle corresponds to the centre tile, whereas the corner fields corresponds to the corner tiles of the mosaic. Green shows the confocal image acquired with 488 nm excitation and red shows the confocal image acquired with 560 nm excitation.*

The chromatic shift can be illustrated in a two-color laser scanning microscope, as shown in Figure 7.11 (a) for 485 nm and 560 nm incident beams scattering off a gold bead sample and detected in wide-field detection mode using the setup described in section 7.1. But for this image the hologram for the depletion laser was not applied, so at the sample the 560 nm is also a diffraction-limited spot. The images were split in 5 x 5 tiles with 20 μm x 20 μm each and subregions with 10 μm x 10 μm are displayed for better visualization. Two images acquired consecutively with 485 nm and 560 nm laser beams show that in the corners of the FOV the 485 nm detected signal is not overlapping with the 560 nm in uncorrected mode. In mosaic mode, the shift between the 485 nm and 560 nm beams can be corrected, as demonstrated in Figure 7.11

(b). The required correction for the 560 nm beam was determined by measuring the shift between the 485 nm and 560 nm beams for two opposite outermost image tiles and the values for the remaining tiles were calculated assuming a radial linear chromatic shift, for more details refer to subsection 9.5.4.

The performance of STED microscopy is critically dependent on the overlap of the excitation and depletion PSF in the sample plane with sub-diffraction accuracy and the consequences of any chromatic shift cannot be compensated in post processing, as may be possible with two color imaging. This limits the effective FOV for many STED microscopes. With easySLM-STED, however, the mosaic mode enables the usable FOV to be increased by adjusting the position of the depletion doughnut to overlay it with the excitation focus for each tile, as illustrated in Figure 7.12. For this experiment the easySLM-STED system was aligned to the centre of the FOV (i.e. the optic axis) and the light scattered from an isolated gold bead at 9 positions across the extended FOV separated by approximately 40 μm was imaged to indicate the depletion and the excitation lateral PSF. In the conventional mode (i.e. with same SLM setting applied for whole FOV, the excitation and depletion PSF are overlaid in the centre of the FOV but walk-off is apparent in the images for the surrounding tiles. For the corrected mode, the excitation and depletion PSF are much closer to coincidence for all the tiles. The images were acquired with a pixel integration time of 50 μs, 3-frame accumulation and a pixel size of 5 nm.

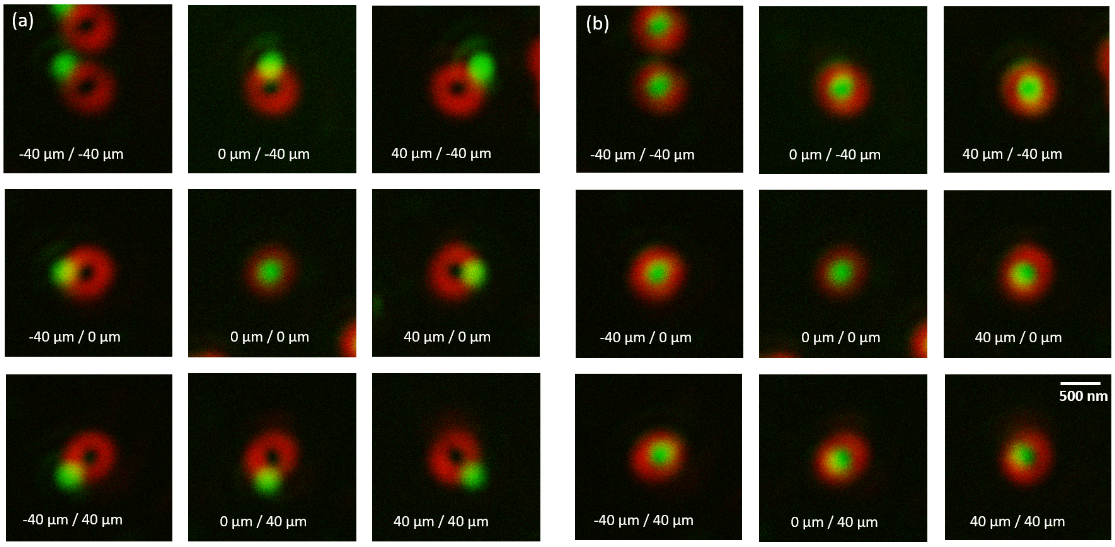

Figure 7.12: *(a) gold bead sample without and (b) with aberration correction in easySLM-STED mode. 485 nm in green and 560 nm in red for the centre tile and 40 μm distance from the centre [Gö18].*

7.2.2 Sequential aberration correction for mosaic easySLM-STED

The benefits of mosaic easySLM-STED with aberration correction were explored using a fluorescent bead sample. For each image tile, three different corrections are applied: a position correction to ensure that the excited fluorescence continues to be focused onto to the pinhole as the excitation beam is scanned across the extended FOV; a correction to ensure that the depletion beam is coincident with the excitation at the sample and a correction to the z offset that must be applied to correct for a tilt of the sample. An image over 100 μm x 100 μm was acquired with a pixel size of 25 nm and a pixel integration time of 300 μs. The excitation and depletion powers in the sample plane were 8 μW and 7 mW respectively. For the mosaic acquisition, the FOV was divided into 25 tiles of 20 μm x 20 μm each. Figure 7.13 illustrates that the uncorrected STED resolution became significantly degraded away from the optical axis, eventually approaching that of the confocal microscope as the excitation and depletion PSF no longer overlapped although still presenting some degradation with respect to optimised confocal microscopy since the fluorescent signal becomes misaligned to the confocal pinhole. In contrast, the sub-diffraction resolution for the corrected mosaic approach was more consistent across the full FOV. It should be noted, that due to bleaching, the FOV was changed between the corrected and uncorrected easySLM-STED to ensure similar sample conditions for both approaches.

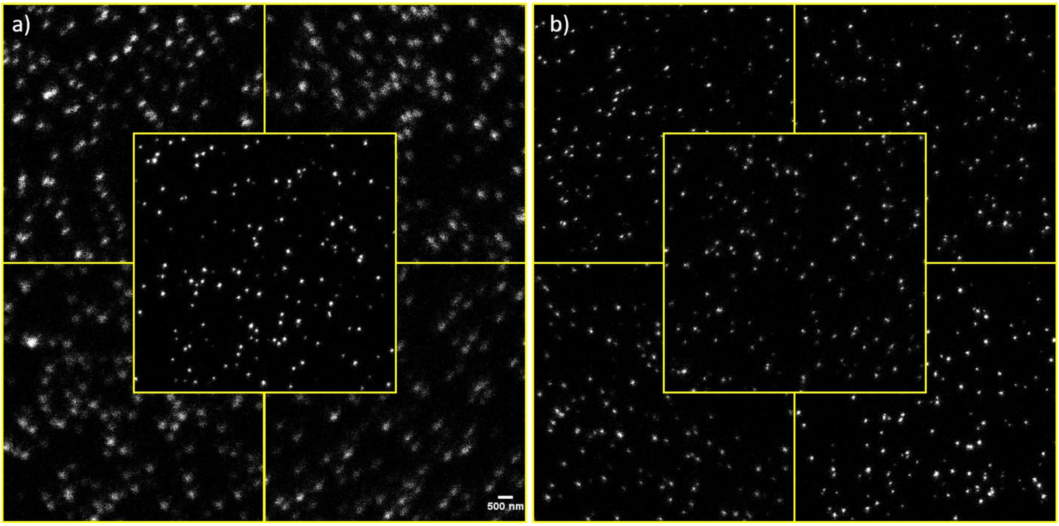

Figure 7.13: *easySLM-STED fluorescent bead sample (a) without and (b) with aberration correction in mosaic mode. The field in the middle corresponds to the centre tile, whereas the corner fields corresponds to the corner tiles of the mosaic. Each panel shows a FOV of 9 μm x 9 μm, the entire FOV imaged was 100 μm x 100 μm, and the outer tiles show the image from the corners of the entire FOV [Gö18].*

The differences between uncorrected and mosaic easySLM-STED can be quantified by analysing the fluorescent bead images using the ThunderSTORM software [Ove14], which can fit isolated point-like structures to a Gaussian function. The returned data includes the x and y co-ordinates, the intensity and the FWHM of each identified bead "event". This ThunderSTORM information was analysed using *MATLAB* by reconstructing the images and plotting the intensity or FWHM of each bead, as displayed in Figure 7.14 and Figure 7.15 respectively, hereon called intensity and FWHM "localization images". Note that the loss of beads in to the bottom of the uncorrected confocal scan is due to a tilt of the coverslip that was successfully compensated in the mosaic approach.

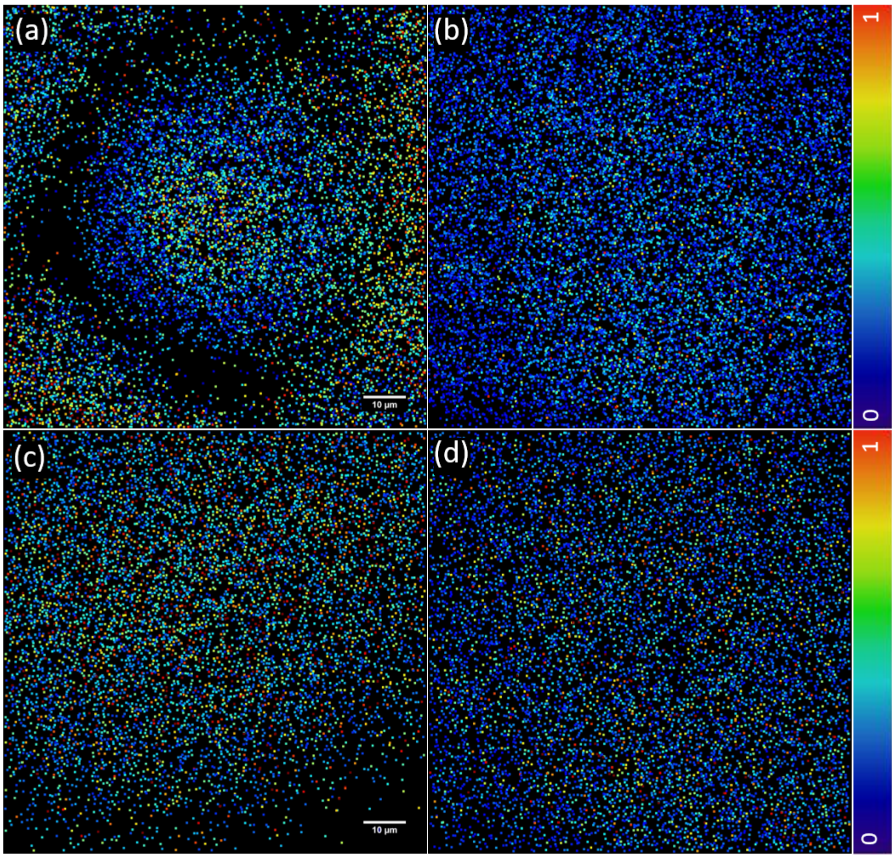

Figure 7.14: *Normalised intensity localization images in (a) uncorrected, (b) mosaic easySLM-STED modes; (c) normal confocal and (d) aberration-corrected mosaic confocal modes (colour scale from 0 – 2000 for STED and 0 – 4000 for confocal mode; black indicates no beads were found).*

The ring pattern seen at 25 – 30 μm from the centre in the intensity localization image for the uncorrected STED mode is due to onset of the chromatic shift between the excitation and depletion beams that produces a drop in intensity as the peak ring intensity of the depletion doughnut overlaps with the peak excitation intensity, as presented in Figure 7.16 (a). At this point, the

STED PSF is depleting most of the excited fluorophores. Further from the centre, the excitation PSF no longer overlaps the depletion PSF and the fluorescence signal recovers. The mosaic STED mode shows a more constant fluorescence intensity over the entire FOV. The confocal mode (i.e. with no depletion beam present) shows similar intensity distributions remaining constant over the complete FOV (Figure 7.16 b).

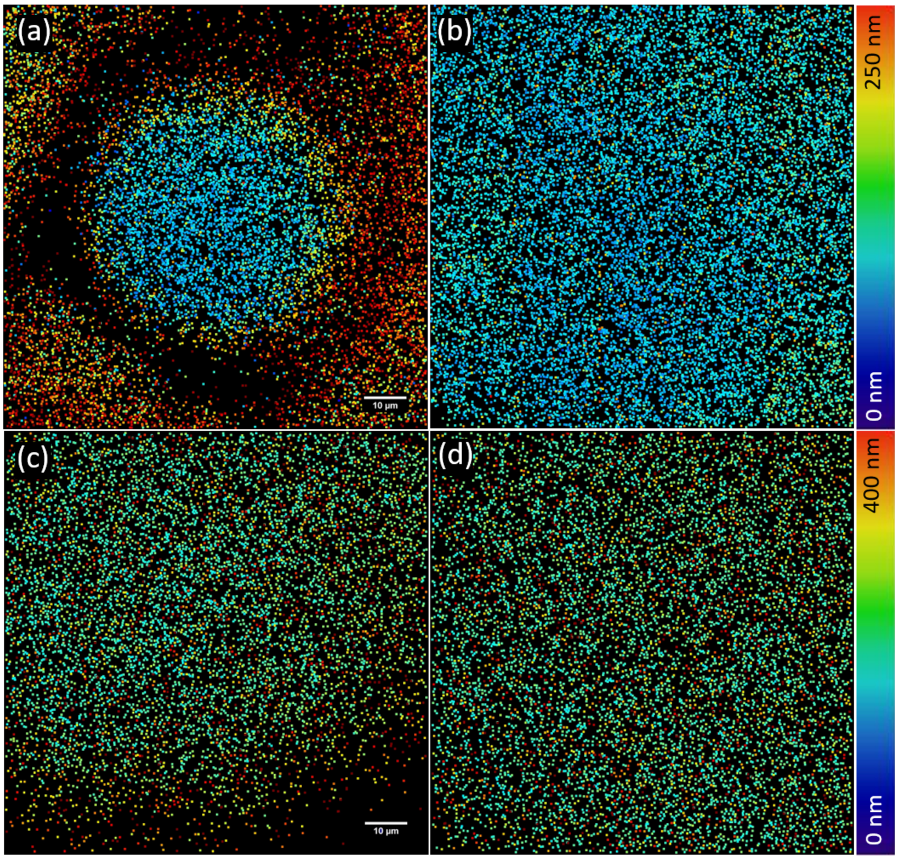

Figure 7.15: *FWHM localization images in (a) uncorrected, (b) mosaic easySLM-STED modes; (c) normal confocal and (d) aberration-corrected mosaic confocal mode (colour scale from 0–250 nm for STED and 0–400 nm for confocal mode; black indicates no beads were found). Adapted from [Gö18].*

An even more pronounced ring pattern is observable in the FWHM localization image, as presented in Figure 7.15. The FWHM localization variations of the "normal" uncorrected STED and corrected mosaic STED images are plotted against the distance from the centre in Figure 7.16 (c), where it is apparent that the measured FWHM starts to increase after 20 μm as the perfect overlap of excitation and depletion starts to decrease. After 40 μm from the centre, the FWHM reaches a plateau value where the two laser beams do not overlap any more, which is the confocal microscope resolution, as shown in Figure 7.16 (c). The corrected mosaic STED plots do not follow this trend but present a reasonably constant sub-diffraction FWHM over the entire FOV. Figure 7.16 (d) shows the analogous plot in the absence of the depletion beam, where the FWHM remain reasonably constant over the full FOV.

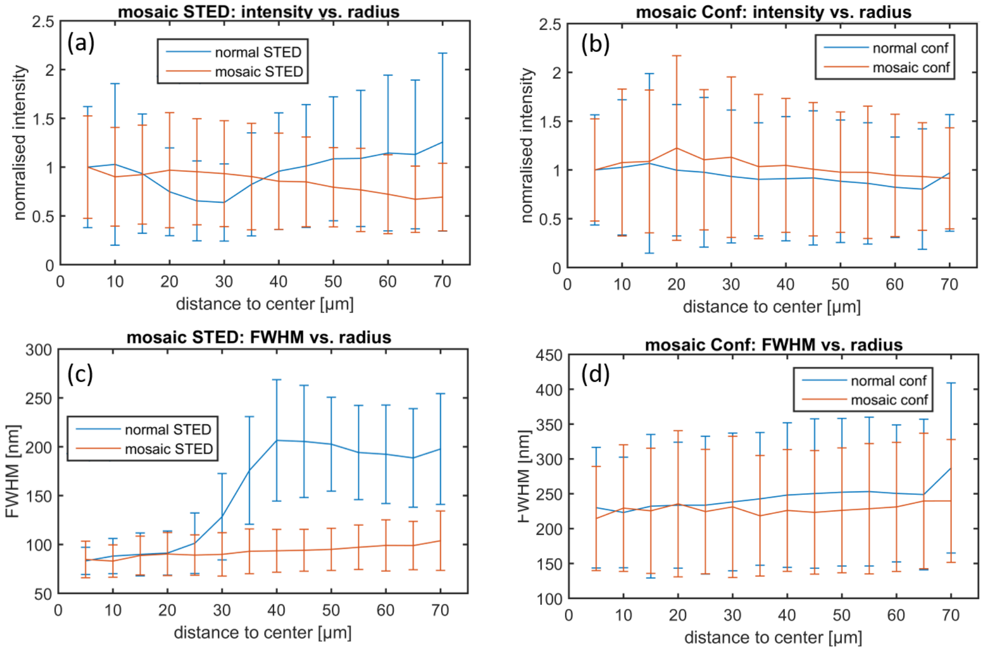

Figure 7.16: *Radial dependence of localized intensities and FWHM of fluorescent beads in mosaic and normal imaging modes: (a) easySLM-STED image intensity, (b) confocal image intensity, (c) easySLM-STED image FWHM and (d) confocal image FWHM. Adapted from [Gö18].*

In Figure 7.16, the intensities were normalised because the data were acquired on different days with varying powers coupled into the optical fibre. Figure 7.17 shows similar plots for confocal microscopy data acquired on the same day for normal and corrected mosaic modes that did not need to be normalised.

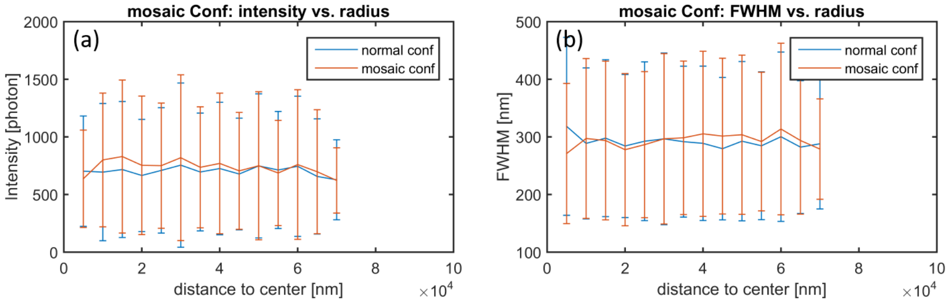

Figure 7.17: *Performance comparison of normal and mosaic approach in confocal mode. (a) confocal image intensity and (b) FWHM.*

7.2.3 Mosaic easySLM-STED of biological samples: vimentin in Vero cells

A sample of fixed Vero cells with fluorescently labelled vimentin sample was used to demonstrate mosaic easySLM-STED in biological samples. A 100 μm x 100 μm FOV was scanned in normal confocal and mosaic easySLM-STED modes. The mosaic easySLM-STED approach resolves smaller structures over the extended FOV, as shown in Figure 7.18. For this data, the pixel size was 50 nm with an integration time of 150 μs per pixel. The excitation and depletion powers were 7 μW and 2 mW respectively.

The edges of the tiles are clearly visible in the mosaic easySLM-STED image (Figure 7.18 b). The reason is that, while scanning a tile, the beam overlaps with the first lines of the next tile. This increased light exposure for the lines close to the edges of the tiles increases results in more discernible photobleaching in the easySLM-STED images compared to the normal confocal microscopy images where they are not apparent.

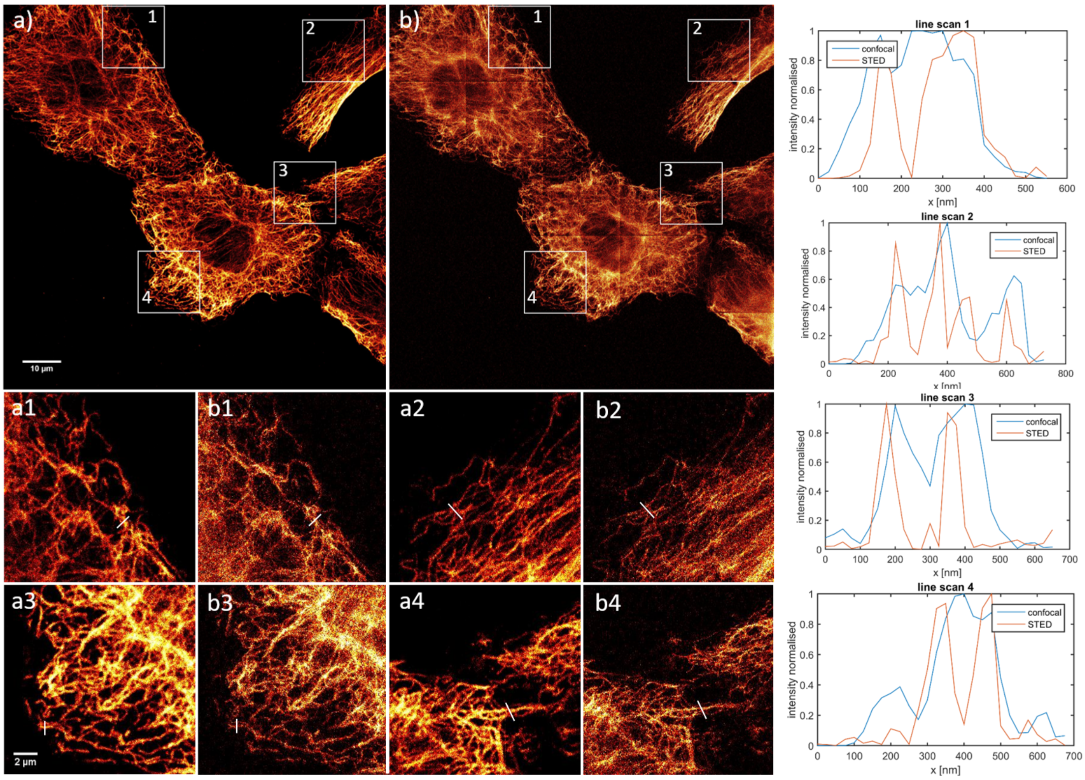
a)
b)
1
2
3
4
10 µm
a1
b1
a2
b2
a3
b3
a4
b4
2 µm
line scan 1
line scan 2
line scan 3
line scan 4
confocal
STED
intensity normalised
x [nm]
0
0.2
0.4
0.6
0.8
1
100
200
300
400
500
600
700
800

Figure 7.18: *Mosaic easySLM-STED image of vimentin in Vero cells. (a) confocal mosaic and (b) easySLM-STED mosaic image with inserts (1–4) and linescans [Gö18].*

7.3 Multibeam easySLM-STED

Increasing the image acquisition speed of STED is important, particularly for live cell or in vivo applications. Like other laser scanning microscopy techniques, it lacks the highly parallel image acquisition of wide-field detection techniques but can be accelerated to some extend through the use of parallel scanned beams, which was demonstrated before using separated depletion beams [Bin11] or a lattice of depletion beams with several thousand zero points [Chm13, Ber15]. Here we take advantage of the capability of an SLM to generate multiple beams from a single computer-generated hologram and extend the easySLM-STED concept to generate and scan multiple excitation and depletion PSFs simultaneously.

The easySLM-STED microscope from section 7.1 was modified to generate and detect multiple pairs of excitation and depletion beams. In the detection path, the single detection optical fiber served as the confocal aperture was replaced with an array of 13 linear spaced graded index optical fibers of the same model as for the single beam setup (i.e. 62.5 μm, diameter, M31L03, Thorlabs). Seven of these fibers were purchased as patch cables with fiber mounts at both ends. These were cut in half, stripped and the bare fibers were mounted into a linear array with Epoxy (F112 – Epoxy for Fiber Optic Connectors, Thorlabs) using a custom-made mount. The optical fiber array was polished, and four of the fibers were connected to separate photomultipliers (H7422, Hamamatsu). The electrical signals from these detectors were amplified (HFAC-26, Becker & Hickl) and read out with a TCSPC card (SPC-830, Becker & Hickl) using a router (HRT-41, Becker & Hickl). Images were acquired using *SPCM* (Becker & Hickl) and analysed with *SPCimage* (Becker & Hickl).

7.3.1 Generation of multiple beams

To generate a specific intensity pattern in the sample plane the computer-generated hologram was designed by calculating the intensity diffracted by the SLM using a scalar theory, building on previous work by Prof. Mark Neil [Nei00b]. Only the intensity in the sample plane is of interest and so the phase becomes a free variable. The computer-generated hologram was iteratively optimised using a "direct binary search" algorithm [Sel87]. Briefly, a scalar calculation of the diffracted intensity at each target point in the focal plane of the objective lens was performed for an input wavefront that was the conjugate of the desired wavefront. For the desired doughnut-shaped intensity profile, the input wavefront is helical. The target intensities for these points is 1, which effectively requires the hologram to generate the desired wavefront for each target point if a plane input wavefront is used. Each pixel is examined in a random sequence and the pixel phase is chosen to minimise a cost function [Dam91] based on the difference between the calculated intensities and the target intensities across all target points. The pixel phases were examined in steps of $\pi/8$ (16 phase levels in total), which should give a performance in terms of diffraction efficiency that is 99% of that of a continuous phase mask. In performing the optimisation, each pixel of the hologram was iterated four times, which was sufficient to produce an effective hologram. The algorithm was written in *MATLAB* by Prof. Mark Neil and converted to a C based MEX (*MATLAB* executable) using *MATLAB* coder. The MEX was incorporated into the *LabVIEW* hologram software to apply a specific phase pattern to a corresponding target intensity profile. The simulations of the intensity distribution in the sample plane presented were calculated using a fast Fourier transformation [Coo65]. These simulations are scalar and neglect possible unwanted z-components in the sample plane, which is significant for high NA approaches. However, the choice of the correct combination of polarisation and helicity of the wavefront avoided additional z-components, a wrong combination is shown in Figure 9.6. This approach can be extended to a full vector-based analysis, as is discussed for some aberrations in subsection subsection 9.5.6.

The variable parameters are the number and positions of the beams and whether the PSF should be a regular Gaussian focus or a doughnut-shaped depletion function. Different focal patterns were generated and quantified by imaging light scattered from an isolated gold bead using the wide-field detector. The following paragraphs present exemplar images of the intensity distributions in the focal plane to illustrate the capabilities of the system. Each experimental image is displayed with the applied hologram and the simulation of the corresponding image plane.

Type of pattern (linear or lattice): Different focal intensity patterns can be generated, as illustrated in Figure 7.19, which shows lines of four beams separated by 1 μm between each beam, orientated in x or y, and lattice patterns with spacings of 1 μm or 2 μm. For the following easySLM-STED experiments, the y line pattern of Figure 7.19 (a) was chosen because of its superior linearity and lower intensity minimum at the centre of the doughnut. The lattice pattern was not selected because the detector fiber array would have been much more complex to build than for the single line.

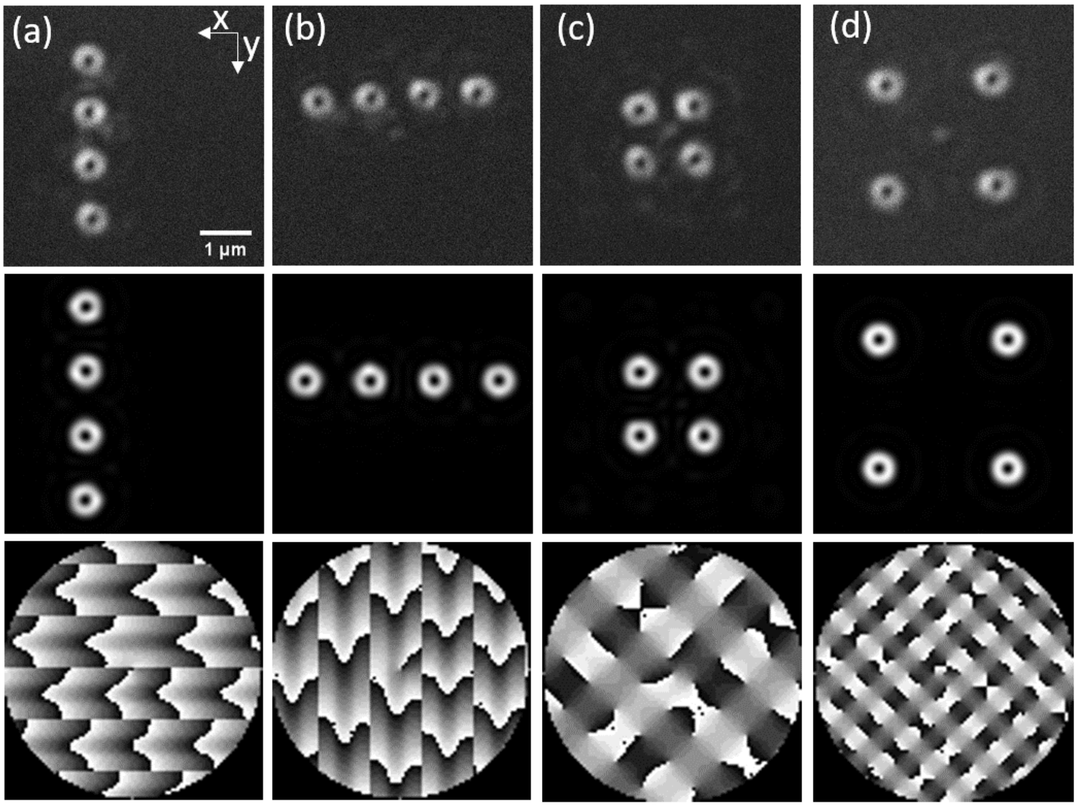

Figure 7.19: *Multibeam easySLM-STED line and lattice pattern generation: (a,b) line of 4 depletion beams orientated along y, x axes with 1 μm spacing; (c,d) lattice patterns with 1 μm and 2 μm spacings. Top row: experimental image of focal plane intensity distributions, middle row: simulated sample plane image and bottom row: hologram applied to SLM.*

Spacing between beams: The spacing between four doughnut-shaped beams was changed from 0.5 μm to 4.5 μm as presented in Figure 7.20 with column I → 0.5 μm, II → 1.0 μm, III → 1.5 μm, IV → 2.0 μm, V → 2.5 μm, VI → 3.0 μm, VII → 3.5 μm, VIII → 4.0 μm and IX → 4.5 μm. The data for each condition was acquired separately and they were combined into a single image for better visualisation. The wide-field detected scattered light images are almost identical to the theoretical patterns. Even where higher orders are observed in the experimental data, as seen in pattern VIII, a corresponding higher order beam, albeit with much lower intensity, can be identified in the simulation and in the wide-field image. In pattern VIII and IX, the beams with the largest distance to the optical axis are not imaged clearly or not imaged at all, due to the limited lateral extent of the wide-field detector. This is not a problem if a wide-field detector with a larger FOV or a corresponding fiber array is used, or if the current wide-field detector could be translated in the y direction to collect all the light. In pattern I, the beams are too close together and interference occurs, resulting in a difference between simulation and experiment. All patterns show an additional beam in the centre of the FOV. This is unmodulated light, which is not considered in the simulation.

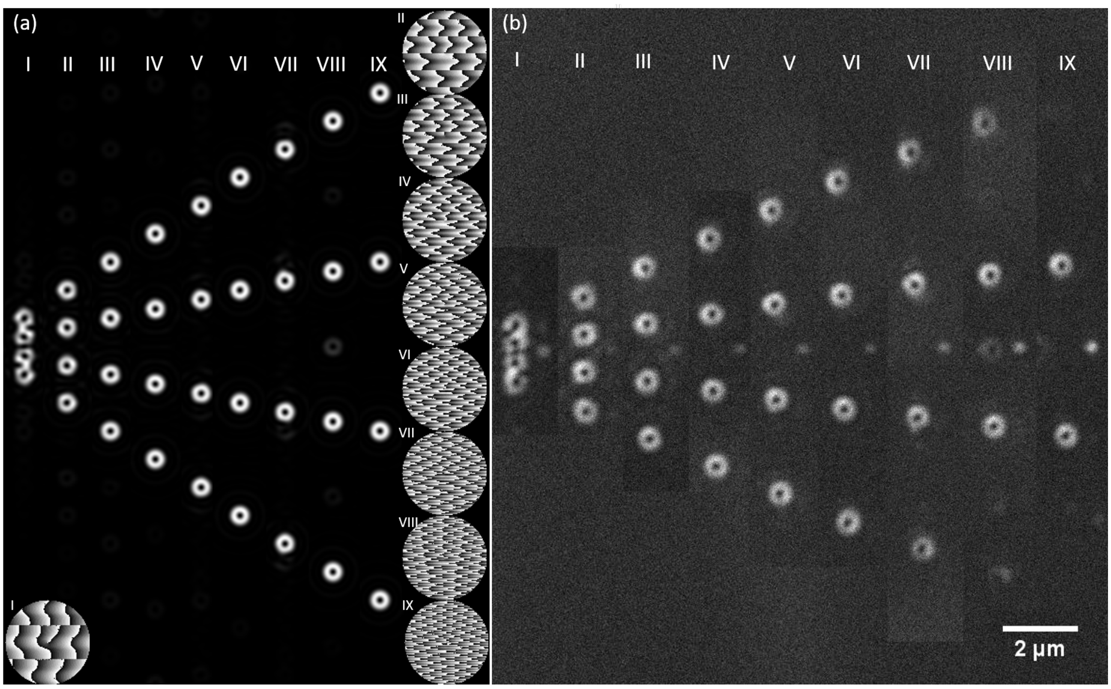

Figure 7.20: *Generation of differently spaced easySLM-STED beams: (a) simulation and applied holograms for different beam spacings and (b) experimental measurements of corresponding focal plane intensity distributions.*

Number of beams: The number of generated beams was varied from 1 to 8, with a constant spacing of 1 μm, as illustrated in Figure 7.21. The experimental data (b) particularly shows how the quality (contrast) of the depletion PSF degrades with increasing number of beams. This is due to the limited number of adjustable SLM elements and the increased complexity of the hologram pattern, which can be seen in (a) right, and the laser intensity per beam is reduced by the number of beams applied.

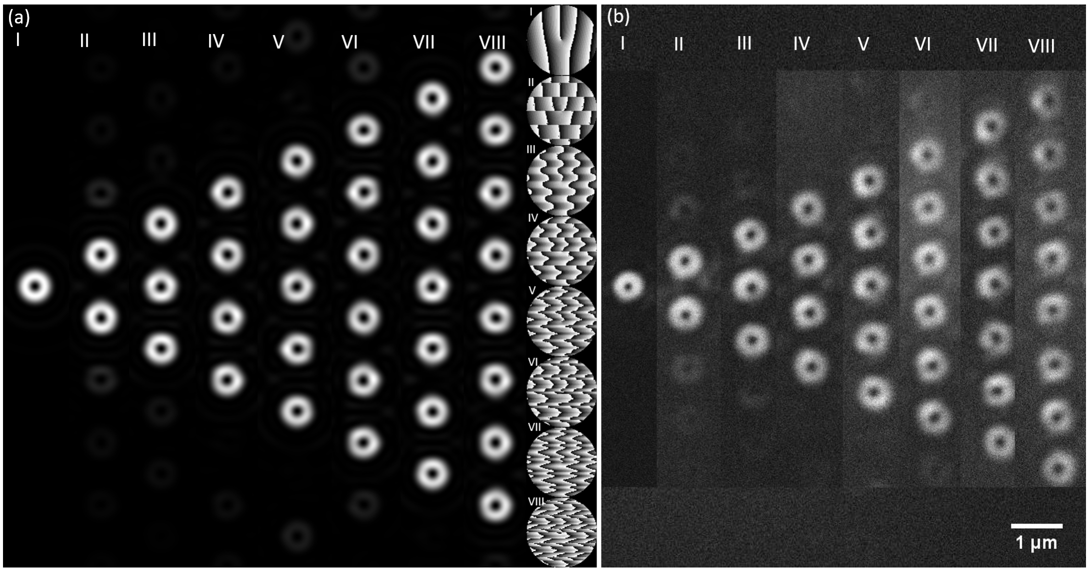

Figure 7.21: *Generation of different numbers of easySLM-STED beams: (a) simulation and applied holograms for different numbers of spots and (b) experimental measurements of corresponding focal plane intensity distributions [Gö18].*

Quality of multiple PSF: The impact of astigmatism correction in x and y were studied using four beams to produce four PSF with a spacing of 1 μm. The quality of the doughnut PSF can be enhanced by adjusting the holograms for every beam separately to achieve similar quality to a single beam, as shown in Figure 7.22. Without any correction, the doughnut is not as radially symmetric as is the case for corrected beams (Figure 7.22 a). The corrections for the first three beams are marginal, for the last beam minor astigmatism could be compensated. If the axial scans are considered, the corrected x-y scans are reasonable, but the y-z scans show a tilt in the zero-intensity line (Figure 7.22 b). This tilt is largest where the beams are further from the optical axis (and therefore from the centre of the objective lens) and changes direction when passing the centre of the FOV. This aberration is discussed further in subsection 9.5.6.

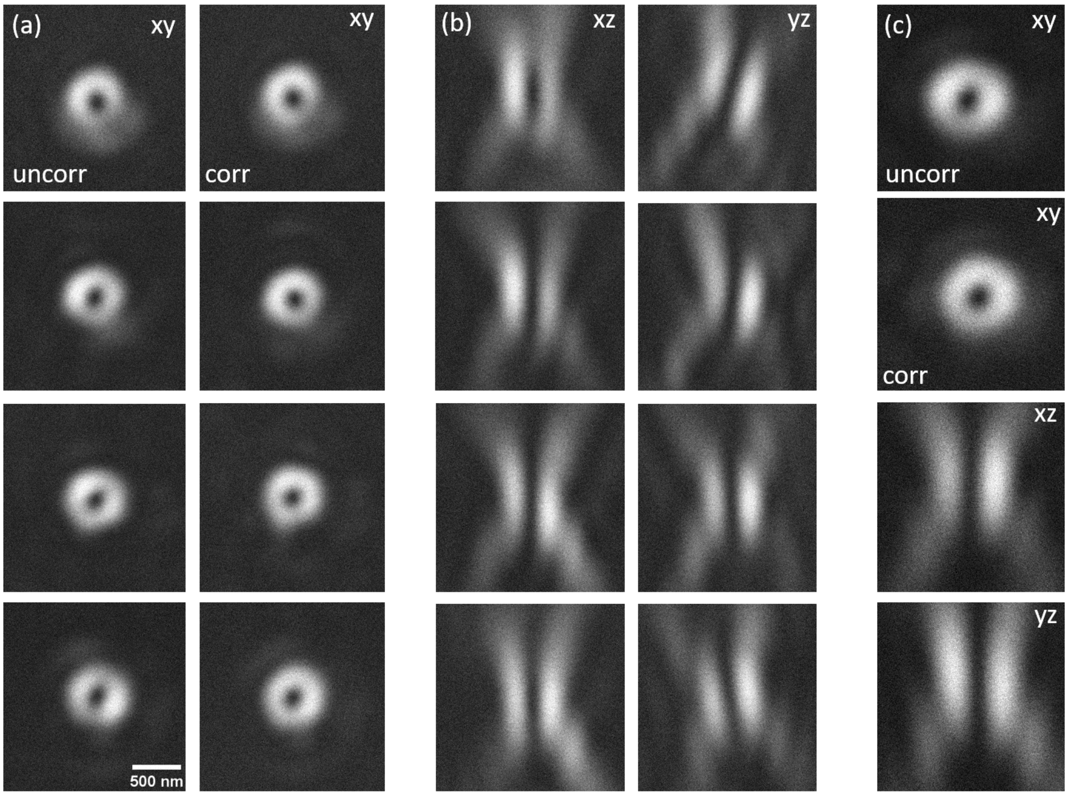

Figure 7.22: *Four beam easySLM-STED beams compared to single beam easySLM-STED. (a) First column: x-y images of 4 uncorrected beams. Second column: x-y images of the corresponding corrected beams. (b) First column: high quality x-z scan of multiple beams with astigmatism correction. Second column: y-z scan with correction. (c) single beam easySLM-STED beam for comparison, from top: x-y uncorrected, x-y corrected, x-z corrected and y-z corrected beam profiles.*

7.3.2 Performance of multibeam easySLM-STED scanning separate sub-regions

Parallelization in scanning microscopy can improve the image acquisition speed by reducing the total image integration time by a factor equal to the number of beams. This can be realised by scanning separate sub-regions with each beam in parallel. This approach reduces the image (frame) acquisition time and can be implemented by scanning with equally spaced spots that interrogate different rows of pixels in parallel, but this requires the detector fibre array to be precisely equally spaced, otherwise the sub-regions will overlap or miss areas between them.

Using the approach of scanning multiple sub-regions in parallel, a fluorescent bead sample was used to demonstrate the impact on performance of increased imaging speeds. Using 4 pairs of excitation/depletion beams, the expected speed improvement was realised without losing resolution, as illustrated in Figure 7.23. For comparison, the same sample was imaged by scanning a single beam pair and using the third of the fibers used for the four-beam approach, thus the FOVs are slightly shifted. The FOV size for the single beam scan was 10 μ x 10 μm with a pixel size of 25 nm and a pixel integration time of 300 μs. For the four-beam method each sub-region size was 10 μm x 2.5 μm, with the other scan parameters being kept constant. The intensity of each excitation/depletion beam pair at the sample was adjusted to be equal for the single beam pair scan. The FWHM and intensity localisation images were calculated using ThunderSTORM as described previously and can be found in Table 7.1.

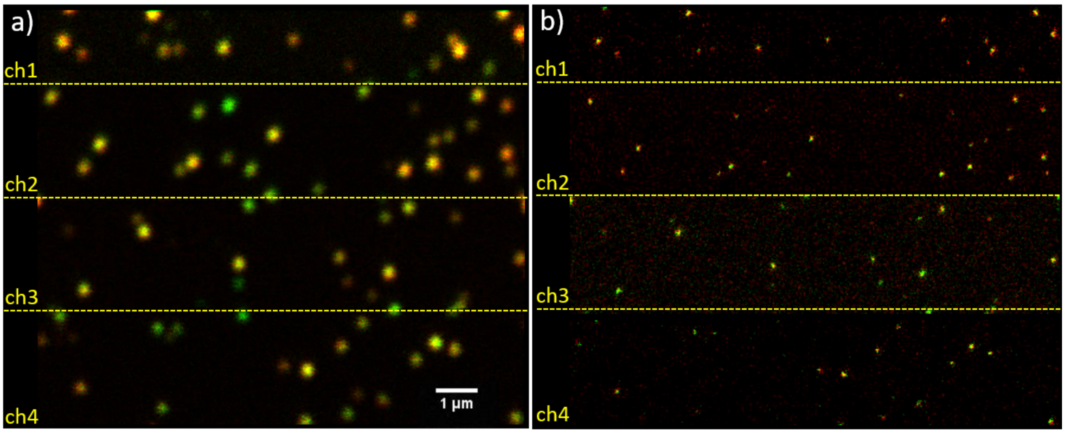

Figure 7.23: *Multibeam easySLM-STED images of fluorescent beads. (a) confocal image acquired with single scanning beam pair (red) and 4 scanning beam pairs (green), (b) corresponding easySLM-STED images. Note that the images are adjusted such that the centres of the brightest beads saturate the image in order that more of the dimmer beads can be seen [Gö18].*

The confocal images show no significant difference in resolution for the single scanned beam (FWHM: 203 nm, stdev: 33 nm), and the four scanned beams (FWHM: 190 nm, stdev: 31 nm). Similarly, the STED performance is not reduced, achieving similar resolutions for the single scanned beam STED (FWHM: 65 nm, stdev: 24 nm), and for the four scanned beam STED (FWHM: 61 nm, stdev: 17 nm). Comparing the four sub-regions, the resolutions achieved were similar, however, the intensity was consistently lower for ch4. This might be due to poor alignment or a damaged detection fiber. The easySLM-STED acquisition time was reduced from 48 s for the single scanned beam to 12 s for the four scanned beam approach.

The laser intensities for the single beam approach were 8 μW and 7 mW for the excitation and depletion respectively, measured before the objective. For the multi-beam scan the intensities were increased by a factor of four to guaranty equal resolution performance for both approaches.

	FWHM [nm]	stdev [nm]	intensity
confocal ch1	184	34	6743
confocal ch2	194	42	6874
confocal ch3	203	30	4419
confocal ch4	181	16	2938
confocal mean of all ch	190	31	5243
confocal single beam	203	33	5681
STED ch1	61	14	609
STED ch2	64	18	609
STED ch3	65	23	796
STED ch4	54	13	219
STED mean of all ch	61	17	558
STED single beam	65	24	618

Table 7.1: *Multibeam easySLM-STED of fluorescent bead sample data. The mean of the FWHM with stdev and the mean of the intensity [Gö18]. Data analysed from Figure 7.23.*

Line profiles corresponding to Table 7.1 show the superior resolution of STED and similar improvements for the single and the multi beam approach in each channel (Figure 7.24). To generate the graph for every condition three random fluorescent beads were chosen to produce line profiles. They were normalised and averaged to be comparable to their corresponding confocal line profiles.

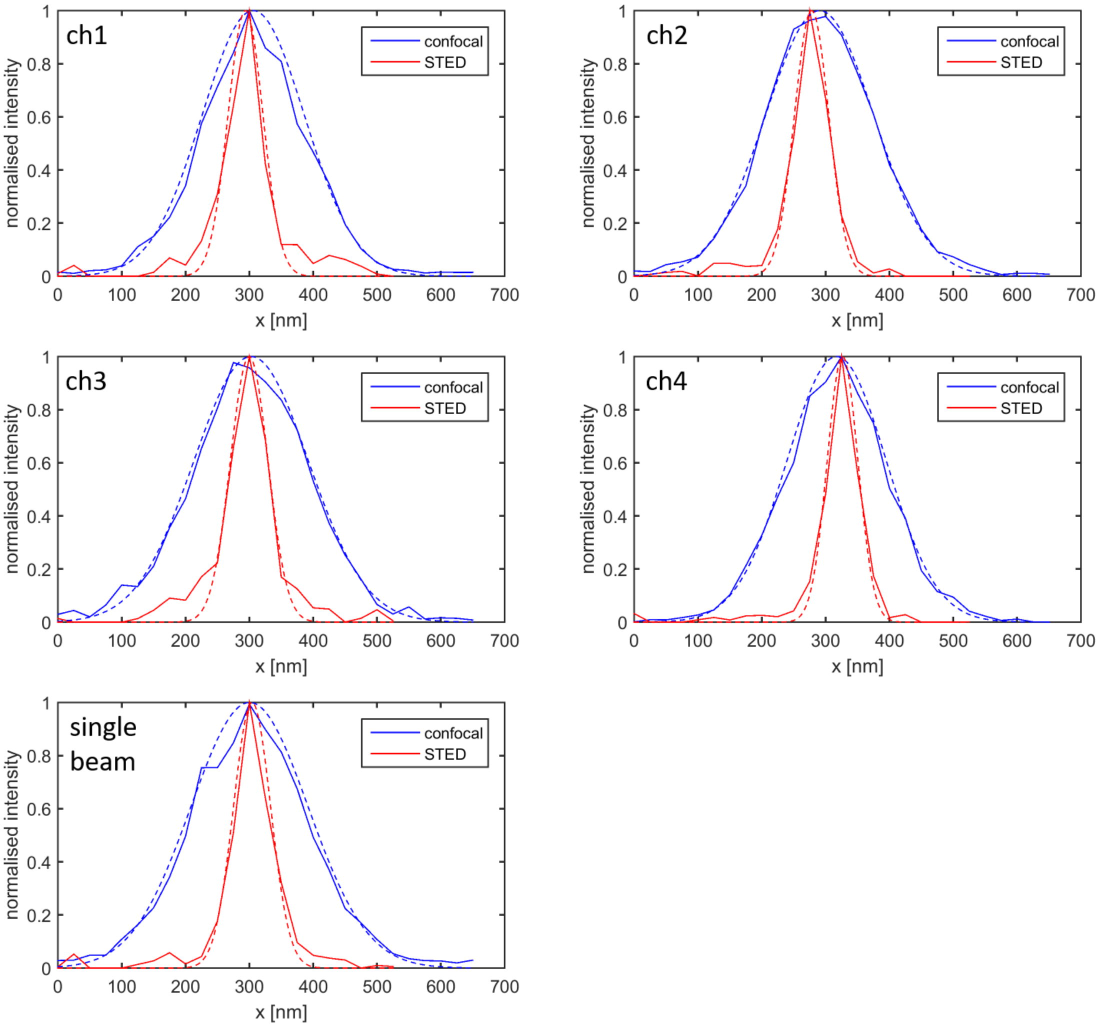

Figure 7.24: *Line profiles over fluorescent beads acquired via multibeam easySLM-STED. Experimental data shown in straight lines and a Gaussian profile with a FWHM from Table 7.1 is presented as dotted lines. Corresponding images are shown in Figure 7.23.*

Multibeam easySLM-STED of biological sample - *C. elegans*: The germlines of *C. elegans* were imaged with the multibeam easySLM-STED method, as described above, to visualise the synaptonemal complex, as seen in Figure 7.25. Scanning 4 beam pairs in parallel reduced the image acquisition time from 48 s to 12 s. A pixel size of 25 nm with a pixel dwell time of 100 μs was applied over a 10 μm x 10 μm FOV using three-frame accumulations. The sub-region size for the four scanning beam approach was 10 μm x 2.5 μm with the same scan parameters as the single scanned beam image.

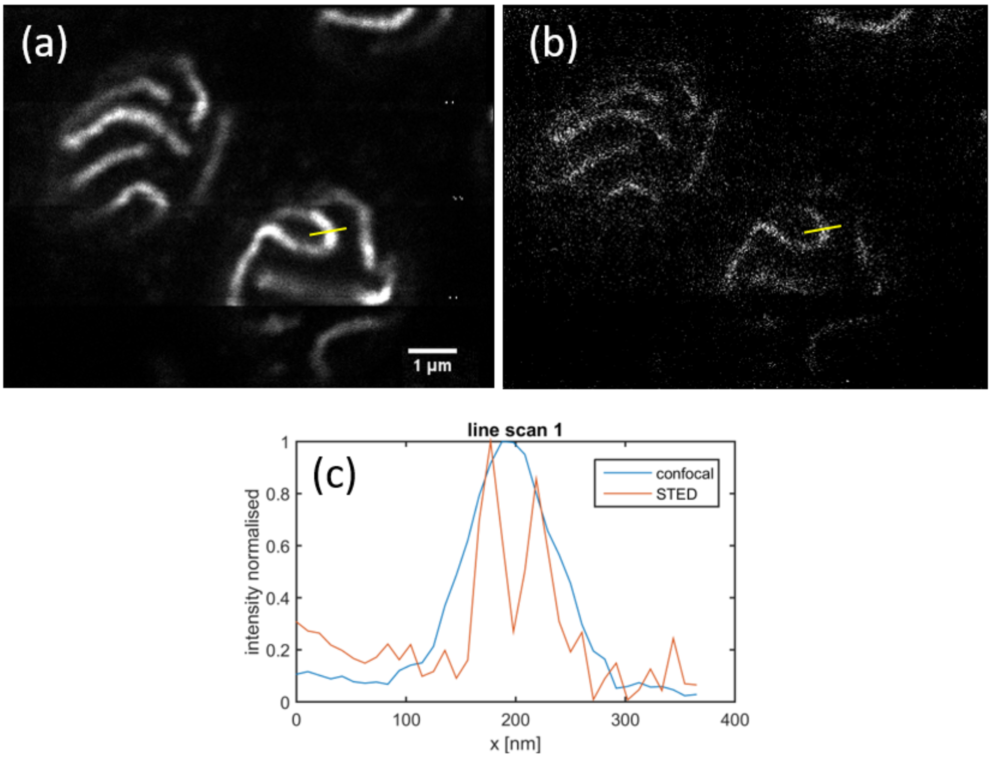
(a)
1 µm
(b)
line scan 1
(c)
confocal
STED
intensity normalised
0
0.2
0.4
0.6
0.8
1
0
100
200
300
400
x [nm]

Figure 7.25: *Multibeam STED image of synaptonemal complex in C. elegans. (a) confocal multibeam image, (b) corresponding easySLM-STED multibeam image and (c) line scan of synaptonemal complex gap.*

7.4 Summary

Summary This chapter introduced a new concept for STED microscopy: "easySLM-STED", which uses a single SLM to shape excitation and depletion pulses, correct for aberrations, including in a mosaic mode to enhance the usable STED FOV, and generate parallel beams to increase image acquisition time. It aims to provide a more user-friendly approach to implement and operate a STED microscope. Because it offers the capability to electronically control the overlay of the excitation and depletion PSF, it has the potential to be automated to maintain a consistent performance. The electronically programmed compensation of aberrations also provides the potential for machine-learning approaches to compensate for aberrations, e.g. in biological samples.

easySLM-STED was demonstrated imaging fluorescent beads and Vero cells with antibody-labelled vimentin and the imaging performance was quantified. It was also applied to image germlines of *C. elegans* and was able to resolve the synaptonemal complex. The mosaic easySLM-STED technique with chromatic aberration correction was shown to increase the usable FOV for STED microscopy up to 100 μm. A fluorescent bead sample was used to validate this approach and it was also applied to image labelled vimentin in Vero cells. Finally, the extension to multibeam easySLM-STED was shown to decrease the total STED image acquisition time through parallel scanning of multiple beams and the concept was demonstrated using four scanning excitation/depletion beam pairs. The speed gain was shown on fluorescent bead and *C. elegans* samples.

Contribution I designed and built the easySLM-STED set-up and its extension to mosaic and multibeam imaging. I undertook the experiments and data analysis reported in this chapter. I prepared the gold nanoparticle and fluorescent bead samples. The fixed Vero cell sample with labelled vimentin was purchased from Abberior GmbH. The *C. elegans* samples were prepared by Angel Jaso-Tamame.

I wrote the instrumentation control program. The hologram program was initially written by Dr. Hugo Sinclair and modified by me, including the addition of a *MATLAB* function to optimise holograms that was originally written by Prof. Mark Neil.

Chapter 8

Conclusion and outlook

The development and application of several fluorescence imaging technologies for studying biological processes on scales below the diffraction limit have been described in this thesis.

Chapter 2 summarized the photophysics of fluorescence imaging and spectroscopy, including wide-field and laser scanning fluorescence microscopy techniques, FLIM and FRET and different approaches to super-resolved fluorescence microscopy. An overview of adaptive optics for the compensation of optical aberrations was also presented. Super-resolved fluorescence microscopy has still a lot of potential for development, especially in respect to live cell imaging, where all presented methods have their disadvantages such as structured illumination microscopy with the limited resolution, localisation methods need special toxic buffers and stimulated emission of depletion microscopy utilizes a high-power laser beam leading to phototoxicity.

In **Chapter 3** an open source FLIM HCA instrument was presented, for which I wrote the data acquisition software in the open source program, *µManager*, and developed a workflow and short instruction manual that was published in the Journal of Visualised Experiments [JoV17]. The hardware configuration and links to the open source software for "openFLIM-HCA" were published at `https://github.com/imperial-photonics/openFLIM-HCA`. We hope that this open source project encourages other research groups without the necessary expertise to develop their own automated FLIM platereader. With the provided open source code the functionality of the system can be adjusted or extended to adapt individual experiments. I characterised the open FLIM HCA instrument performance using reference samples based on known dye solutions experiments and demonstrated the ability to quantify mixtures of fluorophores with a standard deviation <0.04%. I also evaluated the system performance when imaging COS-7 cells expressing fluorescent protein(FP)-based FRET constructs and demonstrated standard deviations of <30 ps when measuring fluorescent protein lifetimes. I evaluated the performance of the system for FRET experiments by imaging multiwell plates with arrays of mixtures of different FP-based FRET constructs, which can provide a reproducible test sample for FLIM HCA instruments. In this interdisciplinary field of research measurements are not limited to a single system, technique or laboratory, therefore it is essential to guaranty consistency between measurements. These standardized experiments allow an evaluation between different instruments, laboratories and FLIM techniques. Further, I applied the system to a live cell FRET assay of HEK293T cells expressing an Epac biosensor for cAMP and the response to forskolin stimulation. This engineered biosensor has an enhanced performance for FLIM experiments and provides a functional readout of activation processes inside living cell.

In **Chapter 4** I worked to improve the performance of the wide-field time-gated imaging that is the heart of the open FLIM HCA instrumentation. To achieve a uniform excitation intensity across the field of view, it is necessary to remove any laser speckle and to flatten the Gaussian beam profile that is associated with laser beams. Laser speckle can be removed by time-averaging within the image acquisition time and the flattening of the intensity distribution can be achieved by using an engineered holographic diffuser or the light output from a multimode fibre. I explored these approaches and also the use of a compact deformable mirror and found the best performance when using the engineered diffuser, which could be translated or used in conjunction with the DM or a vibrating multimode fibre to time-average the speckle.

The crucial optical element of time-gated wide-field FLIM is the optical image intensifier (GOI) with its limited resolution and the low effective quantum efficiency. To improve the performance of FLIM experiments Kentech Instruments Ltd developed a new prototype of GOIs. This device incorporates a magnetic field to improve the spatial resolution by decreasing the lateral spread of photoelectrons between the photocathode and the microchannel plate and it enables longer time-gate widths to be used, which increases the number of detected photons and therefore the precision of lifetime determination. I compared the performance of this prototype (GOI) with the commercially available state-of-the-art using the open FLIM HCA instrument to image test samples of HEK293T cells expressing fluorescent protein-based FRET constructs, in order to ensure that the measurements were made under conditions relevant to cell-based assays.

The open FLIM HCA instrument could be improved in a number of ways: for the specific implementation with the Olympus IX-81 frame, the autofocus is the limiting factor for the total multiwell plate image acquisition time of the current system. This could be addressed by either using a commercial microscope frame with a faster optical autofocus unit or by implementing a separate autofocus module.

The next limitation is the time to acquire the sets of time-gated fluorescence images. This could be decreased if the modulated CMOS approach could be employed [Esp06, Che15b]. This would entail changing the system to a frequency domain FLIM system, which would require different analysis software tools. Alternatively, an array of detectors with integrated TCSPC on each pixel could be used [Pol15] although the current state of technology is limited by the maximum practical data rate and the availability of sensor arrays with sufficient pixels. Even with the demonstrated resolution improvement, other FLIM techniques such as TCSPC or frequency domain FLIM are acquiring images with higher resolution as wide-field time-gated FLIM. The resolution of camera-based frequency domain FLIM is similar to GOI-based wide-field time-gated FLIM, however the reduction in resolution, introduced by the GOI, is not present. TCSPC is commonly combined with confocal scanning microscopy and can achieve resolutions close the diffraction limit. Both techniques are also superior in quantum efficiency compared to wide-field time-gated FLIM. However, frequency domain FLIM is limited in the applicable fitting models and TCSPC in acquisition speed. For applications where time is not crucial or a simple fitting model is utilized, the FLIM detection could be changed to either frequency domain FLIM or TCSPC.

The signal to noise ratio could be improved by increasing the duration of the time-gates but currently there is an upper limit imposed by the repetition rate of the excitation lasers ($40 - 80$ MHz) since it is difficult to analyse the data when the time-gate also detects fluorescence from the next excitation pulse. Using a lower repetition rate excitation laser would provide some benefit, although the lifetimes of most typical fluorophores used for cell-based assays is <5 ns and so time gates >10 ns are unlikely to provide further advantage.

The current illumination system is based on the translating “top-hat” engineered diffuser, which works well but the translation of the diffuser is noisy and leads to vibrations on the optical table. This could be eliminated if a static engineered diffuser were used with either the deformable mirror or a multimode fibre with a vibrator attached to the fibre but not in contact with the optical table.

The “standard” biological reference samples based on fluorescent protein FRET constructs would be more useful if stable cell lines were generated, noting that transient transfection was used for the work reported in this thesis and the variation in the expression levels is one of the key sources of noise in a FRET assay [Kel15b]. For future work, it is important for cell-based assays to be based on labelled endogenous proteins, rather than over-expressed constructs. It would be useful to generate stable cell lines of such a test sample to evaluate FLIM HCA systems.

In **Chapter 5**, I reported the development and characterisation of a novel microscope that combined molecular readouts via FLIM-FRET with super-resolved imaging using SIM. This combination enables a unique feature to correlate FLIM-FRET experiments, which provides a functional (not spatial) readout of protein interactions below 10 nm, and super-resolved structures. The widefield limited FLIM-FRET image can be used to localize subcellular regions where a specific protein is active, and the super-resolved SIM image offers an analysis of the cell compartment structure below the diffraction limit. The capabilities of this instrument were demonstrated through its application to image changes in DNA compaction during the cell cycle. A fluctuation of DNA density during mitosis was visualized which is contra-intuitive and may correspond to specific states of mitosis. I also applied SIM+FLIM to study interactions between cell organelles and the results obtained indicated that the Golgi protein Gorasp2 did not bind to CROCC, a protein in the ciliary rootlet, which is of interest to understand the role of the CROCC protein, which is not yet established.

The SIM+FLIM instrument could be further developed by integrating the data acquisition software for the two modalities. One approach could be for the commercial SIM software, ZEN, to call the home-written FLIM software as a “slave” module in order to apply the full functionality of ZEN to the SIM+FLIM experiments, including time courses, z-stacks or automated FOV reading. The observation of different FRET lifetimes during mitosis for the DNA compaction measurements may be correlated with different mitotic phases. To explore this further, a study of many mitotic cells could be made to enable the FRET lifetimes, obtained from the FLIM port, to be correlated with mitotic state, as defined by the morphology observed in the SIM image. Currently, the common method to identify the mitotic state of a cell is the morphology analysis of the DNA which is prone to misinterpretations. The FLIM-SIM approach has the potential to substitute common techniques to identify the mitotic state of a cell via the functional FLIM readout and offers a super-resolved DNA structure simultaneously. Both FLIM and SIM are compatible with live cell imaging and a SNAP-tag approach to label the histone 2B could be used to follow this density fluctuation in live cells during mitosis. The histone 2B method can also be utilized to read out open and closed chromatin, which is used in molecular biology to identify active regions in the genome. The activation of different gens can then be compared to super-resolved conformational changes in the cell or specific cell compartments.

The negative colocalisation between CROCC and Gorasp2 does not exclude any interactions between the Golgi apparatus and the ciliary rootlets. A different antibody against the target proteins could change the position of the fluorophore and this might lead to colocalisation being revealed by FRET. The SIM+FLIM approach could be used to explore interactions between other proteins in these two cell organelles and could generally be used to study other organelle interactions. Confirmation of protein interactions may be obtainable using biochemical techniques or fluorescence cross correlation spectroscopy. SIM is currently being applied to study biological processes in the nucleus [Sme14] and SIM+FLIM may provide further information for such studies.

To obtain a true super-resolved FLIM image the SIM+FLIM approach cannot be applied. But it can be extended to acquire a time-gated series of images for each grating position. This would result in longer acquisition times, higher photobleaching and a more sophisticated image analysis. Localisation microscopy, as another SRM method, cannot easily be combined with FLIM, however the implementation with STED is straight forward and possibly the most promising SRM technique to acquire true super-resolved FLIM images.

In **Chapter 6** I reported the application of both open FLIM HCA, SIM and SIM+FLIM to image aggregation processes of DDR1 following stimulation by collagen using different labelling techniques for FRET. In general, SNAP-tags conjugated to dyes were found to be superior to fluorescent proteins in terms of their photostability and the magnitude of the FRET lifetime change upon DDR1 aggregation (attributed to a higher FRET efficiency). For SIM the SNAP-tag approach was found to be superior to antibody labelling because the latter approach led to an artefact perceptible as double structures, which was thought to be due to the antibodies not being able not reach the epitopes of the highly aggregated receptors. These observations indicate that SNAP-tags, with their superior photophysics compared to fluorescent proteins, should be used as labelling technique for specialized experiments where the signal-to-noise ratio is crucial such as long-term, single molecule or FLIM imaging.

Further, I applied the SIM+FLIM technique to aggregated DDR1 samples to correlate the molecular oligomerisation levels reported by FLIM-FRET with the nanostructure indicated by SIM. By inspection there seemed to be a degree of correlation, but I did not find any quantitative metrics to confirm this. The studies of DDR1 aggregation could be improved by establishing the new homo-staining approach, which could be applied to acquire a response curve upon collagen stimulation. This process could be studied using SIM+FLIM to get a more accurate understanding of the aggregation process. The antibody-labelling artefact could be further studied using a higher resolution modality such as dSTORM or STED microscopy.

In **Chapter 7**, I introduced a new approach to STED microscopy: “easySLM-STED” that is designed to simplify the alignment of the instrument while enabling correction of aberrations in the excitation and depletion beams, and which provides improved performance in terms of extended field of view and the ability to scan multiple pairs of excitation and depletion beams. The implementation of STED in a laboratory is challenging and specific expertise is necessary for a successful realization, because an accurate overlay of excitation and depletion has to be achieved. The easySLM-STED concept simplifies the sophisticated optical setup and the time-consuming alignment procedure due to the intrinsic overlay of both laser beams. The presented simplifications aim to open STED as a super-resolved microscopy technique for a broader range of research groups. The performance of easySLM-STED was evaluated using sub-resolution fluorescent nanoparticles and a test sample of fixed Vero cells where vimentin was stained with a dye. I also applied the easySLM-STED microscope to image the synaptonemal complex in germlines of *C. elegans*, proving the usability of the new concept in sophisticated biological applications.

For large scan angles chromatic aberrations forces the excitation and depletion beam to diverge, which leads to a significant reduction of signal-to-noise ratio and resolution. I demonstrated that the easySLM-STED microscope could compensate for walk-off between the excitation and depletion beams due to chromatic aberrations (attributed to the scanner) such that a mosaic approach could provide super-resolved STED images over a field of view up to 100 x 100 μm. Larger or several cells in a population can be imaged in one scan with the increased field of view.

I also showed how the holograms written to the SLM could be programmed to produce multiple pairs of excitation/depletion beams that could be scanned in parallel to increase the image acquisition speed. I demonstrated this with a multiplexing factor of four and showed that the resolution achieved when imaging the fluorescent nanoparticles and *C. elegans* germlines were comparable to that achieved when scanning a single beam pair. This new method to parallelized STED is more flexible in the number and pattern of the beams, and the laser wavelengths than other approaches of parallelized STED [Bin11, Chm13, Ber15].

Additional, I provided a user manual for the easySLM-STED microscope, which is included in this thesis as an appendix. This includes the various alignment procedures, a "doughnut first aid" trouble-shooting section and a manual for the control and hologram software. The easySLM-STED concept could be utilised for multicolor STED microscopy by simply reprogramming the holograms written to the SLM, which is an advantage over the existing easySTED method that is restricted to specific excitation/depletion wavelengths. And it can easily be applied to FLIM using TCSPC detection. I already implemented TCSPC detection for time-gating of the detected fluorescence and acquired some easySLM-STED data but did not have time to make a proper study.

The easySLM-STED approach could also be extended to 3D STED with pairs of orthogonally polarized depletion beams [Len14] but this would require additional elements to enable the excitation and two depletion beams to address three spatially separated holograms written to the SLM and be recombined. The mosaic easySLM-STED approach not only permits chromatic aberrations to be corrected but can also provide correction of other aberrations. In principle this could extend the aberration free field of view for STED microscopes using a range of different scanners and optical systems. Mosaic easySLM-STED is currently slow but this could be addressed by combining it with multibeam easySLM-STED, noting that the number of beams can be increased providing there is sufficient laser power available.

The electronically programmable nature of easySLM-STED offers considerable scope for automation, particularly with respect to fine alignment. If the detection path could be motorized, particularly the coupling of the fluorescence into the confocal detection optical fibre, the whole alignment could be automated, eliminating the need for manual optimisation of the system.

Chapter 9

Supplementary

9.1 Cell culturing and transfection

Poly-L-Lysin treatment for 96-well plate

- 1:100 dilution of $1\frac{mg}{mL}$ Poly-L-Lysin
- add 50 μL dilution per well
- incubate (37°, CO_2) for at least 1 h
- clean with PBS (2x)
- seed immediately

Transfection in 6-well plate

- seed 150 000 cells per well
- incubate (37°, CO_2) for 24 h
- in a vial, mix 75 μL OptiMEM with 4.5 μL xtremeGeneDNA9
- in another vial, mix 75 μL OptiMEM with 1.5 ng DNA
  - to obtain different plasmid ratios, the stock solution of the DNA was analysed with a NanoDrop to derive the DNA concentration for each stock solution. The DNA of the two different plasmids were then mixed into the specific ratio considering the

different stock concentrations.

- mix the two vials together, gently
- remove old growth media
- add 150 μL of transfection solution per well
- add new growth media

Transfer cells from 6-well plate to 96-well plate

- remove old growth media (6-well plate)
- wash with 1 mL PBS (6-well plate)
- add 250 μL TE (6-well plate)
- incubate (37°, CO_2) for 5 min (6-well plate)
- add 3 mL growth media (6-well plate)
- add 140 μL of cell mixture per well (96-well plate)

9.2 Switch on procedure SIM+FLIM setup

For a general understanding of the SIM+FLIM, please see chapter 5 or [Gö17a]. For an understanding of wide-field FLIM and how to use the corresponding *µManager* plugin, please see chapter 3 or go to `https://github.com/imperial-photonics/openFLIM-HCA/wiki` .

The switch on process can be divided into three parts; hardware, software and set properties:

- Hardware:
    - Turn on interlock
    - Turn on laser power (back of laser), needs 10 min to warm up.
    - Turn on PC (Name: MRC-8807\Fred; password: !mittwoch1)

  - Turn on power strip (back of table, upper shelf)
  - Turn on Thorlabs shutter control (red box on table)
  - Turn on CSU-X1 (key) and open shutter (button)
- Software:
  - Start Fianium software, FIRST! If *LabView* error message shows up, ignore. Fianium should be detected at COM7.
  - Start Netbeans:
    - in Netbeans run FLIMPlateReaderGUI in debug mode ⇒ *μManager* will start automatically.
    - in *μManager* select hardware configuration file "UseThis.cfg". If it does not work there are two reasons, first the Fianium is not located at COM7 or the delay box needs to be restarted. If Fianium is located at COM7 (see Fianium software control), unplug and plug in again the power supply of the delay box. Close *μManager*, stop program in Netbeans and run in debug mode again.
    - in *μManager* navigate to "Plugins" and launch "OpenFLIM-HCA Plugin"
- Set properties, for detailed information please see [Kel15a] or [Gö17b]:
  - set HRI properties (e.g. 4 ns; 60 MHz; 750 V; -T, 50, +0.00 V)
  - load delay box calibration file "Hammersmith_Fred.csv"
  - properties for scattered IRF (ND 0.5; excitation 525/50; dichroic 405/488/561/647; emission 485/20; course delay box 19800 ps; right hand port selected at SIM controller)
  - properties for Coumarin 6 only valid for Alexa-594 experiment or similar (ND 0; excitation 500/24; dichroic Di01; emission 629/62; course delay box 7800 ps; left hand port selected at SIM controller)
- Switch between SIM and FLIM:
  - From FLIM to SIM acquisition: shutter laser on FLIM section, check focus and start SIM measurement
  - From SIM to FLIM acquisition: choose at SIM software and empty dichroic (Di1) and

switch to left hand port. Open laser shutter on FLIM setup, check focus and start measurement.

9.3 Procedure for SIM+FLIM image registration

For the registration of the SIM+FLIM images proceed as follows:

- Analyse SIM image. SIM analysis and chromatic shift correction with Zen Black edition.
- Analyse FLIM image. Fit expected lifetime model with *FLIMfit* and save lifetime map and intensity-weighted FLIM image.
- Load SIM images into *Fiji* [Sch12].
    - if 3D SIM image stack make z projection (z Projection)
    - split channels (Stack to images)
    - save wide-field and SIM images separately as TIFF
- Load TIFF images saved in step 3 into *MATLAB* and use home written code which performs the following functions:
    - match images; resize (imresize), translate in x and y (imtranslate) and rotate (imrotate)
    - cut out ROI
    - save processed SIM images as TIFF images in *Icy* [dC12]
    - load SIM and FLIM TIFF images into *MATLAB* and add them with a scaling factor
- Load final images in *Icy* and save as image format preferred.

9.4 DDR1 staining techniques

The cell culture and labelling techniques for the DDR1 experiments were performed by David Corcoran and detailed information can be found in his PhD thesis, written in the research group of Birgit Leitinger (Molecular Medicine, National Heart and Lung Institute, Faculty of Medicine, Imperial College London).

Fluorescent proteins, mutants

The transfection reagent was Lipofectamine 3000. The plasmid for the wild type experiments were pRK-DDR1-GFP and pRK-DDR1-mCherry from Leitinger lab. The mutants were adapted from [Noo06] pRK-DDR1-TM1 and pRK-DDR1-ECTM.

SNAP-tags, homo-hetero labelling

The SNAP-tag protein was introduced after serine at position 397 using the FastCloning method [Li11].

Hetero labelling

- labelling with SNAP-surface AlexaFuor488 (NEB, UK) and SNAP-surface AlexaFluor546 (NEB, UK) in a 1:1 ratio, 19 h after transfection
- washing
- stimulation
- fixation (4% PFA)

Homo labelling

- labelling with SNAP-surface AlexaFluor546 (NEB, UK), 19 h after transfection
- washing
- blocked with SNAP-surface Block (NEB, UK) for 20 min at 37°
- washing
- 5 hours incubation
- labelled with SNAP-surface AlexaFluor488 (NEB, UK)
- washing
- stimulation
- fixation (4% PFA)

Antibodies, two and three color SIM

- primary antibodies incubated on ice
- fixation (4% PFA)
- immunostain intracellular, permeabilised with 0,1 Triton X-100
- secondary antibody incubated at room temperature over 1 h

primary antibodies

- for phosphorylation; pY-513; Antigen phosphorylated Tyr-513 of DDR1; origin rabbit; Abbexa UK
- for collagen; Anti-rat Type 1 Collagen Antibody Clone 1F10C2; Antigen type 1 collagen from rat only; origin mouse lgG2b; AMS Biotechnology from Chondrex
- for DDR1; DDR1 specifically DS-domain; Antigen mouse lgG1; Leitinger Lab

secondary antibodies

- for phosphorylation; AlexaFluor647 goat-anti rabbit; Invitrogen UK
- for collagen; AlexaFluor546 goat-anti-mouse lgG2b; Invitrogen UK
- for DDR1; AlexaFluor488 goat-anti-mouse lgG1; Invitrogen UK

Collagen stimulation

Stimulated with 20 $\frac{\mu g}{mL}$ collagen, 24 h after transfection in DMEM without Phenol Red.

9.5 STED setup manual

This section presents a manual outlining how to set up and operate the easySLM-STED microscope, including general and fine alignment procedures, a discussion of common misalignments with suggested solutions, instructions to align the mosaic and the multibeam easySLM-STED systems and an outline of how to use the microscope and hologram control software. The last section summarizes the bead sample preparation for gold and fluorescent beads.

The alignment of the easySLM-STED setup can be divided into two steps. The first step is a general alignment procedure with optical fiber coupling, alignment of laser beams from the optical fibre to the holograms on the SLM with the double bounce configuration and alignment of the output diffracted beams to the objective lens, where the beams have to fill the back aperture of the objective lens. This alignment entails imaging the holograms on the SLM onto the back focal plane of the objective lens via the scanner. The last points for the general alignment are the polarisation states of the beams incident at the objective lens and alignment of the emission to the confocal pinhole. The second step is the fine alignment procedure that ensures the general alignment is correct and fine tunes the overlay of the excitation and depletion beams in space and time.

The microscope control software is explained, including the generation of the scan pattern, including for the mosaic mode with aberration correction and the pitfalls are discussed. The operation of the hologram control software is outlined, which is used to generate the doughnut-shaped depletion beam and to facilitate precise adjustments of the alignment of the exaction and depletion beams for single beam and multibeam easySLM-STED.

A scheme to identify abbreviations and terms in the following description is shown in Figure 9.1.

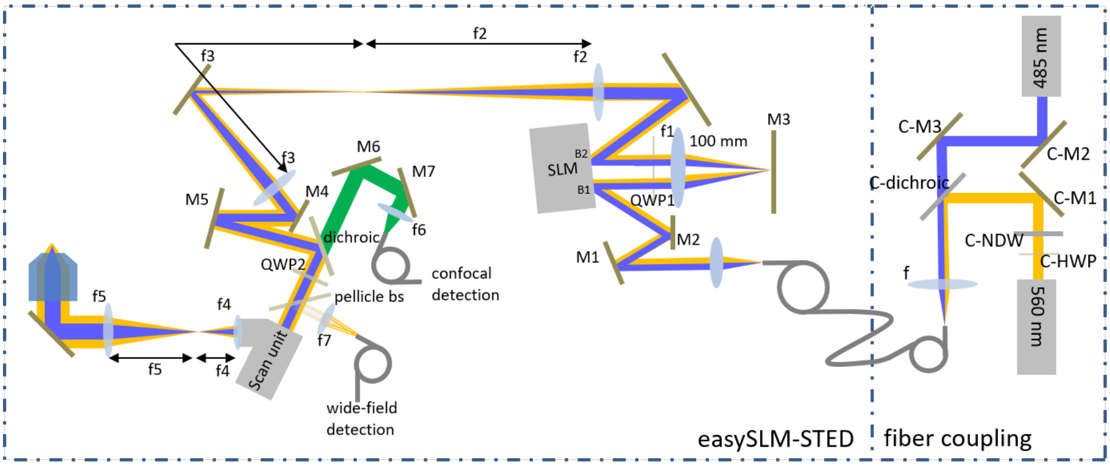
f2
f3
f2
f3
M6
M7
M5
M4
f1
100 mm
M3
B2
SLM
B1
QWP1
dichroic
f6
M2
M1
QWP2
confocal
detection
pellicle bs
f5
f4
Scan unit
f7
f5
f4
wide-field
detection
easySLM-STED
fiber coupling
485 nm
C-M3
C-M2
C-dichroic
C-M1
C-NDW
C-HWP
f
560 nm

Figure 9.1: *easySLM-STED design with abbreviations. Adapted from [Gö18].*

9.5.1 Switch on procedure for easySLM-STED

Detailed information about the switching on process of the depletion laser can be found in the manual provided at the laser or in Appendix A, written by Dr. Timothy Runcorn [Run15a], which includes also error handling information.

- Hardware:
  - Turn on interlock
  - Turn on SLM control box (Hamamatsu, LCOS-SLM controller, X10468), allowing for a 10 minute warm up
  - Turn on PC (HP Z420 workstation)
  - Turn on excitation laser (PicoQuant, PDL 828-S driver ("Sepia II"), LDH-D-C-485 laser head) using the key at the back of laser control unit
  - Turn on depletion laser (please refer to Appendix A)
  - Turn on DAQ box (National Instruments, USB-6259)
  - Turn on XYZ stage (Mad City Labs, Nano-Drive 85 controller, MCLS02098)
  - Turn on scan unit (FEI) by switching on the power supply and the scan control unit
  - Turn on precision delay box (Kentech Instruments Ltd, Precision programmable 50 Ω delay line)
  - Turn on microscope frame (Leica Microsystems GmbH, DMIRE2)
- Software:
  - Start *LabVIEW* hardware control program, aSTEDmain20171022, or latest version under `C:\FredGFPSTED\LabviewNew\MainApplication`
  - Start *LabVIEW* hologram control program, HologramGenerator_MarkOpti under `C:\FredGFPSTED\LabviewNew\SLMFiles`
  - Start Becker & Hickl software DCC100 and SPC64 (desktop)
  - Start *Sepia* (desktop)

9.5.2 General alignment

The general alignment provides the basis for further fine alignment and should only need to be undertaken once unless the significant optical elements in the beam path are changed. On a daily basis, only the fine alignment should need adjustment. Please note that the detectors are very light sensitive. Always work with the lowest possible laser intensities, especially if using scattered light, and increase the intensity slowly for imaging experiments while constantly monitoring the detector counts to ensure they remain below 10^5 photons per second.

Be aware that several alignment steps are dependent on one another. Therefore, the alignment from the SLM, through the scanner and objective to the detection path need to be repeated iteratively until an improvement can be observed.[1]

Optical fiber coupling

The excitation and depletion beam need to be coupled into the single mode optical fiber that ensures they are collinear. First, direct the depletion beam into the fiber by adjusting the mirror, C-M1, and the dichroic, C-dichroic, to walk the beam and adjust the objective lens position using the three axis stage. Then, couple the excitation laser into the optical fiber by adjusting the two mirrors, C-M2 and C-M3. To ensure that the excitation and depletion beam should have orthogonal linear polarisation states before coupling into the optical fiber, a $\frac{\lambda}{2}$-plate (C-HWP) is used in the depletion beam path before the optical fibre with a filter wheel (C-NDW) with continually variable neutral density filters that is used to adjust the intensity of the depletion beam.

Beam size

To be able to achieve the best possible resolution, the beam size should overfill the back aperture of the objective lens (here 5.6 mm). If the beam diameter is too small, the whole NA of the objective is not used, and if the beam diameter is too large, light will be lost.

Aligning the beams with respect to the holograms on the SLM

The holograms have to be aligned with respect to the laser beams such that they are both centred on the optical axis. If this condition is not fulfilled, the PSF becomes tilted and the depletion doughnut intensity distribution is degraded. When a vortex phase ramp is written to the hologram at B2 in Figure 9.1, the beam diffracted from this second hologram can be observed on a white screen (or business card). Centre the hole of the phase ramp to the middle of the depletion beam, by either moving the hologram using the hologram control software or steering the beam using mirrors M1 and M2. The mirrors should only be used for the initial alignment, because they also impact the alignment of the beam paths to objective lens. The hologram at B1 should then be adjusted to ensure that the excitation beam is collinear with the depletion beam doughnut after diffraction from B2. The SLM double bounce configuration also requires careful adjustment of the focusing lens and the $\frac{\lambda}{4}$-plate (QWP1). The focusing lens images the hologram of the first bounce at B1 onto the hologram of the second bounce at B2. The distance between lens f1 (100 mm) and mirror M3 has to be optimised until the beams reflected from the second bounce are collimated. That can be checked using a shear plate or focusing the emerging beams at a distance far from the set-up. The QWP1 should be set to rotate both beams about 90° so that only one beam has the correct polarisation to be modulated per bounce. The QWP1 should be adjusted to rotate both the orthogonal polarisation states of the excitation and depletion beams before the QWP1 by 90° such that they remain orthogonally polarized. This can be checked using a polarising beam splitter.

---

[1] Patience and endurance is the secret of success.

Aligning the beams from the SLM to the scanner

To apply corrections for aberrations, the required correction can be calculated using Zernike polynomials and can be implemented by appropriately modifying the computer-generated hologram. This approach requires the computer-generated hologram on the SLM to be imaged to the back focal plane of the objective lens via the scanner. The first step is realised using a 4f system from the SLM to the scanner, comprising lenses f2 (500 mm) and f3 (750 mm). To correctly set the distance between these lenses, an offset (phase ramp) can be applied to the hologram at B2 (or respectively at B1 for the excitation) and the beam observed at an image plane of the hologram, such as the one of the galvo mirrors or a diffuser in the plane of the back focal plane of the objective lens. If the diffracted beams and the zero-order beams are not overlapped at these image planes, then the 4f configuration is misaligned.

Aligning the beams from the scanner to the objective lens

The scan unit is configured to image the light incident at the first galvo scanner mirror to the second galvo scanner mirror. In turn, the light at the second galvo scanner mirrors inside the scan unit must be imaged onto the back focal plane of the objective lens to realise the desired scan pattern in the sample plane. If this alignment is not achieved, the required intensity distributions will not be realised at the sample, due to defocusing and aberrations.

The lateral alignment is straightforward and requires that the beam should be centred on the galvo mirrors and the scan lens f4, when the scanner mirrors are set to their centred positions. The galvo mirror closer to the objective lens is imaged via a 4f configuration onto the back focal plane of the objective lens using the tube lens f5 (250 mm) and the scan lens f4 (50 mm). This alignment can be checked with an item located in the plane corresponding to the back focal plane of the objective lens. If the scanner is correctly aligned and set to scanning over its full scan range, the beam should not move at the back focal plane of the objective. If it is moving, the 4f configuration is not correctly aligned.

Aligning the excitation and depletion beams into the objective lens

The excitation and depletion beams should be collinear with the optic axis and centred in the back aperture of the objective lens. If they are incident at an angle to the optic axis, the resulting PSF will be tilted and the doughnut shaped beam will not have a radially homogeneous intensity distribution. To achieve this alignment, the objective lens can be replaced with a double pinhole arrangement (i.e. a component containing two diffusers, each with a hole in their centre and one located in the plane corresponding to the objective lens) that screws into the objective lens holder. Adjust the mirror M4 to centre the beam at the lower diffuser and then adjust mirror M5 to centre the beam at the upper diffuser. Repeat this procedure until the beam is aligned to the centre of the upper and lower diffusers.

Aligning the detection path

The detection path is less critical to align for the single beam easySLM-STED compared to multi-beam scanning or even wide-field imaging techniques. The imaging involved is simple, but sub-optimal alignment will reduce the detected signal. For multibeam easySLM-STED the alignment is more critical since the multiple excitation foci must be imaged to the multiple optical fibre detectors. Since the axial discrimination is that of a confocal microscope, the pinhole size (i.e. the size of the optical fibre core) should be slightly less than one Airy to achieve good confocality. A fluorescent slide can be imaged to provide a bright fluorescence signal with which the focusing lens f6 (300 mm) and mirrors M6 and M7 can be used for adjustment in order to optimise the focusing of the fluorescence into the detection optical fibre(s).

For a fine adjustment, the emission filter can be removed and a mirror can be imaged in the sample plane. A z-scan should show a single symmetric line. If two or more lines are visible the pinhole (detection fiber) is misaligned.

For wide-field detection, a removable pellicle beam splitter can be inserted and the detected signal (e.g. back scattered light from gold nanoparticles) can be focused into an optical fibre using lens f7. The pellicle should be removed for any confocal fluorescence or STED microscopy experiments.

Polarisation

Circular polarisation is necessary to efficiently excite and deplete fluorophores and ensure that the imaging is independent of the fluorophore dipole orientation. An achromatic $\frac{\lambda}{4}$-plate (QWP2) located before the scanner ensures circular polarisation for excitation and depletion beam. This can be checked by replacing the objective lens with a rotating polarizer and measuring the transmitted signal, which should be periodic with a modulation depth that goes to zero when perfect circular polarisation is achieved.

Temporal alignment of excitation and depletion pulses

The relative timing of the excitation and depletion laser pulses affects the efficient depletion of the excited fluorophores. If the depletion beam arrives too late after the excitation pulse, too many fluorophores will have already emitted light to contribute to a diffraction-limited (confocal microscopy) image. If the depletion pulse arrives too early, there will not be sufficient fluorophores in the excited state. The optimal temporal condition is for the depletion pulse to arrive as soon as possible after the excitation pulse. This optimal temporal alignment is a function of the fluorophore properties and the profile of the excitation and depletion pulses and should be determined empirically for each experiment. To vary the temporal position of the excitation pulses, a delay box (Kentech Instruments) can shift the pulse over a range of ∼20 ns. If a larger shift is needed, the cable length between trigger output of the depletion laser and trigger input of the excitation laser can be adjusted. The accurate temporal position can be measured with a scattering sample (e.g. a mirror or gold bead sample), and a time-resolved detector signal, such as the TSCPC card.

9.5.3 Fine alignment

A fine alignment procedure comprising four steps should be repeated daily in following order:

Check quality of depletion beam "doughnut" profile

A single bead from a gold bead sample should be imaged using the wide-field detector. It is important to image a single isolated bead, because scattered light from other beads can interfere with the signal and beads can cluster or have aspherical shapes that could impact the measured PSF. Therefore, it is essential that this check is repeated with multiple isolated beads. For a detailed description of misalignment effects please refer to the *Doughnut first aid* (subsection 9.5.6).

Overlay of excitation and depletion PSF in x-y-z

Once an acceptable quality of depletion doughnut profile has been achieved, the excitation PSF should be aligned to be coincident with the depletion PSF. This can be done imaging a gold bead sample by adjusting the excitation focus position by changing the hologram written to the SLM. Due to the easySLM-STED design, the beams should not drift apart once they have been aligned and this step should become unnecessary after the first full alignment.

Overlay of excitation and depletion laser pulses in time

Using fluorescent beads, the depletion laser pulses should be shifted in time until the detected fluorescence signal is minimized, at which point the super-resolved contribution to the detected signal should be maximised. This step should ideally be repeated with a sample labeled with the fluorophore because this alignment can be fluorophore dependent.

Check STED resolution using standard fluorescent bead sample

Using sub-diffraction resolution (e.g. ∼40 nm diameter) fluorescent beads, the resolution should be compared between STED and confocal microscopy. If no significant reduction is observed, the alignment should be repeated.

9.5.4 Specific alignment procedures for mosaic easySLM-STED

The alignment for mosaic easySLM-STED to correct for chromatic aberration should be undertaken once the fine alignment outlined above has been successfully completed. When imaging extended fields of view as discussed in section 7.2, there are three challenges to be addressed to correct for the chromatic aberration that is particularly evident in the peripheral tiles of the extended field of view:

1. The sample may be tilted: this can be problematic when imaging thin samples over extended fields of view. The variation of the z-offset can be measured using a fluorescent bead sample or using the experiment sample itself if it is known to be flat.
2. Chromatic aberration can result in the focused fluorescence signal in the detection path walking off the detection optical fibre core for large scan angles. This offset can be determined by imaging a fluorescent bead sample in confocal mode with no depletion beam. A scan position-dependent correction to the beam focus can then be applied by changing the hologram written to the SLM to maximize the detected fluorescence intensity.
3. Chromatic aberration can result in a shift between excitation and detection foci, which is most evident at large scan angles. This chromatic shift can be measured by imaging a gold bead sample in wide-field detection mode with both laser beams.

The chromatic shifts are not directly measured but are empirically determined by applying offsets to the computer-generated holograms that define the location of the excitation and emission foci in the sample plane. First the offsets to optimise the position of the excitation foci should be determined using a fluorescent bead sample and identifying the offset values applied to the excitation hologram in each tile that maximise the confocal fluorescence signal. Then the required offsets of the STED hologram can be determined by imaging an isolated gold bead in every tile with wide-field detection and moving the depletion doughnut PSF to overlay the excitation PSF.

If a radial dependence of the chromatic shift can be assumed, the offsets of excitation and depletion beam can be rapidly determined by starting with two tiles and then interpolating the shifts for the remaining tiles using the "easySLM-STED control software", which is described in subsection 9.5.7. If the chromatic shifts are not expected to be radially linear from the centre, they need to be determined for every tile separately.

9.5.5 Specific alignment procedures for multibeam easySLM-STED

The multibeam easySLM-STED approach is more complex than the single excitation/depletion beam pair implementation because it requires each of the beam pairs to be aligned to each other and to their specific optical fibre detector. However, the alignment up to the SLM is essentially the same as for the single beam pair case and the fine alignment of the multiple fluorescence beams to their respective detectors can be done electronically by changing the holograms written to the SLM. To set up the multibeam easySLM-STED system, the following procedure should be undertaken:

1. Use the "hologram control software" in multibeam mode. For a detailed description please refer to subsection 9.5.8.
2. With a mirror in the sample plane, coarsely align the fluorescence beams to the optical fiber cores by maximizing the transmission intensity with no depletion beams present.
3. Use a fluorescent sample to precisely set the positions of the excitation beams, by maximizing the detection of the fluorescent signal.
4. Using a gold bead sample and wide-field detection, check the overlap of the excitation and depletion foci. The excitation focus position should not be changed at this stage but only the depletion foci positions should be changed to overlay the excitation foci.
5. Using a gold bead sample and wide-field detection, check the quality of the depletion doughnut profile and optimise this using the software to change the hologram written to the SLM. The current software is designed to correct chromatic aberration. However, the correction of other aberrations could be implemented.
6. Check that the detection window for time-gated detection is optimised for all beam pairs in the detection software *SPCM* (Becker & Hickle). Due to different cable lengths between the detector and the router, the timing needs to be adjusted for each detector.

9.5.6 Doughnut first aid

The quality of the depletion doughnut PSF is a critical adjustment in a STED alignment procedure. There should be zero intensity at the centre of the PSF. As a rule of thumb, a zero-point intensity of 5% is usable but, to realise resolutions under 50 nm, a zero-point intensity of less than 1% should be achieved. Additionally, the intensity of the ring of the doughnut should be homogeneously distributed to achieve isotropic lateral resolution enhancement.

In the following sections, images displaying simulated 3D intensity distributions of light scattered from a spherical object illuminated with a doughnut-shaped PSF are shown. The simulation program was written by Dr. Johann Engelhardt [Eng18] and is based on equations from Richards and Wolf [Wol59, Ric59b] following a vector Fourier theory as demonstrated by Boruah and Neil [Bor09]. Common misalignments are simulated, and solutions are suggested to correct for them using either an SLM or a phase plate-based set-up. Note that multiple misalignments can occur simultaneously and may partially compensate each other. However, such compensation is undesirable because the zero-point intensity will increase. Therefore, in some cases, iterative corrections are needed to obtain a suitable depletion doughnut.

Perfect doughnut

A perfect aligned system will produce a doughnut-like intensity distribution in the sample plane, as shown in Figure 9.2. This can be measured using light back-scattered from an isolated gold bead in wide-field detection that is scanned in all three dimensions.

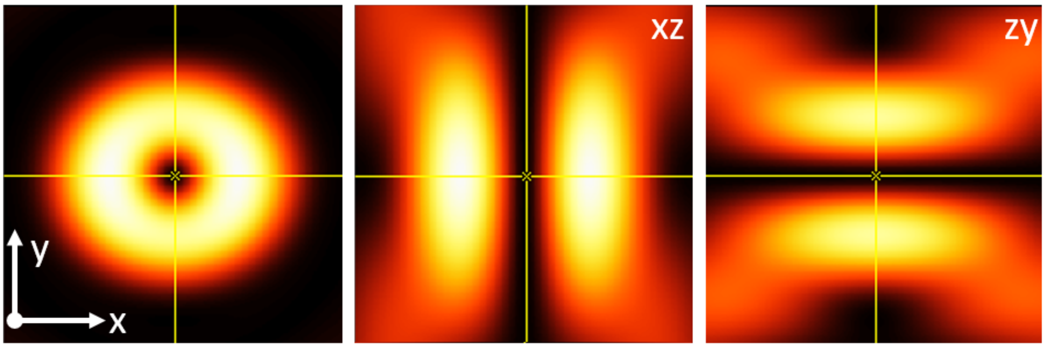

Figure 9.2: *Simulation of ideal depletion PSF.*

Asymmetric doughnut

An asymmetry in the lateral doughnut ring can be due to a misalignment of the laser beams to the holograms or to a misalignment of the laser beam with respect to the objective lens. If the depletion laser beam is shifted with respect to the hologram, the Gaussian intensity distribution of the incident beam is not spread equally over all the step phases of the vortex hologram. Where a phase group contains more intensity, the point of destructive interference shifts away from this intensity dominating region, as presented in Figure 9.3. To correct for this, please see section 9.5.2. If the depletion beam is not centred on the objective lens, the PSF will be tilted, leading to an energy density shift along the z axis and asymmetric intensity contributions across the lateral plane, as shown in Figure 9.4. To correct for this, please see section 9.5.2.

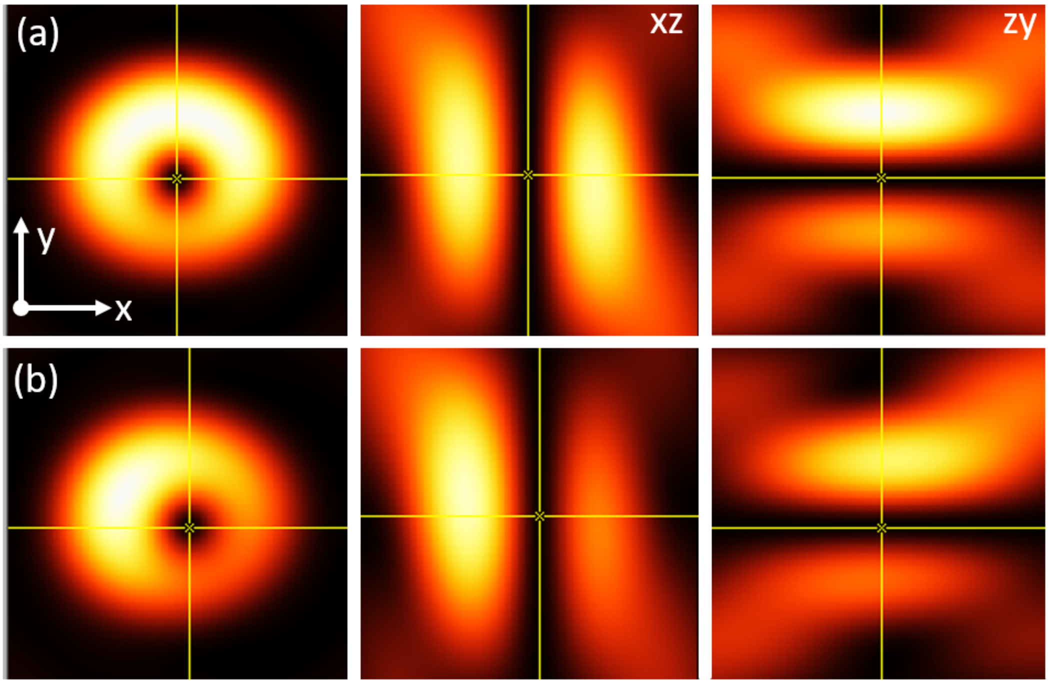

Figure 9.3: *Simulation of depletion PSF with beam-hologram misalignment, (a) in y direction and (b) in x and y direction.*

The difference between a confocal PSF subject to these alignments would not be distinguishable as both would appear as a tilted PSF in a z scan. For a doughnut-shaped (depletion) PSF, however, a characteristic difference is visible in z scans: for a beam-to-hologram misalignment, there is a vertical region of minimum ("zero") intensity along the optic axis and only the intensity ratio of the two side maxima change with the misalignment. For a beam-to-objective lens misalignment, the region of minimum ("zero") the zero line is tilted, whereas the intensity between the two side maxima remains constant. Additionally, the side maxima are shifted in z in respect to each other. If a vortex phase plate is used, any "beam to phase-plate" misalignment produces similar changes in the depletion PSF and can be addressed by centering the phase-plate on the incident depletion beam.

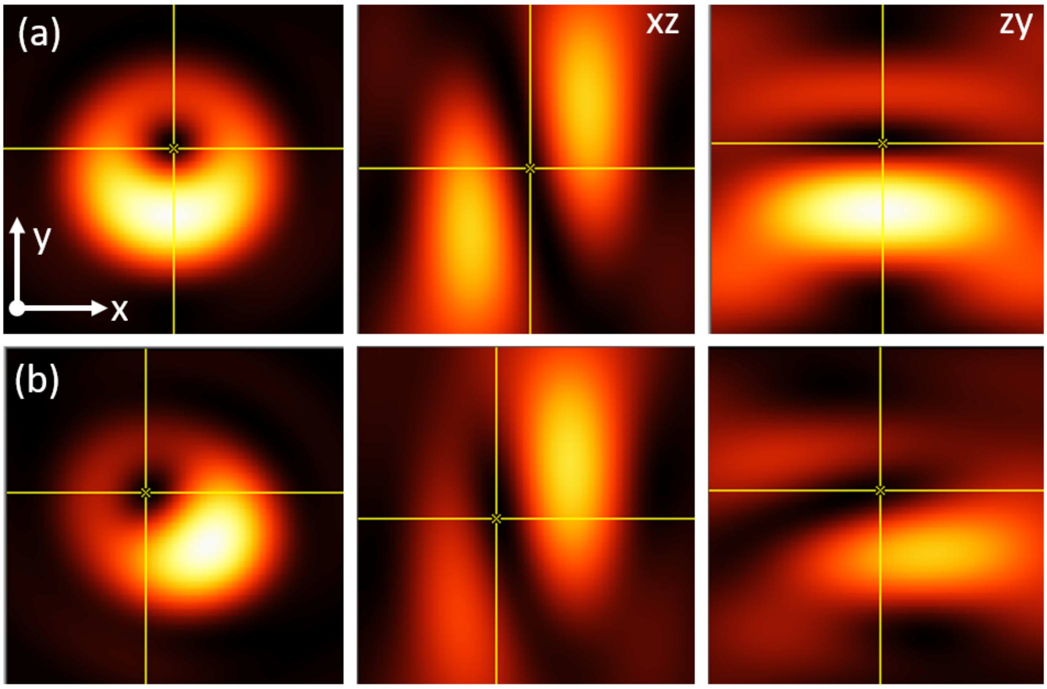

Figure 9.4: *Simulation of the depletion PSF with beam-objective misalignment, (a) in y direction and (b) in x and y directions.*

Aberration correction (astigmatism and spherical aberrations)

Many optical aberrations can occur in confocal and STED microscopes and only the two most common are discussed here. Astigmatism can occur if an optical signal is not collimated when passing through an optical medium with interfaces at an angle to the optic axis, such as a dichroic beamsplitter. Figure 9.5 (a) shows a typical intensity distribution that would result from astigmatism. Astigmatism can be compensated by appropriately modifying the hologram written to the SLM.

Spherical aberrations can arise for many reasons, including when the beam is not collimated before the objective lens or when light is focused into a medium of higher refractive index. Figure 9.5 (b) shows a characteristic signature of spherical aberrations, i.e. a broadening of the top of the two side maxima of the 3D PSF and the presence of higher order intensity maxima at the bottom of the PSF. To minimise spherical aberrations, the collimation of the light incident at the objective lens can be checked using a shear plate. For easySLM-STED, the hologram written to the SLM can be adjusted to correct for some spherical aberrations. In STED microscopes using phase-plates to shape the depletion beam, it is difficult to compensate for spherical aberrations and they must be minimized through a rigorous alignment.

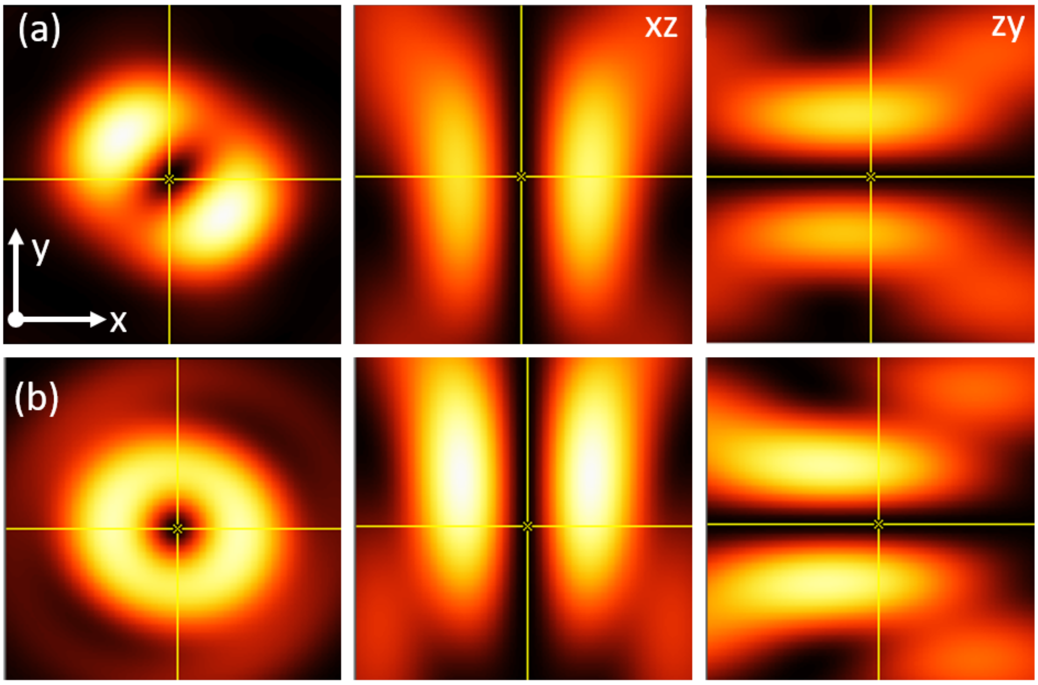

Figure 9.5: *Simulation of the depletion PSF with (a) astigmatism and (b) spherical aberrations.*

Polarisation and blazed grating misalignment

Two misalignments that can occur during the initial set-up of the easySLM-STED microscope which are polarisation and blazed grating mismatch. If the beams incident at the objective lens are not circularly polarized, the destructive interference at the optic axis will not be complete and the intensity will not be zero, as depicted in Figure 9.6 (a). To optimise the beam polarisation states, it is important to ensure that the laser beams are linearly polarized before the $\frac{\lambda}{4}$-plate (QWP2) and that this is set to the correct angle.

If the wavelength of the depletion laser does not produce a phase change of exactly 2π across the vortex ramp, the doughnut ring intensity will be shifted to one side, as simulated in Figure 9.6 (b) for a small mismatch. This may also be an indication that the amplitude of the hologram blazed grating [Loe77] written to the SLM is not chosen correctly since the highest phase shift on the hologram should be 2π at the applied wavelength. This can be resolved by changing the blazed grating amplitude using the hologram control software. A calibration provided by Hamamatsu indicates the grey values written to the SLM that produce a 2π phase change for each wavelength. In a STED microscope incorporating a vortex phase plate, this needs to be matched to the depletion wavelength. Usually, commercial vortex phase-plates have arrays of vortex phase ramps for a range of wavelengths and so the most suitable needs to be selected.

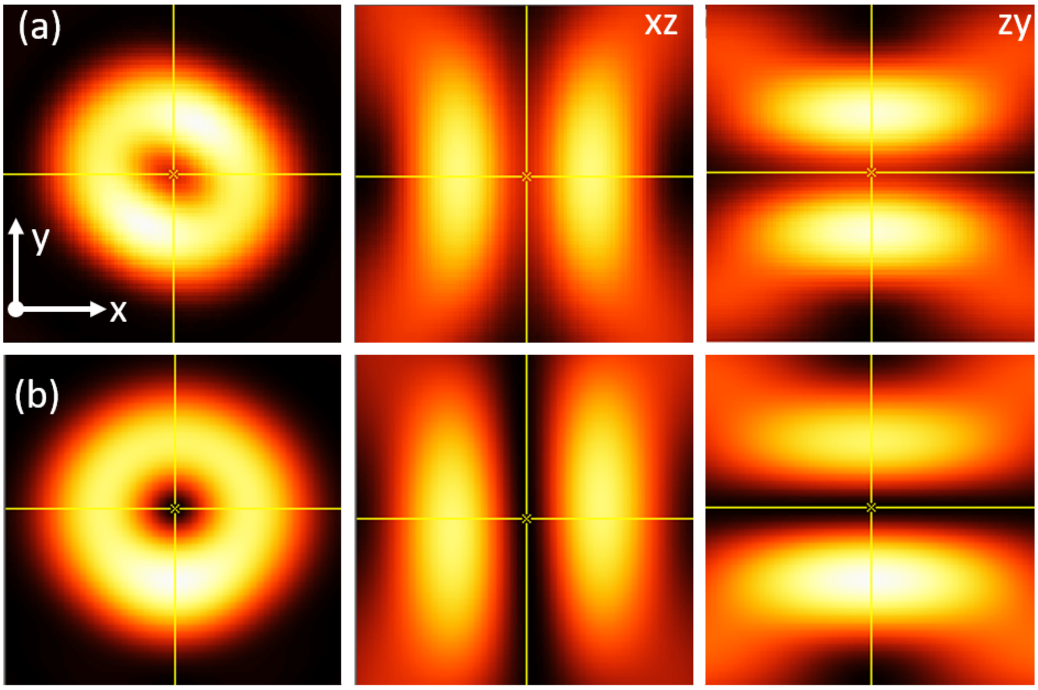

Figure 9.6: *Simulation of the depletion PSF with (a) polarisation and (b) blaze grating mismatch.*

9.5.7 Software manual: easySLM-STED control program

The control software generates scan patterns and controls a data acquisition box with digital and analogue inputs and outputs to operate several hardware components. It sends an analogue scan pattern to the scan unit and a synchronized digital scan pattern to the TCSPC card, while reading the signal from the detector. It provides a pseudo-live visualisation of the image, controls the depletion laser shutter and applies a correction for chromatic aberration during mosaic easySLM-

STED.

The main panel contains control elements for saving data, setting different scan modes, the visualisation of the image and the mosaic mode, as shown in Figure 9.7. The visualisation window contains the 2D image with two cursors. The red circle cursor can be used to centre the FOV to a target structure and the green cross sets the x and y lines displayed in the corresponding line scan windows.

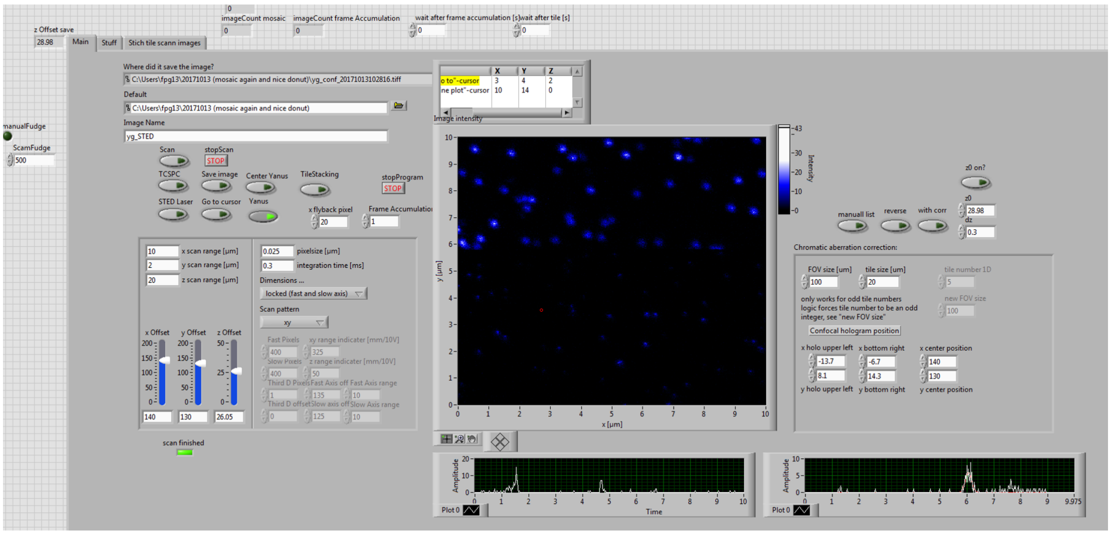
z Offset save 28.98
imageCount mosaic 0
imageCount frame Accumulation 0
wait after frame accumulation [s] 0
wait after tile [s] 0
Where did it save the image? C:\Users\fpg13\20171013 (mosaic again and nice donut)\yg_conf_20171013102816.tiff
Default C:\Users\fpg13\20171013 (mosaic again and nice donut)
Image Name yg_STED
ScamFudge 500
x flyback pixel 20
Frame Accumulation 1
x scan range [µm] 10
y scan range [µm] 2
z scan range [µm] 20
pixelsize [µm] 0.025
integration time [ms] 0.3
Dimensions ... locked (fast and slow axis)
Scan pattern xy
Fast Pixels 400
xy range indicater [mm/10V] 325
Slow Pixels 400
z range indicater [mm/10V] 50
Third D Pixels 1
Fast Axis off 135
Fast Axis range 10
Third D offset 0
Slow axis off 125
Slow Axis range 10
x Offset 140
y Offset 130
z Offset 26.05

	X	Y	Z
o to"-cursor	3	4	2
ine plot"-cursor	10	14	0

z0 28.98
dz 0.3
Chromatic aberration correction:
FOV size [um] 100
tile size [um] 20
tile number 1D 5
new FOV size 100
only works for odd tile numbers logic forces tile number to be an odd integer, see "new FOV size"
x holo upper left -13.7
y holo upper left 8.1
x bottom right -6.7
y bottom right 14.3
x center position 140
y center position 130

Main
Stuff
Stich tile scann images
manualFudge
Scan
stopScan
STOP
TCSPC
Save image
Center Yanus
TileStacking
stopProgram
STOP
STED Laser
Go to cursor
Yanus
scan finished
Image intensity
y [µm]
x [µm]
0
1
2
3
4
5
6
7
8
9
10
Intensity
43
30
20
10
0
z0 on?
manuall list
reverse
with corr
Confocal hologram position
Amplitude
20
10
0
Time
Plot 0
Amplitude
10
5
0
9.975
Plot 0

Figure 9.7: *Control software overview.*

Scan parameters

The scan pattern area on the left-hand side of the main frame can be divided into three regions, as presented in Figure 9.8. The top part presents the data saving information, the first string *"Where did it save the image?"* shows the path where the last image was saved. The second string *"Default"* defines the default saving path, which can be chosen using the file button to the right. The *"Image Name"* is the name of the file saved to the default saving path.

The middle region contains several buttons enabling different scan and acquisition modes:

- *"Scan"* starts the scan and the scan will repeat continuously as long as this is left switched on. If only one image is required, this button needs to be switched off after starting the scan.
- *"stopScan"* stops the scan at the current line.
- *"stopProgram"* stops the complete *LabVIEW* program.

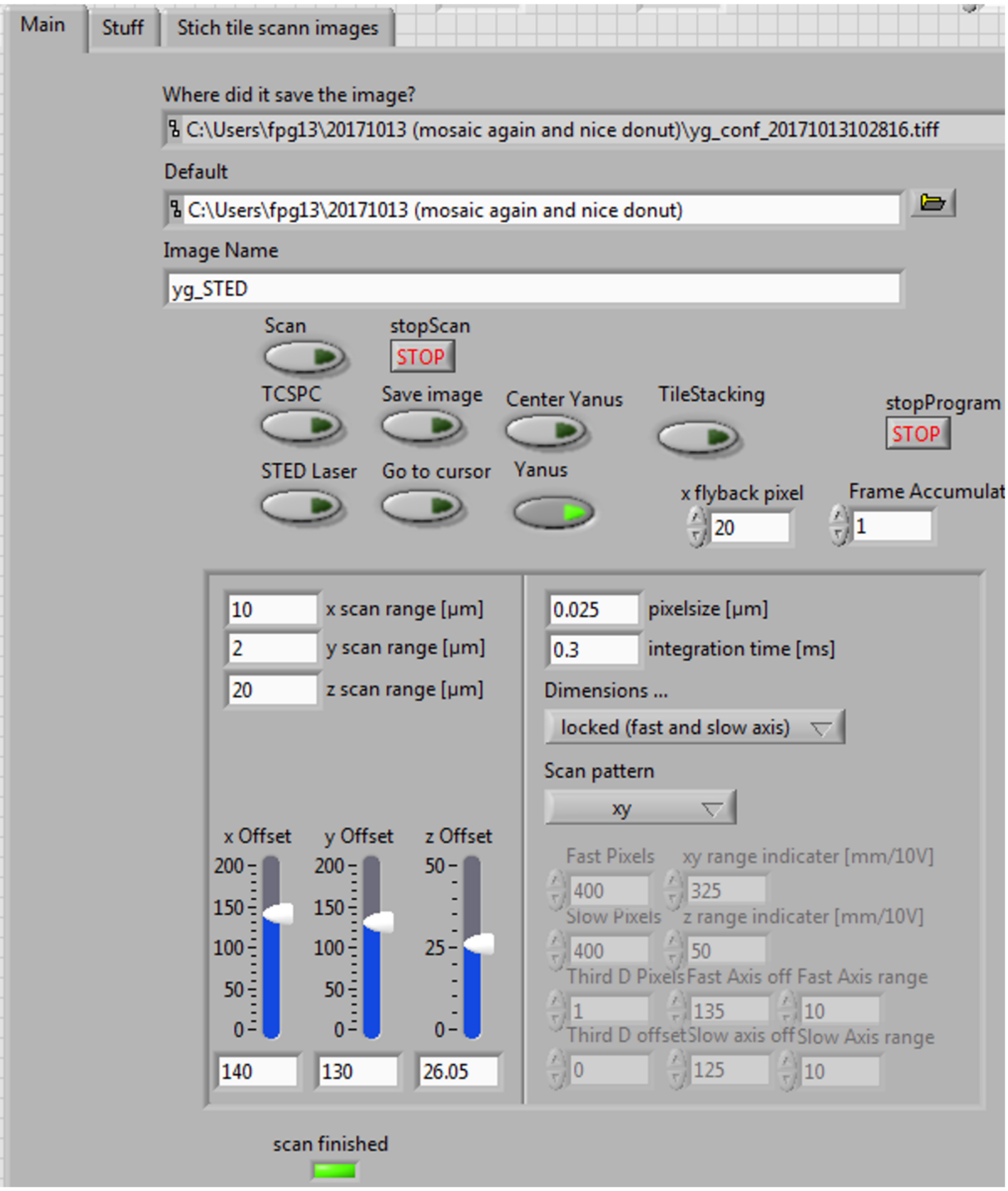
Main
Stuff
Stich tile scann images
Scan
stopScan
STOP
TCSPC
Save image
Center Yanus
TileStacking
stopProgram
STOP
STED Laser
Go to cursor
Yanus
scan finished

Where did it save the image?
C:\Users\fpg13\20171013 (mosaic again and nice donut)\yg_conf_20171013102816.tiff

Default
C:\Users\fpg13\20171013 (mosaic again and nice donut)

Image Name
yg_STED

x flyback pixel 20

Frame Accumulat 1

10 x scan range [μm]
2 y scan range [μm]
20 z scan range [μm]

x Offset 140
y Offset 130
z Offset 26.05

0.025 pixelsize [μm]
0.3 integration time [ms]

Dimensions ...
locked (fast and slow axis)

Scan pattern
xy

Fast Pixels 400
xy range indicater [mm/10V] 325
Slow Pixels 400
z range indicater [mm/10V] 50
Third D Pixels 1
Fast Axis off 135
Fast Axis range 10
Third D offset 0
Slow axis off 125
Slow Axis range 10

Figure 9.8: *Control software for setting scan patterns.*

- *"TCSPC"* activates the sending of the digital scan pattern to the TCSPC card and, in combination with the *SPCM* software, can be used to acquire a time resolved image.
- *"Save image"* saves the displayed image once the scan is finished or stopped. The status of the scan is displayed in *"scan finished"*.
- *"Centre Yanus"* sends a constant voltage, independent of the applied scan dimensions, that centres the scan unit. This mode is used in the alignment procedure from beam to objective lens (section 9.5.2).
- *"TileStacking"* enables the mosaic mode, see section 9.5.7.
- *"STED laser"* open and closes the depletion lasers. This functionality is run in a different thread to be (de-)activated in parallel to the main program.
- *"Go to cursor"* stops the scan and centres the FOV at the position marked with the red cursor.
- *"Yanus"* sets the scan properties for the Yanus IV scan head unit. If this is deactivated, the settings are optimized for the x-y-z scan stage. It is important to ensure that the correct setting is selected for the specific scan unit that is connected. A wrong combination can damage the scan unit, because the galvo scanner needs negative voltages, which is damaging for the x-y-z stage. Ensure the cables from the DAQ box are connected to the correct device.

The lower region controls the scan pattern with the parameters described below. The remaining indicators show information for debugging purposes.

- *"x flyback pixel"* defines the number of pixel used for line and frame flyback. Be aware that the input is half the fly-back pixels.
- *"Frame accumulation"* identifies how many frames should be accumulated.
- *"x scan range [μm]"*sets the image scan size along the x axis.
- *"y scan range [μm]"*sets the image scan size along the y axis.
- *"z scan range [μm]"*sets the image scan size along the z axis.
- *"x Offset"* sets the offset position in μm to define the centre of the FOV in the x dimension.
- *"y Offset"*sets the offset position in μm to define the centre of the FOV in the y dimension.
- *"z Offset"* sets the offset position in μm to define the centre of the FOV in the z dimension.

- *"pixelsize [µm]"* sets the size of every pixel in all three dimensions.
- *"integration time [ms]"* sets the pixel dwell time, i.e. how long a beam stays on a certain pixel before moving to the next one.
- *"Dimensions ..."* sets whether the FOV is square (for which the mode: *"locked (fast and slow axis)"* should be chosen) or if it is to free dimensions, (for which the mode: *"free"* should be chosen). If the axes are locked, the scan range from the first dimension (fast axis) is copied to the slow axis.
- *"Scan pattern"* enables the plane of the scan to be changed between xy, yx, xz and yz. (Please be aware that yx scan patterns are not fully tested and errors can occur, especially with the fly-back.)

Mosaic easySLM-STED with chromatic aberration correction

The mosaic mode can be used with and without aberration correction or z-offset compensation. To use the mosaic mode only, the button *"TileStacking"* described above needs to be enabled.

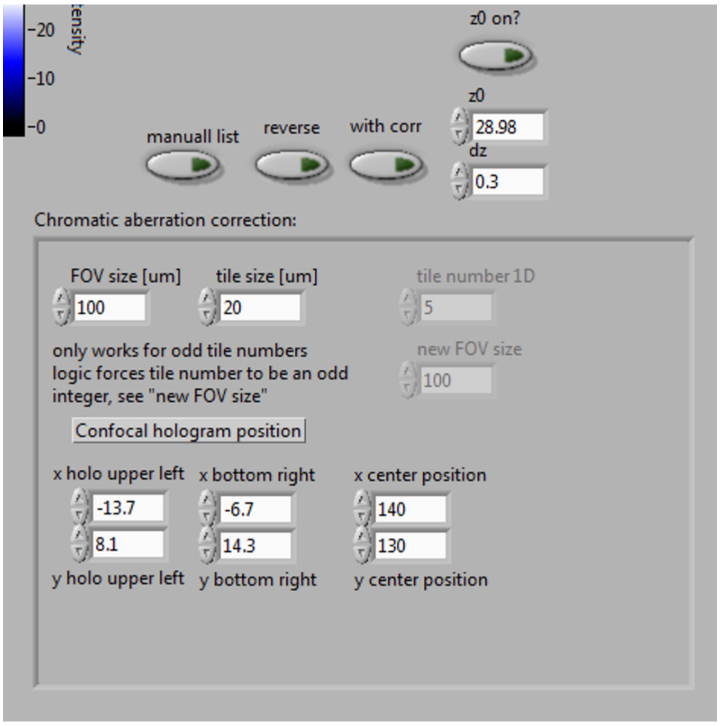

z0: 28.98

dz: 0.3

FOV size [um]: 100

tile size [um]: 20

tile number 1D: 5

only works for odd tile numbers
logic forces tile number to be an odd integer, see "new FOV size"

new FOV size: 100

x holo upper left: -13.7

y holo upper left: 8.1

x bottom right: -6.7

y bottom right: 14.3

x center position: 140

y center position: 130

Figure 9.9: *Control software mosaic with aberration correction.*

The mosaic controls, as shown in Figure 9.9, are defined below:

- *"z0 on?"* activates the z-offset correction for a tilted sample. The z-offset for each tile is calculated assuming a tilt from the lower left to the upper right of the sample plane, which is characteristic for this instrument.
- *"z0"* describes the z position of the tile in the centre of the FOV.
- *"dz"* is the difference between the centre and the upper right tile.
- *"with corr"* if activated the mosaic mode is used with chromatic aberration correction.
- *"reverse"* changes the sequence of the tile acquisition.
- *"manual list"* enables the use of a manually inserted list of hologram offsets. These lists are found below the main frame. For hologram 1, three lists can be entered, called *manual holo tilt STED 128D*, *manual holo tilt STED 90D* and *manual holo tilt STED 70D*. The list for the offset values of hologram 2 is called *xyPosList*. *"Which list (0 → 128 D, 1 → 90 D, 2 → 70 D)"* can be used to set which list is chosen. If *"manuall list"* is disabled, the software calculates an offset for the STED beam for every tile assuming a linear radial relationship.
- *"x holo upper left"* and *"y holo upper left"* describe the hologram position of the depletion beam in the upper left, assuming a linear shift.
- *"x holo bottom right"* and *"y holo bottom right"* describe the hologram position of the depletion beam in the bottom right, assuming a linear shift.
- *"FOV size [μm]"* sets the image size for the full mosaic FOV.
- *"tile size [μm]"* sets the size of a single tile. The automatically calculated numbers of tiles in one dimension is shown in *"tile number 1D"*. Be aware that the installed logic only can handle odd numbers of tiles and will adjust the FOV size accordingly, as displayed in *"new FOV size"*.
- *"x centre position"* is the coordinate of the centre tile in x.
- *"y centre position"* is the coordinate of the centre tile in y.

The doughnut and excitation hologram can be defined using the inputs below the main frame *Holo 1 STED* and *Holo 2 conf changing*. For a detailed description, please refer to the hologram software manual (subsection 9.5.8). The dimension of the hologram can be adjusted separately.

Easter eggs

There are several pitfalls of which all user should be aware, especially anyone wanting to change the software. This list covers some of the most obvious pitfalls:

- How the program handles pixel counts: Internally, the program generates arrays of voltages to output to the scanner (X and Y control), line and pixel clocks. Each of these internal arrays has one value per pixel in the final image. However, the TCSPC card only triggers on the rising edge of a digital (TTL) signal and therefore two pixels within the internally generated scan pattern are used to provide a high and a low output to the pixel clock. This does not influence the end user, but this information is provided for programmers who want to change the code and might otherwise be confused.
- The Yanus IV scan head tries to optimize its acceleration voltage depending on the pixel dwell time, due to the voltage ramp incline. This leads to a pixel shift of each line. For several pixel integration times (0.05 ms, 0.1 ms, 0.2 ms, 0.3 ms, 0.4 ms, 0.5 ms, 0.6 ms, 0.7 ms, 0.8 ms, 0.9 ms, 1 ms and 1.1 ms), these shifts have been compensated. If another integration time is used, it may be necessary to change this offset manually (*s...Fudge*) indicated by the boolean output *manual fudge*.

9.5.8 Software manual: hologram control program

The hologram software controls the SLM display and can apply holograms for the two different laser beams. In the main frame there are three graphical windows, the *"SLM display"* shows the output on the SLM, *"Holo 1"* and *"Holo 2"* display the individual holograms. Underneath, there are options to load and save the two holograms (*"Save Holo 1"*, *"Save Holo 2"*, *"Load Holo 1"* and *"Load Holo 2"*). The *"Dimensions"* entry defines the dimension size of both holograms. If this is changed it will always needs to be followed by activation of the *"Update dimension"* button, as shown in Figure 9.10.

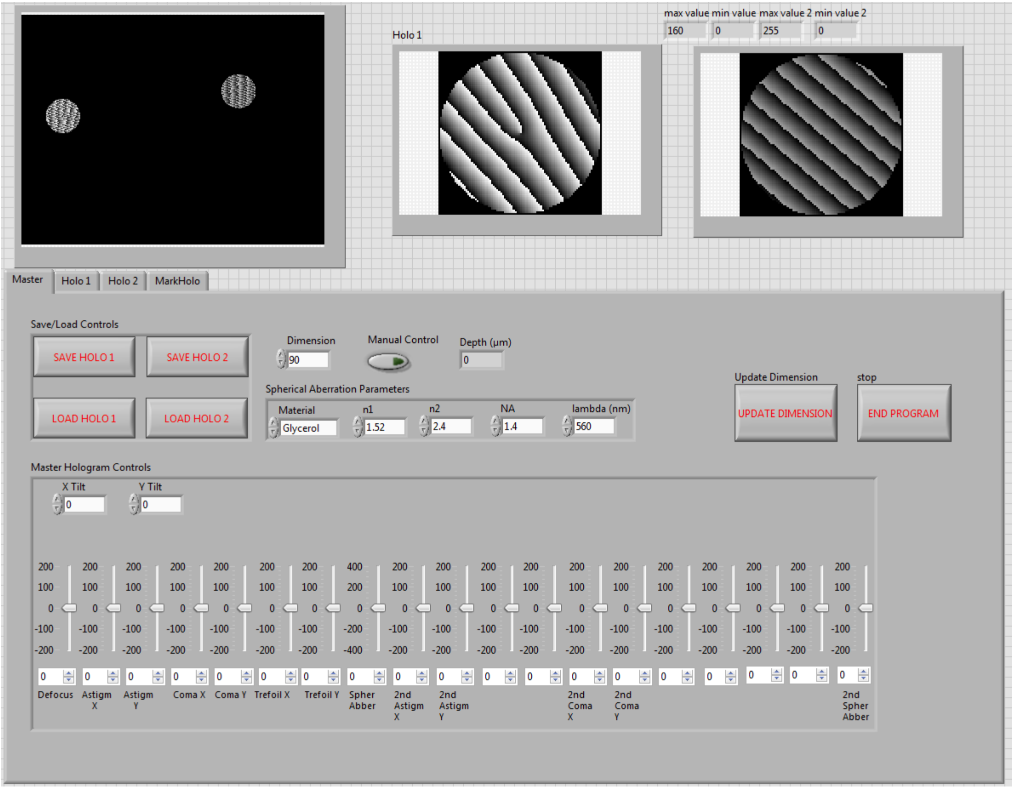
Holo 1
Master
Holo 1
Holo 2
MarkHolo
Save/Load Controls
SAVE HOLO 1
SAVE HOLO 2
LOAD HOLO 1
LOAD HOLO 2
Manual Control
Spherical Aberration Parameters
Update Dimension
UPDATE DIMENSION
stop
END PROGRAM
Master Hologram Controls

max value 160
min value 0
max value 2 255
min value 2 0
Dimension 90
Depth (µm) 0
Material Glycerol
n1 1.52
n2 2.4
NA 1.4
lambda (nm) 560
X Tilt 0
Y Tilt 0
Defocus 0
Astigm X 0
Astigm Y 0
Coma X 0
Coma Y 0
Trefoil X 0
Trefoil Y 0
Spher Abber 0
2nd Astigm X 0
2nd Astigm Y 0
2nd Coma X 0
2nd Coma Y 0
2nd Spher Abber 0

Figure 9.10: *Hologram control software main frame.*

Hologram 1 and 2

With the *"Holo 1"* and *"Holo 2"* panel the two holograms, displayed in Figure 9.11, can be adjusted using following settings:

- *"Beam type"* defines the PSF mode. *"Normal"* should be used to obtain a confocal PSF, *"helical"* for a doughnut shaped PSF and *"StepPhaseDoughnut"* for a top-hat shaped PSF for 3D STED.

- *"Topological charge"* is only activated if the helical *"Beam type"* is used. It defines how many 2π ramps are in one vortex. The minus sign indicates the incline direction, which might need to be changed depending on the circularity direction of the polarisation.

- *"StepRad"* describes the diameter of the *pi*-shifted ring in *"StepPhaseDoughnut"* *"Beam type"* mode.

- *"X Tilt"* sets the offset that the hologram applies to the beam in the x direction in the sample plane.

- *"Y Tilt"* sets the offset that the hologram applies to the beam in the y direction in the sample plane.

- *"MaxBlazedGrating"* defines the amplitude of the blazed grating. This needs to be defined for the wavelength of each beam separately. A misalignment will redistribute more intensity into the zero order beam at the SLM.

- *"Holo X co-ordinates"* defines the overall x offset of the hologram with respect to the SLM display.

- *"Holo Y co-ordinates"* defines the overall y offset of the hologram with respect to the SLM display.

- *"Defocus", "Astigmatism X", "Astigmatism Y", "Coma X", "Coma Y", "Trefoil X", "Trefoil Y"* and related second order aberrations can be adjusted using the controller.

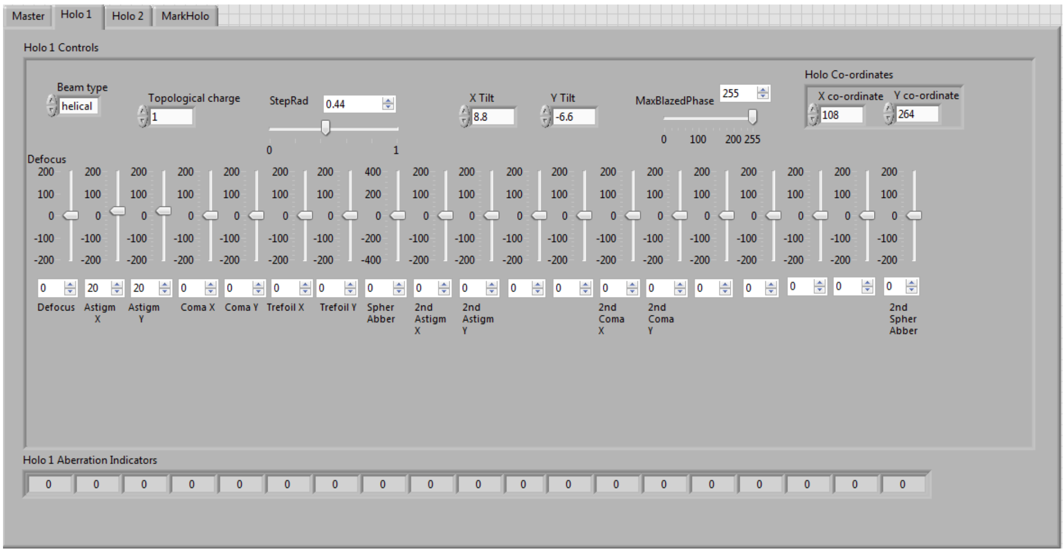

Beam type: helical
Topological charge: 1
StepRad: 0.44
X Tilt: 8.8
Y Tilt: -6.6
MaxBlazedPhase: 255
X co-ordinate: 108
Y co-ordinate: 264

Defocus	Astigm X	Astigm Y	Coma X	Coma Y	Trefoil X	Trefoil Y	Spher Abber	2nd Astigm X	2nd Astigm Y			2nd Coma X	2nd Coma Y					2nd Spher Abber
0	20	20	0	0	0	0	0	0	0	0	0	0	0	0	0	0	0	0

Holo 1 Aberration Indicators: 0 0 0 0 0 0 0 0 0 0 0 0 0 0 0 0 0 0 0

Figure 9.11: *Hologram software aberration frame.*

Multibeam hologram

The panel *"MarkHolo"* contains all parameters required to generate up to four foci, as presented in Figure 9.12. The four graphic windows display the holograms (*"STED holo"* and *"conf Holo"*) and the simulated images using a Fourier transformation of the hologram (*"STED sample plane"* and *"conf sample plane"*). The code is based on a *MATLAB* program written by Prof. Mark Neil. The following parameters can be changed:

- *"itMax"* describes the maximum intensity in one foci. If several focused bean intensities overlap, than a value over 100% (for the software code) can be achieved. *itMax* can set this value higher than four but there are no more than four beams possible with the present instrumentation.

- *"phase levels"* sets how many different phase levels are calculated and therefore the bit-depth of the holograms.
- *"spot #"* sets the number of foci in the sample plane. If one is chosen, the parameters for the first spot are used for all four beams, which are therefore overlaid.
- *"zoom"* is a zoom parameter for the image in the sample plane for visualisation reasons only and does not affect the experimental setup.
- *"Conf settings"* sets the positions for all beams emerging from hologram conf. These are the x (*"conf x"*) and y (*"conf y"*) positions and astigmatism in x (*"Astig x"*) and y (*"Astig y1"*).
- *"update"* is used to apply changes to the hologram after a parameter is changed.
- *"optiMark"* applies the multibeam parameters if enabled. If not, the parameters from panel *Holo 1* and *Holo 2* are used.
- *"phase blazed"* sets the blaze grating amplitude for the confocal and STED holograms separately.

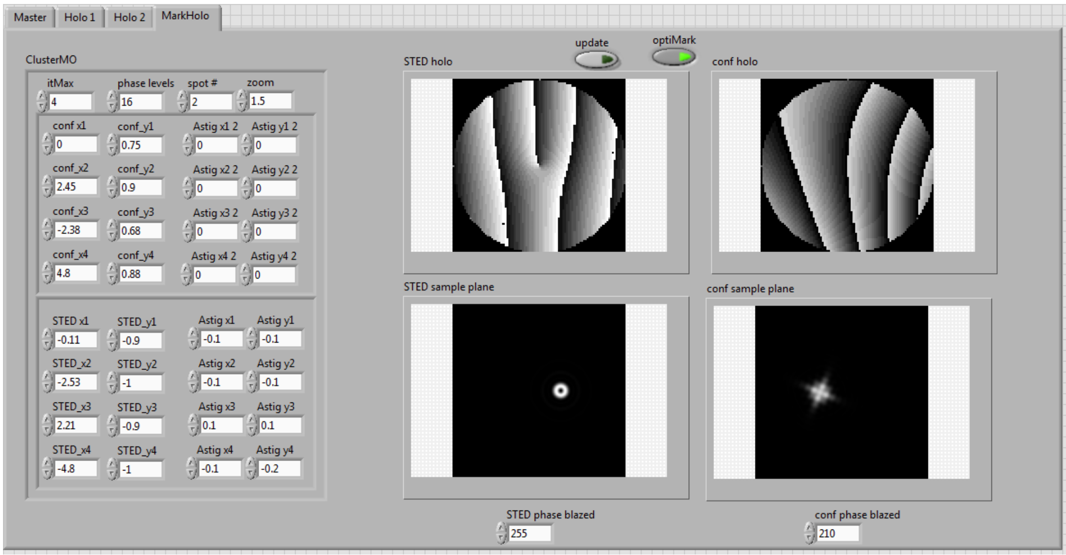

itMax	phase levels	spot #	zoom
4	16	2	1.5
conf x1	conf_y1	Astig x1 2	Astig y1 2
0	0.75	0	0
conf_x2	conf_y2	Astig x2 2	Astig y2 2
2.45	0.9	0	0
conf_x3	conf_y3	Astig x3 2	Astig y3 2
-2.38	0.68	0	0
conf_x4	conf_y4	Astig x4 2	Astig y4 2
4.8	0.88	0	0
STED x1	STED_y1	Astig x1	Astig y1
-0.11	-0.9	-0.1	-0.1
STED_x2	STED_y2	Astig x2	Astig y2
-2.53	-1	-0.1	-0.1
STED_x3	STED_y3	Astig x3	Astig y3
2.21	-0.9	0.1	0.1
STED_x4	STED_y4	Astig x4	Astig y4
-4.8	-1	-0.1	-0.2

STED phase blazed	conf phase blazed
255	210

Figure 9.12: *Hologram control software multibeam frame.*

9.5.9 Bead sample preparation

To prepare bead samples using either gold beads (gold nanoparticles, 80 nm, Sigma-Aldrich) or fluorescence beads (yellow green beads, 46 nm, Invitrogene):

- clean coverslip with ethanol and acetone
- wash coverslip with milliQ, blow dry
- add 200 μL poly-l-lysin to coverslip
- incubate coverslip for 20 minutes at room temperature
- wash coverslip with milliQ, blow dry
- add 200 μL of bead solution (1:50 000 for fluorescence beads or 1:500 for gold beads from stock solution) to coverslip
- incubate coverslip with beads for 20 minutes at room temperature
- wash coverslip with milliQ, blow dry
- add 5 μL TDE to coverslip
- seal with nail polish

Publications

Unpublished (manuscript submitted 14.03.2018):

Frederik Görlitz, Stina Guldbrand, Timothy Runcorn, Robert Murray, Angel Jaso-Tamane, Hugo Sinclair, Enrique Martinez-Perez, James Taylor, Mark Neil, Christopher Dunsby, Paul French, "easySLM-STED: stimulated emission depletion microscopy with aberration correction, extended field of view and multiple beam scanning", *Journal of Biophotonics* (2018)

Frederik Görlitz, David S. Corcoran, Edwin A. Garcia Castano, Birgit Leitinger, Mark A. A. Neil, Christopher Dunsby, Paul M. W. French,“Mapping Molecular Function to Biological Nanostructure: Combining Structured Illumination Microscopy with Fluorescence Lifetime Imaging (SIM + FLIM)”; *Photonics*, 4(3), 40; doi:10.3390/photonics4030040, 2017

Frederik Görlitz*, Douglas J. Kelly*, Sean C. Warren, Dominic Alibhai, Lucien West, Sunil Kumar, Yuriy Alexandrov, Ian Munro, Edwin Garcia, James McGinty, Clifford Talbot, Remigiusz A. Serwa, Emmanuelle Thinon, Vincenzo da Paola, Edward J. Murray, Frank Stuhmeier, Mark A. A. Neil, Edward W. Tate, Christopher Dunsby, Paul M. W. French; “Open Source High Content Analysis Utilizing Automated Fluorescence Lifetime Imaging Microscopy”; *Journal of Visualized Experiments*; URL: http://www.jove.com/video/55119, DOI: doi:10.3791/55119, 2017.

H. Sparks*, **F. Görlitz***, D. J. Kelly, S. C. Warren, P. A. Kellett, E. Garcia, A. K. L. Dymoke-Bradshaw, J. D.Hares, M. A. A. Neil, C. Dunsby, P. M. W. French; “Characterisation of new gated optical image intensifiers for fluorescence lifetime Imaging”; *Review of Scientific Instruments*; 88, 013707, 2017

T. H. Runcorn, **F. Görlitz**, R. T. Murray, E. J. R. Kelleher, “Visible Raman-shifted Fiber Lasers for Biophotonic Applications”, *IEEE Journal of Selected Topics in Quantum Electronics*, DOI:10.1109/JSTQE.2017.2770101, 2017

Elizabeth Noble, Sunil Kumar, **Frederik Görlitz**, Chris Stain, Chris Dunsby, Paul M. W. French, "In vivo label-free mapping of the effect of a photosystem II inhibiting herbicide in plants using chlorophyll fluorescence lifetime", *Plant Methods*, DOI: 10.1186/s13007-017-0201-7, 2017

Emiliano Cortés, Paloma A. Huidobro, Hugo G. Sinclair, Stina Guldbrand, William J. Peveler, Timothy Davies, Simona Parrinello, **Frederik Görlitz**, Chris Dunsby, Mark A. A. Neil, Yonatan Sivan, Ivan P. Parkin, Paul M. W. French, and Stefan A. Maier, "Plasmonic Nanoprobes for Stimulated Emission Depletion Nanoscopy", *ACS Nano*, 10 (11), 10454-10461, DOI: 10.1021/acsnano.6b06361, 2016

Copyright Clearances

All article content, except where otherwise noted (see below), is licensed under a Creative Commons Attribution (CC BY) license (`http://creativecommons.org/licenses/by/4.0/`).

Figure 2.1

License Number	4240220066279
License date	Dec 01, 2017
Licensed Content Publisher	Nature Publishing Group
Licensed Content Publication	Nature
Licensed Content Title	Efficiency of Anti-Stokes Fluorescence in Dyes
Licensed Content Author	A. Jablonski
Licensed Content Date	Jun 10, 1933
Licensed Content Volume	131
Licensed Content Issue	3319
Type of Use	reuse in a dissertation / thesis
Requestor type	academic/educational
Format	electronic
Portion	figures/tables/illustrations
Number of figures/tables/illustrations	1
Figures	Figure 1: Energy level on a phosphorescence molecule
Author of this NPG article	no
Title of your thesis/dissertation	Development and application of fluorescence lifetime imaging and super resolution microscopy
Expected completion date	Apr 2018
Estimated size (number of pages)	200
Total	0.00 USD

Figure 2.4

License Number	4245390817482
License date	Dec 10, 2017
Licensed Content Publisher	Royal Society of Chemistry
Licensed Content Publication	Chemical Society Reviews
Licensed Content Title	Upconverting nanoparticles: a versatile platform for wide-field two-photon microscopy and multi-modal in vivo imaging
Licensed Content Author	Yong Il Park,Kang Taek Lee,Yung Doug Suh,Taeghwan Hyeon
Licensed Content Date	Jul 21, 2014
Licensed Content Volume	44
Licensed Content Issue	6
Type of Use	Thesis/Dissertation
Requestor type	academic/educational
Portion	figures/tables/images
Number of figures/tables/illustrations	1
Format	electronic
Will you be translating?	no
Title of your thesis/dissertation	Development and application of fluorescence lifetime imaging and super resolution microscopy
Expected completion date	Apr 2018
Estimated size (number of pages)	200
Total	0.00 USD

Figure 2.8 a) + b)

License Number	4240270896163
License date	Dec 01, 2017
Licensed Content Publisher	AIP Publishing LLC
Licensed Content Publication	Applied Physics Letters
Licensed Content Title	Measurement of the 4Pi-confocal point spread function proves 75 nm axial resolution
Licensed Content Author	S. W. Hell, S. Lindek, C. Cremer, et al
Licensed Content Date	Mar 14, 1994
Licensed Content Volume	64
Licensed Content Issue	11
Type of Use	Thesis/Dissertation
Requestor type	University or Educational Institution
Portion	Figure/Table
Number of figures/tables/illustrations	1
Format	electronic
Will you be translating?	no
Title of your thesis/dissertation	Development and application of fluorescence lifetime imaging and super resolution microscopy
Expected completion date	Apr 2018
Estimated size (number of pages)	200
Total	0.00 USD

Figure 2.8 c)

License Number	4245400127819
License date	Dec 10, 2017
Licensed Content Publisher	John Wiley and Sons
Licensed Content Publication	Annalen der Physik
Licensed Content Title	Uber Sichtbarmachung und Größenbestimmung ultramikoskopischer Teilchen, mit besonderer Anwendung auf Goldrubingläser
Licensed Content Author	H. Siedentopf,R. Zsigmondy
Licensed Content Date	Mar 14, 2006
Licensed Content Pages	39
Type of Use	Thesis/Dissertation
Requestor type	University/Academic
Portion	Figure/Table
Number of figures/tables/illustrations	1
Original Wiley figure/table number(s)	Figure 3
Format	electronic
Will you be translating?	no
Title of your thesis/dissertation	Development and application of fluorescence lifetime imaging and super resolution microscopy
Expected completion date	Apr 2018
Estimated size (number of pages)	200
Total	0.00 USD

Figure 2.9

License Number	4245391134811
License date	Dec 10, 2017
Licensed Content Publisher	Nature Publishing Group
Licensed Content Publication	Nature Methods
Licensed Content Title	Sub-diffraction-limit imaging by stochastic optical reconstruction microscopy (STORM)
Licensed Content Author	Michael J Rust, Mark Bates, Xiaowei Zhuang
Licensed Content Date	Aug 9, 2006
Licensed Content Volume	3
Licensed Content Issue	10
Type of Use	reuse in a dissertation / thesis
Requestor type	academic/educational
Portion	figures/tables/illustrations
Number of figures/tables/illustrations	1
Format	electronic
High-res required	no
Figures	Figure 1
Will you be translating?	no
Title of your thesis/dissertation	Development and application of fluorescence lifetime imaging and super resolution microscopy
Expected completion date	Apr 2018
Estimated size (number of pages)	200
Total	0.00 USD

Figure 2.11

License Number	4240260619278
License date	Dec 01, 2017
Licensed Content Publisher	John Wiley and Sons
Licensed Content Publication	Journal of Microscopy
Licensed Content Title	Surpassing the lateral resolution limit by a factor of two using structured illumination microscopy
Licensed Content Author	M. G. L. Gustafsson
Licensed Content Date	Dec 24, 2001
Licensed Content Pages	6
Type of Use	Dissertation/Thesis
Requestor type	University/Academic
Format	electronic
Number of figures/tables	1
Original Wiley figure/table number(s)	Figure 1
Will you be translating?	no
Title of your thesis/dissertation	Development and application of fluorescence lifetime imaging and super resolution microscopy
Expected completion date	Apr 2018
Estimated size (number of pages)	200
Total	0.00 USD

Figure 2.13 and Figure 2.14

License Number	4240280283774
License date	Dec 01, 2017
Licensed Content Publisher	The American Association for the Advancement of Science
Licensed Content Publication	Science
Licensed Content Title	Far-Field Optical Nanoscopy
Licensed Content Author	Stefan W. Hell
Licensed Content Date	May 25, 2007
Licensed Content Volume	316
Licensed Content Issue	5828
Type of Use	Thesis / Dissertation
Requestor type	Scientist/individual at a research institution
Format	electronic
Portion	figures/tables/illustrations
Number of figures/tables/illustrations	1
Figures	Figure 1
Will you be translating?	no
Title of your thesis/dissertation	Development and application of fluorescence lifetime imaging and super resolution microscopy
Expected completion date	Apr 2018
Estimated size (number of pages)	200
Total	0.00 USD

Figure 2.16 b) and Figure 2.17

License Number	4245390464435
License date	Dec 10, 2017
Licensed Content Publisher	John Wiley and Sons
Licensed Content Publication	Journal of Biophotonics
Licensed Content Title	3-D stimulated emission depletion microscopy with programmable aberration correction
Licensed Content Author	Martin O. Lenz, Hugo G. Sinclair, Alexander Savell, James H. Clegg, Alice C. N. Brown, Daniel M. Davis, Chris Dunsby, Mark A. A. Neil,Paul M. W. French
Licensed Content Date	Jun 21, 2013
Licensed Content Pages	8
Type of Use	Thesis / Dissertation
Requestor type	University/Academic
Format	electronic
Portion	Figure/table
Number of figures/tables/illustrations	1
Original Wiley figure/table number(s)	Figure 1
Will you be translating?	no
Title of your thesis/dissertation	Development and application of fluorescence lifetime imaging and super resolution microscopy
Expected completion date	Apr 2018
Estimated size (number of pages)	200
Total	0.00 USD

Figure 2.24 b) and Figure 2.25

License Number	4240250873639
License date	Dec 01, 2017
Licensed Content Publisher	John Wiley and Sons
Licensed Content Publication	Cancer Science
Licensed Content Title	Stable expression of FRET biosensors: A new light in cancer research
Licensed Content Author	Kazuhiro Aoki, Naoki Komatsu, Eishu Hirata, Yuji Kamioka, Michiyuki Matsuda
Licensed Content Date	Feb 3, 2012
Licensed Content Pages	6
Type of Use	Thesis / Dissertation
Requestor type	University/Academic
Format	electronic
Portion	Figure/table
Number of figures/tables/illustrations	1
Original Wiley figure/table number(s)	Figure 1
Will you be translating?	no
Title of your thesis/dissertation	Development and application of fluorescence lifetime imaging and super resolution microscopy
Expected completion date	Apr 2018
Estimated size (number of pages)	200
Total	0.00 USD

Figure 5.7

License Number	4240211230309
License date	Dec 01, 2017
Licensed Content Publisher	Nature Publishing Group
Licensed Content Publication	Nature
Licensed Content Title	Controlling the double helix
Licensed Content Author	Gary Felsenfeld, Mark Groudine
Licensed Content Date	Jan 23, 2003
Licensed Content Volume	421
Licensed Content Issue	6921
Type of Use	reuse in a dissertation / thesis
Requestor type	academic/educational
Format	electronic
Portion	figures/tables/illustrations
Number of figures/tables/illustrations	1
High-res required	no
Figure	Figure 1 : Packaging DNA
Author of this NPG article	no
Title of your thesis/dissertation	Development and application of fluorescence lifetime imaging and super resolution microscopy
Expected completion date	Apr 2018
Estimated size (number of pages)	200
Total	0.00 USD

Figure 5.12

License Number	4245391461133
License date	Dec 10, 2017
Licensed Content Publisher	John Wiley and Sons
Licensed Content Publication	EMBO Reports
Licensed Content Title	LEGOs® and legacies of centrioles and centrosomes
Licensed Content Author	Gerald Schatten,Calvin Simerly
Licensed Content Date	Aug 6, 2015
Licensed Content Pages	3
Type of Use	Dissertation/Thesis
Requestor type	University/Academic
Format	electronic
Portion	Figure/table
Number of figures/tables	1
Original Wiley figure/table number(s)	Figure 1
Will you be translating?	no
Title of your thesis/dissertation	Development and application of fluorescence lifetime imaging and super resolution microscopy
Expected completion date	Apr 2018
Estimated size (number of pages)	200
Total	0.00 USD

Figure 7.8 a) + b)

License Number	4240280573703
License date	Dec 01, 2017
Licensed Content Publisher	Elsevier
Licensed Content Publication	Developmental Biology
Licensed Content Title	Multi-pathway control of the proliferation versus meiotic development decision in the Caenorhabditis elegans germline
Licensed Content Author	Dave Hansen,E.Jane Albert Hubbard,Tim Schedl
Licensed Content Date	Apr 15, 2004
Licensed Content Volume	268
Licensed Content Issue	2
Licensed Content Pages	16
Start Page	342
End Page	357
Type of Use	reuse in a dissertation / thesis
Intended publisher of new work	other
Portion	figures/tables/illustrations
Number of figures/tables/illustrations	1
Format	electronic
Are you the author of this Elsevier article?	No
Will you be translating?	No
Original figure numbers	Figure 1
Title of your thesis/dissertation	Development and application of fluorescence lifetime imaging and super resolution microscopy
Expected completion date	Apr 2018
Estimated size (number of pages)	200
Total	0.00 USD

Figure 7.8 c) + d)

License Number	4240280916745
License date	Dec 01, 2017
Licensed content publisher	Oxford University Press
Licensed content publication	Nucleic Acids Research
Licensed content title	WormBook: the online review of Caenorhabditis elegans biology
Licensed content author	Girard, Lisa R.; Fiedler, Tristan J.
Licensed content date	Nov 11, 2006
Type of Use	Thesis/Dissertation
Title of your thesis/dissertation	Development and application of fluorescence lifetime imaging and super resolution microscopy
Expected completion date	Apr 2018
Estimated size (number of pages)	200
Total	0.00 USD

Bibliography

[Abb73] Abbe, E. 'Beiträge zur Theorie des Mikroskops und der mikroskopischen Wahrnehmung'. *Archiv für mikroskopische Anatomie*, **9**:(1873), 413–468.

[Air35] Airy, G.B. 'On the Diffraction of an Object-glass with Circular Aperture'. *Transactions of the Cambridge Philosophical Society*, **5**:(1835), 283.

[Aok12] Aoki, K., Komatsu, N., Hirata, E., Kamioka, Y., and Matsuda, M. 'Stable expression of FRET biosensors: A new light in cancer research'. *Cancer Science*, **103(4)**:(2012), 614–619. ISSN 1349-7006. doi:10.1111/j.1349-7006.2011.02196.x.

[Att15] Attardo, A., Fitzgerald, J.E., and Schnitzer, M.J. 'Impermanence of dendritic spines in live adult CA1 hippocampus'. *Nature*, **523**:(2015), 592–596. doi:10.1038/nature14467.

[Auk08] Auksorius, E., Boruah, B.R., Dunsby, C., Lanigan, P.M.P., Kennedy, G., Neil, M.A.A., and French, P.M.W. 'Stimulated emission depletion microscopy with a supercontinuum source and fluorescence lifetime imaging'. *Opt. Lett.*, **33(2)**:(2008), 113–115. doi:10.1364/OL.33.000113.

[Axe81] Axelrod, D. 'Cell-substrate contacts illuminated by total internal reflection fluorescence.' *The Journal of Cell Biology*, **89(1)**:(1981), 141–145. ISSN 0021-9525. doi:10.1083/jcb.89.1.141.

[Axe01] Axelrod, D. 'Total Internal Reflection Fluorescence Microscopy in Cell Biology'. *Traffic*, **2(11)**:(2001), 764–774. ISSN 1600-0854. doi:10.1034/j.1600-0854.2001.21104.x.

[Bü11] Bückers, J., Wildanger, D., Vicidomini, G., Kastrup, L., and Hell, S.W. 'Simultaneous multi-lifetime multi-color STED imaging for colocalization analyses'. *Opt. Express*, **19(4)**:(2011), 3130–3143. doi:10.1364/OE.19.003130.

[Bö16] Böhm, U., Hell, S.W., and Schmidt, R. '4Pi-RESOLFT nanoscopy'. *Nature Communica-*

tion, **7**:(2016), 10504. doi:10.1038/ncomms10504.

[Bah05] Bahe, S., Stierhof, Y.D., Wilkinson, C.J., Leiss, F., and Nigg, E.A. 'Rootletin forms centriole-associated filaments and functions in centrosome cohesion'. *The Journal of Cell Biology*, **171(1)**:(2005), 27–33. ISSN 0021-9525. doi:10.1083/jcb.200504107.

[Bal16] Balzarotti, F., Eilers, Y., Gwosch, K.C., Gynnå, A.H., Westphal, V., Stefani, F.D., Elf, J., and Hell, S.W. 'Nanometer resolution imaging and tracking of fluorescent molecules with minimal photon fluxes'. *Science*. ISSN 0036-8075. doi:10.1126/science.aak9913.

[Bar17] Baryshnikov, G., Minaev, B., and Ågren, H. 'Theory and Calculation of the Phosphorescence Phenomenon'. *Chemical Reviews*, **117(9)**:(2017), 6500–6537. doi:10.1021/acs.chemrev.7b00060. PMID: 28388041.

[Bas99] Bastiaens, P.I. and Squire, A. 'Fluorescence lifetime imaging microscopy: spatial resolution of biochemical processes in the cell'. *Trends in Cell Biology*, **9(2)**:(1999), 48 – 52. ISSN 0962-8924. doi:10.1016/S0962-8924(98)01410-X.

[Bas12] Basak, K., Manjunatha, M., and Dutta, P.K. 'Review of laser speckle-based analysis in medical imaging'. *Medical & Biological Engineering & Computing*, **50(6)**:(2012), 547–558. doi:10.1007/s11517-012-0902-z.

[Beb86] Bebelaar, D. 'Time response of various types of photomultipliers and its wavelength dependence in time-correlated single-photon counting with an ultimate resolution of 47 ps FWHM'. *Review of Scientific Instruments*, **57(6)**:(1986), 1116–1125. doi:10.1063/1.1138666.

[Bec02] Becker, W. 'Verfahren und Vorrichtung zur zeitkorrelierten Einzelphotonenzählung mit hoher Registrierrate' (2002). DE Patent 4,339,784.

[Bec14] Becker, W. *The bh TCSPC Handbook*. Becker & Hickl GmbH (2014).

[Bee92] Beechem, J.M. 'Global analysis of biochemical and biophysical data'. *Methods in enzymology*, **210**:(1992), 37–54.

[Ber03] Berney, C. and Danuser, G. 'FRET or no FRET: a quantitative comparison'. *Biophysical journal*, **84(6)**:(2003), 3992–4010.

[Ber15] Bergermann, F., Alber, L., Sahl, S.J., Engelhardt, J., and Hell, S.W. '2000-fold parallelized dual-color STED fluorescence nanoscopy'. *Opt. Express*, **23(1)**:(2015), 211–223. doi:10.1364/OE.23.000211.

[Bet06] Betzig, E., Patterson, G.H., Sougrat, R., Lindwasser, O.W., Olenych, S., Bonifacino, J.S., Davidson, M.W., Lippincott-Schwartz, J., and Hess, H.F. 'Imaging Intracellular Fluorescent Proteins at Nanometer Resolution'. *Science*, **313(5793)**:(2006), 1642–1645. ISSN 0036-8075. doi:10.1126/science.1127344.

[Bin86] Binnig, G., Quate, C.F., and Gerber, C. 'Atomic Force Microscope'. *Phys. Rev. Lett.*, **56**:(1986), 930–933. doi:10.1103/PhysRevLett.56.930.

[Bin11] Bingen, P., Reuss, M., Engelhardt, J., and Hell, S.W. 'Parallelized STED fluorescence nanoscopy'. *Opt. Express*, **19(24)**:(2011), 23716–23726. doi:10.1364/OE.19.023716.

[Bol89] Bolin, F.P., Preuss, L.E., Taylor, R.C., and Ference, R.J. 'Refractive index of some mammalian tissues using a fiber optic cladding method'. *Appl. Opt.*, **28(12)**:(1989), 2297–2303. doi:10.1364/AO.28.002297.

[Boo07] Booth, M.J. 'Adaptive optics in microscopy'. *Philosophical Transactions of the Royal Society of London A: Mathematical, Physical and Engineering Sciences*, **365(1861)**:(2007), 2829–2843. ISSN 1364-503X. doi:10.1098/rsta.2007.0013.

[Boo14] Booth, M.J. 'Adaptive optical microscopy: the ongoing quest for a perfect image'. *Light: Science & Applications*, **3(e165)**. ISSN 1364-503X. doi:10.1038/lsa.2014.46.

[Bor09] Boruah, B. and Neil, M. 'Focal field computation of an arbitrarily polarized beam using fast Fourier transforms'. *Optics Communications*, **282(24)**:(2009), 4660 – 4667. ISSN 0030-4018. doi:10.1016/j.optcom.2009.09.019.

[Bor12] Boron, W.F. and Boulpaep, E.L. *Medical Physiology, 2e Updated*. Elsevier Health Sciences (2012).

[Bou15] Bourg, N., Mayet, C., Dupuis, G., Barroca, T., Bon, P., Lécart, S., Fort, E., and Lévêque-Fort, S. 'Direct optical nanoscopy with axially localized detection'. *Nature Photonics*, **9(587)**. doi:10.1038/nphoton.2015.132.

[Buc08] Buck, S.B., Bradford, J., Gee, K.R., Agnew, B.J., Clarke, S.T., and Salic, A. 'Detection of S-phase cell cycle progression using 5-ethynyl-2'-deoxyuridine incorporation with click chemistry, an alternative to using 5-bromo-2'-deoxyuridine antibodies.' *Biotechniques*, **44(7)**:(2008), 927–929.

[Bue11] Bueno, J.M., Giakoumaki, A., Gualda, E.J., Schaeffel, F., and Artal, P. 'Analysis of the chicken retina with an adaptive optics multiphoton microscope'. *Biomed. Opt. Express*,

2(6):(2011), 1637–1648. doi:10.1364/BOE.2.001637.

[Bug89] Bugiel, I., König, K., and Wabnitz, H. ‘Investigation of cells by fluorescence laser scanning microscopy with subnanosecond time resolution’. *Lasers Life Sci*, **3(1)**:(1989), 47–53.

[Bur15] Burke, D., Patton, B., Huang, F., Bewersdorf, J., and Booth, M.J. ‘Adaptive optics correction of specimen-induced aberrations in single-molecule switching microscopy’. *Optica*, **2(2)**:(2015), 177–185. doi:10.1364/OPTICA.2.000177.

[Bus26] Busch, H. ‘Berechnung der Bahn von Kathodenstrahlen im axialsymmetrischen elektromagnetischen Felde’. *Annalen der Physik*, **386(25)**:(1926), 974–993. ISSN 1521-3889. doi:10.1002/andp.19263862507.

[Byr91] Byron, C.M. and Werner, T.C. ‘Experiments in synchronous fluorescence spectroscopy for the undergraduate instrumental chemistry course’. *Journal of Chemical Education*, **68(5)**:(1991), 433. doi:10.1021/ed068p433.

[Cha06] Charrière, F., Marian, A., Montfort, F., Kuehn, J., Colomb, T., Cuche, E., Marquet, P., and Depeursinge, C. ‘Cell refractive index tomography by digital holographic microscopy’. *Opt. Lett.*, **31(2)**:(2006), 178–180. doi:10.1364/OL.31.000178.

[Cha17] Chang, J.B., Chen, F., Yoon, Y.G., Jung, E.E., Babcock, H., Kang, J.S., Asano, S., Suk, H.J., Pak, N., Tillberg, P.W., Wassie, A.T., Cai, D., and Boyden, E.S. ‘Iterative expansion microscopy’. *Nature Methods*, **14**. doi:10.1038/nmeth.4261.

[Che06] Chen, H., Puhl, H.L., Koushik, S.V., Vogel, S.S., and Ikeda, S.R. ‘Measurement of FRET Efficiency and Ratio of Donor to Acceptor Concentration in Living Cells’. *Biophysical Journal*, **91(5)**:(2006), L39 – L41. ISSN 0006-3495. doi:10.1529/biophysj.106.088773.

[Che09a] Chehrehasa, F., Meedeniya, A.C., Dwyer, P., Abrahamsen, G., and Mackay-Sim, A. ‘EdU, a new thymidine analogue for labelling proliferating cells in the nervous system’. *Journal of Neuroscience Methods*, **177(1)**:(2009), 122 – 130. ISSN 0165-0270. doi:10.1016/j.jneumeth.2008.10.006.

[Che09b] Chehrehasa, F., Meedeniya, A.C., Dwyer, P., Abrahamsen, G., and Mackay-Sim, A. ‘EdU, a new thymidine analogue for labelling proliferating cells in the nervous system’. *Journal of neuroscience methods*, **177(1)**:(2009), 122–130.

[Che15a] Chen, F., Tillberg, P.W., and Boyden, E.S. ‘Expansion microscopy’. *Science*, **347(6221)**:(2015), 543–548. ISSN 0036-8075. doi:10.1126/science.1260088.

[Che15b] Chen, H., Holst, G., and Gratton, E. ‘Modulated CMOS camera for fluorescence lifetime microscopy’. *Microscopy Research and Technique*, **78(12)**:(2015), 1075–1081. ISSN 1097-0029. doi:10.1002/jemt.22587.

[Che16] Chennell, G., Willows, R.J., Warren, S.C., Carling, D., French, P.M., Dunsby, C., and Sardini, A. ‘Imaging of Metabolic Status in 3D Cultures with an Improved AMPK FRET Biosensor for FLIM’. *Sensors*, **16(8)**:(2016), 1312.

[Chm13] Chmyrov, A., Keller, J., Grotjohann, T., Ratz, M., d’Este, E., Jakobs, S., Eggeling, C., and Hell, S.W. ‘Nanoscopy with more than 100,000’doughnuts”. *Nature methods*, **10(8)**:(2013), 737–740.

[Cla04] Clayton, A., Hanley, Q.S., and Verveer, P.J. ‘Graphical representation and multicomponent analysis of single-frequency fluorescence lifetime imaging microscopy data’. *Journal of microscopy*, **213(1)**:(2004), 1–5.

[Col00] Cole, M.J., Siegel, J., Webb, S.E.D., Jones, R., Dowling, K., French, P.M.W., Lever, M.J., Sucharov, L.O.D., Neil, M.A.A., Juškaitis, R., and Wilson, T. ‘Whole-field optically sectioned fluorescence lifetime imaging’. *Opt. Lett.*, **25(18)**:(2000), 1361–1363. doi:10.1364/OL.25.001361.

[Con26] Condon, E. ‘A theory of intensity distribution in band systems’. *Physical Review*, **28**:(1926), 1182–1201. doi:10.1103/PhysRev.28.1182.

[Con17] Contributors, W. ‘Franck–Condon principle — Wikipedia, The Free Encyclopedia’ (2017). [Online; accessed 27-December-2017].

[Coo65] Cooley, J.W. and Tukey, J.W. ‘An algorithm for the machine calculation of complex Fourier series’. *Mathematics of computation*, **19(90)**:(1965), 297–301.

[Coo00] Cooper, G. *The cell: a molecular approach*, volume 2nd ed. Washington, D.C: ASM Press (2000).

[Cur15] Curdt, F., Herr, S.J., Lutz, T., Schmidt, R., Engelhardt, J., Sahl, S.J., and Hell, S.W. ‘isoSTED nanoscopy with intrinsic beam alignment’. *Opt. Express*, **23(24)**:(2015), 30891–30903. doi:10.1364/OE.23.030891.

[Dü86] Dürig, U., Pohl, D.W., and Rohner, F. ‘Near-field optical-scanning microscopy’. *Journal of Applied Physics*, **59(10)**:(1986), 3318–3327. doi:10.1063/1.336848.

[Dé07] Débarre, D., Booth, M.J., and Wilson, T. ‘Image based adaptive optics through optimisation of low spatial frequencies'. *Opt. Express*, **15(13)**:(2007), 8176–8190. doi:10.1364/OE.15.008176.

[Dé08] Débarre, D., Botcherby, E.J., Booth, M.J., and Wilson, T. 'Adaptive optics for structured illumination microscopy'. *Opt. Express*, **16(13)**:(2008), 9290–9305. doi:10.1364/OE.16.009290.

[Dai84] Dainty, J.C. *Laser Speckle and Related Phenomena.* Springer (1984).

[Dam91] Dames, M.P., Dowling, R.J., McKee, P., and Wood, D. 'Efficient optical elements to generate intensity weighted spot arrays: design and fabrication'. *Appl. Opt.*, **30(19)**:(1991), 2685–2691. doi:10.1364/AO.30.002685.

[DB23] De Broglie, L. 'Waves and quanta'. *Nature*, **112**:(1923), 540–540. doi:10.1038/112540a0.

[DB84] Dymoke-Bradshaw, A.K.L., Kilkenny, J.D., and Westlake, J. 'A Gated X-Ray Intensifier With A Resolution Of 50 Picoseconds'. *Proc.SPIE*, **0427**:(1984), 0427 – 0427 – 5. doi:10.1117/12.936263.

[dC12] de Chaumont, F., Dallongeville, S., Chenouard, N., Hervé, N., Pop, S., Provoost, T., Meas-Yedid, V., Pankajakshan, P., Lecomte, T., Montagner, Y.L., Lagache, T., Dufour, A., and Olivo-Marin, J.C. 'Icy: an open bioimage informatics platform for extended reproducible research'. *Nature Methods*, **9(7)**:(2012), 690–696. doi:10.1038/nmeth.2075.

[DD09] Diermeier-Daucher, S., Clarke, S.T., Hill, D., Vollmann-Zwerenz, A., Bradford, J.A., and Brockhoff, G. 'Cell type specific applicability of 5-ethynyl-2-deoxyuridine (EdU) for dynamic proliferation assessment in flow cytometry'. *Cytometry Part A*, **75(6)**:(2009), 535–546.

[Den90] Denk, W., Strickler, J., and Webb, W. 'Two-photon laser scanning fluorescence microscopy'. *Science*, **248(4951)**:(1990), 73–76. ISSN 0036-8075. doi:10.1126/science.2321027.

[Den09] Deng, S., Liu, L., Cheng, Y., Li, R., and Xu, Z. 'Investigation of the influence of the aberration induced by a plane interface on STED microscopy'. *Opt. Express*, **17(3)**:(2009), 1714–1725. doi:10.1364/OE.17.001714.

[Dic98] Dickson, R.M., Norris, D.J., and Moerner, W.E. 'Simultaneous Imaging of Individual Molecules Aligned Both Parallel and Perpendicular to the Optic Axis'. *Phys. Rev. Lett.*, **81**:(1998), 5322–5325. doi:10.1103/PhysRevLett.81.5322.

[Dig08] Digman, M.A., Caiolfa, V.R., Zamai, M., and Gratton, E. 'The Phasor Approach to Fluorescence Lifetime Imaging Analysis'. *Biophysical Journal*, **94(2)**:(2008), L14 – L16. ISSN 0006-3495. doi:10.1529/biophysj.107.120154.

[Dow98] Dowling, K., Dayel, M., Lever, M., French, P., Hares, J., and Dymoke-Bradshaw, A. 'Fluorescence lifetime imaging with picosecond resolution for biomedical applications'. *Optics letters*, **23(10)**:(1998), 810–812.

[Dox05] Doxsey, S., McCollum, D., and Theurkauf, W. 'Centrosomes in cellular regulation'. *Annual Review of Cell and Developmental Biology*, **21(1)**:(2005), 411–434. doi:10.1146/annurev.cellbio.21.122303.120418. PMID: 16212501.

[dR98] de Rooij, J., Zwartkruis1, F.J.T., Verheijen, M.H.G., Cool, R.H., Nijman1, S.M.B., Wittinghofer, A., and Bos, J.L. 'Epac is a Rap1 guanine-nucleotide-exchange factor directly activated by cyclic AMP'. *Nature*, **396**:(1998), 474–477. doi:doi:10.1038/24884.

[Ebe77] Eberhardt, E.H. 'Image transfer properties of proximity focused image tubes'. *Appl. Opt.*, **16(8)**:(1977), 2127–2133. doi:10.1364/AO.16.002127.

[Ede14] Edelstein, A., Tsuchida, M., Amodaj, N., Pinkard, H., Vale, R., and Stuurman, N. 'Advanced methods of microscope control using uManager software'. *Journal of Biological Methods*, **1(2)**. ISSN 2326-9901.

[Ega05] Egami, N., Nanba, M., Takiguchi, Y., Miyakawa, K., Watabe, T., Okazaki, S., Osada, K., Obara, Y., Tanaka, M., and Itoh, S. '50*50 μm pixel magnetic focus field emitter array image sensor with high-gain avalanche rushing amorphous photoconductor target'. *Journal of Vacuum Science & Technology B: Microelectronics and Nanometer Structures Processing, Measurement, and Phenomena*, **23(5)**:(2005), 2056–2062. doi:10.1116/1.2050658.

[Egn02] Egner, A., Andresen, V., and Hell, S.W. 'Comparison of the axial resolution of practical Nipkow-disk confocal fluorescence microscopy with that of multifocal multiphoton microscopy: theory and experiment'. *Journal of Microscopy*, **206(1)**:(2002), 24–32. ISSN 1365-2818. doi:10.1046/j.1365-2818.2002.01001.x.

[Ein17] Einstein, A. 'Zur Quantentheorie der Strahlung'. *Physikalische Zeitschrift*, **18**.

[Eld08] Elder, A., Schlachter, S., and Kaminski, C.F. 'Theoretical investigation of the photon efficiency in frequency-domain fluorescence lifetime imaging microscopy'. *J. Opt. Soc. Am. A*, **25(2)**:(2008), 452–462. doi:10.1364/JOSAA.25.000452.

[Eld09] Elder, A.D., Kaminski, C.F., and Frank, J.H. 'φ2FLIM: a technique for alias-free frequency domain fluorescence lifetime imaging'. *Opt. Express*, **17(25)**:(2009), 23181–23203. doi: 10.1364/OE.17.023181.

[Els04] Elson, D.S., Munro, I., Requejo-Isidro, J., McGinty, J., Dunsby, C., Galletly, N., Stamp, G.W., Neil, M.A.A., Lever, M.J., Kellett, P.A., Dymoke-Bradshaw, A., Hares, J., and French, P.M.W. 'Real-time time-domain fluorescence lifetime imaging including single-shot acquisition with a segmented optical image intensifier'. *New Journal of Physics*, **6(1)**:(2004), 180.

[Eng18] Engelhard, J. 'with kind approval of Dr. Johann Engelhardt, DKFZ (Deutsches Krebsf-Forschungszentrum), Heidelberg' (2018).

[Eri01] Erickson, M.G., Alseikhan, B.A., Peterson, B.Z., and Yue, D.T. 'Preassociation of Calmodulin with Voltage-Gated Ca2+ Channels Revealed by FRET in Single Living Cells'. *Neuron*, **31(6)**:(2001), 973 – 985. ISSN 0896-6273. doi:10.1016/S0896-6273(01)00438-X.

[Ern09] Erni, R., Rossell, M.D., Kisielowski, C., and Dahmen, U. 'Atomic-Resolution Imaging with a Sub-50-pm Electron Probe'. *Phys. Rev. Lett.*, **102**:(2009), 096101. doi:10.1103/PhysRevLett.102.096101.

[Esn18] Esner, M., Meyenhofer, F., and Bickle, M. *High Content Screening*. Springer (2018).

[Esp06] Esposito, A., Gerritsen, H., Oggier, T., Lustenberger, F., and Wouters, F.S. 'Innovating lifetime microscopy: a compact and simple tool for life sciences, screening, and diagnostics'. *Journal of Biomedical Optics*, **11**:(2006), 11 – 11 – 8. doi:10.1117/1.2208999.

[Fö48] Förster, T. 'Zwischenmolekulare Energiewanderung und Fluoreszenz'. *Annalen der Physik*, **437(1-2)**:(1948), 55–75. ISSN 1521-3889. doi:10.1002/andp.19484370105.

[Fav92] Favro, L., Thomas, R., Kuo, P., and Chen, L. 'Confocal microscope' (1992). US Patent 5,162,941.

[Fel03] Felsenfeld, G. and Groudine, M. 'Controlling the double helix'. *Nature*, **421(6921)**:(2003), 448–453.

[Fer09] Ferullo, D.J., Cooper, D.L., Moore, H.R., and Lovett, S.T. 'Cell cycle synchronization of Escherichia coli using the stringent response, with fluorescence labeling assays for DNA content and replication'. *Methods*, **48(1)**:(2009), 8–13.

[Flo11] Flors, C. and Earnshaw, W.C. 'Super-resolution fluorescence microscopy as a tool to study the nanoscale organization of chromosomes'. *Current Opinion in Chemical Biology*, **15(6)**:(2011), 838 – 844. ISSN 1367-5931. doi:10.1016/j.cbpa.2011.10.004. Molecular Imaging.

[Fol08] Folling, J., Bossi, M., Bock, H., Medda, R., Wurm, C.A., Hein, B., Jakobs, S., Eggeling, C., and Hell, S.W. 'Fluorescence nanoscopy by ground-state depletion and single-molecule return'. *Nature Methods*, **5(11)**:(2008), 943–945.

[Fra15] Franke, R. and Holst, G.A. 'Frequency-domain fluorescence lifetime imaging system (pco.flim) based on a in-pixel dual tap control CMOS image sensor'. *Proc.SPIE*, **9328**:(2015), 9328 – 9328 – 19. doi:10.1117/12.2087589.

[Fri11] Friedrich, M., Gan, Q., Ermolayev, V., and Harms, G.S. 'STED-SPIM: Stimulated Emission Depletion Improves Sheet Illumination Microscopy Resolution'. *Biophysical Journal*, **100(8)**:(2011), L43 – L45. ISSN 0006-3495. doi:10.1016/j.bpj.2010.12.3748.

[Gö13] Göttfert, F., Wurm, C.A., Mueller, V., Berning, S., Cordes, V.C., Honigmann, A., and Hell, S.W. 'Coaligned Dual-Channel STED Nanoscopy and Molecular Diffusion Analysis at 20 nm Resolution'. *Biophysical Journal*, **105(1)**:(2013), L01 – L03. ISSN 0006-3495. doi:10.1016/j.bpj.2013.05.029.

[Gö14] Görlitz, F., Hoyer, P., Falk, H., Kastrup, L., Engelhardt, J., and Hell, S.W. 'A STED microscope designed for routine biomedical applications'. *Progress In Electromagnetics Research*, **147**:(2014), 57–68. doi:10.2528/PIER14042708.

[Gö17a] Görlitz, F., Corcoran, D.S., Garcia Castano, E.A., Leitinger, B., Neil, M.A.A., Dunsby, C., and French, P.M.W. 'Mapping Molecular Function to Biological Nanostructure: Combining Structured Illumination Microscopy with Fluorescence Lifetime Imaging (SIM + FLIM)'. *Photonics*, **4(3)**. ISSN 2304-6732. doi:10.3390/photonics4030040.

[Gö17b] Görlitz, F., Kelly, D.J., Warren, S.C., Alibhai, D., West, L., Kumar, S., Alexandrov, Y., Munro, I., Garcia, E., McGinty, J., Talbot, C., Serwa, R.A., Thinon, E., da Paola, V., Murray, E.J., Stuhmeier, F., Neil, M.A.A., Tate, E.W., Dunsby, C., and French, P.M.W. 'Open Source High Content Analysis Utilizing Automated Fluorescence Lifetime Imaging Microscopy'. *Journal of Visualized Experiments*, **e55119(119)**. ISSN 1940-087X.

[Gö17c] Göttfert, F., Pleiner, T., Heine, J., Westphal, V., Görlich, D., Sahl, S.J., and Hell, S.W. 'Strong signal increase in STED fluorescence microscopy by imaging regions of subdiffraction extent'. *Proceedings of the National Academy of Sciences*. doi:10.1073/pnas.1621495114.

[Gö18] Görlitz, F., Guldbrand, S., Runcorn, T., Murray, R., Jaso-Tamane, A., Sinclair, H., Martinez-Perez, E., Taylor, J., Neil, M., Dunsby, C., and French, P. 'easySLM-STED: stimulated emission depletion microscopy with aberration correction, extended field of view and multiple beam scanning' (2018). Unpublished (manuscript submitted 14.03.2018). Correction: published 05.07.2018, e201800087. doi:10.1002/jbio.201800087.

[Gad93] Gadella, T.W., Jovin, T.M., and Clegg, R.M. 'Fluorescence lifetime imaging microscopy (FLIM): Spatial resolution of microstructures on the nanosecond time scale'. *Biophysical Chemistry*, **48(2)**:(1993), 221 – 239. ISSN 0301-4622. doi:10.1016/0301-4622(93)85012-7.

[Gad95] Gadella, T.W. and Jovin, T.M. 'Oligomerization of epidermal growth factor receptors on A431 cells studied by time-resolved fluorescence imaging microscopy. A stereochemical model for tyrosine kinase receptor activation.' *The Journal of Cell Biology*, **129(6)**:(1995), 1543–1558. ISSN 0021-9525. doi:10.1083/jcb.129.6.1543.

[Gad11] Gadella, T.W. *FRET and FLIM techniques*, volume 33. Elsevier (2011).

[GM31] Göppert-Mayer, M. 'Über Elementarakte mit zwei Quantensprüngen'. *Annalen der Physik*, **401(3)**:(1931), 273–294. ISSN 1521-3889. doi:10.1002/andp.19314010303.

[Goe10] Goedhart, J., van Weeren, L., Hink, M.A., Vischer, N.O.E., Jalink, K., and Gadella, T.W.J. 'Bright cyan fluorescent protein variants identified by fluorescence lifetime screening'. *Nature Methods*, **7(2)**:(2010), 137–139. doi:doi:10.1038/nmeth.1415.

[Gou12] Gould, T.J., Burke, D., Bewersdorf, J., and Booth, M.J. 'Adaptive optics enables 3D STED microscopy in aberrating specimens'. *Opt. Express*, **20(19)**:(2012), 20998–21009. doi:10.1364/OE.20.020998.

[Gou13] Gould, T.J., Kromann, E.B., Burke, D., Booth, M.J., and Bewersdorf, J. 'Auto-aligning stimulated emission depletion microscope using adaptive optics'. *Opt. Lett.*, **38(11)**:(2013), 1860–1862. doi:10.1364/OL.38.001860.

[Gra82] Gratzner, H.G. 'Monoclonal antibody to 5-bromo-and 5-iododeoxyuridine: a new reagent for detection of DNA replication'. *Science*, **218(4571)**:(1982), 474–475.

[Gra83] Gratton, E. and Limkeman, M. 'A continuously variable frequency cross-correlation phase fluorometer with picosecond resolution'. *Biophysical Journal*, **44(3)**:(1983), 315 – 324.

ISSN 0006-3495. doi:10.1016/S0006-3495(83)84305-7.

[Gus00] Gustafsson, M.G.L. 'Surpassing the lateral resolution limit by a factor of two using structured illumination microscopy'. *Journal of Microscopy*, **198(2)**:(2000), 82–87. ISSN 1365-2818. doi:10.1046/j.1365-2818.2000.00710.x.

[Gus05] Gustafsson, M.G.L. 'Nonlinear structured-illumination microscopy: Wide-field fluorescence imaging with theoretically unlimited resolution'. *Proceedings of the National Academy of Sciences of the United States of America*, **102(37)**:(2005), 13081–13086. doi:10.1073/pnas.0406877102.

[Gus17] Gustavsson, A.K., Petrov, P.N., Lee, M.Y., Shechtman, Y., and Moerner, W. '3D Single-Molecule Super-Resolution Microscopy With A Tilted Light Sheet'. *bioRxiv*, page 135699.

[Han89] Hansma, P., Drake, B., Marti, O., Gould, S., and Prater, C. 'The scanning ion-conductance microscope'. *Science*, **243(4891)**:(1989), 641–643. ISSN 0036-8075. doi:10.1126/science.2464851.

[Han04] Hansen, D., Hubbard, E.A., and Schedl, T. 'Multi-pathway control of the proliferation versus meiotic development decision in the Caenorhabditis elegans germline'. *Developmental Biology*, **268(2)**:(2004), 342 – 357. ISSN 0012-1606. doi:10.1016/j.ydbio.2003.12.023.

[Har98] Hardy, J.W. *Adaptive optics for astronomical telescopes*, volume 16. Oxford University Press on Demand (1998).

[Har08a] Harke, B., Keller, J., Ullal, C.K., Westphal, V., Schönle, A., and Hell, S.W. 'Resolution scaling in STED microscopy'. *Opt. Express*, **16(6)**:(2008), 4154–4162. doi:10.1364/OE.16.004154.

[Har08b] Harke, B., Ullal, C.K., Keller, J., and Hell, S.W. 'Three-Dimensional Nanoscopy of Colloidal Crystals'. *Nano Letters*, **8(5)**:(2008), 1309–1313. doi:10.1021/nl073164n. PMID: 18166070.

[Hei08] Hein, B., Willig, K.I., and Hell, S.W. 'Stimulated emission depletion (STED) nanoscopy of a fluorescent protein-labeled organelle inside a living cell'. *Proceedings of the National Academy of Sciences*, **105(38)**:(2008), 14271–14276. doi:10.1073/pnas.0807705105.

[Hei10] Hein, B., Willig, K.I., Wurm, C.A., Westphal, V., Jakobs, S., and Hell, S.W. 'Stimulated Emission Depletion Nanoscopy of Living Cells Using SNAP-Tag Fusion Proteins'. *Biophysical Journal*, **98(1)**:(2010), 158 – 163. ISSN 0006-3495. doi:10.1016/j.bpj.2009.09.053.

[Hei17] Heine, J., Reuss, M., Harke, B., D'Este, E., Sahl, S.J., and Hell, S.W. 'Adaptive-illumination STED nanoscopy'. *Proceedings of the National Academy of Sciences*, **114(37)**:(2017), 9797–9802. doi:10.1073/pnas.1708304114.

[Hel93] Hell, S., Reiner, G., Cremer, C., and Stelzer, E.H.K. 'Aberrations in confocal fluorescence microscopy induced by mismatches in refractive index'. *Journal of Microscopy*, **169(3)**:(1993), 391–405. ISSN 1365-2818. doi:10.1111/j.1365-2818.1993.tb03315.x.

[Hel94a] Hell, S.W., Lindek, S., Cremer, C., and Stelzer, E.H.K. 'Measurement of the 4Pi-confocal point spread function proves 75 nm axial resolution'. *Applied Physics Letters*, **64(11)**:(1994), 1335–1337. doi:10.1063/1.111926.

[Hel94b] Hell, S.W. and Wichmann, J. 'Breaking the diffraction resolution limit by stimulated emission: stimulated-emission-depletion fluorescence microscopy'. *Opt. Lett.*, **19(11)**:(1994), 780–782. doi:10.1364/OL.19.000780.

[Hel96] Hell, S.W., Karsten Bahlmann, M.S., Soini, A., Malak, H.M., Gryczynski, I., and Lakowicz, J.R. 'Three-photon excitation in fluorescence microscopy'. *Journal of Biomedical Optics*, **1**:(1996), 1 – 1 – 4. doi:10.1117/12.229062.

[Hel07] Hell, S.W. 'Far-Field Optical Nanoscopy'. *Science*, **316(5828)**:(2007), 1153–1158. ISSN 0036-8075. doi:10.1126/science.1137395.

[Hen11] Henriques, R., Griffiths, C., Hesper Rego, E., and Mhlanga, M.M. 'PALM and STORM: Unlocking live-cell super-resolution'. *Biopolymers*, **95(5)**:(2011), 322–331. ISSN 1097-0282. doi:10.1002/bip.21586.

[Hil17] Hillers, K.J., Jantsch, V., Martinez-Perez, E., and Yanowitz, J.L. 'Meiosis.' *WormBook: the online review of C. elegans biology*, pages 1–43.

[Hof00] Hoffnagle, J.A. and Jefferson, C.M. 'Design and performance of a refractive optical system that converts a Gaussian to a flattop beam'. *Appl. Opt.*, **39(30)**:(2000), 5488–5499. doi:10.1364/AO.39.005488.

[Hof05] Hofmann, M., Eggeling, C., Jakobs, S., and Hell, S.W. 'Breaking the diffraction barrier in fluorescence microscopy at low light intensities by using reversibly photoswitchable proteins'. *Proceedings of the National Academy of Sciences of the United States of America*, **102(49)**:(2005), 17565–17569. doi:10.1073/pnas.0506010102.

[Hoo65] Hooke, R. 'Micrographia: Or Some Physiological Descriptions of Minute Bodies Made by Magnifying Glasses, with Observations and Inquiries Thereupon' (1665).

[Hop02] Hoppe, A., Christensen, K., and Swanson, J.A. 'Fluorescence Resonance Energy Transfer-Based Stoichiometry in Living Cells'. *Biophysical Journal*, **83(6)**:(2002), 3652 – 3664. ISSN 0006-3495. doi:10.1016/S0006-3495(02)75365-4.

[Hou16] Houzet, J., Faure, N., Larochette, M., Brulez, A.C., Benayoun, S., and Mauclair, C. 'Ultrafast laser spatial beam shaping based on Zernike polynomials for surface processing'. *Opt. Express*, **24(6)**:(2016), 6542–6552. doi:10.1364/OE.24.006542.

[Hoy16] Hoyer, P., de Medeiros, G., Balázs, B., Norlin, N., Besir, C., Hanne, J., Kräusslich, H.G., Engelhardt, J., Sahl, S.J., Hell, S.W., and Hufnagel, L. 'Breaking the diffraction limit of light-sheet fluorescence microscopy by RESOLFT'. *Proceedings of the National Academy of Sciences*, **113(13)**:(2016), 3442–3446. doi:10.1073/pnas.1522292113.

[Hua08] Huang, B., Wang, W., Bates, M., and Zhuang, X. 'Three-Dimensional Super-Resolution Imaging by Stochastic Optical Reconstruction Microscopy'. *Science*, **319(5864)**:(2008), 810–813. ISSN 0036-8075. doi:10.1126/science.1153529.

[Hui04] Huisken, J., Swoger, J., Del Bene, F., Wittbrodt, J., and Stelzer, E.H.K. 'Optical Sectioning Deep Inside Live Embryos by Selective Plane Illumination Microscopy'. *Science*, **305(5686)**:(2004), 1007–1009. ISSN 0036-8075. doi:10.1126/science.1100035.

[Inc17] Inc., E.G. 'Complete Solutions for Histone Modification Studies'. `http://www.epigentek.com/catalog/histone-modification.php` (2017).

[Jab33] Jablonski, A. 'Efficiency of anti-Stokes fluorescence in dyes'. *Nature*, **131(839-840)**:(1933), 21.

[JE06] Jares-Erijman, E.A. and Jovin, T.M. 'Imaging molecular interactions in living cells by FRET microscopy'. *Current Opinion in Chemical Biology*, **10(5)**:(2006), 409 – 416. ISSN 1367-5931. doi:10.1016/j.cbpa.2006.08.021. Analytical techniques / Mechanisms.

[Jes09] Jesacher, A., Thayil, A., Grieve, K., Débarre, D., Watanabe, T., Wilson, T., Srinivas, S., and Booth, M. 'Adaptive harmonic generation microscopy of mammalian embryos'. *Opt. Lett.*, **34(20)**:(2009), 3154–3156. doi:10.1364/OL.34.003154.

[Ji09] Ji, N., Milkie, D.E., and Betzig, E. 'Adaptive optics via pupil segmentation for high-resolution imaging in biological tissues'. *Nature Methods*, **7(141)**. doi:10.1038/nmeth.1411.

[JoV17] JoVE. ‘Journal of Visualized Experiments’. `https://www.jove.com/` (2017). [Online; accessed 27-February-2018].

[Jue08] Juette, M.F., Gould, T.J., Lessard, M.D., Mlodzianoski, M.J., Nagpure, B.S., Bennett, B.T., Hess, S.T., and Bewersdorf, J. ‘Three-dimensional sub–100 nm resolution fluorescence microscopy of thick samples’. *Nature methods*, **5(6)**:(2008), 527–529.

[Jui03] Juillerat, A., Gronemeyer, T., Keppler, A., Gendreizig, S., Pick, H., Vogel, H., and Johnsson, K. ‘Directed Evolution of O6-Alkylguanine-DNA Alkyltransferase for Efficient Labeling of Fusion Proteins with Small Molecules In Vivo’. *Chemistry and Biology*, **10(4)**:(2003), 313–317. doi:https://doi.org/10.1016/S1074-5521(03)00068-1.

[Kö92] Köllner, M. and Wolfrum, J. ‘How many photons are necessary for fluorescence-lifetime measurements?’ *Chemical Physics Letters*, **200(1)**:(1992), 199 – 204. ISSN 0009-2614. doi:10.1016/0009-2614(92)87068-Z.

[Kam01] Kam, Z., Hanser, B., Gustafsson, M., Agard, D., and Sedat, J. ‘Computational adaptive optics for live three-dimensional biological imaging’. *PNAS*, **98(7)**:(2001), 3790–3795. doi:10.1073/pnas.071275698.

[Kav10] Kavitha, C., Rajamani, K., and Vadivel, E. ‘Coleus forskohlii: A comprehensive review on morphology, phytochemistry and pharmacological aspects’. *Journal of Medicinal Plants Research*, **4(4)**:(2010), 278–285. ISSN 1996-0875. doi:10.1186/1550-2783-7-7.

[Kel08] Keller, P.J., Schmidt, A.D., Wittbrodt, J., and Stelzer, E.H. ‘Reconstruction of Zebrafish Early Embryonic Development by Scanned Light Sheet Microscopy’. *Science*, **322(5904)**:(2008), 1065–1069. ISSN 0036-8075. doi:10.1126/science.1162493.

[Kel14] Kelly, D.J., Warren, S.C., Kumar, S., Lagarto, J.L., Dyer, B.T., Margineanu, A., Lam, E.W.F., Dunsby, C., and French, P.M.W. ‘An automated multiwell plate reading flim microscope for live cell autofluorescence lifetime assays’. *Journal of Innovative Optical Health Sciences*, **07(05)**:(2014), 1450025. doi:10.1142/S1793545814500254.

[Kel15a] Kelly, D. and Görlitz, F. ‘GitHub’. `https://github.com/imperial-photonics/openFLIM-HCA/` (2015). [Online; accessed 24-April-2017].

[Kel15b] Kelly, D.J., Warren, S.C., Alibhai, D., Kumar, S., Alexandrov, Y., Munro, I., Margineanu, A., McCormack, J., Welsh, N.J., Serwa, R.A., Thinon, E., Kongsema, M., McGinty, J., Talbot, C., Murray, E.J., Stuhmeier, F., Neil, M.A.A., Tate, E.W., Braga, V.M.M., Lam, E.W.F., Dunsby, C., and French, P.M.W. ‘Automated multiwell fluorescence lifetime imaging for Forster resonance energy transfer assays and high content analysis'. *Anal. Methods*, **7**:(2015), 4071–4089. doi:10.1039/C5AY00244C.

[Kla00] Klar, T.A., Jakobs, S., Dyba, M., Egner, A., and Hell, S.W. 'Fluorescence microscopy with diffraction resolution barrier broken by stimulated emission'. *Proceedings of the National Academy of Sciences*, **97(15)**:(2000), 8206–8210. doi:10.1073/pnas.97.15.8206.

[Kla01] Klar, T.A., Engel, E., and Hell, S.W. 'Breaking Abbe's diffraction resolution limit in fluorescence microscopy with stimulated emission depletion beams of various shapes'. *Phys. Rev. E*, **64**:(2001), 066613. doi:10.1103/PhysRevE.64.066613.

[Kla14] Klar, T.A., Wollhofen, R., and Jacak, J. 'Sub-Abbe resolution: from STED microscopy to STED lithography'. *Physica Scripta*, **T162**:(2014), 014049. doi:doi:10.1088/0031-8949/2014/T162/014049.

[Kla15] Klarenbeek, J., Goedhart, J., van Batenburg, A., Groenewald, D., and Jalink, K. 'Fourth-Generation Epac-Based FRET Sensors for cAMP Feature Exceptional Brightness, Photostability and Dynamic Range: Characterization of Dedicated Sensors for FLIM, for Ratiometry and with High Affinity'. *PLOS ONE*, **10(4)**:(2015), 1–11. doi:10.1371/journal.pone.0122513.

[Kno32] Knoll, M. and Ruska, E. 'Das Elektronenmikroskop'. *Zeitschrift für Physik*, **78(5)**:(1932), 318–339. ISSN 0044-3328. doi:10.1007/BF01342199.

[Kou06] Koushik, S.V., Chen, H., Thaler, C., III, H.L.P., and Vogel, S.S. 'Cerulean, Venus, and VenusY67C FRET Reference Standards'. *Biophysical Journal*, **91(12)**:(2006), L99 – L101. ISSN 0006-3495. doi:10.1529/biophysj.106.096206.

[Kre10] Kreider, R.B., Wilborn, C.D., Taylor, L., Campbell, B., Almada, A.L., Collins, R., Cooke, M., Earnest, C.P., Greenwood, M., Kalman, D.S., Kerksick, C.M., Kleiner, S.M., Leutholtz, B., Lopez, H., Lowery, L.M., Mendel, R., Smith, A., Spano, M., Wildman, R., Willoughby, D.S., Ziegenfuss, T.N., and Antonio, J. 'ISSN exercise & sport nutrition review: research & recommendations'. *Journal of the International Society of Sports Nutrition*, **7(1)**:(2010), 7. ISSN 1550-2783. doi:10.1186/1550-2783-7-7.

[Kri14] Kristoffersen, A.S., Erga, S.R., Hamre, B., and Frette, Ø. 'Testing Fluorescence Lifetime Standards using Two-Photon Excitation and Time-Domain Instrumentation: Rhodamine B, Coumarin 6 and Lucifer Yellow'. *Journal of Fluorescence*, **24(4)**:(2014), 1015–1024. ISSN 1573-4994. doi:10.1007/s10895-014-1368-1.

[Kun00] Kuner, T. and Augustine, G.J. 'A Genetically Encoded Ratiometric Indicator for Chloride'. *Neuron*, **27(3)**:(2000), 447 – 459. ISSN 0896-6273. doi:10.1016/S0896-6273(00) 00056-8.

[Lak85] Lakowicz, J.R. and Maliwal, B.P. 'Construction and performance of a variable-frequency phase-modulation fluorometer'. *Biophysical Chemistry*, **21(1)**:(1985), 61 – 78. ISSN 0301-4622. doi:10.1016/0301-4622(85)85007-9.

[Lak06] Lakowicz, J.R. *Principles of fluorescence spectroscopy.* Springer (2006).

[Lan07] Lang, M.C., Engelhardt, J., and Hell, S.W. '4Pi microscopy with linear fluorescence excitation'. *Opt. Lett.*, **32(3)**:(2007), 259–261. doi:10.1364/OL.32.000259.

[Lea04] Leach, J., Yao, E., and Padgett, M.J. 'Observation of the vortex structure of a non-integer vortex beam'. *New Journal of Physics*, **6(1)**:(2004), 71.

[Lei03] Leitinger, B. 'Normal Activation of Discoidin Domain Receptor 1 Mutants with Disulfide Cross-links, Insertions, or Deletions in the Extracellular Juxtamembrane Region'. *J Biol Chem*, **289**:(2003), 13565–13574. doi:doi:10.1074/jbc.M301370200.

[Lei11] Leitinger, B. 'Transmembrane Collagen Receptors'. *Annual Review of Cell and Developmental Biology*, **27(1)**:(2011), 265–290. doi:10.1146/annurev-cellbio-092910-154013. PMID: 21568710.

[Lei14] Leitinger, B. 'Discoidin Domain Receptor Functions in Physiological and Pathological Conditions'. *International Review of Cell and Molecular Biology*, **310**:(2014), 39 – 87. ISSN 1937-6448. doi:10.1016/B978-0-12-800180-6.00002-5.

[Lem10] Lemmon, M.A. and Schlessinger, J. 'Cell Signaling by Receptor Tyrosine Kinases'. *Cell*, **141(7)**:(2010), 1117 – 1134. ISSN 0092-8674. doi:10.1016/j.cell.2010.06.011.

[Lem12] Lemeer, S., Bluwstein, A., Wu, Z., Leberfinger, J., Müller, K., Kramer, K., and Kuster, B. 'Phosphotyrosine mediated protein interactions of the discoidin domain receptor 1'. *Journal of Proteomics*, **75(12)**:(2012), 3465 – 3477. ISSN 1874-3919. doi: 10.1016/j.jprot.2011.10.007. Understanding genome regulation and genetic diversity by mass spectrometry.

[Len14] Lenz, M.O., Sinclair, H.G., Savell, A., Clegg, J.H., Brown, A.C.N., Davis, D.M., Dunsby, C., Neil, M.A.A., and French, P.M.W. '3-D stimulated emission depletion microscopy with programmable aberration correction'. *Journal of Biophotonics*, **7(1-2)**:(2014), 29–

36. ISSN 1864-0648. doi:10.1002/jbio.201300041.

[Ler13] Leroux, C.E., Grichine, A., Wang, I., and Delon, A. ‘Correction of cell-induced optical aberrations in a fluorescence fluctuation microscope’. *Opt. Lett.*, **38(14)**:(2013), 2401–2403. doi:10.1364/OL.38.002401.

[Li11] Li, C., Aiyun, W., Benchang, S., Jia, L., Yao, H., and Yongchang, C. ‘FastCloning: A Highly Simplified, Purification-Free, Sequence- and Ligation-Independent PCR Cloning Method’. *BMC Biotechnology*, **11(1)**:(2011), 92. doi:10.1186/1472-6750-11-92.

[Li15] Li, D., Shao, L., Chen, B.C., Zhang, X., Zhang, M., Moses, B., Milkie, D.E., Beach, J.R., Hammer, J.A., Pasham, M., Kirchhausen, T., Baird, M.A., Davidson, M.W., Xu, P., and Betzig, E. ‘Extended-resolution structured illumination imaging of endocytic and cytoskeletal dynamics’. *Science*, **349(6251)**. ISSN 0036-8075. doi:10.1126/science.aab3500.

[Lid03] Lidke, D., Nagy, P., Barisas, B., Heintzmann, R., Post, J., Lidke, K., Clayton, A., Arndt-Jovin, D., and Jovin, T. ‘Imaging molecular interactions in cells by dynamic and static fluorescence anisotropy (rFLIM and emFRET)’. *Biochemical Society Transactions*, **31(5)**:(2003), 1020–1027. ISSN 0300-5127. doi:10.1042/bst0311020.

[Lin10] Lin, G., Wang, G., Banie, L., Ning, H., Shindel, A.W., Fandel, T.M., Lue, T.F., and Lin, C.S. ‘Treatment of stress urinary incontinence with adipose tissue-derived stem cells’. *Cytotherapy*, **12(1)**:(2010), 88–95.

[Lis15] Liss, V., Barlag, B., Nietschke, M., and Hensel, M. ‘Self-labelling enzymes as universal tags for fluorescence microscopy, super-resolution microscopy and electron microscopy’. *Scientific Reports*, **5**:(2015), 17740. doi:10.1038/srep17740.

[Liv16] Liv, N., van Oosten Slingeland, D.S.B., Baudoin, J.P., Kruit, P., Piston, D.W., and Hoogenboom, J.P. ‘Electron Microscopy of Living Cells During in Situ Fluorescence Microscopy’. *ACS Nano*, **10(1)**:(2016), 265–273. doi:10.1021/acsnano.5b03970.

[LJ31] Lennard-Jones, J.E. ‘Cohesion’. *Proceedings of the Physical Society*, **43(5)**:(1931), 461.

[Llè09] Llères, D., James, J., Swift, S., Norman, D.G., and Lamond, A.I. ‘Quantitative analysis of chromatin compaction in living cells using FLIM–FRET’. *The Journal of Cell Biology*, **187(4)**:(2009), 481–496. ISSN 0021-9525. doi:10.1083/jcb.200907029.

[Loe77] Loewen, E.G., Nevière, M., and Maystre, D. ‘Grating efficiency theory as it applies to blazed and holographic gratings'. *Appl. Opt.*, **16(10)**:(1977), 2711–2721. doi:10.1364/AO.16.002711.

[Ma17] Ma, Y., Xu, J., Gao, H., and Xiong, X. 'Intensity profile stabilities of high order vectorial modes of optical fibers'. *Optik - International Journal for Light and Electron Optics*, **149**:(2017), 277 – 287. ISSN 0030-4026. doi:https://doi.org/10.1016/j.ijleo.2017.09.053.

[Mah94] Mahajan, V.N. 'Zernike Circle Polynomials and Optical Aberrations of Systems with Circular Pupils'. *Appl. Opt.*, **33(34)**:(1994), 8121–8124. doi:10.1364/AO.33.008121.

[Man06] Mank, M., Reiff, D.F., Heim, N., Friedrich, M.W., Borst, A., and Griesbeck, O. 'A FRET-Based Calcium Biosensor with Fast Signal Kinetics and High Fluorescence Change'. *Biophysical Journal*, **90(5)**:(2006), 1790 – 1796. ISSN 0006-3495. doi:10.1529/biophysj.105.073536.

[Mar14] Marcu, L., French, P.M., and Elson, D.S. *Fluorescence lifetime spectroscopy and imaging: principles and applications in biomedical diagnostics*. CRC Press (2014).

[Mar16] Margineanu, A., Chan, J.J., Kelly, D.J., Warren, S.C., Flatters, D., Kumar, S., Katan, M., Dunsby, C.W., and French, P.M. 'Screening for protein-protein interactions using Förster resonance energy transfer (FRET) and fluorescence lifetime imaging microscopy (FLIM)'. *Scientific reports*, **6**:(2016), 28186.

[Mau08] Maurel, D., Comps-Agrar, L., Brock, C., Rives, M.L., Bourrier, E., Ayoub, M.A., Bazin, H., Tinel, N., Durroux, T., Prézeau, L., Trinquet, E., and Pin, J.P. 'Cell-surface protein-protein interaction analysis with time-resolved FRET and snap-tag technologies: application to GPCR oligomerization'. *Nature Methods*, **5**:(2008), 561. doi:10.1038/nmeth.1213.

[Mau11] Maurer, C., Jesacher, A., Bernet, S., and Ritsch-Marte, M. 'What spatial light modulators can do for optical microscopy'. *Laser & Photonics Reviews*, **5(1)**:(2011), 81–101. ISSN 1863-8899. doi:10.1002/lpor.200900047.

[May07] Maycock, J., Hennelly, B.M., McDonald, J.B., Frauel, Y., Castro, A., Javidi, B., and Naughton, T.J. 'Reduction of speckle in digital holography by discrete Fourier filtering'. *J. Opt. Soc. Am. A*, **24(6)**:(2007), 1617–1622.

[MB07a] Mora-Bermúdez, F. and Ellenberg, J. 'Measuring structural dynamics of chromosomes in living cells by fluorescence microscopy'. *Methods*, **41(2)**:(2007), 158 – 167. ISSN 1046-2023. doi:10.1016/j.ymeth.2006.07.035. Methods in Cell Cycle Research.

[MB07b] Mora-Bermúdez, F., Gerlich, D., and Ellenberg, J. 'Maximal chromosome compaction occurs by axial shortening in anaphase and depends on Aurora kinase'. *Nature cell biology*, **9(7)**:(2007), 822.

[McG09] McGinty, J., Requejo-Isidro, J., Munro, I., Talbot, C.B., Kellett, P.A., Hares, J.D., Dunsby, C., Neil, M.A.A., and French, P.M.W. 'Signal-to-noise characterization of time-gated intensifiers used for wide-field time-domain FLIM'. *Journal of Physics D: Applied Physics*, **42(13)**:(2009), 135103.

[Mic16] Microsoft, C. 'Microsoft Corporation'. `https://www.visualstudio.com/` (2016). [Online; accessed 24-April-2017].

[Mih09] Mihai, C., Chotani, M., Elton, T.S., and Agarwal, G. 'Mapping of DDR1 Distribution and Oligomerization on the Cell Surface by FRET Microscopy'. *Journal of Molecular Biology*, **385(2)**:(2009), 432 – 445. ISSN 0022-2836. doi:10.1016/j.jmb.2008.10.067.

[Mil11] Milkie, D.E., Betzig, E., and Ji, N. 'Pupil-segmentation-based adaptive optical microscopy with full-pupil illumination'. *Opt. Lett.*, **36(21)**:(2011), 4206–4208. doi:10.1364/OL.36.004206.

[Min61] Minsky, M. 'Microscopy apparatus' (1961). US Patent 3,013,467.

[Min88] Minsky, M. 'Memoir on inventing the confocal scanning microscope'. *Scanning*, **10(4)**:(1988), 128–138. ISSN 1932-8745. doi:10.1002/sca.4950100403.

[Miy97] Miyawaki, A., Llopis, J., Heim, R., McCaffery, J.M., et al. 'Fluorescent indicators for Ca2+ based on green fluorescent proteins and calmodulin'. *Nature*, **388(6645)**:(1997), 882.

[Mon09] Moneron, G. and Hell, S.W. 'Two-photon excitation STED microscopy'. *Opt. Express*, **17(17)**:(2009), 14567–14573. doi:10.1364/OE.17.014567.

[MP08] Martinez-Perez, E., Schvarzstein, M., Barroso, C., Lightfoot, J., Dernburg, A.F., and Villeneuve, A.M. 'Crossovers trigger a remodeling of meiotic chromosome axis composition that is linked to two-step loss of sister chromatid cohesion'. *Genes & Development*, **22(20)**:(2008), 2886–2901. doi:10.1101/gad.1694108.

[Mue13] Mueller, V., Honigmann, A., Ringemann, C., Medda, R., Schwarzmann, G., and Eggeling, C. 'FCS in STED Microscopy'. *Methods in Enzymology*, **519**:(2013), 1 – 38. ISSN 0076-6879. doi:10.1016/B978-0-12-405539-1.00001-4. Fluorescence Fluctuation Spectroscopy

(FFS), Part B.

[Nei00a] Neil, M.A.A., Booth, M.J., and Wilson, T. ‘New modal wave-front sensor: a theoretical analysis’. *J. Opt. Soc. Am. A*, **17(6)**:(2000), 1098–1107. doi:10.1364/JOSAA.17.001098.

[Nei00b] Neil, M.A.A., Juškaitis, R., Wilson, T., Laczik, Z.J., and Sarafis, V. ‘Optimized pupil-plane filters for confocal microscope point-spread function engineering’. *Opt. Lett.*, **25(4)**:(2000), 245–247. doi:10.1364/OL.25.000245.

[Nez06] Nezu, A., Tanimura, A., Morita, T., Shitara, A., and Tojyo, Y. ‘A novel fluorescent method employing the FRET-based biosensor “LIBRA” for the identification of ligands of the inositol 1,4,5-trisphosphate receptors’. *Biochimica et Biophysica Acta (BBA) - General Subjects*, **1760(8)**:(2006), 1274 – 1280. ISSN 0304-4165. doi:10.1016/j.bbagen.2006.04.004.

[Nis08] Nishioka, T., Aoki, K., Hikake, K., Yoshizaki, H., Kiyokawa, E., and Matsuda, M. ‘Rapid Turnover Rate of Phosphoinositides at the Front of Migrating MDCK Cells’. *Molecular Biology of the Cell*, **19(10)**:(2008), 4213–4223. doi:10.1091/mbc.E08-03-0315.

[Nob15] Nobelprize.org. ‘The Nobel Prize in Physiology or Medicine 1971’. `http://www.nobelprize.org/nobel_prizes/medicine/laureates/1971/` (2015). [Online; accessed 01-May-2017].

[Noo06] Noordeen, N.A., Federico, C., Erhard, H., Michael, A.H., and Birgit, L. ‘A Transmembrane Leucine Zipper Is Required for Activation of the Dimeric Receptor Tyrosine Kinase DDR1’. *The Journal of Biological Chemistry*, **281(32)**:(2006), 22744–51. doi:10.1074/jbc.M603233200.

[Nyq28] Nyquist, H. ‘Certain Topics in Telegraph Transmission Theory’. *Transactions of the American Institute of Electrical Engineers*, **47(2)**:(1928), 617–644. ISSN 0096-3860. doi:10.1109/T-AIEE.1928.5055024.

[Okk16] Okkelman, I.A., Dmitriev, R.I., Foley, T., and Papkovsky, D.B. ‘Use of Fluorescence Lifetime Imaging Microscopy (FLIM) as a Timer of Cell Cycle S Phase’. *PLOS ONE*, **11(12)**:(2016), 1–18. doi:10.1371/journal.pone.0167385.

[Oli09] Olivier, N., Débarre, D., and Beaurepaire, E. ‘Dynamic aberration correction for multiharmonic microscopy’. *Opt. Lett.*, **34(20)**:(2009), 3145–3147. doi:10.1364/OL.34.003145.

[Ora16] Oracle, C. ‘Oracle Corporation’. `https://netbeans.org/` (2016). [Online; accessed 24-April-2017].

[Ove14] Ovesný, M., Křížek, P., Borkovec, J., Švindrych, Z., and Hagen, G.M. 'ThunderSTORM: a comprehensive ImageJ plug-in for PALM and STORM data analysis and super-resolution imaging'. *Bioinformatics*, **30(16)**:(2014), 2389–2390. doi:10.1093/bioinformatics/btu202.

[Par15] Park, Y.I., Lee, K.T., Suh, Y.D., and Hyeon, T. 'Upconverting nanoparticles: a versatile platform for wide-field two-photon microscopy and multi-modal in vivo imaging'. *Chem. Soc. Rev.*, **44**:(2015), 1302–1317. doi:10.1039/C4CS00173G.

[Pat00] Paterson, C., Munro, I., and Dainty, J.C. 'A low cost adaptive optics system using a membrane mirror'. *Opt. Express*, **6(9)**:(2000), 175–185. doi:10.1364/OE.6.000175.

[Pat16] Patton, B.R., Burke, D., Owald, D., Gould, T.J., Bewersdorf, J., and Booth, M.J. 'Three-dimensional STED microscopy of aberrating tissue using dual adaptive optics'. *Opt. Express*, **24(8)**:(2016), 8862–8876. doi:10.1364/OE.24.008862.

[Pau25] Pauli, W. 'Über den Zusammenhang des Abschlusses der Elektronengruppen im Atom mit der Komplexstruktur der Spektren'. *Zeitschrift für Physik*, **31(1)**:(1925), 765–783. ISSN 0044-3328. doi:10.1007/BF02980631.

[PB11] Pietraszewska-Bogiel, A. and Gadella, T. 'FRET microscopy: from principle to routine technology in cell biology'. *Journal of Microscopy*, **241(2)**:(2011), 111–118. ISSN 1365-2818. doi:10.1111/j.1365-2818.2010.03437.x.

[Pel04] Pelet, S., Previte, M., Laiho, L., and So, P. 'A fast global fitting algorithm for fluorescence lifetime imaging microscopy based on image segmentation'. *Biophysical journal*, **87(4)**:(2004), 2807–2817.

[Pho07a] Photonics, H. *Phase spatial light modulator LCOS-SLM*. Hamamatsu Photonics K.K. (2007).

[Pho07b] Photonics, H. *Photomultiplier tubes: Basics and applications*. Hamamatsu Photonics K.K. (2007).

[Pho16] Photonics, H. *Image intensifiers*. Hamamatsu Photonics K.K. (2016).

[Pol15] Poland, S.P., Krstajić, N., Monypenny, J., Coelho, S., Tyndall, D., Walker, R.J., Devauges, V., Richardson, J., Dutton, N., Barber, P., Li, D.D.U., Suhling, K., Ng, T., Henderson, R.K., and Ameer-Beg, S.M. 'A high speed multifocal multiphoton fluorescence lifetime imaging microscope for live-cell FRET imaging'. *Biomed. Opt. Express*, **6(2)**:(2015), 277–296. doi:10.1364/BOE.6.000277.

[Pri06] Price, D.L., Chow, S.K., MacLean, N.A.B., Hakozaki, H., Peltier, S., Martone, M.E., and Ellisman, M.H. 'High-resolution large-scale mosaic imaging using multiphoton microscopy to characterize transgenic mouse models of human neurological disorders'. *Neuroinformatics*, **4(1)**:(2006), 65–80. doi:10.1385/NI:4:1:65.

[Raj01] Rajan, R.S., Illing, M.E., Bence, N.F., and Kopito, R.R. 'Specificity in intracellular protein aggregation and inclusion body formation'. *Proceedings of the National Academy of Sciences*, **98(23)**:(2001), 13060–13065. doi:10.1073/pnas.181479798.

[Ran11] Rankin, B.R., Moneron, G., Wurm, C.A., Nelson, J.C., Walter, A., Schwarzer, D., Schroeder, J., Colón-Ramos, D.A., and Hell, S.W. 'Nanoscopy in a Living Multicellular Organism Expressing GFP'. *Biophysical Journal*, **100(12)**:(2011), L63 – L65. ISSN 0006-3495. doi:10.1016/j.bpj.2011.05.020.

[Ray79] Rayleigh, F. 'XXXI. Investigations in optics, with special reference to the spectroscope'. *Philosophical Magazine*, **8(49)**:(1879), 261–274. doi:10.1080/14786447908639684.

[Reg12] Rego, E.H., Shao, L., Macklin, J.J., Winoto, L., Johansson, G.A., Kamps-Hughes, N., Davidson, M.W., and Gustafsson, M.G.L. 'Nonlinear structured-illumination microscopy with a photoswitchable protein reveals cellular structures at 50-nm resolution'. *Proceedings of the National Academy of Sciences*, **109(3)**:(2012), E135–E143. doi: 10.1073/pnas.1107547108.

[Reu10] Reuss, M., Engelhardt, J., and Hell, S.W. 'Birefringent device converts a standard scanning microscope into a STED microscope that also maps molecular orientation'. *Opt. Express*, **18(2)**:(2010), 1049–1058. doi:10.1364/OE.18.001049.

[Ric59a] Richards, B. and Wolf, E. 'Electromagnetic Diffraction in Optical Systems. II. Structure of the Image Field in an Aplanatic System'. *Proceedings of the Royal Society of London A: Mathematical, Physical and Engineering Sciences*, **253(1274)**:(1959), 358–379. ISSN 0080-4630. doi:10.1098/rspa.1959.0200.

[Ric59b] Richards, B. and Wolf, E. 'Electromagnetic diffraction in optical systems, II. Structure of the image field in an aplanatic system'. *Proceedings of the Royal Society of London A: Mathematical, Physical and Engineering Sciences*, **253(1274)**:(1959), 358–379. ISSN 0080-4630. doi:10.1098/rspa.1959.0200.

[Rit09] Rittweger, E., Han, K.Y., Irvine, S.E., Eggeling, C., and Hell, S.W. 'STED microscopy reveals crystal colour centres with nanometric resolution'. *Nature Photonics*, **3**:(2009), 144–147. doi:10.1038/nphoton.2009.2.

[Roy16] Royer, L.A., Lemon, W.C., Chhetri, R.K., Wan, Y., Coleman, M., Myers, E.W., and Keller, P.J. 'Adaptive light-sheet microscopy for long-term, high-resolution imaging in living organisms'. *Nature Biotechnology*, **34(1267)**. doi:10.1038/nbt.3708.

[RP06] Reck-Peterson, S.L., Yildiz, A., Carter, A.P., Gennerich, A., Zhang, N., and Vale, R.D. 'Single-Molecule Analysis of Dynein Processivity and Stepping Behavior'. *Cell*, **126(2)**:(2006), 335 – 348. ISSN 0092-8674. doi:10.1016/j.cell.2006.05.046.

[Ruc00] Ruckstuhl, T., Enderlein, J., Jung, S., and Seeger, S. 'Forbidden Light Detection from Single Molecules'. *Analytical Chemistry*, **72(9)**:(2000), 2117–2123. doi:10.1021/ac991358k. PMID: 10815974.

[Run15a] Runcorn, T.H. *Extending the wavelength coverage of frequency-doubled fibre lasers*. Ph.D. thesis, Imperial College London (2015).

[Run15b] Runcorn, T.H., Murray, R.T., Kelleher, E.J.R., Popov, S.V., and Taylor, J.R. 'Duration-tunable picosecond source at 560&#x2009;&#x2009;nm with watt-level average power'. *Opt. Lett.*, **40(13)**:(2015), 3085–3088. doi:10.1364/OL.40.003085.

[Run17] Runcorn, T.H., Görlitz, F., Murray, R.T., and Kelleher, E.J.R. 'Visible Raman-shifted Fiber Lasers for Biophotonic Applications'. *IEEE Journal of Selected Topics in Quantum Electronics*, **PP(99)**:(2017), 1–1. ISSN 1077-260X. doi:10.1109/JSTQE.2017.2770101.

[Rus06] Rust, M.J., Bates, M., and Zhuang, X. 'Sub-diffraction-limit imaging by stochastic optical reconstruction microscopy (STORM)'. *Nature methods*, **3(10)**:(2006), 793—795. ISSN 1548-7091. doi:10.1038/nmeth929.

[Sal08] Salic, A. and Mitchison, T.J. 'A chemical method for fast and sensitive detection of DNA synthesis in vivo'. *Proceedings of the National Academy of Sciences*, **105(7)**:(2008), 2415–2420.

[Sch04] Schwertner, M., Booth, M., and Wilson, T. 'Characterizing specimen induced aberrations for high NA adaptive optical microscopy'. *Opt. Express*, **12(26)**:(2004), 6540–6552. doi:10.1364/OPEX.12.006540.

[Sch05] Schwertner, M., Booth, M.J., and Wilson, T. 'Simple optimization procedure for objective lens correction collar setting'. *Journal of Microscopy*, **217(3)**:(2005), 184–187. ISSN 1365-2818. doi:10.1111/j.1365-2818.2005.01431.x.

[Sch08] Schermelleh, L., Carlton, P.M., Haase, S., Shao, L., Winoto, L., Kner, P., Burke, B., Cardoso, M.C., Agard, D.A., Gustafsson, M.G.L., Leonhardt, H., and Sedat, J.W. 'Subdiffraction Multicolor Imaging of the Nuclear Periphery with 3D Structured Illumination Microscopy'. *Science*, **320(5881)**:(2008), 1332–1336. ISSN 0036-8075. doi: 10.1126/science.1156947.

[Sch12] Schindelin, J., Arganda-Carreras, I., Frise, E., Kaynig, V., Longair, M., Pietzsch, T., Preibisch, S., Rueden, C., Saalfeld, S., Schmid, B., Tinevez, J.Y., White, D.J., Hartenstein, V., Eliceiri, K., Tomancak, P., and Cardona, A. 'Fiji: an open-source platform for biological-image analysis'. *Nat Meth*, **9(7)**:(2012), 676–682.

[Sch15] Schatten, G. and Simerly, C. 'LEGOs® and legacies of centrioles and centrosomes'. *EMBO reports*, **16(9)**:(2015), 1052–1054. ISSN 1469-221X. doi:10.15252/embr.201540875.

[Scu96] Scully, A.D., MacRobert, A.J., Botchway, S., O'Neill, P., Parker, A.W., Ostler, R.B., and Phillips, D. 'Development of a laser-based fluorescence microscope with subnanosecond time resolution'. *Journal of Fluorescence*, **6(2)**:(1996), 119–125. doi:10.1007/BF00732051.

[Sel87] Seldowitz, M.A., Allebach, J.P., and Sweeney, D.W. 'Synthesis of digital holograms by direct binary search'. *Appl. Opt.*, **26(14)**:(1987), 2788–2798. doi:10.1364/AO.26.002788.

[Sha08] Sharma, A., Sheoran, G., Jaffery, Z., and Moinuddin. 'Improvement of signal-to-noise ratio in digital holography using wavelet transform'. *Optics and Lasers in Engineering*, **46(1)**:(2008), 42 – 47. ISSN 0143-8166. doi:10.1016/j.optlaseng.2007.07.004.

[She91] Sheppard, C.J.R. and Gu, M. 'Aberration compensation in confocal microscopy'. *Appl. Opt.*, **30(25)**:(1991), 3563–3568. doi:10.1364/AO.30.003563.

[Shr97] Shrivastava, A., Radziejewski, C., Campbell, E., Kovac, L., McGlynn, M., Ryan, T.E., Davis, S., Goldfarb, M.P., Glass, D.J., Lemke, G., and Yancopoulos, G.D. 'An Orphan Receptor Tyrosine Kinase Family Whose Members Serve as Nonintegrin Collagen Receptors'. *Molecular Cell*, **1(1)**:(1997), 25 – 34. ISSN 1097-2765. doi:10.1016/S1097-2765(00)80004-0.

[Sie02] Siedentopf, H. and Zsigmondy, R. 'Über Sichtbarmachung und Größenbestimmung ultramikoskopischer Teilchen, mit besonderer Anwendung auf Goldrubingläser'. *Annalen der Physik*, **315(1)**:(1902), 1–39. ISSN 1521-3889. doi:10.1002/andp.19023150102.

[Sin14] Singer, C. 'Notes on the Early History of Microscopy'. *Proceedings of the Royal Society of Medicine*, **7**:(1914), 247–79.

[Slu05] Sluder, G. *Centrosome Duplication and its Regulation in the Higher Animal Cell*, pages 167–189. Wiley-VCH Verlag GmbH & Co. KGaA (2005). ISBN 9783527603800. doi: 10.1002/3527603808.ch9.

[Sme14] Smeets, D., Markaki, Y., Schmid, V.J., Kraus, F., Tattermusch, A., Cerase, A., Sterr, M., Fiedler, S., Demmerle, J., Popken, J., Leonhardt, H., Brockdorff, N., Cremer, T., Schermelleh, L., and Cremer, M. 'Three-dimensional super-resolution microscopy of the inactive X chromosome territory reveals a collapse of its active nuclear compartment harboring distinct Xist RNA foci'. *Epigenetics & Chromatin*, **7(1)**:(2014), 8. doi:10.1186/1756-8935-7-8.

[So95] So, P.T.C., French, T., Yu, W.M., Berland, K.M., Dong, C.Y., and Gratton, E. 'Time-resolved fluorescence microscopy using two-photon excitation'. *Bioimaging*, **3(2)**:(1995), 49–63. ISSN 1361-6374. doi:10.1002/1361-6374(199506)3:2⟨49::AID-BIO1⟩3.0.CO;2-E.

[Spa15] Sparks, H. *Development and biomedical application of fluorescence lifetime imaging endoscopes*. Ph.D. thesis, Imperial College London (2015).

[Spa17] Sparks, H., Görlitz, F., Kelly, D.J., Warren, S.C., Kellett, P.A., Garcia, E., Dymoke-Bradshaw, A.K.L., Hares, J.D., Neil, M.A.A., Dunsby, C., and French, P.M.W. 'Characterisation of new gated optical image intensifiers for fluorescence lifetime imaging'. *Review of Scientific Instruments*, **88(1)**:(2017), 013707. doi:10.1063/1.4973917.

[Spe17] Specht, E.A., Braselmann, E., and Palmer, A.E. 'A Critical and Comparative Review of Fluorescent Tools for Live-Cell Imaging'. *Annual Review of Physiology*, **79(1)**:(2017), 93–117. doi:10.1146/annurev-physiol-022516-034055. PMID: 27860833.

[Squ00] Squire, A., Verveer, P.J., Bastiaens, P., et al. 'Multiple frequency fluorescence lifetime imaging microscopy'. *Journal of Microscopy*, **197(2)**:(2000), 136–149.

[Sto52] Stokes, G.G. 'On the Change of Refrangibility of Light'. *Philosophical Transactions of the Royal Society of London*, **142**:(1852), 463–562. doi:10.1098/rstl.1852.0022.

[Sto05] Stockholm, D., Bartoli, M., Sillon, G., Bourg, N., Davoust, J., and Richard, I. 'Imaging Calpain Protease Activity by Multiphoton FRET in Living Mice'. *Journal of Molecular Biology*, **346(1)**:(2005), 215 – 222. ISSN 0022-2836. doi:10.1016/j.jmb.2004.11.039.

[Tö95] Török, P., Varga, P., and Németh, G. 'Analytical solution of the diffraction integrals and interpretation of wave-front distortion when light is focused through a planar interface between materials of mismatched refractive indices'. *J. Opt. Soc. Am. A*, **12(12)**:(1995), 2660–2671. doi:10.1364/JOSAA.12.002660.

[Tao11] Tao, X., Fernandez, B., Azucena, O., Fu, M., Garcia, D., Zuo, Y., Chen, D.C., and Kubby, J. 'Adaptive optics confocal microscopy using direct wavefront sensing'. *Opt. Lett.*, **36(7)**:(2011), 1062–1064. doi:10.1364/OL.36.001062.

[Tao12] Tao, X., Crest, J., Kotadia, S., Azucena, O., Chen, D.C., Sullivan, W., and Kubby, J. 'Live imaging using adaptive optics with fluorescent protein guide-stars'. *Opt. Express*, **20(14)**:(2012), 15969–15982. doi:10.1364/OE.20.015969.

[Tao13] Tao, X., Norton, A., Kissel, M., Azucena, O., and Kubby, J. 'Adaptive optical two-photon microscopy using autofluorescent guide stars'. *Opt. Lett.*, **38(23)**:(2013), 5075–5078. doi:10.1364/OL.38.005075.

[Tay57] Taylor, J.H., Woods, P.S., and Hughes, W.L. 'The organization and duplication of chromosomes as revealed by autoradiographic studies using tritium-labeled thymidinee'. *Proceedings of the National Academy of Sciences*, **43(1)**:(1957), 122–128.

[Tei09] Teif, V.B. and Rippe, K. 'Predicting nucleosome positions on the DNA: combining intrinsic sequence preferences and remodeler activities'. *Nucleic Acids Research*, **37(17)**:(2009), 5641–5655. doi:10.1093/nar/gkp610.

[Tha11] Thayil, A., Jesacher, A., Wilson, T., Booth, M., Watanabe, T., and Srinivas, S. 'Long-term imaging of mouse embryos using adaptive harmonic generation microscopy'. *Journal of Biomedical Optics*, **16**:(2011), 16 – 16 – 9. doi:10.1117/1.3569614.

[Tho10] Thomas, N. 'Review Article: High-Content Screening: A Decade of Evolution'. *Journal of Biomolecular Screening*, **15(1)**:(2010), 1–9. doi:10.1177/1087057109353790. PMID: 20008124.

[Tho17a] Thorlabs. 'Engineered Diffusers'. `https://www.thorlabs.com/newgrouppage9.cfm?objectgroup_id=1660` (2017).

[Tho17b] Thorn, K. and Kellogg, D. 'Genetically encoded fluorescent tags'. *Molecular Biology of the Cell*, **28(7)**:(2017), 848–857. doi:10.1091/mbc.e16-07-0504. PMID: 28360214.

[Tok08] Tokunaga, M., Imamoto, N., and Sakata-Sogawa, K. 'Highly inclined thin illumination enables clear single-molecule imaging in cells'. *Nature Methods*, **5**. doi:10.1038/nmeth1171.

[Tom13] Tomer, R., Khairy, K., and Keller, P.J. *Light Sheet Microscopy in Cell Biology*, pages 123–137. Humana Press, Totowa, NJ (2013). ISBN 978-1-62703-056-4. doi:10.1007/

978-1-62703-056-4_7.

[Tor02] Tornøe, C.W., Christensen, C., and Meldal, M. ‘Peptidotriazoles on solid phase:[1, 2, 3]-triazoles by regiospecific copper (I)-catalyzed 1, 3-dipolar cycloadditions of terminal alkynes to azides’. *The Journal of organic chemistry*, **67(9)**:(2002), 3057–3064.

[Tur14] Turgeman, L. and Fixler, D. ‘The influence of dead time related distortions on live cell fluorescence lifetime imaging (FLIM) experiments’. *Journal of Biophotonics*, **7(6)**:(2014), 442–452. ISSN 1864-0648. doi:10.1002/jbio.201300018.

[Tys15] Tyson, R.K. *Principles of adaptive optics*. CRC press (2015).

[Uey02] Ueyama, H., Takagi, M., and Takenaka, S. ‘A Novel Potassium Sensing in Aqueous Media with a Synthetic Oligonucleotide Derivative. Fluorescence Resonance Energy Transfer Associated with Guanine Quartet Potassium Ion Complex Formation’. *Journal of the American Chemical Society*, **124(48)**:(2002), 14286–14287. doi:10.1021/ja026892f. PMID: 12452685.

[Urb11] Urban, N.T., Willig, K.I., Hell, S.W., and Nägerl, U.V. ‘STED Nanoscopy of Actin Dynamics in Synapses Deep Inside Living Brain Slices’. *Biophysical Journal*, **101(5)**:(2011), 1277 – 1284. ISSN 0006-3495. doi:10.1016/j.bpj.2011.07.027.

[Val12] Valiathan, R.R., Marco, M., Leitinger, B., Kleer, C.G., and Fridman, R. ‘Discoidin domain receptor tyrosine kinases: new players in cancer progression’. *Cancer and Metastasis Reviews*, **31(1)**:(2012), 295–321. doi:10.1007/s10555-012-9346-z.

[vdL08] van de Linde, S., Kasper, R., Heilemann, M., and Sauer, M. ‘Photoswitching microscopy with standard fluorophores’. *Applied Physics B*, **93(4)**:(2008), 725. ISSN 1432-0649. doi:10.1007/s00340-008-3250-9.

[Ver11] Vermeulen, P., Muro, E., Pons, T., Loriette, V., and Fragola, A. ‘Adaptive optics for fluorescence wide-field microscopy using spectrally independent guide star and markers’. *Journal of Biomedical Optics*, **16**:(2011), 16 – 16 – 9. doi:10.1117/1.3603847.

[Vic07] Vicky, K., Axel, B., and Wolfgang, B. ‘How fast can TCSPC FLIM be made?’ *Proc.SPIE*, **6771**:(2007), 6771 – 6771 – 7. doi:10.1117/12.735550.

[Vic11] Vicidomini, G., Moneron, G., Han, K.Y., Westphal, V., Ta, H., Reuss, M., Engelhardt, J., Eggeling, C., and Hell, S.W. ‘Sharper low-power STED nanoscopy by time gating’. *Nature Methods*, **8**:(2011), 571–573. doi:10.1038/nmeth.1624.

[Vin11] Vinke, F.P., Grieve, A.G., and Rabouille, C. 'The multiple facets of the Golgi reassembly stacking proteins'. *Biochemical Journal*, **434(3)**:(2011), 575–576. ISSN 0264-6021. doi: 10.1042/BJ4340575u.

[Vog97] Vogel, W., Gish, G.D., Alves, F., and Pawson, T. 'The Discoidin Domain Receptor Tyrosine Kinases Are Activated by Collagen'. *Molecular Cell*, **1(1)**:(1997), 13 – 23. ISSN 1097-2765. doi:10.1016/S1097-2765(00)80003-9.

[Wan13] Wang, Y., Meng, P., Wang, D., Rong, L., and Panezai, S. 'Speckle noise suppression in digital holography by angular diversity with phase-only spatial light modulator'. *Opt. Express*, **21(17)**:(2013), 19568–19578. doi:10.1364/OE.21.019568.

[War10] Warber, M., Maier, S., Haist, T., and Osten, W. 'Combination of scene-based and stochastic measurement for wide-field aberration correction in microscopic imaging'. *Appl. Opt.*, **49(28)**:(2010), 5474–5479. doi:10.1364/AO.49.005474.

[War13] Warren, S.C., Margineanu, A., Alibhai, D., Kelly, D.J., Talbot, C., Alexandrov, Y., Munro, I., Katan, M., Dunsby, C., and French, P.M.W. 'Rapid Global Fitting of Large Fluorescence Lifetime Imaging Microscopy Datasets'. *PLOS ONE*, **8(8)**:(2013), 1–17. doi:10.1371/journal.pone.0070687.

[War14] Warren, S.C. *Development and application of multiplexed fluorescence imaging to chemotaxis signalling pathways*. Ph.D. thesis, Imperial College London (2014).

[Wat10] Watanabe, T., Thayil, A., Jesacher, A., Grieve, K., Debarre, D., Wilson, T., Booth, M., and Srinivas, S. 'Characterisation of the dynamic behaviour of lipid droplets in the early mouse embryo using adaptive harmonic generation microscopy'. *BMC Cell Biology*, **11(1)**:(2010), 38. ISSN 1471-2121. doi:10.1186/1471-2121-11-38.

[Wei15] Weigel, D., Kiessling, A., and Kowarschik, R. 'Aberration correction in coherence imaging microscopy using an image inverting interferometer'. *Opt. Express*, **23(16)**:(2015), 20505–20520. doi:10.1364/OE.23.020505.

[Wil84] Wilson, T. and Sheppard, C. *Theory and practice of scanning optical microscopy*, volume 180. Academic Press London (1984).

[Wil08] Willoughby, D. and Cooperand, D.M.F. 'Live-cell imaging of cAMP dynamics'. *Nature Methods*, **5(1)**:(2008), 29–36. doi:doi:10.1038/nmeth1135.

[Wil11] Wilson, T. 'Resolution and optical sectioning in the confocal microscope'. *Journal of Mi-*

croscopy, **244(2)**:(2011), 113–121. ISSN 1365-2818. doi:10.1111/j.1365-2818.2011.03549.x.

[Wil16] Wilding, D., Pozzi, P., Soloviev, O., Vdovin, G., and Verhaegen, M. 'Adaptive illumination based on direct wavefront sensing in a light-sheet fluorescence microscope'. *Opt. Express*, **24(22)**:(2016), 24896–24906. doi:10.1364/OE.24.024896.

[Wol59] Wolf, E. 'Electromagnetic diffraction in optical systems - I. An integral representation of the image field'. *Proceedings of the Royal Society of London A: Mathematical, Physical and Engineering Sciences*, **253(1274)**:(1959), 349–357. ISSN 0080-4630. doi:10.1098/rspa.1959.0199.

[Xu14] Xu, H., Abe, T., Liu, J.K.H., Zalivina, I., Hohenester, E., and Leitinger, B. 'Molecular Analysis of Collagen Binding by the Human Discoidin Domain Receptors, DDR1 and DDR2'. *JBC*, **2781**:(2014), 16761–16769. doi:doi:10.1074/jbc.M113.536144.

[Yan02] Yang, J., Liu, X., Yue, G., Adamian, M., Bulgakov, O., and Li, T. 'Rootletin, a novel coiled-coil protein, is a structural component of the ciliary rootlet'. *The Journal of Cell Biology*, **159(3)**:(2002), 431–440. ISSN 0021-9525. doi:10.1083/jcb.200207153.

[Yan14] Yang, B., Przybilla, F., Mestre, M., Trebbia, J.B., and Lounis, B. 'Large parallelization of STED nanoscopy using optical lattices'. *Opt. Express*, **22(5)**:(2014), 5581–5589. doi:10.1364/OE.22.005581.

[Yan16] Yang, M.H., Abashin, M., Saisan, P.A., Tian, P., Ferri, C.G.L., Devor, A., and Fainman, Y. 'Non-degenerate 2-photon excitation in scattering medium for fluorescence microscopy'. *Opt. Express*, **24(26)**:(2016), 30173–30187. doi:10.1364/OE.24.030173.

[Yil03] Yildiz, A., Forkey, J.N., McKinney, S.A., Ha, T., Goldman, Y.E., and Selvin, P.R. 'Myosin V Walks Hand-Over-Hand: Single Fluorophore Imaging with 1.5-nm Localization'. *Science*, **300(5628)**:(2003), 2061–2065. ISSN 0036-8075. doi:10.1126/science.1084398.

[Yu09] Yu, Y., Arora, A., Min, W., Roifman, C.M., and Grunebaum, E. 'EdU incorporation is an alternative non-radioactive assay to [3 H] thymidine uptake for in vitro measurement of mice T-cell proliferations'. *Journal of immunological methods*, **350(1)**:(2009), 29–35.

[Zei17a] Zeiss, C. 'Carl Zeiss'. `https://www.zeiss.com/` (2017). [Online; accessed 19-July-2017].

[Zei17b] Zeiss, C. 'Elyra.S1'. `https://www.zeiss.com/microscopy/int/products/superresolution-microscopy.html` (2017). [Online; accessed 15-July-2017].

[Zer34] Zernike, F. 'Beugungstheorie des Schneidenverfahrens und seiner verbesserten Form, der

Phasenkontrastmethode'. *Physica*, **1(7)**:(1934), 689 – 704. ISSN 0031-8914. doi:10.1016/S0031-8914(34)80259-5.

[Zim02] Zimmermann, T., Rietdorf, J., Girod, A., Georget, V., and Pepperkok, R. 'Spectral imaging and linear un-mixing enables improved FRET efficiency with a novel GFP2–YFP FRET pair'. *FEBS Letters*, **531(2)**:(2002), 245–249. ISSN 1873-3468. doi:10.1016/S0014-5793(02)03508-1.

[Zin01] Zinchuk, V. and Zinchuk, O. *Quantitative Colocalization Analysis of Confocal Fluorescence Microscopy Images*. John Wiley & Sons, Inc. (2001). ISBN 9780471143031. doi:10.1002/0471143030.cb0419s39.

Appendix A

Depletion laser manual

Written by Dr. Timothy Runcorn. More detailed information can be found in his PhD thesis [Run15a].

femtosecond optics group

RFL-1.0-560-BD

Frequency Doubled Fiber Raman Laser

User's Guide

Contents

1. Device Description 3

2. Precautions Before Use 4

3. Operating Instructions 5

4. Troubleshooting 7

5. Output Specifications 9

1. Device Description

The RFL-0.6-560-BD is a state-of-the art frequency-doubled Raman fibre laser that produces pulsed visible radiation with near diffraction limited beam quality. The novel fibre architecture efficiently converts ytterbium-fibre technology to 1120 nm that is frequency doubled to 560 nm in a periodically-poled lithium tantalate crystal.

The device generates up to 1 W of 560 nm radiation, with a tunable pulse duration from 35 ps – 1.5 ns with the repetition rate correspondingly scaled from 50 MHz – 2.5 MHz. The source provides a variable delay electrical synchronous output or can alternatively be triggered by an external source.

2. Precautions Before Use

The device can output greater than 2 W of invisible IR radiation at 1120 nm and up to 1 W of visible radiation at 560 nm. **Always** ensure that all beam paths are appropriately terminated and that the correct laser safety eyewear is worn whilst the device is operational.

The components of the device can be damaged if the correct turn-on procedure detailed in Section 3 is not followed. **Never** enable the emission of the power amplifier if the seed power is < 1 mW (see Section 4 for solution). **Never** power the pre-amplifier without the 1064 nm seed laser bias and pulse generator being active.

The collimator head has an anti-reflection coated output window that **must** be kept clean. **Do not** attempt to clean dust and debris from the window, contact the supplier if it looks contaminated.

The alignment of the frequency doubling unit is critical, damage may occur if any of the optics are displaced. **Never** alter the alignment of the mounts and **immediately** stop emission if the output beam looks distorted or the power has significantly dropped.

3. Operating Instructions

The device **must** be switched on in the correct order to ensure correct operation and prevent damage to the components. Begin with all of the components in standby/powered off, ensure the precautions in Section 2 have been fulfilled and complete the following procedure:

1. Switch on the frequency doubling crystal oven temperature controller. The temperature should be set to 125.3 °C and the temperature should rise to this over several minutes and settle. If it does not, contact the supplier and **do not** proceed.

2. Switch on the 1120 nm diode power supply (Thulby). The power supply **must** be set to 5.0 V and the current limit set to 3 A **before** the output (right hand switch) is activated. Switch on the output, the LEDs on the diode should illuminate initially as red and then two steady greens, indicating the diode is emitting and the temperature controller is working. **Do not** proceed if the two green LEDs are not illuminated and contact the supplier. When the diode is activated, ~10 mW of 1120 nm is outputted from the collimator head and a dim 560 nm output beam should be visible.

3. Activate the temperature controller for the 1064 nm seed diode. The diode should be set to a resistance of 10 kΩ. Once the output is enabled, the temperature should move to and settle at the set point rapidly, if it does not contact the supplier and **do not** proceed.

4. Activate the 1064 nm seed diode bias. The current should be set to 5.0 mA. Once the output is enabled, the current should increase from zero to the set point, if it does not contact the supplier and **do not** proceed.

5. Turn on the Geozondas pulse generator. Ensure the 2.5 MHz repetition rate is selected and the amplitude and pulse width knobs are turned to the maximum (fully clockwise). Select the 'Internal' trigger option by pressing the 'INT' button, the red LED adjacent will illuminate. Activate the pulse head by pressing the 'Unit A' button, the red LED above will illuminate.

6. Activate the output of the pre-amplifier power supply (Fluke). The power supply **must** be set to a current of 2.5 A **before** the output is activated. When the supply is activated the screen should display ~2 V and 2.5 A, if it does not contact the supplier and **do not** proceed.

7. Switch on the ytterbium fiber amplifier by turning the key to the ‘ON’ position. Once the control window is displayed, press the green start button. The ‘Case T’ and ‘Input’ fields should change from ‘N/A’ to ‘wait’ and then display the case temperature and input power. The input power should read > 1 mW, if it does not contact the supplier and **do not** proceed.

8. Set the desired current set point, either using the slider (ensure ‘Lock’ is displayed beneath to enable the slider, press ‘Lock’ to prevent accident adjustment) or by pressing on the output power indicator and entering the desired current on the keypad that will be displayed. The current set point is displayed next to ‘ACC Set’. Use the provided power output curve (Section 4) to select the desired current point. **Always** ensure the amplifier is in ‘ACC’ control mode rather than ‘APC’ as greater power stability is achieved.

9. **Check** the output collimator widow is uncontaminated, ensure the beam path is unobstructed and that both the 560 nm and residual 1120 nm beams are safely terminated. Press the ‘Emission’ button and ‘OK’ to the start emission prompt. The orange light on the amplifier will flash and turn solid as the output is enabled. The output power indicator should display > 0.03 W.

This procedure should be reversed to power down the system. **Never** adjust the seed diode settings (bias, temperature, pulse parameters) with the amplifier emission switched on. **Always** turn off the power amplifier before the pre-amplifier and the pre-amplifier before the seed.

4. Troubleshooting

Below is a table of potential issues that might occur when using the device. If in any doubt, power the device down by reversing the procedure detailed in Section 3 and contact the supplier.

Issue	Possible Cause	Solution
The amplifier emission is enabled but there is no output power and the power monitor reads 0.02/3 W	The amplifier has a bug which causes this – it typically occurs when the seed power changes whilst the start (green) button is engaged	Press the ‘Emission’ button to turn off the emission then press the ‘Control Mode’ button to switch it to ‘APC’. Ensure the power is set to 0%. Press the ‘Emission’ button and OK to the ‘Start Emission’ prompt. A ‘Modulation error’ or ‘High back reflection’ error will show, clear this error. Press the ‘Control Mode’ button to switch back to ‘ACC’, press the green start button, check the seed power is > 1 mW and then enable emission.
The 1120 nm seed diode is on (two green LEDs illuminated) but the dim 560 nm beam is not visible	The crystal is not at 125.3 °C	Ensure the crystal oven is switched on and is set to 125.3 °C
	The half waveplate after the collimator head is not correctly positioned	Ensure the beam is passing through the waveplate and that the waveplate is rotated to the correct position
	The frequency doubling optics have become misaligned	**Do not** turn on the amplifier, contact the supplier
The amplifier is emitting power but the 560 nm power is less than normal	The 1120 nm seed diode is not emitting	Ensure the two green LEDs on the diode are illuminated and that

		~10 mW of 1120 nm is emitted from the collimator head, if not contact the supplier
	The frequency doubling unit optics have become misaligned	**Do not** turn on the amplifier, contact the supplier
The amplifier input power monitor is < 1 mW	The pre-amplifier is not switched on	Ensure the 1064 nm seed diode bias and pulse generator are active. Set the Fluke power supply current to 2.5 A and the set voltage to 10 V. Activate the output of the power supply, it should display ~2 V and 2.5 A, if not contact the supplier
	The 1064 nm diode bias or pulse generator are not active	Turn off the pre-amplifer **immediately**. The power amplifier input power monitor should read ~0.02 mW if the seed diode bias and pulse generator are active, if not contact the supplier.

5. Output Specifications

Parameter	Value
Maximum 560 nm Output Power	970 mW
Optimised Pulse Duration at 2.5 MHz Repetition Rate	1.9 ns
Central Wavelength	560.0 nm
Spectral Bandwidth	≤ 0.02 nm
Output Beam Diameter	2.0 mm
Output Beam Ellipticity	0.95
Output Beam M^2	≤ 1.11
Polarisation Extinction Ratio	> 30 dB

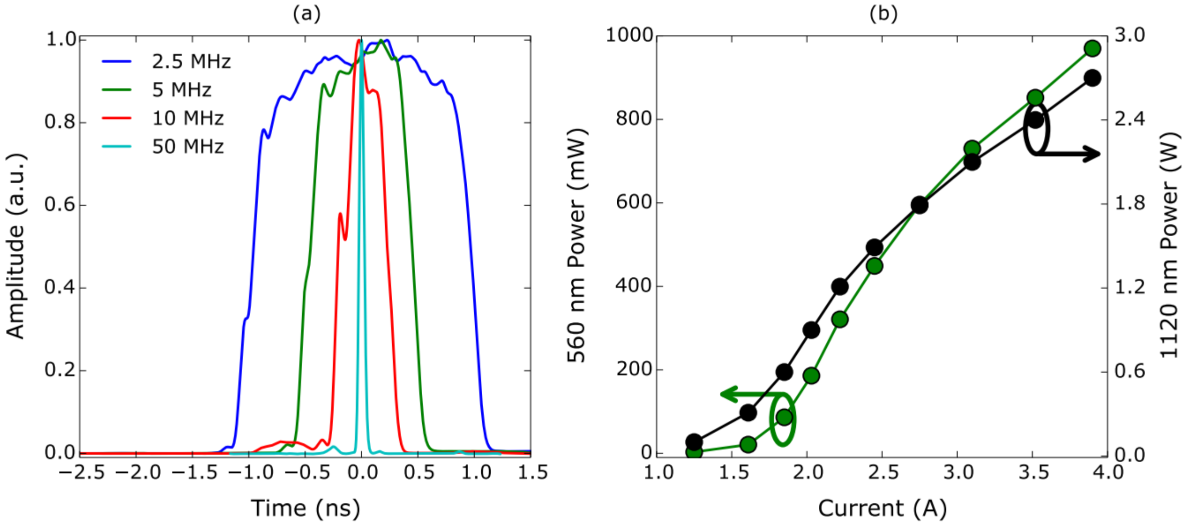

Fig. 1. (a) Sampling optical oscilloscope traces of the optimised pulse durations at different repetition rates. (b) 1120 nm and 560 nm average power as a function of amplifier current for at a repetition rate of 2.5 MHz.

Amp Setting (A)	1120 nm Power (W)	560 nm Power (mW)
3.90	2.70	970
3.52	2.40	852
3.10	2.10	730
2.75	1.79	596
2.45	1.49	449
2.22	1.21	321
2.03	0.90	186
1.85	0.60	86.3
1.61	0.31	20.9
1.25	0.10	3.11

Table 1. Output average power for amplifier set currents at a repetition rate of 2.5 MHz

Repetition Rate (MHz)	1120 nm Power (W)	560 nm Power (mW)	Diode Bias (mA)	Pulse Duration (ps)
2.5	2.70	970	5.0	1900
5	2.43	800	9.0	890
10	2.15	540	7.5	430
25	1.55	120	7.5	40 (pre-pulse present)
50	1.27	65	7.5	35

Table 2. Optimised pulse duration and corresponding output powers for different repetition rates